Investigating and Enhancing Spin Reversal Barriers in Dinuclear 4*f* Single-Molecule Magnets and the Ultimate Shift to Mononuclear 3*d* Complexes

by

Fatemah Habib

Thesis submitted to the
Faculty of Graduate and Postdoctoral Studies
in partial fulfillment of the requirements
for the Doctorate in Philosophy degree in Chemistry

Department of Chemistry
Faculty of Science
University of Ottawa

Abstract

In order for molecular magnetic materials to become applicable, they must retain their magnetisation at reasonable temperatures, which can be achieved with high energy barriers for spin reversal and high blocking temperatures. In the field of Single-Molecule Magnets (SMMs), over the last decade, the main focus has shifted from large spin complexes to highly anisotropic systems which have displayed record energy barriers. There are two main methods of increasing magnetic anisotropy in a complex: i) Choosing a metal ion that boasts high magnetic anisotropy then coupling two such ions through magnetic interactions to induce large global anisotropy, and ii) maintain a low spin or use a mononuclear complex while minimising quantum tunnelling of the magnetisation by controlling the geometric features of the metal ion. Both strategies are equally valid and have been explored in this thesis using dinuclear lanthanide as well as mononuclear 3*d* complexes.

In the pursuit of high-barrier SMMs *via* alignment of anisotropy axes, two dinuclear, quadruple-stranded helicates and one mesocate were isolated and are described in detail herein, both structurally and magnetically. Furthermore, theoretical calculations have been performed to determine the energies of Kramers doublets on each Dy^{III} centre to derive magneto-structural correlations. To induce magnetic interactions between Dy^{III} ions, a centrosymmetric dinuclear SMM was synthesised. Investigation of the crucial $Dy^{III}\ldots Dy^{III}$ interaction as well as its effect on the quantum tunnelling of the magnetisation has been carried out using *ab initio* calculations and magnetic dilution studies. Using the same system, a method of greatly enhancing the energy barriers in SMMs has been developed. It involves modifying the coordinating ligands to include electron withdrawing groups in order to yield more anisotropic metal ions. The energy barrier for spin reversal has been increased 7-fold in one case. While lanthanide chemistry has proven to be quite versatile and promising, a new branch of nanomagnets is currently being pursued: mononuclear 3*d* complexes as SMMs. The advantages of 3*d* metals include high anisotropy per ion, low spin (as anisotropy decreases with increasing spin), well-understood electronic structures and clear correlations between geometry and magnetic anisotropy. The structural and magnetic properties of three complexes based on Co^{II} and terpyridine ligands as well as a seven-coordinate Co^{II} complex with positive anisotropy are discussed at length. The unique slow relaxation dynamics and spin crossover behaviour has been followed using DFT and *ab initio* calculations, as well as EPR and magnetic dilution studies.

Overall, this thesis describes the efforts taken to synthesise high-barrier nanomagnets through understanding the origins and mechanisms of slow magnetic relaxation in both lanthanide and 3*d* metal complexes.

Acknowledgements

There are oh so many people that must be acknowledged in this section for their contributions not just to research, but to everyday life in and out of the lab, 7 days of the week for the duration of my graduate work (and, I expect, for many years to come).

Firstly, I cannot express the extent of my gratitude to my supervisor, Prof. Murugesu. He always found time for my chemistry and I regardless of his more-than-busy schedule. His mentorship and guidance were invaluable over the many years that I have known him and worked with him. My most sincere thank you for all the motivating chats when I desperately needed them, the challenging goals he always set for me and for constantly pushing me to do better throughout my entire time here. I am truly grateful that Muralee trusted me over the years to supervise students in the lab, from summer students to honors students, which helped me immensely by building and honing my leadership and mentoring skills. Furthermore, I am honoured to have had the opportunity to represent the Murugesu group at major international conferences, thank you for your confidence in me. On a more personal note, I will always be indebted to Muralee for his constant support, regardless of which direction I chose to go in, for the endless reference letters he wrote (such elegant letters), for the numerous opportunities to explore the world and widen my horizons, and for the freedom to discover what I wanted to do with my future. As an aside, I would also like to thank baby Ayden for keeping the boss busy for a while so I can become even more independent in the lab and develop some side projects that intrigued me.

One of the great advantages of being at OttawaU, and in the Murugesu group particularly, is the wealth of collaborations not just within the department but on an international scale as well. I would like to extend my heartfelt gratitude to the following collaborators who were invaluable over the years: i) Dr. Ilia Korobkov, for solving every crystal structure in this thesis and always taking my calls no matter what the shape of the queue happened to be, ii) Dr. Serge Gorelsky, for the DFT calculations and stimulating/thought-provoking conversation over the years, I am in awe of your wealth of knowledge, iii) Dr. Liviu F. Chibotaru and his group, for all the *ab initio* calculations presented in this thesis and over the years at many many conferences, vi) Dr. Steve Hill and his students, for all the EPR studies, v) Dr. Crabtree and his group for one of the Co^{II} complexes, vi) Dr. Wolfgang Wernsdorfer for the micro-SQUID measurements, and vii) Dr. Rodolphe Clérac, for his constant support and enthusiasm about anything magnetism and SQUID-related, for giving me the great opportunity of carrying out a research stay in France, working with him and his group and for always answering my emails regardless of how busy

he is. I would also like to thank him for introducing me to the teamviewer app on my phone which ensured the SQUID never slept as long as there was an internet connection.

Next, I want to acknowledge members of the Murugesu group, both in Ottawa and around the world who will remain great friends long after I've defended this thesis. They made the lab environment so stimulating and the end-of-day drinks so motivating that it was hard to stay away for longer than the necessary 6 hours of sleep. Starting with the former members, Dr. Jérome Long, Dr. Cyril Cook, Dr. Matt Jeletic and Dr. Tomoko Aharen. Dr. Po-Heng Lin deserves a special mention here for his ongoing support and help with anything chemistry, and for being just an amazing person to have around, the lab has not been the same since he left (to bigger and better things). All the French exchange students, too many to name, were also great additions to the lab every summer, always so cheerful and gave me the chance to practice my French. All the former undergraduate students who I had the honour of supervising in the lab, especially A. J. Hutchings who was quite the star when it came to science. She inspired me to be a better mentor, not just a good scientist. We will meet again in Germany I'm sure. A special thanks to Dr. Judith Caballero who was the most cheerful person I've had the pleasure to work with, there was not one day when she didn't put a smile on my face (I'm still working on my Spanish numbers!).

Current group members: Jen, Becky, Elena, Amélie and Katie, I could not have asked for better labmates. I've always been told that without a great group of people in the lab, nothing gets done, luckily I have never had that problem (or maybe those people are crazy) but thank you for being such a great support, always willing to go for beers and for all the great times at La Casa and other venues around campus. I had the privilege to supervise Gabe during his undergraduate studies, thanks for being such a willing learner and an awesome labmate and friend (and good luck with the masters!). Yuting has been an amazing friend in and out of the lab, always willing to keep me away from whatever food, alcohol and caffeinated drink I happen to have given up that month. I cannot list all the Murugesu lab members over the years but I really appreciate the contributions of every single one, thank you.

To those within the UOttawa chemistry department (and some who have graduated already), the Brusso Bunch, the Baker group members, the CGSA club members, those that went skydiving and bungee jumping with me, Dr. Robyn Biggs and many more, thank you for helping make my years here exciting and full of adventures.

Last, but certainly not least, my sincere thanks to my family and friends who always stood by me and entertained my wild ideas, cheered me on at my graduations and gave me pep talks when I was down. This would not have been possible without you.

Table of Contents

List of Tables

List of Figures

List of Schemes

0.1 Contribution Statement

The research highlighted in this thesis was carried out over several years with the invaluable guidance and mentorship of Professor Murugesu as well as collaborations that extended across the Atlantic. It is important that I outline my contributions (and those of others) to the different projects discussed in detail herein.

Lanthanide coordination complexes behaving as Single-Molecule Magnets (SMMs) were first isolated by Dr. Po-Heng Lin in the Murugesu group, a few years prior to the start of my graduate work. Some basic synthetic strategies were developed by him, which I was able to tune in order to synthesise the lanthanide complexes discussed in this thesis. Others who contributed significantly to more than one project were Dr. Ilia Korobkov (responsible for measuring and solving all the single crystal X-ray structures in this thesis), Dr. Liviu F. Chibotaru and members of his group in Belgium (responsible for all the *ab initio* calculations) and Dr. Wolfgang Wernsdorfer in Grenoble, France (responsible for all the micro-SQUID measurements).

For the project involving the helicates and mesocate, Dr. Jerome long was instrumental in isolating one of the helical structures. Further ligand design as well as complex synthesis was done by me. The magnetic properties of the helicates with respect to the SQUID were measured, plotted and analysed by myself, with the help of Dr. Lin. The idea of using these helical structures to align anisotropy axes on different metal centres in SMMs was truly a unique and original concept in this field.

The next project involving the $[Dy_2(valdien)_2(NO_3)_2]$ SMM and its analogues was initiated by Dr. Jerome Long, who handed the reins over to me for some of the magnetic studies. The dilution studies of this complex using the Y^{III} analogue (both synthesis and magnetic measurements) were done entirely by me. The micro-SQUID dc measurements were performed by Dr. Wernsdorfer, as mentioned earlier. Using magnetic dilution in order to showcase the magnetic relaxation of a dinuclear *vs.* mononuclear complex as well as the way in which they both contribute to the overall magnetic properties was one of my most important contributions to this field. Additionally, we were able to directly observe the magnetic interaction between the metal centres and its effect on the slow magnetic relaxation. After this work, dilution studies became benchmark studies performed on many complexes to elucidate relaxation dynamics.

The work with ligand exchange on the parent $[Dy_2(valdien)_2(NO_3)_2]$, where terminal ligands were exchanged to create two different systems with varying electronic properties

was carried out mostly by myself (Chapter 4). I performed the synthesis, characterisation (except single-crystal X-ray analysis) and magnetic investigations for all complexes. Gabriel Brunet was involved in the synthesis of one of the analogues. All *ab initio* calculations were carried out in collaboration with Dr. Chibotaru and his student V. Vieru. Through this work we were able to show the significant effects that the electronics of the ligand have on the spin reversal barrier in two different systems. This is also one of my most valuable contributions to this field as it provides a relatively simple synthetic strategy to push the energy barriers even higher. By simply using more electron deficient ligands, the barrier could be increased 7-fold!

The last section of this thesis involves mononuclear 3*d* complexes which behave as SMMs and possess unique features in their ac properties. This is a relatively new branch of this field and hence all contributions are significant to further our understanding of the dynamics of slow relaxation in this type of SMM. For this project, Dr. S. I. Gorelsky performed the DFT calculations to elucidate the *d*-orbital splitting diagrams for different complexes. Additionally, Prof. R. H. Crabtree and his group at Yale University provided the complex, $[Co(terpy)Cl_2]$ for magnetic study. I synthesised the remaining complexes in Chapters 5 and 6, as well as performed all the magnetic studies. The EPR studies were performed in collaboration with Dr. S. Hill and his student M. Shiddiq in Tallahassee, Florida. As for the seven-coordinate Co^{II} complex (Chapter 6), it was already published and studied extensively by T. Mallah and co-workers with no ac measurements reported. At the time, there were only two reports of SMMs exhibiting positive anisotropy, so I decided to take a chance on it and measure its ac properties. To my surprise, it did behave as an SMM under field which then led to further studies using magnetic dilution to prove that the unique features in the ac plots of 3*d*-SMMs are due to intermolecular interactions.

The peer-reviewed articles which resulted from my graduate work, both the projects highlighted in this thesis and those which I did not have the page space for, are listed below. My contributions towards these studies can be gauged relatively well by the order of authorship in the published articles.

Contributions

1. **F. Habib**, I. Korobkov, M. Murugesu, Exposing the Intermolecular Nature of the Second Relaxation Pathway in a Cobalt(II) Single-Ion Magnet with Positive Anisotropy. *Dalton Trans.* 2014, *submitted manuscript.*

2. A.-J. Hutchings, **F. Habib**, P.-H. Lin, I. Korobkov, M. Murugesu, Structural Rearrangement through Lanthanide Contraction in Dinuclear Complexes. *Inorg. Chem.* 53 (2014), 2102-2112.

3. R. J. Holmberg, A.-J. Hutchings, **F. Habib**, I. Korobkov, J. C. Scaiano, M. Murugesu, Hybrid Nanomaterials: Anchoring Magnetic Molecules on Naked Gold Nanocrystals. *Inorg. Chem.* 52 (2013), 14411-14418.

4. **F. Habib**, G. Brunet, V. Vieru, I. Korobkov, L. F. Chibotaru, M. Murugesu, Significant Enhancement of Energy Barriers in Dinuclear Dysprosium Single-Molecule Magnets Through Electron Withdrawing Effects. *J. Am Chem. Soc.* 135 (2013), 13242-13245.

5. **F. Habib**, O. R. Luca, V. Vieru, M. Shiddiq, I. Korobkov, S. I. Gorelsky, M. K. Takase, L. F. Chibotaru, S. Hill, R. H. Crabtree, M. Murugesu, Influence of the Ligand Field on Slow Magnetization Relaxation *versus* Spin Crossover in Mononuclear Cobalt Complexes. *Angew. Chem. Int. Ed.* 52 (2013), 11290-11293.

6. O. R. Luca, S. J. Konezny, E. K. Paulson, **F. Habib**, K. M. Luthy, M. Murugesu, R. H. Crabtree, V. S. Batista, Study of an $S = 1$ Ni(II) pincer electrocatalyst precursor for aqueous hydrogen production based on paramagnetic ^{1}H NMR. *Dalton Trans.* 42 (2013), 8802-8807.

7. T. Aharen, **F. Habib**, I. Korobkov, T. J. Burchell, R. Guillet-Nicolas, F. Kleitz, M. Murugesu, Novel Co-based Metal-Organic Frameworks and Their Magnetic Properties Using Asymmetrically Binding 4-(4'-carboxyphenyl)-1,2,4-triazole. *Dalton Trans.* 42 (2013), 7795-7802.

8. **F. Habib**, M. Murugesu, Lessons Learned From Dinuclear Lanthanide Nano-Magnets. *Chem. Soc. Rev.* 42 (2013), 3278-3288.

9. **F. Habib**, G. Brunet, F. Loiseau, T. Pathmalingam, T. J. Burchell, A. M. Beauchemin, W. Wernsdorfer, R. Clérac, M. Murugesu, Turning on Single-Molecule Magnet Behavior in a Linear $\{Mn_3\}$ Complex. *Inorg. Chem.* 52 (2013), 1296-1303.

10. C. Cook, **F. Habib**, T. Aharen, R. Clérac, F. Zhang, A. Hu, M. Murugesu, High-Temperature Spin Crossover Behavior in a Nitrogen-Rich Fe^{III}-Based System. *Inorg. Chem*. 52 (2013), 1825-1831.

11. K. V. Korpany, **F. Habib**, M. Murugesu, A. Szuchmacher Blum, Stable Water-soluble Iron Oxide Nanoparticles Using Tiron. *Mater. Chem. Phys*. 138 (2013), 29-37.

12. **F. Habib**, J. Long, P.-H. Lin, I. Korobkov, L. Ungur, W. Wernsdorfer, L. F. Chibotaru, M. Murugesu, Supramolecular Architectures For Controlling Slow Magnetic Relaxation in Single-Molecule Magnets. *Chem. Sci*. 3 (2012), 2158-2164. Featured in the Inorganic Chemistry Division Calendar of the Canadian Chemistry Conference and Exhibition (as the month of June 2012).

13. M. U. Anwar, L. K. Thompson, L. N. Dawe, **F. Habib**, M. Murugesu, Predictable Self-assembled [2x2] $Ln(III)_4$ Square Grids (Ln = Dy, Tb) - SMM Behaviour in a New Lanthanide Cluster Motif. *Chem. Commun*. 48 (2012), 4576-4578.

14. **F. Habib**, C. Cook, I. Korobkov, M. Murugesu, Novel *In Situ* Manganese-Promoted Double Aldol Addition. *Inorg. Chim. Acta* 380 (2012), 378-385. (Young Investigator Award Special Issue)

15. G. Brunet, **F. Habib**, C. Cook, T. Pathmalingam, F. Loiseau, I. Korobkov, T. J. Burchell, A. Beauchemin, M. Murugesu, A Novel High-Spin Tridecanuclear Ni^{II} Cluster with an Azido-Bridged Core Exhibiting Disk-like Topology. *Chem. Commun*. 48 (2012), 1287-1289.

16. M. U. Anwar, S. S. Tandon, L. N. Dawe, **F. Habib**, M. Murugesu, L. K. Thompson, Lanthanide Complexes of Tritopic bis-hydrazone Ligands – SMM Behaviour in a Linear $Dy(III)_3$ Complex. *Inorg. Chem*. 51 (2012), 1028-1034.

17. P.-F. Yan, P.-H. Lin, **F. Habib**, T. Aharen, M. Murugesu, Z.-P. Deng, G.-M. Li, W.-B. Sun, A Planar Tetranuclear Dy(III) Single-Molecule Magnet and Its Sm(III), Gd(III) and Tb(III) Analogues Encapsulated By Salen-Type and β-Diketonate Ligands. *Inorg. Chem.* 50 (2011), 7059-7065.

18. **F. Habib**, P.-H. Lin, J. Long, I. Korobkov, W. Wernsdorfer, M. Murugesu, The Use of Magnetic Dilution to Elucidate the Slow Magnetic Relaxation Effects of a Dy_2 Single-Molecule Magnet. *J. Am. Chem. Soc.* 133 (2011), 8830-8833.

19. J. Long, **F. Habib**, P.-H. Lin, I. Korobkov, G. Enright, L. Ungur, W. Wernsdorfer, L. Chibotaru, M. Murugesu, Single-Molecule Magnet Behavior for an

Antiferromagnetically Superexchange-Coupled Dinuclear Dysprosium(III) Complex. *J. Am. Chem. Soc.* 133 (2011), 5319-5328.

20. J. E.W. Cull, **F. Habib**, I. Korobkov, M. Murugesu, J. Scott, Self-assembly of square-lattice copper sheets displaying intra-ferromagnetism. *Inorg. Chim. Acta*, 370 (2011), 98-101.

List of Abbreviations

ac alternating current

dc direct current

PPMS physical property measurement system

QTM quantum tunnelling of the magnetization

SCM single-chain magnetc

SMM single-molecule magnet

SQUID superconducting quantum interference device

T_B blocking temperature

U_{eff} Energy barrier for spin reversal

H applied field

χ Magnetic susceptibility

χ_{dia} diamagnetic susceptibility

M Magnetisation

M_{sat} Saturation magnetisation

M_r Remnant magnetisation

H_c Coercive field

K Kelvin

k Boltzmann constant

J Coupling constant

C Curie constant

$\boldsymbol{\mu_B}$ Bohr magneton

g Landé *g* factor

S Spin

$\boldsymbol{S_T}$ Total spin

HDVV Heisenberg-Dirac-Van Vleck

$\boldsymbol{\theta}$ Weiss constant

$\boldsymbol{E_n}$ Energy level

$\boldsymbol{\mu_n}$ quantized magnetic moment

VSM Vibrating Sample Magnetometry

$\boldsymbol{\Phi_0}$ Flux quantum

T Temperature

T Tesla

v Frequency

h Oscillating field

$\boldsymbol{\omega}$ Angular frequency

t Elapsed time

$\boldsymbol{\chi}$' In-phase magnetic susceptibility

$\boldsymbol{\chi}$" Out-of-phase magnetic susceptibility

χ_S Adiabatic susceptibility

χ_T Isothermal susceptibility

$\boldsymbol{\tau}$ Relaxation time

$\boldsymbol{\tau_m}$ Measurement time

D Axial magnetic anisotropy parameter

E Transverse anisotropy parameter

ZFS Zero field splitting

SIM Single-Ion Magnet

DFT Density functional theory

Oe Oersted

IR Infrared spectroscopy

NMR Nuclear magnetic resonance

TD-DFT Time-dependent density functional theory

ϕ Angle between anisotropy axes

HSAB Hard soft acid base theory

RASSI Restricted active space state interaction

CASSCF Complete active space self-consistent field

SOC Spin-orbit coupling

Overview of the ligands employed in this thesis and their corresponding labels as presented in the text.

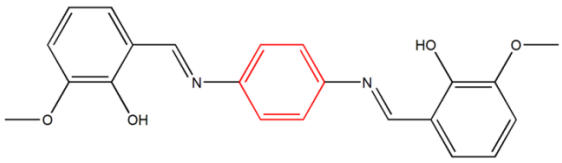

H_2L^1

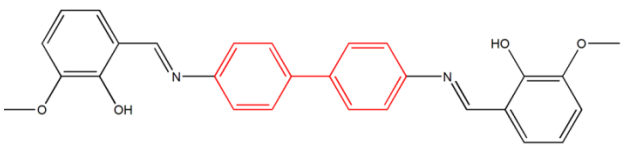

H_2L^2

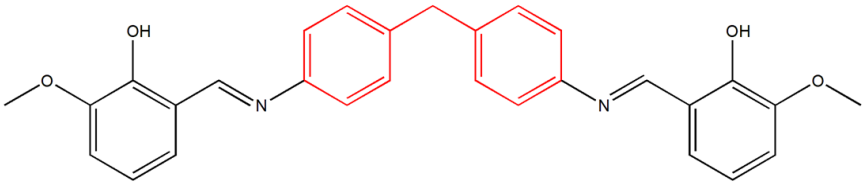

H_2L^3

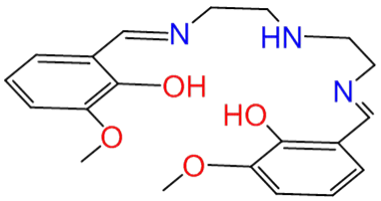

H_2valdien

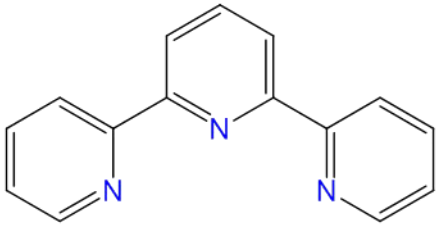

Terpy

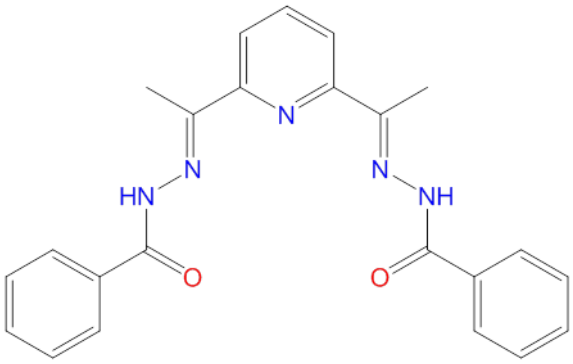

DAPBH

List of numbered complexes and their corresponding chemical formulae.

II-1 $(NEt_4)_2[Dy_2(L^1)_4]((CH_3)_2CO)_{0.25}$
II-2 $(NEt_4)_2[Dy_2(L^2)_4](H_2O)(DMF)_{0.5}$
II-3 $(NEt_4)_2[Dy_2(L^3)_4](Et_2O)_2((CH_3)_2CO)_{1.5}$

$[Ln^{III}_2(valdien)_2(NO_3)_2]$
III-1 $Ln = Dy^{III}$
III-2 $Ln = Gd^{III}$
III-3 $Ln = Y^{III}$

IV-1 $[Dy_2(valdien)_2(CH_3COO)_2]$
IV-2 $[Dy_2(valdien)_2(ClCH_2COO)_2]$
IV-3 $[Dy_2(valdien)_2(Cl_2CHCOO)_2]\cdot 0.5$ MeOH
IV-4 $[Dy_2(valdien)_2(acac)_2]\cdot 2\ CH_2Cl_2$
IV-5 $[Dy_2(valdien)_2(F_6acac)_2]$

V-1 $[Co(terpy)Cl_2]$
V-2 $[Co(terpy)(NCS)_2]$
V-3 $[Co(terpy)_2](NCS)_2\cdot 1.5H_2O$

$[M(DAPBH)(NO_3)(H_2O)](NO_3)$
VI-1 $M = Co^{II}$
VI-2 $M = Zn^{II}$

Chapter 1

Introduction

One of the key limitations of current information storage systems based on metal oxides or mixed metal materials is the density of information that can be stored within them. Hard discs based on inorganic materials rely on domains composed of thousands to millions of metal ions in order to store bits of information encoded in spins. To increase the information density within these discs, we must encode it on a molecular level; while each domain composed of millions of metal ions represents a single bit of information, in a molecular system, each metal ion can now be considered a domain of its own, thereby significantly enhancing the density of information stored. Additionally, a molecular system will be easier to predict and control in terms of structure which, in turn, will allow better control of the magnetic properties as they are highly dependent on the size and shape of the materials used. Molecule-based systems that are currently being investigated include Single-Molecule Magnets (SMMs) and Single-Chain Magnets (SCM). Both SMMs and SCMs are superparamagnetic materials which possess a blocking temperature (T_B) for the magnetisation below which they behave as magnets. As magnetic materials, they possess properties shared by bulk magnets, such as magnetic hysteresis where retention of magnetisation can be observed. Additionally, they can be synthesised in a controlled fashion and can be soluble in organic solvents, which render their manipulation much more favourable than bulk magnets.

In order to stabilise the metal ion, diamagnetic ligands such as small organic molecules or inorganic ligands such as NO_3^-, can be used. The ligand field around the metal centers will control the electronic and magnetic properties of the entire complex. This is extremely important as this is the basis for not only fine-tuning the magnetic properties but also for controlling or imposing certain physical properties on these molecule-based materials such as volatility, luminescence and solubility. By understanding the fundamental magnetic properties of these complexes and deriving magneto-structural relationships, we can develop reliable design strategies in the quest for higher blocking temperatures. Ideally,

we will need to reach a blocking temperature for the magnetisation of at least room temperature if we are to apply these materials in information storage. Without a blueprint it is very difficult to design and synthesise SMMs in a controlled manner and select for the desired magnetic properties which is the focus of this thesis. There are many researchers in the field currently synthesising SMMs in a serendipitous fashion and studying the magnetic properties of the resultant metal complexes. While this can be a worthwhile endeavour, this thesis focuses on our attempts to answer the fundamental questions surrounding slow magnetic relaxation characteristic of SMMs as well as unravelling the origins of the observed magnetic properties in dinuclear lanthanide and mononuclear transition metal systems. We have focused on the main ingredient necessary for SMM behaviour and that is magnetic anisotropy (the preferential alignment of the spin within a complex) which we believe is at the core of any new discovery in this field.

The interplay between spin and magnetic anisotropy is the key in achieving high blocking temperatures and this introductory chapter will walk the reader through the thought process from the initial reports of lanthanide SMMs to where the field stands at this current point in time. The drastic shifts in the field will be evident and can be traced to the fundamental questions about origins of SMM behaviour which we will attempt to answer using techniques such as magnetic dilution and systematic ligand modification.

1.1 General Magnetism Principles

There are two different fundamental types of magnetism known to exist in atoms, diamagnetism and paramagnetism. Diamagnetism is a property possessed by all matter and originates from the interaction of paired electrons with an applied field (H) generating a field which opposes the applied field. Thus, the value of the diamagnetic contribution is always negative and on the order of 10^{-6} cm^3mol^{-1}. Moreover, diamagnetic susceptibility (χ_{dia}) of atoms in molecules is additive and can be estimated using Pascal's constants or the characteristic atomic susceptibilities which are known for all atoms. Diamagnetism in materials is temperature-independent and can be roughly proportional to the molecular weight of the unit. Paramagnetism, on the other hand, is a property possessed by atoms or ions with unpaired electron(s) which leads to an attraction to an applied magnetic field. A characteristic of paramagnetic materials is the absence of magnetisation retention with the removal of the field (Figure 1.1, blue dashed line). In other words, when a field is applied, spins in paramagnetic material will be aligned parallel to it but will revert to a randomised state when the field is removed.

Electrons in paramagnetic ions can interact in different manners yielding magnetically ordered systems such as ferromagnetic materials. When a ferromagnet is placed in a magnetic field and the field strength is increased, the magnetisation will reach a maximum or a saturation value (M_{sat}) where all spins are aligned parallel to the direction of the applied field (Fig. 1.1).[1] As the applied field is removed, remnant magnetisation (M_r) is observed at $H = 0$, indicating retention of magnetic information by the system. As the applied field is reversed in direction and increased in strength, M_{sat} is eventually achieved in the opposite direction with spin alignment parallel to the applied field. Once again, when the field is removed, M_r is observed. Cycling the applied field in this manner yields hysteretic behaviour where the opening of the hysteresis loop is known as the coercive field (H_c) and indicates the strength of field necessary to demagnetise the material. The coercivity or the width of the hysteresis loop is a measure of the strength of the magnet; hard magnets have large hysteresis openings while softer magnets have much smaller coercive fields.

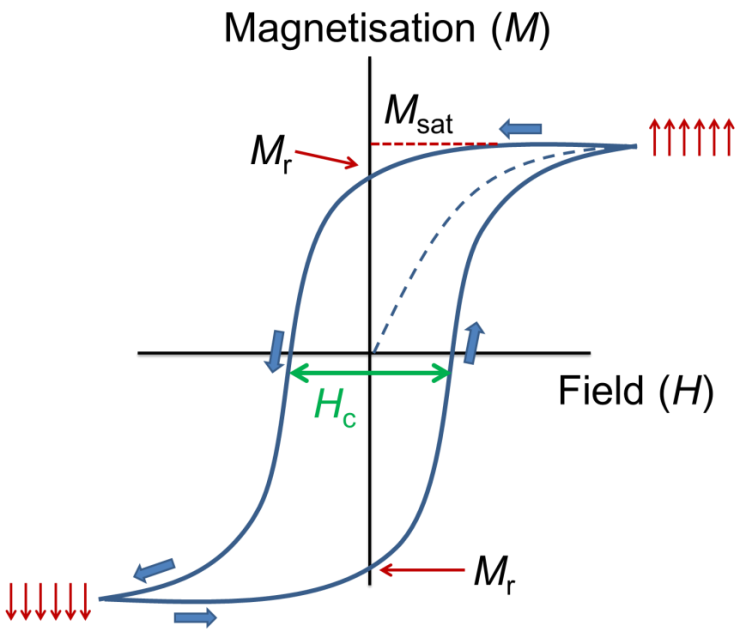

Figure 1.1: Typical hysteresis curve is shown for a ferromagnet plotted as *M vs. H*. The spin saturation is shown in red while the cycling of the field is indicated with blue arrows. H_c denotes the coercive field and is shown as the width of the hysteresis. M_r and M_{sat} indicate remnant and saturation magnetisation, respectively. The dashed blue line indicates the curve observed for paramagnetic materials.

The fundamental principles of magnetism have been studied and published extensively, most of the information in the following section of the introduction can be found

in Ref. 1 and has been a result of the pioneering work of O. Khan and J. H. van Vleck. In an applied magnetic field, the measured response of a material is known as its magnetisation **(Eq. 1.1**):

$$M = \chi * H \quad \text{or} \quad \chi = {}^{M}/_{H} \tag{1.1}$$

where M is the magnetisation, χ is the magnetic susceptibility and H is the applied field. When the applied field is low, χ can be determined according to **Eq. 1.1** since M is experimentally determined and the applied field is known.

1.1.1 Types of Magnetic Interaction

Magnetic interaction in a material consists of spins which are aligned in a certain direction relative to neighbouring spins. This occurs when 3-D ordering within a system is preserved after the applied magnetic field is removed. There are three key types of interactions that can occur: Ferromagnetism, anti-ferromagnetism and ferrimagnetism. It is noteworthy that although magnetic ordering can and does occur, this behaviour is only preserved under a certain temperature characteristic of the material, this temperature is known as the Curie temperature for ferro- and ferrimagnets, and the Néel temperature for anti-ferromagnets. Above these characteristic temperatures, thermal energy is large enough to randomise the spins leading to paramagnetic materials.

Ferromagnetism

A ferromagnetic interaction consists of all spins in a material being aligned in a parallel fashion. When a magnetic field is applied, electrons in a ferromagnetic system will align parallel to the direction of the field, in the same manner as in a paramagnetic system. The difference between the two is apparent once the applied field is removed. In a paramagnetic material, the spins will revert to a randomised state while in a ferromagnetic material the spins will maintain their alignment, as seen in Fig. 1.2 on the left. An example of this type of interaction can be seen in fridge magnets which are magnetised by an applied field then maintain that ferromagnetic state for a long period of time (years).

Anti-ferromagnetism

The second type of interaction, which is the most prevalent within bulk magnets, leads to a zero, non-magnetic state. All spins are aligned anti-parallel to each other and result in a diamagnetic material at absolute 0 K (Fig. 1.2, middle).

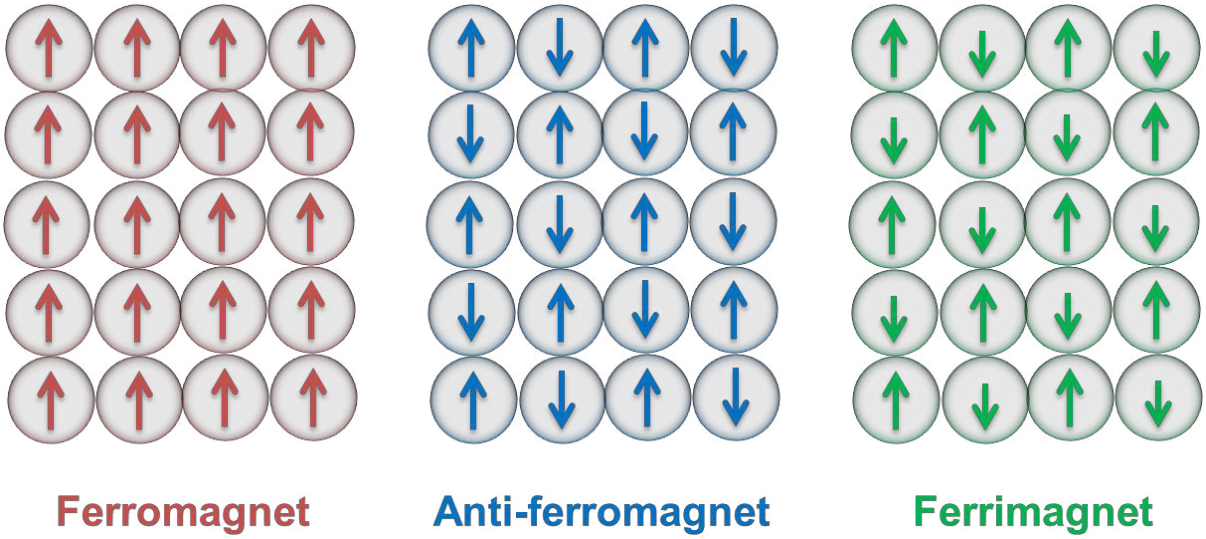

Figure 1.2: Three main types of interaction between spins in two-dimensional magnetic materials. Equal strength magnetic moments align parallel in ferromagnets (left) and anti-parallel in antiferromagnets (middle). Magnetic moments of different strengths align anti-parallel in ferrimagnets (right). Arrows indicate the spins.

Ferrimagnetism

Similar to antiferromagnetic material, all adjacent spins in a ferrimagnet are aligned anti-parallel. The difference lies in the strength of the magnetic moment. In a ferrimagnet, adjacent magnetic moments are not equal in strength leading to residual magnetic moment that is not zero and hence non-diamagnetic material at absolute 0 K. An example would be a material with two different magnetic centres (or metal ions) which are arranged in an alternating fashion and are interacting anti-ferromagnetically (Fig. 1.2, right).

1.1.2 Curie Law and Curie-Weiss Law

Temperature dependence of paramagnetic materials can be described by the Curie law for non-interacting magnetic ions (**Eq. 1.2**):

$$\chi = \frac{N g^2 {\mu_B}^2}{3kT} S\,(S+1) \qquad \textbf{(1.2)}$$

where χ is the molar magnetic susceptibility, N is Avogadro's number, g is the Landé g factor or the spectroscopic splitting factor, μ_B is the Bohr magneton, k is the Boltzmann constant (0.685039 $cm^{-1}.K^{-1}$), T is temperature and S is the spin (of the ground state).[1] The Curie law is only applicable when $H>>kT$ and can be reduced to **Eq. 1.3**, where C is the Curie constant:

$$\chi = \frac{C}{T} \tag{1.3}$$

In order to introduce a magnetic interaction parameter, the Curie law can be modified to the Curie-Weiss law (**Eq. 1.4**) where θ is the strength of the intermolecular exchange interaction. If the sign of the Weiss constant, θ, is positive, we can conclude a ferromagnetic interaction is occurring between metal centers, while a negative θ value indicates anti-ferromagnetic interactions.

$$\chi = \frac{Ng^2{\mu_B}^2 S\,(S+1)}{3kT} \cdot \frac{1}{T-\theta} = \frac{C}{T-\theta} \tag{1.4}$$

From **Eq. 1.4**, θ can lead us to the exchange interaction zJ' which can be derived from **Eq. 1.5** and represents:

$$\theta = \frac{{}_zJ' S_T\,(S_T+1)}{3k} \tag{1.5}$$

Therefore, the expression for the magnetic susceptibility can be seen as **Eq. 1.6**, which takes into account interactions with nearest neighbours and is often employed to account for intermolecular interactions in low applied fields:

$$\chi = \frac{Ng^2{\mu_B}^2 S\,(S+1)}{3kT - {}_zJ' S\,(S+1)} \tag{1.6}$$

The Curie-Weiss law can be used to determine the effective magnetic moment of a sample once the susceptibility is determined experimentally, in addition to the magnetic interaction (at least qualitatively). However, it is no longer being used extensively; instead researchers have now switched to using the Van Vleck equation which relates directly the energy levels with magnetic susceptibility, as opposed to the Curie law which relates susceptibility to the magnetic moment without taking into account the quantum nature of magnetic moments.[1c]

1.1.3 Deriving the Van Vleck Equation

The modern method of theoretically treating paramagnetic systems is to employ the Van Vleck equation. When a material is placed in an applied field, the magnetisation is related to the overall change in energy with the overall change in applied magnetic field:

$$M = \frac{\partial E}{\partial H} \tag{1.7}$$

Since, in this thesis, we are examining molecular magnets, the equation above can be modified to a quantum mechanical expression where each magnetic center is associated with a quantised magnetic moment (μ_n) and an energy level E_n, such that:

$$\mu_n = -\frac{\partial E_n}{\partial H} \tag{1.8}$$

The energy level population is then weighted by a Boltzmann distribution such that the total macroscopic magnetic moment for one mole of substance can be written as:

$$\mu_M = \frac{N \sum_n (-\frac{\partial E_n}{\partial H}) \exp(-\frac{E_n}{kT})}{\sum_n \exp(-\frac{E_n}{kT})} \tag{1.9}$$

In order to proceed, we must consider the energies (E_n) associated with different microstates. To this end, van Vleck proposed developing the energies in powers of H in weak applied fields:

$$E_n = E_n^0 + E_n^1 H + E_n^2 H^2 + \cdots + E_n^x H^x \tag{1.10}$$

where E_n^0 is the energy associated with the level number n under a zero applied magnetic field, $E_n^1 H$ is the first-order Zeeman coefficient, $E_n^2 H^2$ is the second-order Zeeman coefficient, and so on. Since this system is being evaluated at low applied fields, terms greater than 2nd order have a negligible contribution to the overall energy. Additionally, since μ_n is the derivative of E_n with respect to H, **Eq. 1.10** can be written as:

$$-\frac{\partial E_n}{\partial H} = -E_n^1 - 2E_n^2 H$$

(1.11)

Moreover, van Vleck also observed that the 1st and 2nd order Zeeman terms are small with respect to kT, therefore the following approximation can be used:

$$\exp(-\frac{E_n}{kT}) = (1 - \frac{E_n^1 H}{kT}) \exp(-\frac{E_n^0}{kT})$$

(1.12)

By substituting **Eq. 1.11** and **1.12** into **Eq. 1.9**, we can obtain the expression for the molar macroscopic magnetic moment:

$$\mu_M = \frac{N \sum_n (-E_n^1 - 2E_n^2 H)(1 - \frac{E_n^1 H}{kT}) \exp(-\frac{E_n^0}{kT})}{\sum_n (1 - \frac{E_n^1 H}{kT}) \exp(-\frac{E_n^0}{kT})}$$

(1.13)

At zero field, $\mu_M = 0$. Therefore, the following **Eq. 1.14** must be true:

$$\sum_n E_n^1 \exp(-\frac{E_n^0}{kT}) = 0$$

(1.14)

Additionally, in paramagnetic systems with low applied fields, the relationship between μ_M and H is linear hence we can observe the susceptibility is constant and we do not include substances with permanent magnetisation. Thus, we can reduce **Eq. 1.13** taking into account only terms linear with H:

$$\mu_M = \frac{NH \sum_n [\frac{(E_n^1)^2}{kT} - 2E_n^2] \exp(-\frac{E_n^0}{kT})}{\sum_n \exp(-\frac{E_n^0}{kT})}$$

(1.15)

leading to the van Velck equation for molar susceptibility using **Eq. 1.1**:

$$\chi_M = \frac{\mu_M}{H} \quad = \frac{N\sum_n[\frac{(E_n^1)^2}{kT} - 2E_n^2]\exp(-\frac{E_n^0}{kT})}{\sum_n \exp(-\frac{E_n^0}{kT})}$$

(1.16)

where the term E_n^0 includes different sources of zero field splitting and is independent of the applied field. The 1st and 2nd order Zeeman splitting energies are described by E_n^1 and E_n^2, respectively, which are dependent on the external applied field. These energies depend on the interaction between the total spin and orbit angular momenta with the applied field. The van Vleck equation is one of the most useful equations when modelling magnetic data and determining energy levels associated with certain microstates as well as determining coupling constants. However, it does have some limitations; it can only be used when low fields are applied since we must be far from the saturation value where all spins are aligned with the applied field direction (see Fig. 1.1). Additionally, it does not consider permanent magnetisation (long-range ordering in ferro- or ferrimagnetic materials).

In order to solve for the 1st and 2nd order Zeeman splitting energies, we must employ a spin Hamiltonian:

$$\hat{H} = -2J\hat{S}_1.\hat{S}_2$$

(1.17)

Now, we apply the Kambé vector-coupling method and take the sum of S_1 and S_2 as S_T, then square both sides:

$$\hat{S}_T^2 = \hat{S}_1^2 + 2\hat{S}_1.\hat{S}_2 + \hat{S}_2^2$$

$$2\hat{S}_1.\hat{S}_2 = \hat{S}_T^2 - \hat{S}_1^2 - \hat{S}_2^2$$

(1.18)

Substituting **Eq. 1.18** into **1.17**:

$$\hat{H} = -J[\hat{S}_T^2 - \hat{S}_1^2 - \hat{S}_2^2]$$

(1.19)

We can convert **Eq. 1.19** into a modified form which takes into account that the energies or eigenvalues of a Hamiltonian of the form $\hat{S}^2\psi$ are $S(S+1)\psi$, leading to the energy of the zero order term (E_n^0),

$$E(S_T) = -J[S_T(S_T+1) - S_1(S_1+1) - S_2(S_2+1)]$$

(1.20)

After substituting the first order splitting term (E_n^1) which is equal to $g\mu_B H S_T$ and the zero order term (**Eq. 1.20**) into the weak field van Vleck equation (**Eq. 1.16**), we obtain:

$$\chi_M = \frac{Ng^2\mu_B^2}{kT} \frac{\sum(-S_T)^2 \exp(\frac{J\{S_T(S_T+1) - S_1(S_1+1) - S_2(S_2+1)\}}{kT})}{\sum \exp(\frac{J\{S_T(S_T+1) - S_1(S_1+1) - S_2(S_2+1)\}}{kT})} \quad \textbf{(1.21)}$$

Furthermore, we can substitute $\sum(-S_T)^2 = \frac{1}{3}S_T(S_T+1)(2S_T+1)$ into **Eq. 1.21**, and add $(2S_T+1)$ in the denominator to remove the degeneracy of the $S_T(S_T+1)(2S_T+1)$ product in the numerator, leading to:

$$\chi_M = \frac{Ng^2\mu_B^2}{3kT} \frac{\sum S_T(S_T+1)(2S_T+1) \exp(\frac{J\{S_T(S_T+1) - S_1(S_1+1) - S_2(S_2+1)\}}{kT})}{\sum(2S_T+1) \exp(\frac{J\{S_T(S_T+1) - S_1(S_1+1) - S_2(S_2+1)\}}{kT})} \quad \textbf{(1.22)}$$

Throughout this thesis, the spin Hamiltonian above known as the Heisenberg-Dirac-Van Vleck (HDVV) and the expression for the magnetic susceptibility (**Eq. 1.22**) will be used to describe the exchange interaction between two spins and determine the magnetic interaction constant, *J*, between isotropic metal centres such as gadolinium (III) where $S_1 = S_2 = 7/2$. The values for S_T would be $|S_1+S_2|$, $|S_1+S_2-1|$, $|S_1+S_2-2|$, …, $|S_1-S_2|$. Additionally, modelling the experimental data will yield the *g* factor which must be approximately 2 for an isotropic system. The *J* value is the magnetic interaction constant, the sign of which will indicate a ferromagnetic (positive) or antiferromagnetic (negative) interaction.

1.2 Measuring Magnetic Properties

Throughout this thesis, only one method was employed to measure the magnetic data of all complexes discussed, a Superconducting Quantum Interference Device known as a SQUID magnetometer. It is important to note that only samples which were previously characterised using single-crystal x-ray measurements to determine the structure, as well as other techniques to confirm bulk purity were measured using the SQUID. Moreover, we performed impurity magnetic checks on all samples by measuring the magnetisation as a function of the field at 100 K. All of the complexes discussed in this thesis are paramagnetic at 100 K and should give a linear relationship between the magnetisation and field in an *M vs. H* plot with no remnant magnetisation at zero applied field. Deviations from this behaviour indicate

ferromagnetic impurities within the sample. There are two main types of measurements which are performed on all samples: Direct current and alternating current magnetic measurements. Before exploring both types in detail, it is important to describe the working of the magnetometer itself which measures the magnetic moment of the sample.

The SQUID magnetometer is very sensitive to changes in the magnetic field and can be used to determine the magnetic moment of a sample with great accuracy.[2] The SQUID method of measuring magnetic properties relies on flux measurements and can be considered as a special type of Vibrating Sample Magnetometry (VSM).[1d,2a] In VSM, the sample vibrates rapidly between detection coils and an electromotive force is induced by changes in the magnetic flux. The main part of this device consists of two superconductors which are separated by parallel, thin insulating barriers, known as Josephson junctions, creating a superconducting loop (Fig. 1.3). The magnetic flux through the superconducting loop is quantised in units of Φ_0 (the flux quantum, $\Phi_0 = h/2e = 2.0679 \times 10^{-7}$ G cm^{-2}). The tunnelling effect allows for the supercurrent to cross the Josephson junctions, however, quantum interferences are known to occur between the two possible pathways. For Josephson junctions, when a constant bias current is maintained, the voltage at the terminals can be measured. This voltage is known to oscillate due to quantisation when a change in the magnetic flux through the loop is detected. If the sample is moved from a region of no flux through the superconducting loop then the number of quantum flux units as a result of the sample can be measured.[2a]

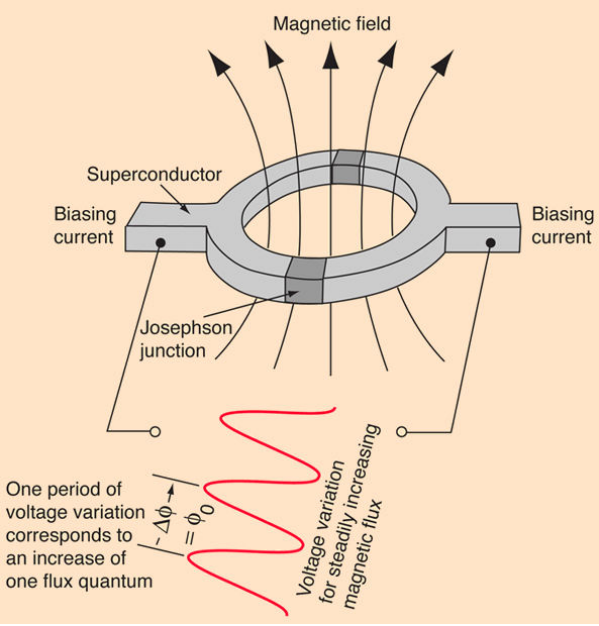

Figure 1.3: Schematic diagram of the main principles behind measuring magnetic moments using a SQUID magnetometer.[3] Adapted from Ref. 3.

The SQUID method can be adapted to study objects on the micro- and nanoscale. A microSQUID will be mentioned in this thesis and was used to carry out measurements at very low temperatures (down to 0.03 K) with controlled field sweep rates. It consists of an array of miniaturised SQUIDs and is very quick to respond to perturbations. The studies in this thesis were carried out at the Néel Institute in Grenoble, France, by Dr. Wolfgang Wernsdorfer and will be discussed further in different chapters.

1.2.1 DC Magnetism Plots

Two of the most useful plots that we can generate from the dc magnetic data are shown in Fig. 1.4, the χ^{-1} *vs.* T and the χT *vs.* T plots. The shape of the curves obtained as well as the fitted values yield information regarding the magnetic interactions within the sample as well as their strengths. In χ^{-1} *vs.* T, the linear fit of the data yields the θ value, known as the Weiss constant (Section 1.1.2) which indicates a ferromagnetic interaction if positive, or anti-ferromagnetic interactions if negative.[1a] The θ value is taken as the intersection of the fit line with the x-axis (T) (Fig. 1.4, left). In the χT *vs.* T plot, a paramagnetic sample with no magnetic interactions would follow the Curie law for non-interacting spins and would appear as a straight horizontal line. When magnetic interactions do occur, the data curves will deviate from Curie behaviour and either increase (ferromagnetic interactions) or decrease (anti-ferromagnetic interactions) with decreasing temperature (Fig. 1.4, right).

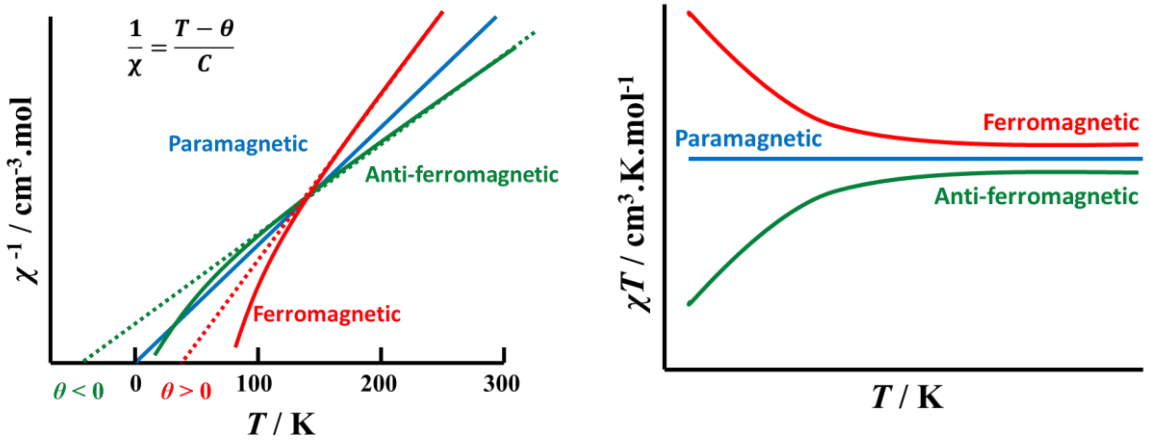

Figure 1.4: The inverse of the magnetic susceptibility (χ^{-1}) is plotted as a function of temperature (left) showing the linear fits of the curves with different types of magnetic interactions while the χT product is plotted as a function of T on the right.

The shape of the curves can, thus, yield important qualitative information regarding the dominant magnetic interactions present. Additionally, if the curves are fit using the Van Vleck equation (**Eq. 1.22**) the strength of the magnetic interaction can be obtained. Other plots which are commonly employed include the magnetisation as a function of applied field (H) and/or as a function of reduced applied field (H/T).[1a,d] In these plots, the magnetisation is measured at various temperatures (1.8 – 7 K, curves are known as iso-temperature curves) and the shape as well as the saturation value at low temperature and high applied fields are considered. In the M *vs.* H plot (Fig. 1.5, left) the characteristic behaviour of an isotropic system is saturation of the magnetisation at 1.8 K and H = 7 T where $M = g.S$; since M is obtained experimentally and S is the known spin value of the complex, we can determine the value of the g factor. For the M *vs.* H/T plot (Fig. 1.5, right) an isotropic system would yield overlapping curves forming one mastercurve, this overlap indicates the isotropic nature of the complex (as will be seen for Gd^{III} for example). For an anisotropic system, which is the case for most of the complexes in this thesis based mainly on Dy^{III} or Co^{II} ions, the iso-temperature curves will not saturate nor overlap/superimpose on a single mastercurve. When this occurs, only qualitative information can be extracted from these plots.

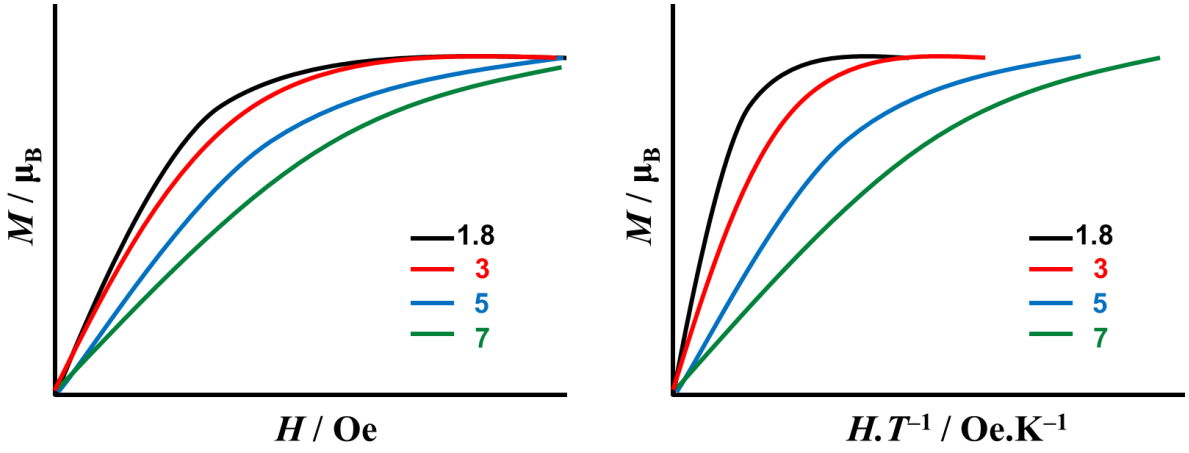

Figure 1.5: Magnetisation as a function of applied field (H, left) and as a function of reduced field (H/T, right) at the indicated temperatures.

1.2.2 AC Magnetism

One of the most useful measurements for SMMs is alternating current (ac) susceptibility. This type of study investigates the dynamics of the magnetisation when a weak magnetic field is oscillating at a certain frequency (ν).[2a] As opposed to direct current (dc) magnetometry, which measures the magnetic moment at constant applied field by measuring the current induced in a set of superconducting pickup coils, ac magnetometry depends on a small alternating current drive field which is overlaid with a dc magnetic field resulting in a time-dependent magnetic moment in the sample. The field generated by the time-dependent moment then induces a current in the pickup coils which allows the measurement to occur without sample motion. The ac-SQUID relies on a set of coils known as the primary and secondary coils. The primary coil is involved in inducing the magnetic moment in the sample through a weak alternating field, generally less than 10 Oe. Inside the primary coil lays the secondary coil which detects the time-dependent moment and measures all the properties we will discuss in later sections. When a sample is inserted in the sample chamber and a magnetic field is generated by the alternating field, the voltage induced by the oscillating magnetic field can be detected in both phase and amplitude by the secondary coil.[2] The overall magnetic field can be described as:

$$H = H_0 + h\cos\omega t \tag{1.23}$$

where H_0 is the applied static field parallel to h which is the oscillating field induced by the sample, ω is the angular frequency of the ac current in the primary coil, and t is the elapsed time.

Unlike dc susceptibility where $\chi_{dc} = {}^{M}/_{H}$, in ac measurements $\chi_{ac} = {}^{\partial M}/_{\partial H}$. The ac measurement is much more sensitive to small changes in $M(H)$. An advantage to using ac measurements is it is much more sensitive to changes in the slope of $M(H)$ and not the absolute value; even at higher magnetic moment values small changes in the magnetic field can be detected with great accuracy. While in dc susceptibility, the magnetisation varies linearly with applied field (H), in an ac measurement, χ_{ac} can be measured in the region where M is not linear with H. Thus, we can obtain two values from the ac measurement: the susceptibility (χ_{ac}) and the phase shift relative to the drive signal (φ).[2] One way to look at χ_{ac} is having an in-phase or real component (χ') and an out-of-phase or imaginary component (χ''):

$$\chi' = \chi\cos(\varphi) \tag{1.24}$$

$$\chi'' = \chi\sin(\varphi) \tag{1.25}$$

$$\chi = \sqrt{\chi'^2 + \chi''^2} \tag{1.26}$$

In the low-field limit, the real component, χ', is the slope of the *M*/*H* curve while χ" (imaginary component) represents the dissipative processes in the sample. This measurement is key for SMMs, where a non-zero χ" signal that is frequency and temperature dependent is indicative of remnant magnetisation and slow magnetic relaxation. If the magnetisation of the sample follows the drive field completely or not at all, χ" would be equal to zero. In order to measure the dynamics of the magnetisation, the angular frequency (ω) can be varied according to the following equation:

$$\chi(\omega) = \chi_S + \frac{(\chi_T - \chi_S)}{1 + i\omega\tau} \tag{1.27}$$

where χ_S and χ_T are the adiabatic and isothermal susceptibility, respectively, ω is the ac field frequency and τ is the relaxation time or the time it takes for thermal equilibrium to be established. At large oscillating frequency of the field, the adiabatic susceptibility (χ_S) can be measured where the measurement time (τ_m) is much smaller than the relaxation time of the sample (τ) indicating that the system can be considered as isolated from the surroundings. On the other hand, the isothermal susceptibility, χ_T, is when $\tau_m >> \tau$ such that magnetisation equilibrium can be achieved in the time scale of the measurement. Therefore, χ_S should be less than χ_T as seen in Fig. 1.6. The real and imaginary parts of χ_{ac} are given by:

$$\chi'(\omega) = \chi_S + \frac{(\chi_T - \chi_S)}{1 + \omega^2\tau^2} \tag{1.28}$$

$$\chi''(\omega) = \frac{(\chi_T - \chi_S)\omega\tau}{1 + \omega^2\tau^2} \tag{1.29}$$

The maximum of χ" can then be reached when $\omega\tau = 1$, where $\omega = 2\pi\nu$ and, hence, $\tau = {}^{1}/_{2\pi\nu}$. When the relaxation process is not characterised by a single relaxation time (τ), the following equations are used to describe χ_{ac}:

$$\chi(\omega) = \chi_S + \frac{(\chi_T - \chi_S)}{1 + (i\omega\tau)^{1-\alpha}} \tag{1.30}$$

where the α value can take on a value between 0 and 1, and represents the distribution of the relaxation times of the magnetisation in a sample. If the α value is 0, then Eq. **1.30** can be reduced to **Eq. 1.27** and only a single relaxation time is observed for the sample. If, however, the α value is greater than 0 then there exists a distribution of relaxation times. In order to characterise the relaxation times for a certain sample, a Cole-Cole plot (or Argand plot) can be studied where χ" is plotted as a function of χ' at a certain temperature and frequency.[4]

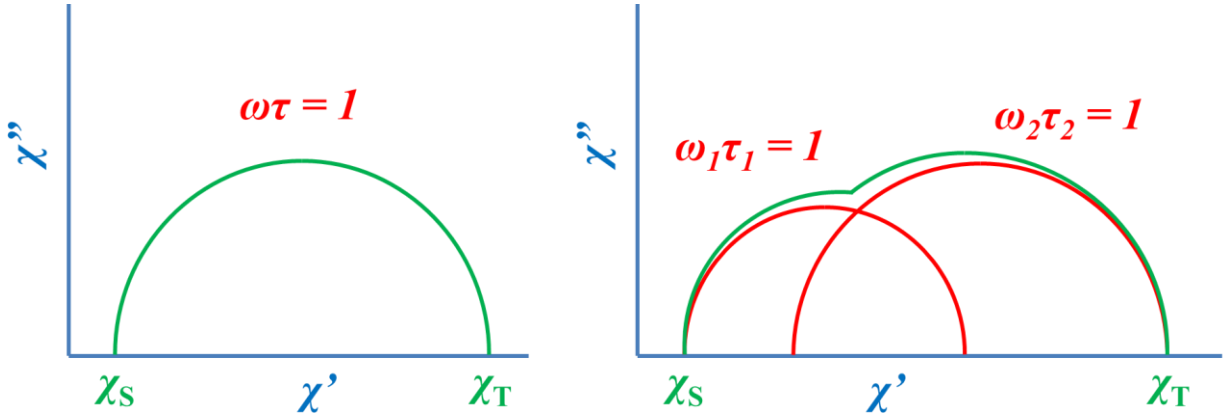

Figure 1.6: Argand or Cole-Cole plots illustrating a system with a single relaxation process (left) where a perfect semi-circle is observed at a certain temperature/frequency and multiple relaxation processes (right) where the red fit lines yield two different relaxation times.

The shape of the Cole-Cole plot indicates a single relaxation time when the curve is a perfect semi-circle and the following relationship is true:

$$\chi_{\max} = \frac{1}{2}(\chi_T - \chi_S) \tag{1.31}$$

where the relaxation time can be determined using $\omega\tau = 1$. If the semi-circle appears unsymmetrical and the maximum of the susceptibility is not reached then we must determine

the value of the α parameter which will deviate from 0 indicating a wider distribution of relaxation times the closer the α value is to 1.[4] Moreover, if there are two distinct relaxation times which are sufficiently separated (Fig. 1.6, right) then two relaxation times can be obtained by de-convoluting the curves.

1.3 Single-Molecule Magnets

The quest for higher density information storage has led to the investigation of Single-Molecule Magnets (SMMs) as potential molecules to be applied in materials such as hard discs. As opposed to storing information in domains which consist of thousands – millions of spins, one can store information in each metal centre or complex leading to significantly higher density memory storage materials. In order for this to occur, one must first design metal complexes which can retain magnetic information at temperatures where these applications become possible.

Single-Molecule Magnets belong to a new class of magnetic materials in which the magnet-like behaviour arises from the intrinsic large spin ground state (S) and uniaxial magnetic anisotropy ($|D|$).[5] The combination of non-negligible spin ground state (S) and uniaxial Ising-like anisotropy $|D|$ (taking into account the Hamiltonian: $H = DS_z^2$) gives rise to an energy barrier (U, defined as $S^2|D|$ or $(S^2–1/4)|D|$ for integer or half integer spins, respectively). Traditionally, a double-well energy diagram has been used to describe both magnetisation and relaxation processes (Fig. 1.7) where each well represents the M_s values with a certain sign (either $+M_s$ or $–M_s$).[6] It is important to note the M_s values for a complex range from $+S_T$, to $–S_T$ in increments of 1. In the absence of an applied field, the $\pm M_s$ levels are paired and are at equal energies of different wells. With the application of a field parallel to the magnetisation axis, referred to as the z-axis, the $–M_s$ levels become stabilised while the $+M_s$ levels are destabilised. The system is saturated when only $M_s = –S$ is populated as can be seen in Fig. 1.7, middle. Upon removal of the applied field, the system will return to thermal equilibrium through magnetic relaxation (after a certain period of time) when the $\pm M_s$ levels are, once again, degenerate. The characteristic time to reach thermal equilibrium is known as the relaxation time, τ, and can reach several years depending on the strength of the magnet.

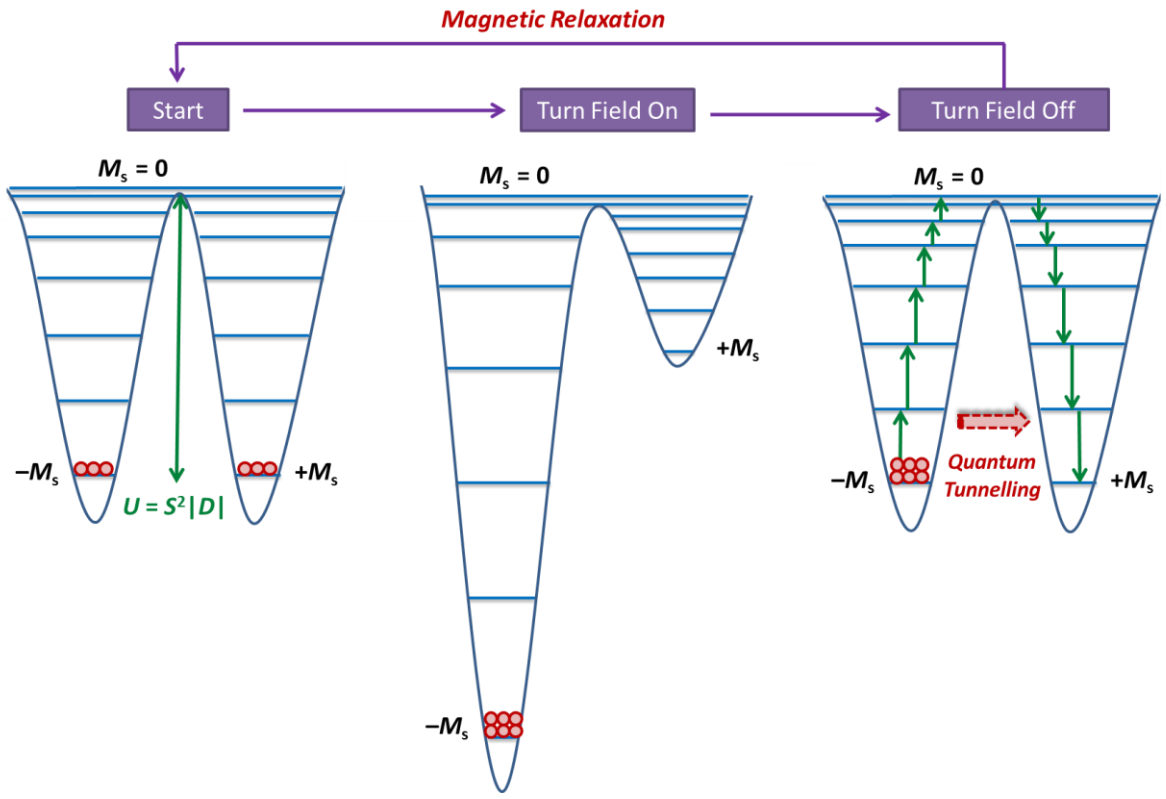

Figure 1.7: Schematic representation of the magnetisation and relaxation processes observed in Single-Molecule Magnets.

While an energy barrier for spin reversal is the most common measure of how good an SMM can be and is the value that researchers quote most often when describing SMMs in publications, it is not the most practical value. The most important experimentally determined value is the blocking temperature for the magnetisation. The blocking temperature is the temperature at which the magnetisation becomes blocked, below which the system behaves as a magnet, but above which it becomes paramagnetic. The energy barrier describes, either theoretically and/or experimentally, the energy required in order for the spin to flip from $+z$ to $-z$ through the xy plane and can give a qualitative indication of how high the blocking temperature will be. However, only experimentally measuring the blocking temperature will yield the necessary information regarding the magnetisation blocking. Ideally, we are aiming for a system that behaves as a magnet around room temperature such that no cooling is necessary when storing information which would be lost if we approached and exceeded the blocking temperature. Currently, the highest blocking temperature that has been achieved is 15 K.[7]

1.3.1 Magnetic Anisotropy

One of the most important concepts to understand when studying SMMs is the magnetic anisotropy and its origins. Magneto-anisotropy is the preferential alignment of the magnetic moment in a certain direction. This can occur along an axis which is known as the easy-axis and is assigned as the *z*-direction or along the *xy* plane which is known as the easy plane. Consequently, the direction perpendicular to the easy axis is known as the hard plane and the axis perpendicular to the easy plane is known as the hard axis. For SMMs, the magnetic behaviour is largely dependent on the anisotropic zero-field splitting parameters, *D* and *E*, as shown in the following Hamiltonian:

$$\widehat{H} = DS_z^2 + E(S_x^2 - S_y^2) \tag{1.23}$$

where *D* is the axial and *E* is the rhombic zero-field splitting parameter.[6] The *D* parameter is responsible for lifting the degeneracy of the 2*S*+1 microstates in the absence of an applied field and scales linearly with the energy between the microstates. One of the most important aspects of the *D* parameter is its sign. A positive *D* value (or easy-plane anisotropy) indicates that the lowest $\pm M_s$ states are stabilised ($M_s = 0$ or ±1/2 in an integer or a half-integer system, respectively) which precludes the observation of an energy barrier and hence SMM behaviour. Alternatively, a negative *D* value (or easy-axis anisotropy) leads to the stabilisation of the highest $\pm M_s$ level ($M_s = \pm S$) and SMM behaviour. The two types of magnetic anisotropy are illustrated in Fig. 1.8. Having $D<0$ is a fundamental requirement in complexes exhibiting SMM properties which allows for magnetic bistability and differential population of the $\pm M_s$ manifold. Let us consider a case with uni-axial magnetic anisotropy, along the *z*-axis, meaning that *D* is negative. This indicates that the magnetic moment is preferentially aligned in the *z* direction along a single axis. For relaxation of the spin to occur, it must flip from –*z* to +*z* or vice versa. In order for this to occur the spin must traverse the *xy* plane which is a region with high electron-electron repulsion and, hence, energetically unfavourable. This is the origin of the energy barrier for spin reversal; the barrier to the spin flipping from –*z* to +*z* or vice versa through the *xy* plane.

There are three main phenomena that result in magnetic anisotropy: First order spin-orbit coupling, second order zero-field splitting and out-of-state spin-orbit coupling or coupling of thermally populated excited states with the ground state. Let us address the second order ZFS first, which serves to lift the degeneracy of the molecular orbitals in the absence of an applied magnetic field. This can occur through structural distortions such as Jahn-Teller elongations or compressions often seen for Mn^{III} and Cu^{II} ions of the first row

transition metals. The *D* value per metal ion generally associated with this type of anisotropy is relatively low, compared to spin-orbit coupling. For ions with degenerate T states such as high-spin Co^{II}, spin-orbit coupling becomes more important and can lead to higher *D* values (> 20 cm^{-1}). It is well-known that ions with half integer spins are more desirable as SMMs since the axial ZFS results in Kramer's doublets thereby removing the degeneracy of the orbitals. This will become important when we discuss quantum tunnelling of the magnetisation which is prevented from occurring in Kramer's ions.

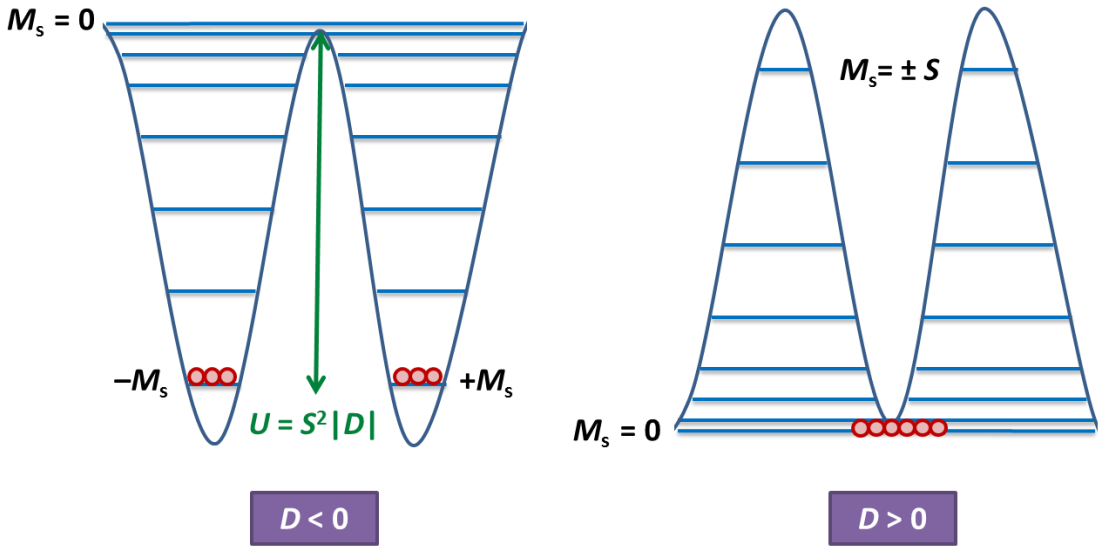

Figure 1.8: Schematic representation of the double-well energy diagram for two different cases where *D* is negative (left) or positive (right).

1.3.2 Quantum Tunnelling of the Magnetisation (QTM)

Quantum tunnelling is a well-known phenomenon in quantum mechanics which occurs at low temperatures for small particles. It is particularly important in the context of SMMs since it serves to minimise or diminish the energy barrier for spin reversal. Hence, it is extremely important that it is recognised in the magnetic data and prevented from occurring within the sample. In order to explain quantum tunnelling, let us consider a double well diagram with a ball in one of the wells (Fig. 1.9a). The position of the ball can be in either well, however, when we say the ball is in the left well then its position is now fixed and cannot be switched to the right well without overcoming a certain barrier separating the two wells. For quantum objects which also behave as waves, the state of the particle can be described as a superposition of both states given that the wavefunction of the left well extends to the right

well and vice versa. This results in a non-zero probability of observing the left well particle in the right well and vice versa since the wavefunction describing the left well extends into the right well. Essentially, the particle could pass from the left to the right well without overcoming the energy barrier and this is what is known as quantum tunnelling of the magnetisation (QTM). For SMMs, QTM is one of the major contributors to the low energy barriers observed or the total absence of a barrier for spin reversal without an applied dc field. It is noteworthy that any object can theoretically exhibit quantum effects regardless of its size; however the tunnelling probability is known to depend exponentially on the mass of the particle as well as the height of the barrier. Hence, this effect is only observed at low temperatures and for small particles. It is important to understand that in order for tunnelling to occur, interaction between the two wavefunctions must occur and the strength of the interaction relates to the degree of tunnelling. If tunnelling does occur, then the wavefunctions must be interacting.[8]

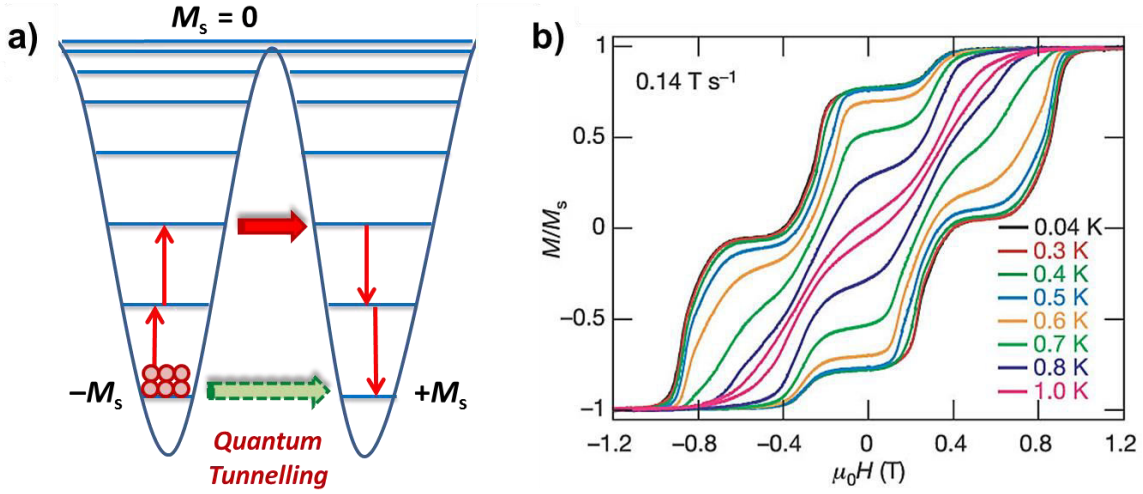

Figure 1.9: Schematic diagram illustrating the tunnelling effect in a double well system (a) and the manifestation of the quantum tunnelling in a hysteresis curve as "steps" in the magnetisation as a function of applied field plot (b).[9]

When studying SMMs, quantum tunnelling becomes very important since it can significantly reduce the size of the barrier and the efficiency of the spin relaxation over the thermal barrier. There are two main types of QTM observed in most SMMs: pure quantum tunnelling at the ground state between the ±*M*s levels of the two wells (Fig. 1.9a, green arrow) or thermally assisted quantum tunneling where the interacting states are ±*M*s ≠ *S* (Fig. 1.9a, red arrow). There are two requirements for QTM to occur: the *M*s levels involved must

be at the same energy and they must interact through mixing of their wavefunctions. Tunnelling is known to be forbidden in half-integer spins since the wavefunctions cannot interact, even if the ±*M*s states are in resonance. Hence, for SMMs it is more desirable to employ metal ions which have a half-integer spin; they are known as Kramer's ions such as Dy^{III} and Co^{II}.[10]

The quantum tunnelling phenomenon is easiest to observe in hysteresis curves where step-like features give an indication as to which *M*s levels are involved in the tunnelling pathways. If coercivity is not observed, then the tunnelling is extremely efficient such that no spin relaxation is observed over the thermal energy barrier. In order to prevent this from occurring, a dc magnetic field can be applied while conducting the ac measurements which will remove the degeneracy of the *M*s levels by stabilising the –*M*s well and destabilising the +*M*s levels as can be seen in Fig. 1.7. When the application of a field is necessary to reveal the thermal energy barrier in a complex, it is known as a field-induced Single-Molecule Magnet.

1.3.3 Slow Magnetic Relaxation Features of SMMs

Since all paramagnetic samples at low temperatures will exhibit an in-phase magnetic susceptibility (χ') signal, SMMs are generally characterised by their out-of-phase susceptibility (χ") responses with varying temperatures, frequencies and applied fields. All measurements involving a χ" signal are performed at low temperatures (below 50 K) since the blocking temperatures of SMMs have not exceeded 15 K to date.[7] There are several plots which are commonly used to study ac data and derive the energy barrier for spin reversal including χ" *vs.* *T*, χ" *vs.* ν (both in a range of temperatures at constant field, and in a range of fields at constant temperature) as well as an Arrhenius plot ln(τ) *vs.* 1/*T*. Characteristic features of an SMM include not only a signal in the χ" *vs.* *T* (or ν) plot but rather peaks that are temperature- and frequency-dependent as can be seen in Fig. 1.10. A set of shifting peaks, whether at different frequencies or different temperatures, indicates slow relaxation of the magnetisation which is a prerequisite to SMM behaviour. Initially, the χ" *vs.* *T* plots were the standard in the field, where frequencies ranged from 0.1 – 1500 Hz (the limits of the most commonly used SQUID magnetometers). In this plot, if the shifting peaks towards lower temperatures increased in intensity then intermolecular interactions could be regarded as negligible. However, if the peaks increased in intensity initially then decreased at lower temperatures, intermolecular interactions were seen as significant within the sample. This is important since SMMs exhibit magnetic behaviour that is molecular in origin and intermolecular interactions must be minimised (or non-existent) for it to be truly a molecular

property. Often, an increase at the end of the curves (Fig. 1.10a) is observed and is attributed to quantum tunnelling pathways through the energy barrier for spin reversal discussed previously.

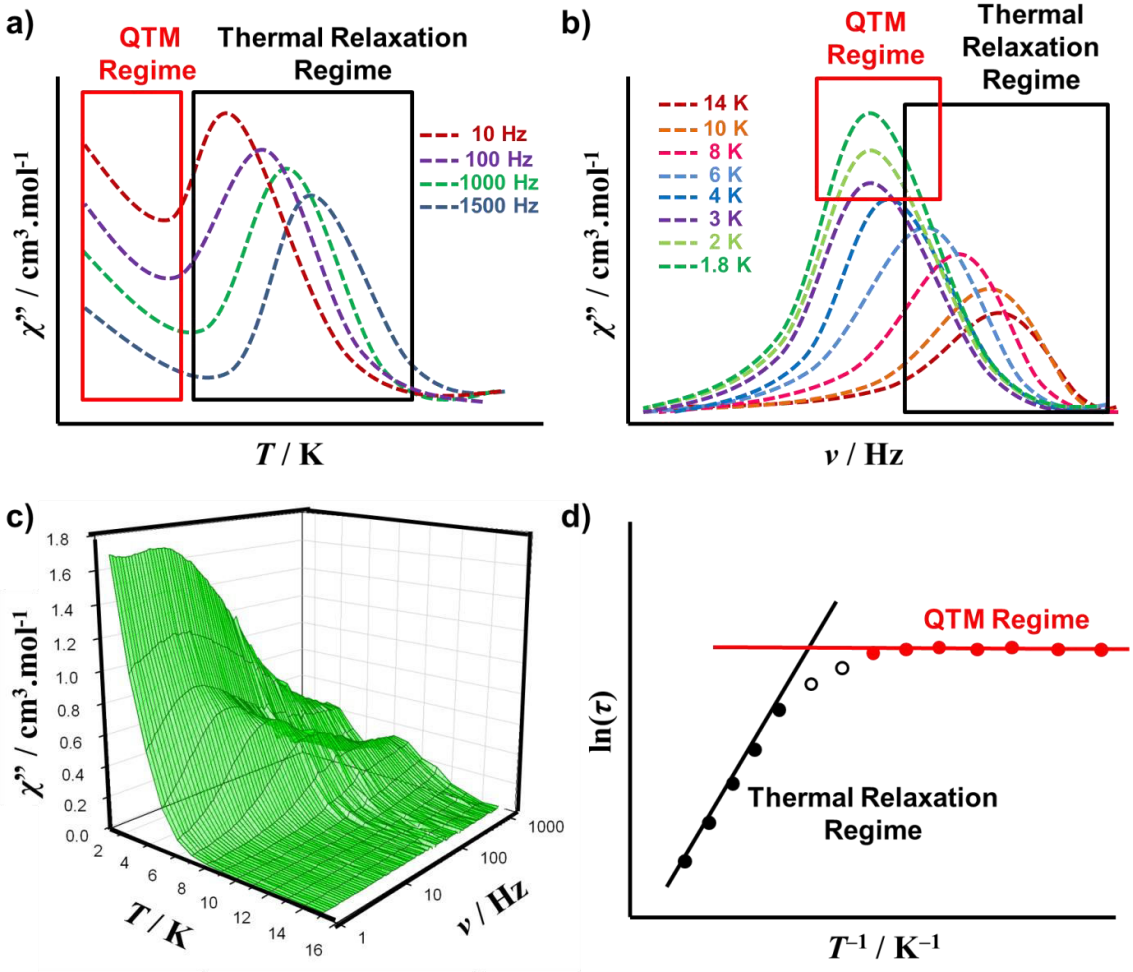

Figure 1.10: Alternating current (ac) data plots which are relevant when studying SMMs. Out-of-phase magnetic susceptibility, χ", is plotted as a function of temperature (a) and frequency (b) where both the quantum tunnelling regime and the thermal relaxation regime are indicated. c) 3-D plot using both temperature-dependence and frequency-dependence of χ".[11] d) Arrhenius plot highlighting both regimes where the slope of the linear fit in the thermal relaxation region yields the energy barriers for spin reversal.

More recently, the ac data has been analysed using χ" *vs.* ν plots which yield more information and slightly more reliable data due to the accuracy with which the frequency can be controlled as opposed to the temperature. In the aforementioned plot, the curves represent

different temperatures of the measurement and shifting peaks again indicate SMM behaviour with the quantum tunneling regime clearly marked as overlapping peaks at low temperature (Fig. 1.10b). Combining both sets of data in a 3-D plot allows the visualisation of peaks which are found in both sets of plots, and can often reveal hidden peaks when only one *x*-axis is used. The example shown in Fig. 1.10c shows two peaks which are visible when the *x*-axis is temperature but not frequency. Using the 3-D plot, we can visualise how and where the two peaks become one when the *x*-axis is frequency. In the χ" *vs.* ν plot, the peaks at different temperatures correspond to $\tau = (2\pi\nu)^{-1}$, meaning that by calculating the frequency at which the peaks occur using a simple Gaussian fit, the relaxation time can be obtained at that particular temperature. Finally, the last plot is the Arrhenius plot (Fig. 1.10d) which is $\ln(\tau)$ *vs.* $1/T$ where τ is the relaxation time of the magnetisation obtained from the χ" *vs.* ν data. There are two clear regimes in the graph, the thermal relaxation and quantum tunnelling regimes. The slope of the fit line in the thermal relaxation regime yields the energy barrier for spin reversal, before the curve approaches the tunnelling region where the barrier is essentially zero due to quantum tunnelling of the spins through the barrier.

One of the most cited example for an SMM is the $\{Mn_{12}\}$ complex which was the first SMM to be studied in the early 1990's.[12] The overall spin arises from eight Mn^{III} ions on the periphery and four Mn^{IV} ions in the centre. The anisotropy axes in this complex are all aligned in a parallel fashion with the overall experimentally observed barrier corresponding to $U_{eff} = S^2|D|$. It is noteworthy that this relationship applies well to transition metal systems with small anisotropy values but fails to represent accurately the observed barriers in highly anisotropic compounds such as lanthanide complexes. For lanthanide-based SMMs more anisotropic terms are needed (in addition to D) for a correct representation of U. Each molecule is a single domain nanoscale magnetic particle. Since 2003, lanthanide SMMs have been an important research focus due to large relaxation barriers along with hysteresis loop openings clearly surpassing any other metal systems. The single-ion anisotropy of lanthanide ions is extremely large.[13] This combined with the unpaired electrons of the metal centre leads to significant energy barriers.[7,14,15] In 2003, Ishikawa and co-workers reported observation of slow magnetic relaxation for mononuclear phthalocyanine Dy^{III} ($[Pc_2Dy]^-$ •TBA^+) and Tb^{III} ($[Pc_2Tb]^-$ •TBA^+ where $TBA^+ = N(C_4H_9)_4^+$) double-decker complexes.[16] The latter molecules clearly exhibit magnet-like behaviour of slow relaxation of the magnetisation below 50 K. In order to provide clear evidence that such behaviour is not due to intermolecular interactions or long-range ordering, ac-susceptibility measurements were carried out for the terbium analogue doped in diamagnetic (($[Pc_2Y]^-$ •TBA^+) matrix. The latter measurements subsequently demonstrated the observed signals are indeed molecular in origin. Moreover, Ishikawa and Wernsdorfer further demonstrated that the isolated molecules exhibit hysteresis loops by performing measurements at subkelvin temperatures on oriented

single-crystals which were magnetically diluted in the yttrium analogue, further confirming the SMM nature of these mononuclear complexes.[17]

1.4 Dinuclear Lanthanide Single-Molecule Magnets

Lanthanide ions are commonly employed in modern technologies as a result of their intrinsic optical [18] and magnetic properties.[19] The latter properties mainly arise from the unpaired electrons residing in *f* orbitals. The *f* orbitals are core orbitals and thus interact poorly with those of the ligand. Compared to first row transition metals the ligand field effect is almost negligible yielding large unquenched orbital angular momentum in most 4*f* systems. As a result, significant magnetic anisotropy in these systems is observed which can greatly influence the coercive fields of magnets.[13] Magnets with large and small coercive fields are called hard and soft magnets, respectively.[20] Commercially employed hard permanent magnets such as SmCo [21] or FeNdB [22] magnets, take advantage of the intrinsic magnetic anisotropy of lanthanide and transition metal ions. With this in mind, researchers in the field of molecular magnetism have turned their attention towards introducing lanthanide ions in molecular systems such as SMMs, including Single-Ion Magnets (SIMs),[23] SCMs [24] or other magnetic molecules.[25]

While mononuclear lanthanide complexes have shown promise in obtaining high energy barriers for the reversal of the magnetisation they are limited to Single-Ion Magnet behaviour intrinsic to one metal centre with a limited number of unpaired electrons. As a way of increasing the effective anisotropic barrier, systems with higher nuclearity have been sought to increase the spin ground state of the molecule. Dinuclear complexes are presented as key compounds in studying and understanding the nature of magnetic interactions between metal ions. This section of the introductory chapter will cover a number of dinuclear 4*f* complexes which have been critical in our understanding of the way in which lanthanide centres in a complex interact magnetically. It will examine key bridging moieties from the more common oxygen-based groups to newly discovered radical-based bridges and draw conclusions regarding the most effective superexchange pathways allowing the most efficient intra-complex interactions.

There are several reviews that have already been published on SMMs which highlight strategies towards their synthesis and optimisation as well as understanding the exchange interactions between lanthanides.[26] However, in this literature review section the main focus will be on the synthesis and magnetic properties of SMMs containing exclusively lanthanide metal centres as well as exhibiting a dinuclear structure. Dinuclear lanthanide

complexes represent the simplest molecular units which allow the study of magnetic interactions between two spin carriers. By investigating such systems one could expect to understand the nature and strength of interactions between lanthanide ions as well as possible alignment of spin vectors and anisotropy axes. These factors can be influenced by the molecular symmetry, the coordination environment and/or the bridging ligands which act as superexchange pathways. It has been commonly believed that lanthanide ions are hardly affected by the coordination/bridging ligands as the 4*f* orbitals are shielded to any ligand field influence by filled 5*s* and 5*p* orbitals.[26] However, recent developments in lanthanide chemistry show that even small ligand changes can drastically influence the overall physical properties of the molecule.[27] If a dinuclear SMM can be designed and isolated in a controllable manner, we could potentially build larger molecules using a bottom up molecular approach and create SMMs with significantly higher blocking temperatures. With this in mind, this section will focus on a thorough analysis of dinuclear lanthanide complexes with the hopes of shedding some light into the coupling mechanisms, slow magnetic relaxation as well as quantum tunnelling effects. These highlighted results provide several approaches to consider when designing new lanthanide SMMs in the future.

Dinuclear lanthanide SMMs are important model systems which can be used to answer fundamental questions regarding single-ion relaxation *versus* slow relaxation arising from the molecule as an entity. SIMs have been published widely as mononuclear complexes as well as polynuclear complexes where the metal centres are significantly separated in the structure.[11,16,23e,26b,28] Drastic differences in magnetic properties can be attributed to the slight changes in bond distances and angles in the coordination spheres of the metal centres. In turn, the coordination sphere is dependent on the coordinating ligand which impacts significantly the orientation of anisotropic axes. While we have been able to gain insight into the effect of slight changes in the coordination sphere of the lanthanide ions on the magnetic properties of different complexes, synthesising larger anisotropic barrier nano-magnets requires coupling of the metal centres. This can be achieved by minimising the distance separating the metal ions as well as providing efficient superexchange pathways to facilitate magnetic interactions. Over the past few years, research into dinuclear systems has not only resulted in complexes with extremely high energy barriers for the reversal of the magnetisation (*vide infra*) but has also guided the way to understanding, in addition to reporting, unique magnetic behaviours.

1.4.1 Probing *f-f* Orbital Interactions in Dinuclear Lanthanide SMMs

Although many lanthanide SMMs are known in the literature, little attention has been directed towards understanding the origin of slow relaxation mechanism(s) for 4*f* polynuclear SMMs.[29] This is mainly due to the dominance of single-ion SMM-like behaviour which renders the elucidation of exchange coupling between spin carriers very difficult. In order to observe and study interactions between 4*f* ions, a model system is required which provides the simplest number of possible interaction modes. Ishikawa and co-workers were successful in adding another layer or deck to the infamous mononuclear lanthanide phthalocyanine complexes.[30,31] These triple-decker lanthanide complexes (Fig. 1.11a) were synthesised using a wide range of lanthanide ions yielding homodinuclear as well as heterodinuclear compounds. This model system was employed in the study of the magnetic properties of dinuclear 4*f* complexes which arise from both the ligand field effects as well as magnetic interactions between 4*f* ions. However, in order to study the magnetic interactions involved the ligand field parameters must be known and herein lays the problem. If the ligand terms alone are to be investigated, two things must be met: 1) only one paramagnetic ion in the complex must be present, and 2) sharp emission and/or absorption bands for the compound must be available. While the former can be solved relatively easily, the latter has proven to be significantly more challenging.

By employing a building block approach, a heterodinuclear complex can be synthesised using an Y^{III} ion at one site and a Ln^{III} ion at the other site (the two sites are indicated in Fig. 1.11a). By varying slightly the phthalocyanine (Pc) derivatives used as ligands (using Pc for one block and Pc* for the other where Pc = dianion of phthalocyanine and Pc* = dianion of 2,3,9,10,16,17,23,24-octabutoxyphthalocyanine) the authors were able to favour the formation of an unsymmetrical complex with a formula of either PcYPcLnPc* or PcLnPcYPc* where only one paramagnetic ion is present. As for obtaining the ligand field parameters, it was impossible to adopt the same strategies that were previously employed since, for this system, no fluorescence data or absorption spectra could be obtained. This is a direct result of the Pc-centred energy levels which were at a low enough energy to quench any fluorescence of the lanthanide ions. Additionally, the intense absorption bands of the ligand played a role in masking those of the metal ions. Therefore, a new strategy was adopted to determine the ligand field parameters that involved using experimental data such as ^{1}H NMR paramagnetic shifts as well as magnetic susceptibility measurements. For a detailed account of this method, the readers are directed to reference 31.

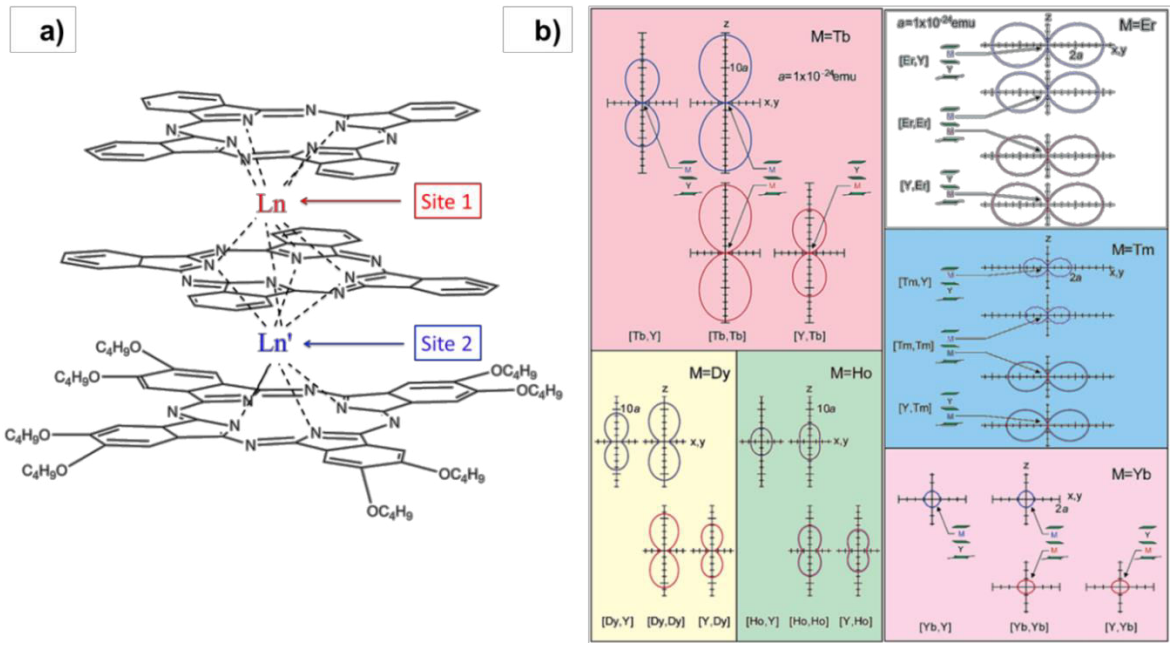

Figure 1.11: a) Schematic structure of a dinuclear triple-decker complex with two different, non-equivalent sites occupied by metal centres. Doping studies involved the synthesis of analogous heterodinuclear complexes using Y at one site and Dy/Tb at the other site. b) Closed surfaces demonstrating anisotropic susceptibility tensors are shown in the *xz* plane for different species of the triple-decker {YLn}, {LnLn} and {LnY} at 4 K. Adapted with permission from Ref. 31. Copyright 2002 American Chemical Society.

With these parameters in hand, the *f*-electronic structure was then determined for the ground states of six different lanthanide ions: Tb^{III}, Dy^{III}, Ho^{III}, Er^{III}, Tm^{III} and Yb^{III}.[31] The magnetic properties of these lanthanide ions arise from the relative ordering of the $2J+1$ substates as well as the difference in energy between the lowest substates and those above them. While the *f*-electronic structure was obtained using {LnY} compounds, it can be extended to homodinuclear {Ln_2} complexes to study the *f-f* orbital interactions as was reported by Ishikawa and co-workers.[32]

Initially, the ^{1}H NMR paramagnetic shifts in the homodinuclear lanthanide complex were shown to arise directly from the sum of the shifts in heterodinuclear complexes {LnY} and {YLn} indicating relatively small interactions between the metal ions.[33] In order to determine the net contribution of these interactions to the magnetic susceptibility, the authors compared the temperature dependence of the magnetic susceptibility plots of both the homo- and heterodinuclear complexes. It is noteworthy that a large number of groups over the years have been able to detect and quantify magnetic interactions between two or more Gd^{III} ions

in a complex due to their isotropic nature.[34] Gd^{III} has a half-filled 4*f*-shell with seven electrons and no orbital angular momentum. This results in an effective magnetic dipole moment that is independent of the temperature and hence, a straight horizontal line is observed in the temperature dependence of the magnetic susceptibility plot. Additionally, the calculated *f-f* orbital interactions in these Gd^{III}_n systems would then be extended to other lanthanide analogues. However, this approach can be seen as flawed due to the temperature dependence of the effective magnetic dipole moment of other lanthanide ions which have significant splitting of the ground-state multiplets.[31] When only the *f-f* orbital interactions were analysed for this system, it was discovered that some lanthanide ions (Dy^{III}, Tb^{III} and Ho^{III}) exhibit ferromagnetic interactions while the dinuclear Er^{III} complex exhibits antiferromagnetic interactions. Furthermore, the Tm^{III} complex displayed unusual behaviour while the interactions in $\{Yb_2\}$ were negligible.[30,31] In order to explain these observations a simplified model with an "ensemble-averaged approximation" of the magnetic susceptibility tensor was employed where the external field inducing a magnetic dipole on one metal ion in this dinuclear complex creates a magnetic field on the second metal ion.[30] Next, the ensemble-averaged magnetic susceptibility tensors were compared for the {LnY}, {YLn} (non-interacting systems) and {LnLn} (interacting system).

The reason for the disagreement between behaviours of different lanthanide ions in the χT *vs*. *T* plots lies in the shape of the closed surfaces that represent the anisotropic magnetic susceptibility tensors (Fig. 1.11b). The nature of the magnetic interaction between metal centres is dipolar and a direct result of the elongation of these closed surfaces either in the *z* direction or horizontally in the *xy* direction. For the ferromagnetically interacting ions ({LnLn} where Ln = Tb^{III}, Dy^{III} and Ho^{III}) the height of the closed surfaces in the *z* direction is greater than the *x* or *y* direction and hence $\Delta\chi_m$ is positive. For the antiferromagnetically interacting species (Ln = Er^{III}), the height of the closed surfaces in the *z* direction is lower than in the *x* or *y* direction resulting in a negative $\Delta\chi_m$ upon interaction. For Tm^{III}, a similar situation is observed with the decreased susceptibility values resulting from decreased χ values in the *x* and *y* direction. Finally, for Yb^{III} the closed surfaces are more spherical in shape indicating magnetic susceptibilities that are nearly isotropic in nature and a $\Delta\chi_m$ of 0. The series of studies performed in order to probe the electronic structure of 4*f* ions as well as understand *f-f* orbital coupling provides a tool for designing SMMs with higher energy barriers.

We have also investigated the use of doping to elucidate *f-f* magnetic interactions in a dinuclear $\{Dy_2\}$ SMM, $[Dy_2(valdien)_2(NO_3)_2]$, which will be described in Chapter 3, structurally and magnetically.[23b,35] While the triple decker complex described earlier is an interesting model, the presence of two non-identical sites for the metal centres complicates

the magnetic properties. In our complex, $[Dy_2(valdien)_2(NO_3)_2]$, there is only one crystallographically independent metal ion leading to the simplification of the origin of observed magnetic behaviour.

1.4.2 Promoting Magnetic Coupling

Determining the origins of slow magnetic relaxation as well as the nature of *f-f* orbital interactions led to the investigation of different bridging moieties between lanthanide metal centres. There are a variety of different bridging groups which promote magnetic interactions to different degrees yielding a wide range of barriers for the reversal of the magnetisation. Selected bridging molecules are discussed below including oxygen-, nitrogen-, and sulphur-based ligands, chloride, arene as well as radical bridges.

SMMs with Oxygen-based Bridges

In 2008, a dinuclear Dy^{III} SMM was reported, $[Dy_2(hmi)_2(NO_3)_2(MeOH)_2]$ (hmi =2-hydroxy-3-methoxyphenyl)methylene (isonicotino)hydrazine), which exists as isolated $\{Dy_2\}$ molecules as well as extended 2-D sheets of $[Dy_2(hmi)_2(NO_3)_2(MeOH)_2]_\infty$•MeCN by slightly varying the reaction conditions.[23a] The rigid hmi^{2-} ligand provides ideal coordination environment for Dy^{III} ions as well as organises the molecular clusters into 2-D sheets. The Dy^{III} ions are bridged by two μ-phenoxide moieties from two ligands creating magnetic superexchange pathways. The magnetic behaviour of these complexes is rather unusual; the Dy^{III} centres exhibit dominant ferromagnetic coupling which had never been previously reported for a Dy-based SMM at the time. The ferromagnetic coupling was only observed in the χT *vs.* T plot at low temperature (below 23 K) due to thermal population of the excited states at higher temperatures which mask the exchange interactions between Dy^{III} centres. The reported effective energy barriers of the dinuclear cluster and the 2-D sheet were some of the highest for lanthanide SMMs with U_{eff} = 56 and 71 K, respectively, and pre-exponential factors (Arrhenius law) of $\tau_0 = 3x10^{-7}$ and $7x10^{-8}$ s, respectively. Additionally, by applying an optimum dc field when performing the ac measurements, the QTM was minimised revealing a dominant thermally-activated regime that corresponds to the zero-field measurements. This confirms the calculated energy barriers which are unaffected by QTM.

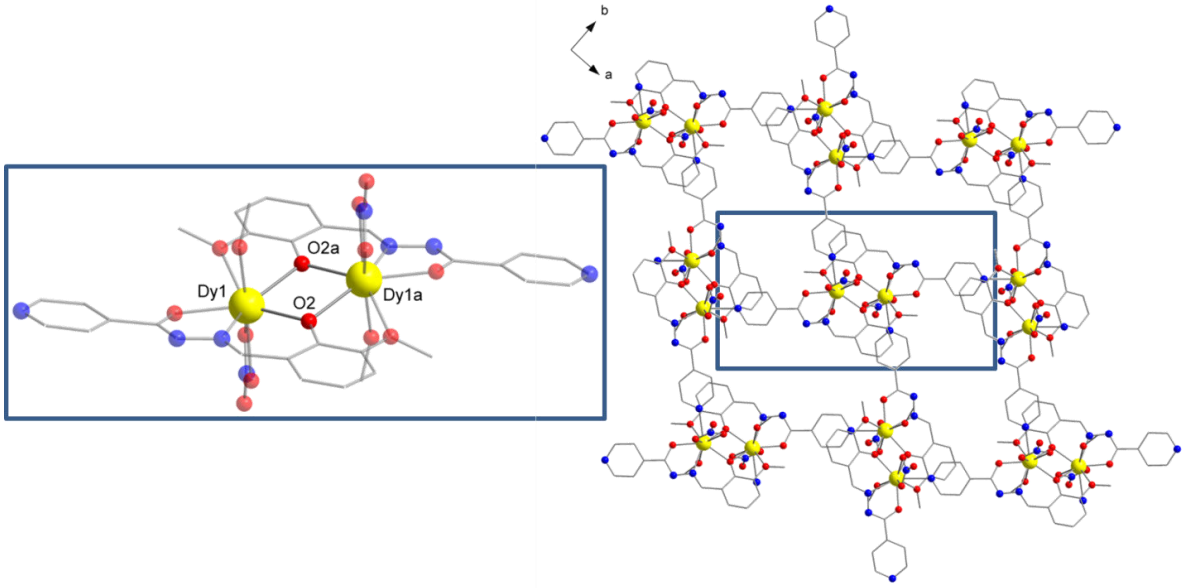

Figure 1.12: Left: Molecular structure of $[Dy_2(hmi)_2(NO_3)_2(MeOH)_2]$ with the bridging oxygen atoms highlighted. Right: 2-D structure of the extended $[Dy_2(hmi)_2(NO_3)_2(MeOH)_2]_\infty$•MeCN complex. Note the Dy^{III} centres are eight-coordinate in the isolated $\{Dy_2\}$ and nine-coordinate in the extended 2-D sheet. Colour code: Yellow (Dy), red (O), blue (N) and grey (C). Hydrogen atoms and solvents have been omitted for clarity. Adapted from Ref. 23a. Copyright 2008 Wiley-VCH Verlag GmbH & Co. KGaA, Weinheim.

It is relatively common for lanthanide ions to exhibit ground state tunnelling of the spins according to the spin-parity effect which predicts low QTM for lanthanide ions with half-integer spins such as Dy^{III} (S = 5/2) but large QTM for integer spin ions.[36] This is seen for many lanthanide-based SMMs reported thus far with Dy^{III} as the ideal candidate for high energy barrier nano-magnets. There are exceptions, however, where even Dy^{III} ions exhibit ground state tunnelling of the magnetisation due to factors such as environmental degrees of freedom as well as hyperfine and dipolar coupling *via* transverse field components.[25] This can be observed in $[Ln^{III}_2(hpd)_6]$•solvent (Ln^{III} = Eu^{III} •2MeCN), Gd^{III} (•2MeCN), Tb^{III} (•MeCN•MeOH), Dy^{III} (•2MeCN), Ho^{III} (•2MeCN) and hpd = 2-hydroxyisophtaldehyde).[37] The Dy^{III} analogue did not exhibit SMM-like behaviour as expected due to ground state tunnelling. Interestingly, coordination of the fluorescent ligand (hpd) with Eu^{III} ions resulted in a fluorescent complex showing characteristic lanthanide emission.

As discussed above, we have recently reported a $\{Ln_2\}$ complex series, $[Ln^{III}_2(valdien)_2(NO_3)_2]$ where Ln^{III} = Eu^{III}, Gd^{III}, Tb^{III}, Dy^{III} and Ho^{III}, which exhibits O-bridged Ln^{III} ions.[23b] The Dy^{III} analogue, shown to exhibit SMM behaviour, as well as the Gd^{III} analogue will be discussed in detail in Chapter 3. Similarly, M. Murugesu and co-workers also reported an unsymmetrical $\{Dy_2\}$ complex which exhibits a similar O-bridging motif.[38] The coordination environment of each metal ion is quite different resulting in different coordination numbers and geometries (Fig. 1.13) leading to two relaxation modes. The dominant single-ion behaviour of the Dy^{III} centres due to negligible magnetic interactions results in different slow relaxation barriers of U_{eff} = 36 K (τ_o = 4x10^{-7} s) and U_{eff} = 80 K (τ_o = 8x10^{-8} s) for the low and high temperature domains, respectively (Fig. 1.13b).

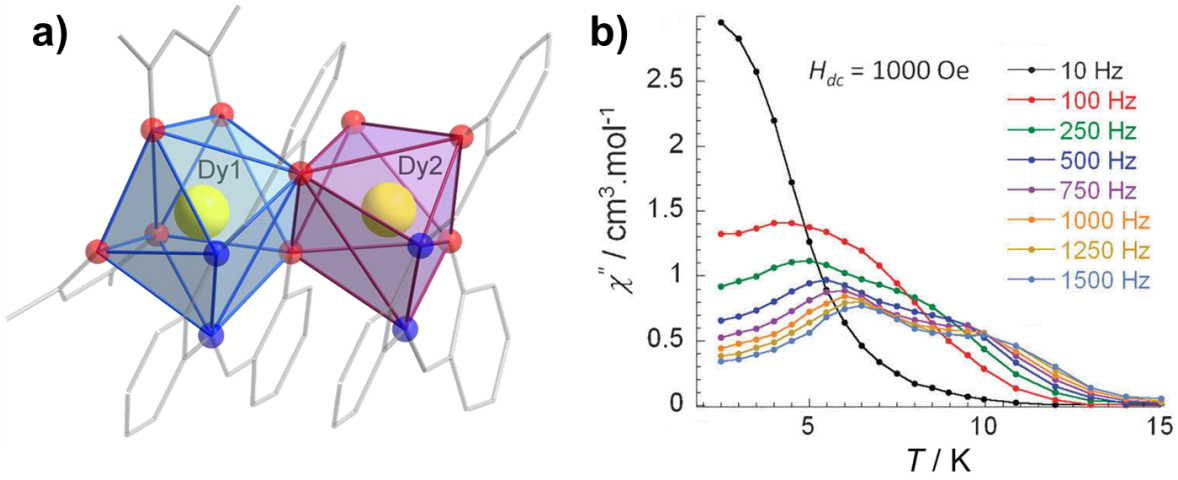

Figure 1.13: a) Molecular structure of $[Dy_2(L_1)_2(acac)_2(H_2O)]$ (L_1 = *N*,*N*′-bis(salicylidene)-*o*-phenylenediamine) with unsymmetric metal ions exhibiting different geometries represented by polyhedra of different colours. b) The corresponding χ" *vs*. *T* plot is shown on the right. Colour code: Yellow (Dy), red (O), blue (N) and grey (C). Coordinating ligands have been shown as faded for clarity with hydrogen atoms omitted from both structures. Adapted from Ref. 38.

Other interesting O-based bridging moieties include oxalate ligands which have been shown to promote weak ferromagnetic interactions at low temperature between lanthanide ions to yield SMM behaviour.[39] Additionally, a recent report of a complex with antiferromagnetically-coupled carbonato-bridged lanthanide ions is also noteworthy as it exhibits field-induced SMM behaviour with a U_{eff} = 55 K.[40] As a step further, it would be useful to investigate the role of different ligands in promoting ferro- or antiferromagnetic interactions; whether the interaction is superexchange or dipole-dipole in nature. Complexes

with O-based bridges have been quite dominant in SMM chemistry due to the fact that O-based ligand systems can be easily designed, are readily available and can bridge between two or more metal centres providing superexchange pathways. However, other bridging groups are gaining popularity in the field and have led to interesting magnetic properties and relatively high anisotropic energy barriers.

SMMs with Nitrogen-based, Sulphur-based and Chloride Bridges

While O-bridging has resulted in key dinuclear lanthanide complexes that exhibit high energy barriers, the magnetic interactions are relatively weak leading researchers to investigate other bridging molecules. Most notably, the Layfield group has performed a thorough study of different bridging atoms such as N, S and Cl and their effects on the strength of the magnetic interaction in $\{Dy_2\}$ organometallic cyclopentadienyl (Cp) complexes. These key studies will be discussed in detail below. By elucidating the electronic structures of two different N-bridged complexes, Layfield and co-workers were able to rationalise the fact that one complex exhibits SMM behaviour while the other does not.[41] The main difference between the two complexes involves the bridging groups where one is N_{amido}-bridged while the other is benzotriazolide-bridged (Fig. 1.14, a and b, respectively). This has significant implications on the exchange pathway between the metal ions leading one to exhibit slow magnetisation relaxation while the other does not. By examining the electronic distribution and bonding interactions between the Dy^{III} ions and the bridging atom(s), it is evident that the N_{amido}-bridge (Fig. 1.14a) allows for more (albeit weak) metal-metal interactions. Alternatively, the benzotriazolide-bridged complex (Fig. 1.14b) involves strong bonding interactions between the Dy^{III} centre and the N atoms on the periphery of the triazolide moiety while relatively weak interactions between Dy^{III} and the central N atom are observed. This is a direct result of the HOMO in the ligand which indicates a node on the central N atom bisecting the bridging molecule and effectively blocking any communication between orbitals of the two halves. Since no communication is occurring between the Dy centres, the complex behaves as a Single-Ion Magnet. As reported by the authors, the magnetic interactions between the metal ions in the N_{amido}-bridged complex are strong enough (although not enough to study the interaction through magnetic susceptibility measurements) to provide a relaxation mechanism for the magnetisation such that no SMM behaviour is observed. However, other factors cannot be neglected such as crystal field effects, dipole-dipole interactions as well as orientations of anisotropy axes. Moreover, fitting of the dc magnetic data would yield coupling constants between the metal centres which could provide further evidence regarding the interactions.

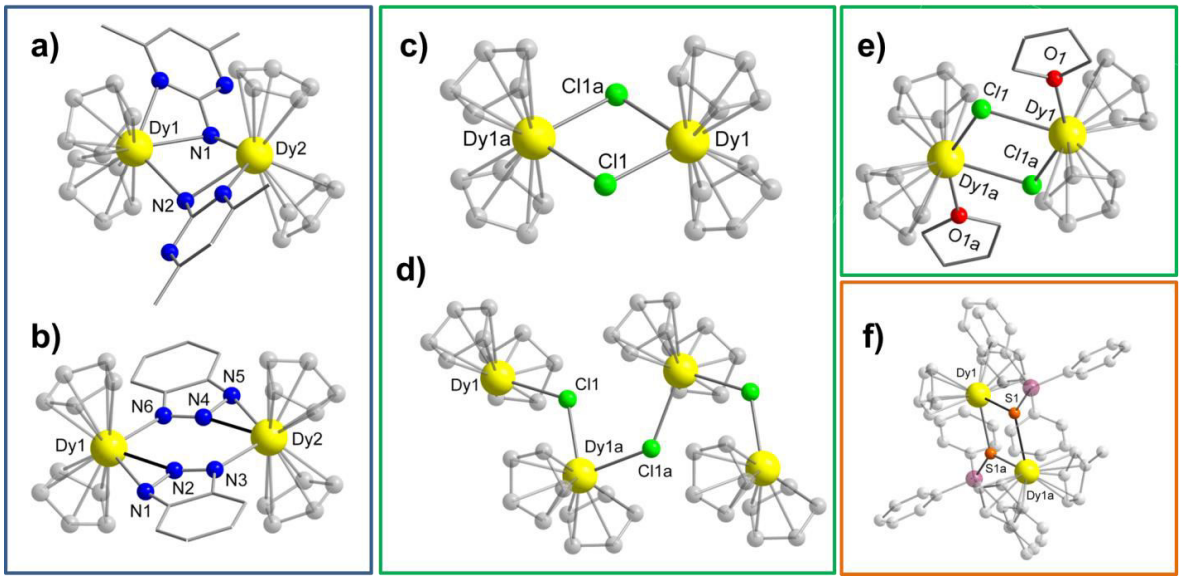

Figure 1.14: Overview showing the molecular structures of cyclopentadienyl Dy^{III} dinuclear complexes comparing N-bridged complexes (a and b) and Cl-bridged complexes (c, d and e) to a S-bridged compound (f). Colour code: Yellow (Dy), red (O), blue (N), green (Cl), purple (Si), orange (S) and grey (C). Hydrogen atoms and solvent molecules have been omitted for clarity. c-e) Adapted from Ref. 42. a, f) Adapted from Ref. 41 and 44. Copyright 2012 Wiley-VCH Verlag GmbH & Co. KGaA, Weinheim.

Exploring other types of bridges by the same research group led to the investigation of Cl-bridged dinuclear lanthanide compounds, one of which crystallises as two polymorphs (Fig. 1.14, c and e).[42] By exploring chloride as a bridge the implications of using an atom with more diffuse orbitals can be studied. It has been postulated that more diffuse orbitals can lead to increased orbital overlap and thus yield stronger interactions between the metal ions.[43] This efficient superexchange pathway can result in SMMs with higher energy barriers for the reversal of the magnetisation. The complex which crystallises as two polymorphs, a molecular complex (Fig. 1.14c) as well as a polymeric chain of Cl-bridged $Dy(Cp)_2$ units (Fig. 1.14d), exhibits two relaxation processes as predicted (the two polymorphs have distinct relaxation modes). The energy barriers were calculated to be approximately U_{eff} = 40 K and 98 K, respectively, which are comparable to other lanthanide complexes mentioned in this review. By performing a Soxhlet extraction on this complex in THF followed by slow cooling of the reaction, crystals of another Cl-bridged complex were obtained where one THF molecule was coordinated to each Dy^{III} centre along with two Cp^{-} ligands (Fig. 1.14e). This compound also exhibits slow magnetisation relaxation which has not been affected by QTM at zero-field. MicroSQUID measurements indicate the presence of

hysteresis loops at zero-field with no quantum tunnelling steps observed. As the applied field is increased, steps in the hysteresis loops begin to appear. This is indicative of exchange-biased interactions between the metal centres lifting the quantum tunnelling in the absence of an applied field. This behaviour was also verified using out-of-phase susceptibility χ" *vs.* T and ν plots at different applied fields. The observed energy barrier was approximately 49 K.

In keeping with the theme of bridging atoms with more diffuse orbitals, sulphur bridges were then examined.[44] By employing soft donors such as S, not only would the magnetic interaction between the metal centres be improved but the crystal field effects, to which the slow relaxation is very sensitive, would be very different compared to harder N- or O-donors. This strategy proved successful in yielding an SMM with one of the highest anisotropic energy barriers for a dinuclear lanthanide complex.[44] The sulphur-bridged compounds, $[\{Cp'_2Ln(\mu\text{-}SSiPh_3)\}_2]$ where Cp' = η^5-C_5H_4Me and Ln = Gd^{III} or Dy^{III} (Fig. 1.14f), were studied for their SMM properties (in the case of Dy^{III}) and for quantifying the magnetic interaction between the centres (in the case of isotropic Gd^{III}). For the $\{Dy_2\}$ complex, the magnetic interaction parameter, J, is a sum of the dipole-dipole interaction as well as the exchange interaction between the metal ions. The interaction J_{dipole} can be calculated since the ground state g matrix on the Dy centres is known while the $J_{exchange}$ can be calculated by fitting the experimental susceptibility data. The dipolar interaction is found to be antiferromagnetic in nature which corresponds to the anisotropic axes of the Dy ions being perpendicular to the intramolecular Dy-Dy axis. The value of the dipolar interaction is comparable for both S-bridged (–2.22550 cm^{-1}) and Cl-bridged (–1.99075 cm^{-1}) complexes investigated by the same group;[42,44] however the magnetic exchange interaction is significantly different (–2.19475 and 0.08550 cm^{-1} for S- and Cl-bridged compounds, respectively). The influence of the valence orbitals of sulphur come into play when looking at this parameter. Since the orbitals are more diffuse in S than in Cl, they allow for greater orbital overlap and hence stronger exchange interactions are observed. Calculating the transverse g values of the ground state Kramer doublets using *ab initio* calculations indicated a more significant QTM process occurring in the Cl-bridged compound as the g_x and g_y were an order of magnitude larger than those of the S-bridged complex. Consequently this leads to higher anisotropic energy barriers and better SMMs as can be seen in the S-bridged dinuclear compound with a barrier for the reversal of the magnetisation of approximately U_{eff} = 190 K.

SMMs with Arene Bridges

The appeal of arene complexes arises from the fact that they have stronger crystal field effects due to greater penetration of the electronic cloud around the lanthanide ions thereby

accessing the 4*f* shell.[45] Using arene molecules as bridging groups has been demonstrated first using uranium as a metal source.[46] The diuranium, arene-bridged complex was reported by Liddle and co-workers to be the first of its kind to display SMM behaviour and was used as a proof-of-principle for synthesising lanthanide analogue complexes. Our group has been previously successful in synthesising as well as fully studying mononuclear lanthanide sandwich complexes using the ligand 1,4-bis(trimethylsilyl)cyclooctatetraenyl (COT") in its dianion form.[45a] These complexes were shown to exhibit Single-Ion Magnet behaviour with multiple relaxation modes under different applied dc fields. This was the first example of a mononuclear Ln^{III} complex to exhibit such clear multiple relaxation pathways due to perturbations in the ligand field caused by the COT" ligands.

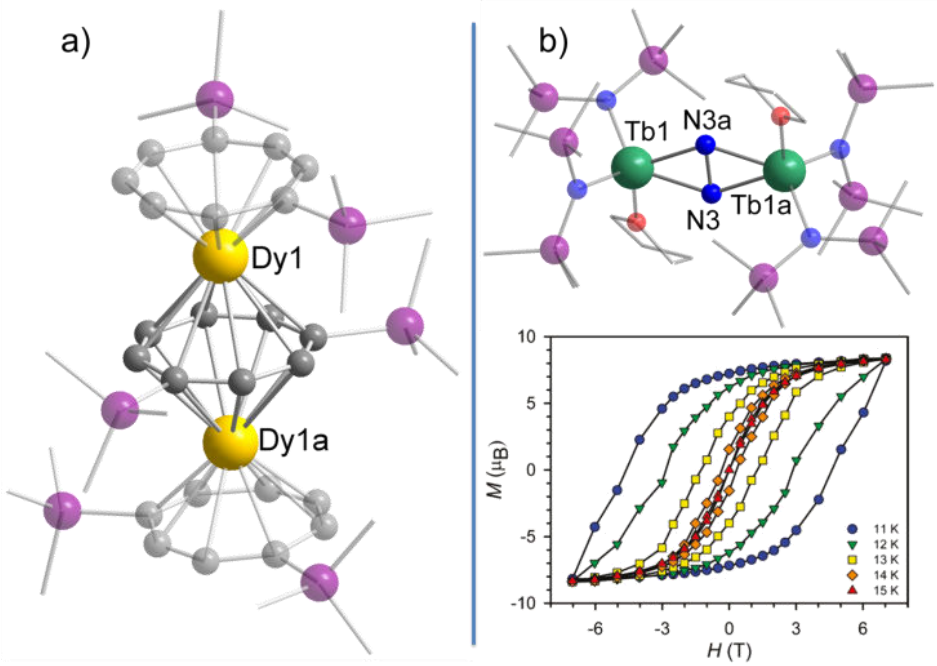

Figure 1.15: Molecular structures of dinuclear complexes $[Dy_2COT"_3]$ (a) and $[Tb_2(\mu\text{-}\eta^2\text{:}\eta^2\text{-}N_2)((Me_3Si)_2N)_4(THF)_2]^-$ (b) with hydrogen atoms omitted and trimethylsilyl groups as well as non-bridging parts of the ligands faded for clarity. Field dependence of the magnetisation plot for b showing coercivity in the hysteresis loops up to 15 K at a sweep rate of 0.9 mT/s is shown. b is adapted with permission from Ref. 7c. Copyright 2011 American Chemical Society.

As an extension of this system, dinuclear organolanthanide complexes have been synthesised using a building block approach based on the aforementioned Ln^{III} mononuclear complexes. The purely organopolymetallic lanthanide SMMs share the formula $[Ln_2COT"_3]$

with a triple-decker structure (Dy^{III} analogue is shown in Fig. 1.15a).[47] DFT calculations were performed on the Dy^{III} analogue in order to provide insight into the electronic structure of the complex. From the electron donation of each ligand as well as electron densities it is evident that the terminal COT" ligands interact more strongly with the Dy^{III} ions as opposed to the central COT" ligand. The central COT" ligand plays a major role in covalent bonding with the Dy^{III} ions thus providing a superexchange pathway and leading to spin interactions between the metal centres. Additionally, a direct bond on the order of 0.04 was found to exist between Dy-Dy which is significant (although weak). The magnetic properties of the dinuclear complex are rather complicated and reveal multiple overlapping relaxation modes with an array of energy barriers.[45a]

SMMs with Radical Bridges

One of the first dinuclear lanthanide complexes, an analogue of which was later shown to behave as an SMM, was reported by Gatteschi and co-workers in 1992.[48] The mononuclear asymmetric unit consists of a Gd^{III} ion bound to two nitronyl nitroxide radicals through the pyridine N of one molecule as well as an O from the NO group of another molecule. The coordination sphere is completed by three hexafluoroacetylacetonate (hfac) ligands resulting in an eight-coordinate Gd^{III} centre. The dimerisation of these units yields a dinuclear lanthanide compound with ferromagnetically interacting metal centres below 50 K. The Dy^{III} analogue, further investigated by Sessoli and co-workers,[49] proved to be an SMM under an applied dc field. The significant QTM was shown to result in a much lower barrier for the reversal of the magnetisation than that calculated under an applied field. It is quite remarkable that, for the first time, the tunnelling frequency for this compound was calculated to be 14 kHz which is responsible for the absence of a magnetic hysteresis loop at low temperature. In order to suppress or minimise the observed QTM it is necessary to lift the degeneracy of the states that are in resonance thereby preventing the spins from tunnelling through the barrier. This can be achieved by applying a dc field, in this case 2 kOe, which revealed an effective energy barrier (U_{eff}) of approximately 13 K. While the barrier is relatively low, this study took an in-depth look at the mechanisms involved in both thermal and quantum relaxation regimes leading to the SMM behaviour. While the exchange interaction between the two metal centres in this dinuclear complex was calculated using the isotropic Gd^{III} analogue, it was further confirmed using the $\{Dy_2\}$ complex through doping studies and ac magnetic measurements, the methods for which were discussed at length in the preceding section.[30,35]

Lanthanide SMMs have achieved celebrity status after the recent discovery of radical-bridged dinuclear lanthanide complexes which exhibit the highest blocking temperatures to date.[7a,c] These complexes feature a N_2^{3-}-radical bridge which mediates magnetic interactions between the metal centres resulting in SMM behaviour (for the Tb^{III} and Dy^{III} analogues). It is favourable to use radical molecules as bridging molecules due to their diffuse spin orbitals which can overlap with 4*f* orbitals regardless of their buried nature. The isolated compounds, $[K(18\text{-crown-6})(THF)_2][\{[(Me_3Si)_2N]_2(THF)Ln\}_2(\mu\text{-}\eta^2\text{:}\eta^2\text{-}N_2)]$ (Ln = Gd^{III}, Tb^{III}, Dy^{III}, Ho^{III}, Er^{III}) are thermally stable and air sensitive. In order to study the magnetic interactions through the radical bridge, analogous complexes were synthesised with a non-radical N_2^{2-} bridging molecule where the Ln metal centres behave as Single-Ion Magnets. By turning on the interaction between metal ions through reduction of the N_2 bridge, SMMs with record high blocking temperatures (up to 15 K for the Tb^{III} analogue, Fig. 1.15b) were observed.[7c] Quantifying the magnetic interaction was achieved using the Gd^{III} analogue of the dinuclear complex (Gd^{III}-N_2^{3-}-Gd^{III}) and was found to be $J = -27$ cm^{-1} between Gd^{III} and $N_2^{\bullet 3-}$ which is the highest magnetic interaction found thus far for a lanthanide system.[7a] The Gd^{III}-Gd^{III} interaction was found to be $J' = 0.07$ cm^{-1}.

In order to confirm the necessity of the radical bridge in creating a highly effective magnetic exchange pathway, the N_2^{2-} non-radical compound was studied as well. The magnetic properties of this compound were drastically different, with only very weak antiferromagnetic coupling that is 50 times lower in magnitude than the radical-bridged counterpart. This difference was also seen in the ac magnetic susceptibility data of the Dy^{III} analogue where the radical-bridged complex showed behaviour that is dominated by the interactions between the ions in the complex while the non-radical bridged complex exhibited mainly behaviour characteristic of single-ion relaxation with little or no interactions seen between the 4*f* ions. The coupled Ln-radical system can be viewed as a giant spin with the entire complex acting as a unit to give extremely high energy barriers for the reversal of the magnetisation and the highest blocking temperatures observed to date. This is an important example which strongly supports the idea that coupling 4*f* lanthanide centres can be achieved resulting in SMMs with higher spin reversal barriers. Another system which supports this strategy involves a dinuclear Dy^{III} complex bridged by radical anion bipyrimidine yielding an effective anisotropic barrier of 123 K and a blocking temperature of 7 K at a sweep rate of 0.002 T/s. Although more research is needed to complement and further these results, it has been clearly demonstrated that understanding the magnetic interactions of a system will provide new pathways for creating molecules with significant energy barriers.

1.4.3 Conclusions

Dinuclear systems involving only lanthanide metal centres have been crucial in our current understanding of magnetisation relaxation characteristic of lanthanide SMMs. As opposed to mononuclear compounds, dinuclear complexes provide ideal models to map magnetic interactions which are highly sought after when designing large anisotropic barrier molecules. When significant interactions are present, larger spin values as well as larger anisotropy can be expected yielding higher spin reversal barriers. In this section, comparisons were drawn between different bridging groups including O-, N-, Cl-, S-, arene-, and radical-based ligands. Of these, S- and radical-based bridges have provided the most promising results in promoting magnetic interactions between lanthanide centres which have been quite elusive due to the core nature of the 4*f* orbitals. The highest blocking temperature to date of 15 K was observed in a dinitrogen radical-bridged $\{Tb_2\}$ complex where interactions between the lanthanide metal centre and the radical were the highest reported for a 4*f* system. By examining these systems, it can be anticipated that a disulphide radical-bridged complex would yield an even higher energy barrier due to increased diffusivity of the orbitals in addition to strong metal-radical bonding.

While dinuclear models can be probed for the most effective superexchange pathways to give the strongest intra-complex interactions, the future of the field could well reside in multinuclear complexes. The interactions between a number of metal centres can provide larger spin ground states while aligning anisotropy axes can provide higher *D* values. It is noteworthy that not only must the spin ground state be large; it must also be well-isolated from the excited states in the electronic structure which greatly depends on the ligand employed. In understanding the magnetic properties of dinuclear units, one can envision an approach which builds on these complexes by either extending the nuclearity of the system or improving the bridging ligand communications thereby moving closer towards potential applications such as high density storage materials.

1.5 Mononuclear Co(II) Single-Molecule Magnets

While the total spin of a complex was thought to be extremely important in evaluating the energy barrier leading to large metal clusters, it has been recently shown that anisotropy is in fact the key parameter. The design strategies developed in the early days based on complexes with record spin values have since been largely abandoned. New strategies for the synthesis of high-barrier SMMs have surfaced focusing on highly anisotropic metal ions with smaller

spin values such as select 3*d* transition metals. The evolution from large transition metal clusters to lanthanide based complexes to mononuclear transition metal SMMs has followed the increase in magnetic anisotropy relative to the spin. Moreover, the focus on half-integer spin systems has thus far led to complexes with the highest energy barriers to date.

The zero-field splitting (ZFS) parameter, *D*, is very important when designing complexes with SMM properties. Moreover, the sign of *D* can yield valuable information regarding the type of magnetic anisotropy present in the complex. A negative value of *D* indicates that the magnetisation is aligned along the easy-axis (in a single direction denoted as *z*) while a positive *D* indicates easy-plane anisotropy within the *xy* plane of the molecule. The goal has been to maximise *D* while minimising transverse anisotropy, *E* (discussed in section 1.3.1). Since *D* decreases with increasing *S*, naturally the field has shifted towards mononuclear 3*d* complexes as SMMs which have significantly lower spin compared to lanthanides but with similar values of *D*. The following section will review the current state of the field in mononuclear 3*d* SMMs based mainly on Co^{II} since this is most relevant for the research outlined in this thesis.

One of the first reports of a Co^{II}-based complex which behaved as an SMM was published in 2003 by N. Koga and co-workers.[50] The complex consisted of a single octahedral metal centre, coordinated to four 4-(α-diazobenzyl)pyridine ligands and two NCS^- groups in a *trans* configuration. The goal of this work was to study the magnetic properties of a heterospin system where 3*d* metal centers are coordinated to carbenes with 2*p* spins. By coupling the two spin-containing moieties, large *D* and *S* values could be obtained leading to, potentially, large barrier SMMs. The carbene was generated *in situ*, with the magnetic properties measured before and after irradiation to provide a reliable comparison. The frozen solution measurements indicated ferromagnetic interactions between the two spin systems after the triplet carbene was generated as well as slow relaxation behaviour characteristic of an SMM. The calculated barrier was reported to be 89 K (τ_0= 2.3 x 10^{-10} s). Hysteresis measurements yielded open hysteresis loops at 3.5 K confirming the SMM nature of this Co^{II}-carbene complex. It is important to note, however, that this complex was not isolated in the carbene form; rather the precursor was isolated and single-crystal X-ray data was obtained.

While this was the first report of SMM behaviour with a single 3*d* ion, the metal is not the sole source of spin and hence cannot be considered a truly mononuclear 3*d* SMM. Since then, other reports have surfaced combining radical ligands with 3*d* ions in order to target large barrier SMMs and the relatively large anisotropy originating from Co^{II} ions.[51] As mentioned previously, however, these complexes have not been isolated in solid form but rather generated *in situ* with SMM properties in frozen solutions. Since then, isolated

mononuclear Co^{II} complexes featuring neutral ligands have been reported to exhibit SMM properties both in the absence of and in the presence of an applied dc field. The following sections will focus on Co^{II} complexes with different coordination numbers dictated mainly by the choice of ligands. The chosen ligand field around the metal centre will play a significant role in the *d*-orbital splitting leading to magnetic anisotropy.

1.5.1 Four-coordinate Co(II) Single-Molecule Magnets

To date, the lowest reported coordination number for a mononuclear Co^{II} SMM is four-coordinate. While there have been a few complexes reported to exhibit such behaviour, most have only shown blocking of the magnetisation under an applied dc field which suppresses the direct relaxation processes or QTM occurring at zero-field. A notable example of a tetrahedral complex presenting slow magnetic relaxation in the absence of an applied field is $[Co(SPh)_4]^{2-}$, reported by J. M. Zadrozny and J. R. Long (Fig. 1.16a).[52] The high-spin Co^{II} ion is shown to possess an $S = 3/2$ spin ground state with large, negative, axial ZFS where $D = -70$ cm^{-1}. Additionally, this complex was shown to possess relatively low rhombicity with $E/D < 0.09$. The large magneto-anisotropy can be studied qualitatively by examining the *d*-orbital splitting of the Co^{II} ion coordinated to four SPh^- ligands (Fig. 1.16b).

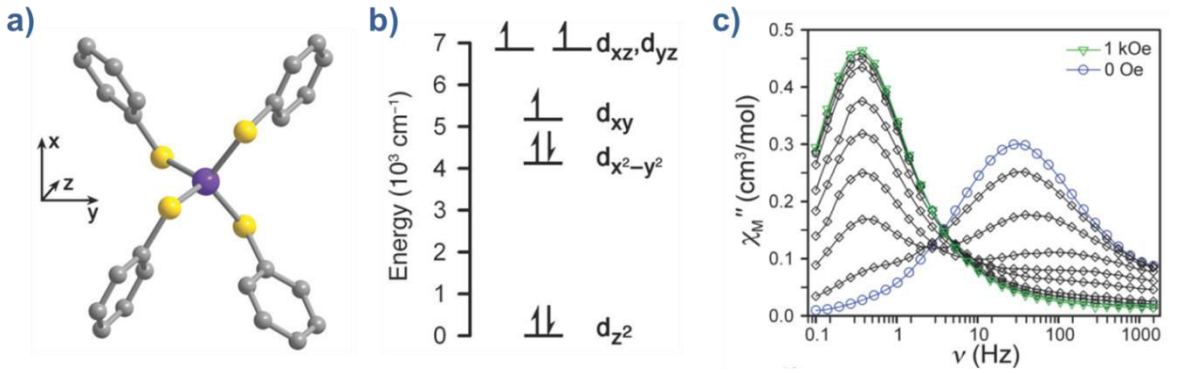

Figure. 1.16: Molecular structure (a), d-orbital splitting diagram (b) and χ" *vs.* ν plot as a function of applied field (c) for $[Co(SPh)_4]^{2-}$. Colour code: Purple (Co), yellow (S), grey (C). Counter cation has been omitted for clarity. Adapted from Ref. 52.

The filled d_{z^2} orbital is calculated to be the lowest in energy, followed by a filled $d_{x^2-y^2}$ orbital. At slightly higher energy lies the singly-occupied d_{xy} orbital which is in close enough proximity, energetically, to the $d_{x^2-y^2}$ orbital such that a low-lying excited electronic state is

generated which can couple to the ground electronic state through spin-orbit coupling yielding large magneto-anisotropy. The last two singly-occupied 3*d* orbitals, d_{xz} and d_{yz}, are calculated to be highest in energy. The large *D* value results in an energy barrier for spin reversal of $U_{eff} = 21$ cm^{-1} which is in good agreement with similar transition metal complexes at the time. When performing the ac measurements on this complex, an interesting feature was observed in the χ" *vs.* ν plot as a function of the applied field (Fig. 1.16c). As the field was increased, one relaxation process (at higher frequencies) decreased in intensity and another process (at lower frequencies) began to appear and gain intensity as the applied field increased. This illustrates the change in the relaxation mechanisms from thermally activated (at higher frequencies) to quantum tunnelling (at lower frequencies) depending on the applied dc field. To further probe this change in relaxation mechanisms, magnetic dilution studies were performed using the diamagnetic Zn^{II} analogue which confirmed the molecular nature of the magnetic properties as the diluted sample still behaved as an SMM. Interestingly, a second relaxation process was not observed, indicating the intermolecular dipolar nature of the second process observed in the parent sample.

A series of complexes with the general formula $[Co(EPh)_4]^{2-}$ where E = O, S and Se, was later reported by the same authors [53] in order to study the relationship between the |*D*| value and the energy barrier for spin reversal. However, no clear relationship could be established since the barriers remained the same for different donor atoms. It is noteworthy, however, that the *D* value did vary, from $D = -11.1(3)$ cm^{-1} in $(Ph_4P)_2[Co(OPh)_4]\cdot(CH_3CN)$ to $-83(1)$ cm^{-1} in $(Ph_4P)_2[Co(SePh)_4]$, which is in accordance with the decrease in the Racah *B* parameter. It is noteworthy that in these complexes the magnetic anisotropy originates from a second order interaction between the low-lying excited electronic state and the ground electronic state. The smaller the energy gap between these states, the greater the interaction leading to higher *D* values. In order to obtain lower energy anisotropic excited electronic states, the energy splitting for the d_{xy} and $d_{x^2-y^2}$ orbitals must be minimised. This can be achieved using weaker ligand fields as is seen in this series of complexes where larger negative magnetic anisotropy is expected and observed for ligands with softer donor atoms. This hypothesis was further supported by K. R. Dunbar and co-worker in a series of pseudo-tetrahedral Co^{II} complexes employing ligands with heavy donor atoms.[54] They also observed an increase in the *D* parameter with softer and heavier main group donor atoms. However, while the metal ions became increasingly anisotropic, the energy barriers for spin reversal did not increase significantly; reasons for which are currently unknown and should be investigated using advanced computational techniques.

Other Co^{II} complexes exhibiting distorted tetrahedral geometry have been reported where SMM behaviour is observed in the absence of or in the presence of an applied dc

field.[55] One such mononuclear field-induced SMM reported by D.-K. Cao and co-workers [55a] (U_{eff} < 60 K) was also shown to exhibit photochromic behaviour in solution, displaying a purple-blue colour after irradiation with 350 nm light. Upon irradiation with 575 nm light, the coloured solution would revert back to colourless (the same effect was also seen if the solution was kept in the dark).

1.5.2 Five-coordinate Co(II) Single-Molecule Magnets

Two of the first mononuclear Co^{II}-based SMMs, reported by M. Murugesu and co-workers, were, in fact, penta-coordinate complexes using bis(imino)pyridine pincer ligands.[56] The complexes, [Co({ArN=CMe}$_2$(NPh))(NCS)$_2$] and [Co({ArN=CPh}$_2$(NPh))(NCS)$_2$] will be referred to herein as [Co(LMe)(NCS)$_2$] and [Co(LPh)(NCS)$_2$], respectively. Ligand design was extremely important in this study in order to favour square pyramidal as opposed to trigonal bipyramidal geometry in a five-coordinate complex. Furthermore, the ligand was designed to create tension within the basal plane such that the metal ion would be pushed out of the plane resulting in spin-orbit coupling. This was achieved by modifying slightly the pincer ligands at the imine position using methyl or phenyl groups in order to induce distortions in the geometry of the metal ions. The remaining coordination sites were occupied by thiocyanate groups as they can accommodate distortions in the geometry of the Co^{II} ions and are quite flexible as ligands. The resultant distorted square-pyramidal geometry, with the metal ion elevated out of the basal plane, generated significant spin-orbit coupling and magnetic anisotropy in the system leading to SMM behaviour.

This set of compounds illustrates the importance of ligand design when targeting specific metal geometries in order to observe desired properties. Slow magnetic relaxation was observed for both complexes under an applied field of 0.2 T with U_{eff} = 16 and 24 K for [Co(LMe)(NCS)$_2$] and [Co(LPh)(NCS)$_2$], respectively. Using simple, planar terpyridine (terpy) ligands, we were able to isolate two more complexes. The penta-coordinate Co^{II} complexes, [Co(terpy)Cl$_2$] and [Co(terpy)(NCS)$_2$] have been known in the literature for quite some time and consist of a tridentate terpy ligand coordinated to Co^{II} centres. The remaining two coordination sites are occupied by monodentate ligands which provide the necessary flexibility such that distortion in the geometry can be accommodated. These complexes, along with their unique magnetic properties, will be discussed in detail in Chapter 5.

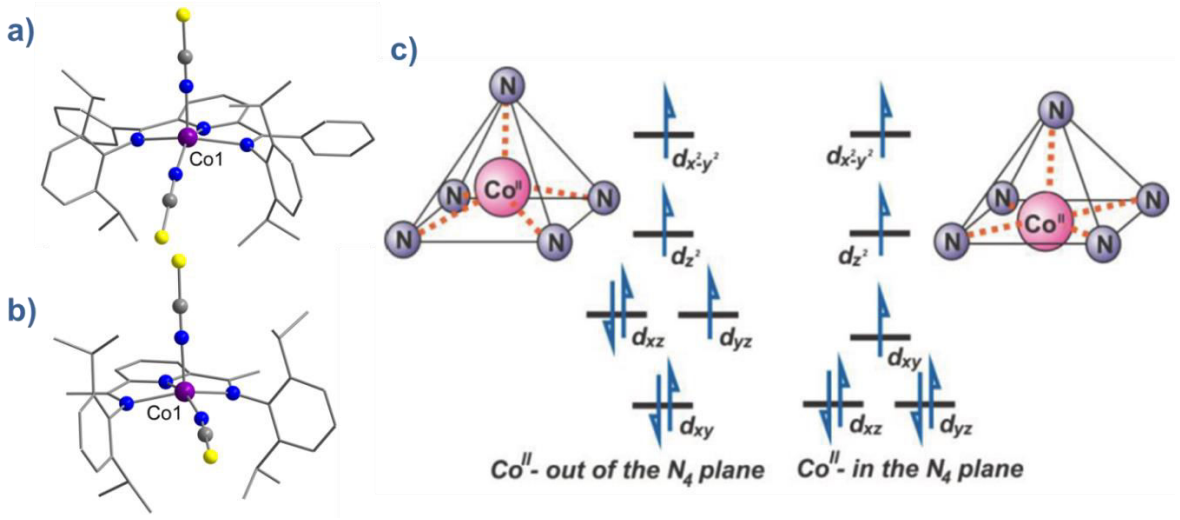

Figure 1.17: Molecular structures of [Co(LPh)(NCS)$_2$] (a) and [Co(LMe)(NCS)$_2$] (b).[58] Colour code: Purple (Co), blue (N), yellow (S), grey (C). c) *d*-orbital splitting diagrams for different geometries of Co^{II}, with the metal ion in and out of the basal plane.

1.5.3 Six- and Higher-coordinate Co(II) Single-Molecule Magnets

Thus far, the majority of mononuclear Co^{II} SMMs with axial magnetic anisotropy have been complexes with coordination numbers ≤ 5. This can be mainly attributed to the dominant positive or easy plane anisotropy observed in complexes with higher coordination numbers. One complex, reported by S. Gao and co-workers,[57] consists of a paramagnetic Co^{II} centre surrounded by three Co^{III} ions which are diamagnetic. The central Co^{II} metal ion is coordinated to six oxygen atoms originating from the Schiff-base ligand used (R-4-bromo-2-((2-hydroxy-1-phenylethylimino)methyl)phenol). This results in slightly distorted triangular prism geometry with D_3 symmetry. The magnetic behaviour of this compound arises solely from the Co^{II} centre and hence this complex can be considered in this category. The ZFS parameter was calculated to be $D = -115$ cm^{-1}, indicating a highly anisotropic system that is uniaxial. The slow magnetic relaxation is observed at zero applied field with $U_{eff} = 109$ K, one of the highest ever reported for a mononuclear Co^{II} SMM. The high relaxation barrier was also attributed to very low transverse anisotropy in this system which reduces the influence of QTM on the thermally assisted relaxation process. Additionally, the three peripheral Co^{III} ions serve to weaken the intermolecular exchange and dipolar interactions between Co^{II} centers thereby producing a dilution-like effect which is well-known to increase the spin reversal barriers. Another complex with a high coordination number for a Co^{II} ion was reported recently to exhibit SMM properties, the first eight-coordinate 3*d* mononuclear

complex to present slow relaxation of the magnetisation (albeit with a low barrier of U_{eff} = 17 cm^{-1}) under an applied dc field.[58]

1.5.4 Conclusions

In recent years, a clear shift has occurred in the field of single-molecule magnets which began with the first discovery of SMM properties in a mononuclear Co^{II} complex. The main factor contributing to high energy barriers for spin reversal has been determined to be the magnetic anisotropy. In fact, as the total spin of a complex increases, overall *D* decreases. This encouraged the pursuit of mononuclear complexes which are highly anisotropic such as Co and Fe compounds adopting certain geometries. While one of the characteristics of SMMs is slow magnetic relaxation at zero field, most reported mononuclear 3*d* SMMs only exhibit the aforementioned properties under an applied field. This limitation must be overcome if applications such as information storage are to be realized. There is no clear relationship between the coordination number of the metal center and the height of the energy barrier for spin reversal. It had been speculated that lower coordination numbers would yield higher anisotropy values; however, this is not supported by the current literature reviewed in this section.

It is important to note that the energy barriers for these mononuclear complexes have surpassed those reported for multinuclear 3*d* clusters as well as some lanthanide complexes. While the highest barriers and blocking temperatures have thus far been obtained using lanthanide metals, the sub-field of mononuclear 3*d* SMMs is in its infancy and has great potential to expand and eventually surpass 4*f*-based SMMs. Additionally, 3*d* metal complexes have the advantage of simpler synthetic techniques and lower cost compared to lanthanide metals. This will play a major role when applications are to be considered and materials design is underway utilising SMMs.

References

[1] (a) O. Kahn, *Molecular magnetism*; 1st ed.; VCH Publishers Inc.: New York, 1993; (b) N. Robertson, G. T. Yee, Molecular materials; 1st ed.; John Wiley and Sons, Ltd.: West Sussex, 2010; (c) J. H. van Vleck, *The Theory of Electric and Magnetic Susceptibility*; Oxford University Press: London, 1932; (d) J.-P. Launay, M. Verdaguer, *Electrons in molecules*; 1st ed.; Oxford University Press: New York, 2014.

[2] (a) D. Gatteschi, R. Sessoli, J. Villain, *Molecular Nanomagnets*; 1st ed.; Oxford University Press: New York, 2006; (b) F. Canepa, M. Solzi, *In Condensed matter*; M. P. Das, Ed.; Nova Science Publishers Inc.: New York, 2007.

[3] R. Nave, (2013) SQUID Magnetometer and Josephson Junctions. In Hyperphysics [Online]. Available: http://hyperphysics.phy-astr.gsu.edu/hbase/solids/squid.html [2014, September 13]

[4] (a) K. S. Cole, R. H. Cole, *J. Chem. Soc.* 9 (1941), 341; (b) S. M. J. Aubin, Z. Sun, L. Pardi, J. Krzystek, K. Folting, L. J. Brunel, A. L. Rheingold, G. Christou, D. N. Hendrickson, *Inorg. Chem.* 38 (1999), 5329.

[5] G. Christou, D. Gatteschi, D. N. Hendrickson, R. Sessoli, *MRS Bull*. 25 (2000), 66.

[6] F. Neese, D. A. Pantazis, *Faraday Discuss*. 148 (2011), 229.

[7] (a) J. D. Rinehart, M. Fang, W. J. Evans, J. R. Long, *Nat. Chem*. 3 (2011), 538; (b) J. J. Le Roy, L. Ungur, I. Korobkov, L. F. Chibotaru, M. Murugesu, *J. Am. Chem. Soc.* 136 (2014), 8003; (c) J. D. Rinehart, M. Fang, W. J. Evans, J. R. Long, *J. Am. Chem. Soc*. 133 (2011), 14236.

[8] (a) L. Bogani, W. Wernsdorfer, *Nat. Mater*. 7 (2008), 179; (b) D. Gatteschi, R. Sessoli, *Angew. Chem. Int. Ed*. 42 (2003), 268.

[9] W. Wernsdorfer, N. Aliaga-Alcalde, D. N. Hendrickson, G. Christou, *Nature* 416 (2002), 406.

[10] (a) W. Wernsdorfer, S. Bhaduri, C. Boskovic, G. Christou, D. N. Hendrickson, *Phys. Rev. B* 65 (2002), 180403; (b) W. Wernsdorfer, N. E. Chakov, G. Christou, *Phys. Rev. Lett*. 95 (2005), 037203.

[11] F. Habib, J. Long, P.-H. Lin, I. Korobkov, L. Ungur, W. Wernsdorfer, L. F. Chibotaru, M. Murugesu, *Chem. Sci*. 3 (2012), 2158.

[12] (a) T. Lis, *Acta Cryst.* B36 (1980), 2042; (b) R. Sessoli, D. Gatteschi, A. Caneschi, A. Novak, *Nature* 45 (1993), 141; (c) R. Sessoli, H.-L. Tsai, A. R. Schake, S. Wang, J. B. Vincent, K. Folting, D. Gatteschi, G. Christou, D. N. Hendrickson, *J. Am. Chem. Soc*. 115 (1993), 1804.

[13] (a) L. F. Chibotaru, L. Ungur, A. Soncini, *Angew. Chem., Int. Ed*. 47 (2008), 4126; (b) C. Benelli, D. Gatteschi, *Chem. Rev*. 102 (2002), 2369.

[14] P.-H. Lin, T. J. Burchell, L. Ungur, L. F. Chibotaru, W. Wernsdorfer, M. Murugesu, *Angew. Chem., Int. Ed*. 48 (2009), 9489.

[15] (a) R. J. Blagg, F. Tuna, E. J. L. McInnes, R. E. P. Winpenny, *Chem. Commun*. 47 (2011), 10587; (b) J. D. Rinehart, M. Fang, W. J. Evans, J. R. Long, *J. Am. Chem. Soc*. 133 (2011), 14236; (d) Y.-N. Guo, G.-F. Xu, P. Gamez, L. Zhao, S.-Y. Lin, R. Deng, J. Tang, H.-J. Zhang, *J. Am. Chem. Soc*. 132 (2010), 8538; (d) S. Demir, J. M. Zadrozny, M. Nippe, J. R. Long, *J. Am. Chem. Soc*. 134 (2012), 18546; (e) L. Ungur, J. J. Le Roy, I. Korobkov, M. Murugesu, L. F. Chibotaru, *Angew. Chem. Int. Ed*. 53 (2014), 4413; (f) J. J.; Le Roy, I. Korobkov, M. Murugesu, *Chem. Commun*. 50 (2014), 1602.

[16] N. Ishikawa, M. Sugita, T. Ishikawa, S. Koshihara, Y. Kaizu, *J. Am. Chem. Soc*. 125 (2003), 8694.

[17] N. Ishikawa, M. Sugita, W. Wernsdorfer, *Angew. Chem., Int. Ed*. 44 (2005), 2931.

[18] (a) M. D. Ward, *Coord. Chem. Rev.* 251 (2007), 1663; (b) K. Binnemans, *Coord. Chem. Rev*. 109 (2009), 4283; (c) L. Charbonnière, R. Ziessel, M. Guardigli, A. Roda, N. Sabbatini, M. Cesario, *J. Am. Chem. Soc.* 123 (2001), 2436; (d) J.-C. G. Bünzli, *Acc. Chem. Res.* 39 (2006), 53; (e) W. C. W. Chan, D. J. Maxwell, X. Gao, R. E. Bailey, M. Han, S. Nie, *Curr. Opin. Biotechnol*. 13 (2002), 40.

[19] (a) K. Binnemans, *Handbook on the Physics and Chemistry Lanthanides of Rare-Earth*; K. A. Gschneidner Jr, J.-C. G. Bünzli, V. K. Pecharsky, Ed.; Elsevier: Amsterdam, The Netherlands, 2005; Vol. 35, Chapter 225, p 107; (b) J. P. André, H. R. Mäcke, É. Tóth, A. E. Merbach, *J. Biol. Inorg. Chem*. 4 (1999), 341; (c) J.-C. G. Bünzli, *Acc. Chem. Res.* 39 (2006), 53.

[20] J. Arcas, A. Hernando, J. M. Barandiarán, C. Prados, M. Vázquez, P. Marín, A. Neuweiler, *Phys. Rev. B* 58 (1998), 5193.

[21] (a) J. F. Liu, T. Chui, D. Dimitrov, G. C. Hadjipanayis, *Appl. Phys. Lett*. 73 (1998), 3007; (b) J. F. Liu, Y. Zhang, D. Dimitrov, G. C. Hadjipanayis, *J. Appl. Phys*. 85 (1999), 2800.

[22] (a) J. Bauer, M. Seeger, A. Zern, H. Kronmüller, *J. Appl. Phys*. 80 (1996), 1667; (b) C. Bauer, H. Raich, G. Jeschke, P. Blümler, *J. Magn. Reson*. 198 (2009), 222.

[23] (a) P.-H. Lin, T. J. Burchell, R. Clérac, M. Murugesu, *Angew. Chem., Int. Ed.* 47 (2008), 8848; (b) J. Long, F. Habib, P.-H. Lin, I. Korobkov, G. Enright, L. Ungur, W. Wernsdorfer, L. F. Chibotaru, M. Murugesu, *J. Am. Chem. Soc*. 133 (2011), 5319; (c) J. Luzon, K. Bernot, I. J. Hewitt, C. E. Anson, A. K. Powell, R. Sessoli, *Phys. Rev. Lett*. 100 (2008), 247205/1; (d) M. A. AlDamen, J. M. Clemente-Juan, E. Coronado, C. Martí-Gastaldo, A. Gaita-Ariño, *J. Am. Chem. Soc.* 130 (2008), 8874; (e) S. Cardona-Serra, J. M. Clemente-Juan, E. Coronado, A. Gaita-Ariño, A. Camón, M. Evangelisti, F. Luis, M. J. Martínez-Pérez, J. Sesé, *J. Am. Chem. Soc*. 134 (2012), 14982.

[24] (a) J.-P. Costes, J. M. Clemente-Juan, F. Dahan, J. Milon, *Inorg. Chem*. **43 (**2004), 8200; (b) D. Visinescu, A. M. Madalan, M. Andruh, C. Duhayon, J.-P. Sutter, L. Ungur, W. V. den Heuvel, L. F. Chibotaru, *Chem. Eur. J*. 15 (2009), 11808; (c) K. Bernot, L. Bogani, A. Caneschi, D. Gatteschi, R. Sessoli, *J. Am. Chem. Soc*. 128 (2006), 7947; (d) H. Miyasaka, M. Julve, M. Yamashita, R. Clérac, *Inorg. Chem*. 48 (2009), 3420 and references therein; (e) R. Liu, C. Zhang, X. Mei, P. Hu, H. Tian, L. Li, D. Liao, J.-P. Sutter, *New J. Chem*. **36 (**2012), 2088.

[25] (a) M. D. Regulacio, K. Bussmann, B. Lewis, S. L. Stoll, *J. Am. Chem. Soc*. 128 (2006), 11173; (b) K. Binnemans, R. Van Deun, C. Görller-Walrand, W. Haase, D. W. Bruce, L. Malykhina, Y. G. Galyametdinov, *Mater. Sci. Eng; C* 18 (2001), 247.

[26] (a) R. Sessoli, A. K. Powell, *Coord. Chem. Rev*. 253 (2009), 2328; (b) L. Sorace, C. Benelli, D. Gatteschi, *Chem. Soc. Rev*. 40 (2011), 3092; (c) J. D. Rinehart, J. R. Long, *Chem. Sci*. 2 (2011), 2078; (d) Y.-N. Guo, G.-F. Xu, Y. Guo, J. Tang, *Dalton Trans*. 40 (2011), 9953; (d) J. Luzon, R. Sessoli, *Dalton Trans*. 41 (2012), 13556; (e) A. V. Palii, B. Tsukerblat, S. Klokishner, K. R. Dunbar, J. M. Clemente-Juan, E. Coronado, *Chem. Soc. Rev*. 40 (2011), 3130; (f) A. V. Palii, B. S. Tsukerblat, J. M. Clemente-Juan, E. Coronado, *Inorg. Chem*. 44 (2005), 3984.

[27] (a) G. Cucinotta, M. Perfetti, J. Luzon, M. Etienne, P.-E. Car, A. Caneschi, G. Calvez, K. Bernot, R. Sessoli, *Angew. Chem., Int. Ed*. 51 (2012), 1606; (b) S. Sakaue, A.

Fuyuhiro, T. Fukuda, N. Ishikawa, *Chem. Commun*. 48 (2012), 5337; (c) T.; Rajeshkumar, G. Rajaraman, *Chem. Commun*. 48 (2012), 7856.

[28] (a) S.-D. Jiang, B.-W. Wang, H.-L. Sun, Z.-M. Wang, S. Gao, *J. Am. Chem. Soc*. 133 (2011), 4730; (b) Y. Wang, X.-L. Li, T.-W. Wang, Y. Song, X.-Z. You, *Inorg. Chem*. 49 (2010), 969.

[29] (a) T. Kajiwara, M. Hasegawa, A. Ishii, K. Katagiri, M. Baatar, S. Takaishi, N. Iki, M. Yamashita, *Eur. J. Inorg. Chem*. (2008), 5565; (b) G. Abbas, Y. Lan, G. Kostakis, C. E. Anson, A. K. Powell, *Inorg. Chim. Acta*, 361 (2008), 3494; (c) G.-F. Xu, Q.-L. Wang, P. Gamez, Y. Ma, R. Clérac, J. Tang, S.-P. Yan, P. Cheng, D.-Z. Liao, *Chem. Commun*. 46 (2010), 1506; (d) J.-B. Peng, Y.-P. Ren, X.-J. Kong, L.-S. Long, R.-B. Huang, L.-S. Zheng, *CrystEngComm*, 13 (2011), 2084.

[30] N. Ishikawa, T. Iino, Y. Kaizu, *J. Am. Chem. Soc*. 124 (2002), 11440.

[31] N. Ishikawa, T. Iino, Y. Kaizu, *J. Phys. Chem. A* 106 (2002), 9543.

[32] N. Ishikawa, S. Otsuka, Y. Kaizu, *Angew. Chem., Int. Ed*. 44 (2005), 731.

[33] N. Ishikawa, T. Iino, Y. Kaizu, *J. Phys. Chem. A* 107 (2003), 7879.

[34] L. E. Roy, T. Hughbanks, *J. Am. Chem. Soc*. 128 (2006), 568.

[35] F. Habib, P.-H. Lin, J. Long, I. Korobkov, W. Wernsdorfer, M. Murugesu, *J. Am. Chem. Soc*. 133 (2011), 8830.

[36] (a) W. Wernsdorfer, S. Bhaduri, C. Boskovic, G. Christou, D. N. Hendrickson, *Phys. Rev. B* 65 (2002), 180403; (b) W. Wernsdorfer, N. E. Chakov, G. Christou, *Phys. Rev. Lett*. 95 (2005), 037203.

[37] P.-H. Lin, M. Leclère, J. Long, T. J. Burchell, I. Korobkov, R. Clérac, M. Murugesu, *Dalton Trans*. 39 (2010), 5698.

[38] P.-H. Lin, W.-B. Sun, M.-F. Yu, G.-M. Li, P.-F. Yan, M. Murugesu, *Chem. Commun*. 47 (2011), 10993.

[39] G.-F. Xu, Q.-L. Wang, P. Gamez, Y. Ma, R. Clérac, J. Tang, S.-P. Yan, P. Cheng, D.-Z. Liao, *Chem. Commun*. 46 (2010), 1506.

[40] J. Vallejo, J. Cano, I. Castro, M. Julve, F. Lloret, O. Fabelo, L. Cañadillas-Delgadoz, E. Pardo, *Chem. Commun*. 48 (2012), 7726.

[41] R. A. Layfield, J. W. McDouall, S. A. Sulway, F. Tuna, D. Collison, R. E. P. Winpenny, *Chem. Eur. J.* 16 (2010), 4442.

[42] S. A. Sulway, R. A. Layfield, F. Tuna, W. Wernsdorfer, R. E. P. Winpenny, *Chem. Commun*. 48 (2012), 1508.

[43] J. D. Rinehart, T. D. Harris, S. A. Kozimor, B. M. Bartlett, J. R. Long, *Inorg. Chem*. 48 (2009), 3382.

[44] F. Tuna, C. A. Smith, M. Bodensteiner, L. Ungur, L. F. Chibotaru, E. J. L. McInnes, R. E. P. Winpenny, D. Collison, R. A. Layfield, *Angew. Chem., Int. Ed*. 51 (2012), 6976.

[45] (a) M. Jeletic, P.-H. Lin, J. J. Le Roy, I. Korobkov, S. I. Gorelsky, M. Murugesu, *J. Am. Chem. Soc*. 133 (2011), 19286; (b) S.-D. Jiang, B.-W. Wang, H. L. Sun, Z. M. Wang, S. Gao, *J. Am. Chem. Soc*. 133 (2011), 4730.

[46] D. P. Mills, F. Moro, J. McMaster, J. van Slageren, W. Lewis, A. J. Blake, S. T. Liddle, *Nat. Chem*. 3 (2011), 454.

[47] J. J. Le Roy, M. Jeletic, S. I. Gorelsky, I. Korobkov, L. Ungur, L. F. Chibotaru, M. Murugesu, *J. Am. Chem. Soc*. 135 (2013), 3502.

[48] C. Benelli, A. Caschi, D. Gatteschi, L. Pardi, *Inorg. Chem*. 31 (1992), 741.

[49] G. Poneti, K. Bernot, L. Bogani, A. Caneschi, R. Sessoli, W. Wernsdorfer, D. Gatteschi, *Chem. Commun*. (2007), 1807.

[50] S. Karasawa, G. Zhou, H. Morikawa, N. Koga, *J. Am. Chem. Soc*. 125 (2003), 13676.

[51] (a) S. Karasawa, D. Yoshihara, N. Watanabe, M. Nakano, N. Koga, *Dalton Trans*. (2008), 1418; (b) S. Karasawa, K. Nakano, J.-i. Tanokashira, N. Yamamoto, T. Yoshizaki, N. Koga, *Dalton Trans*. 41 (2012), 13656.

[52] J. M. Zadrozny, J. R. Long, *J. Am. Chem.Soc*. 133 (2011), 20732.

[53] J. M. Zadrozny, J. Telser, Long, J. R. *Polyhedron* 64 (2013), 209.

[54] M. R. Saber, K. R. Dunbar, *Chem. Commun*. 50 (2014), 12266.

[55] (a) D.-K. Cao, J.-Q. Feng, M. Ren, Y.-W. Gu, W. Song, M. D. Ward, *Chem. Commun.* 49 (2013), 8863; (b) A. Buchholz, A. O. Eseola, W. Plass, *C. R. Chimie* 15 (2012), 929; (c) R. Boča, J. Miklovič, J. Titis, *Inorg. Chem.*, 53 (2014), 2367; (d) M. S.

Fataftah, J. M. Zadrozny, D. M. Rogers, D. E. Freedman, *Inorg. Chem.* 53 (2014), 10716; (e) F. Yang, Q. Zhou, Y. Zhang, G. Zeng, G. Li, Z. Shi, B. Wang, S. Feng, *Chem. Commun*. 49 (2013), 5289.

[56] T. Jurca, A. Farghal, P.-H. Lin, I. Korobkov, M. Murugesu, D. S. Richeson, *J. Am. Chem. Soc*. 133 (2011), 15814.

[57] Y.-Y. Zhu, C. Cui, Y.-Q. Zhang, J.-H. Jia, X. Guo, C. Gao, K. Qian, S.-D. Jiang, B.-W. Wang, Z.-M. Wang, S. Gao, *Chem. Sci*. 4 (2013), 1802.

[58] L. Chen, J. Wang, J.-M. Wei, W. Wernsdorfer, X.-T. Chen, Y.-Q. Zhang, Y. Song, Z.-L. Xue, *J. Am. Chem. Soc*. 136 (2014), 12213.

Chapter 2

Helical Supramolecular Architectures

The shift from 3*d* to 4*d*/5*d* to 4*f*/5*f* metals has illustrated the need for complexes with higher anisotropy values in addition to high spin values if we were to target high spin reversal barriers. Contrary to controlling the spin values, controlling the anisotropy has proven to be extremely difficult. Parallel alignment of the magnetic anisotropy axes in transition metal ions can have an additive effect on total anisotropy of a system. Therefore, aligning the anisotropy axes in a molecule can potentially yield even larger *D* values and hence much higher barriers for spin reversal. This challenging approach prompted the investigation of dinuclear helicate complexes where the helical twist provides a way of tuning the anisotropy axes on the metal centres and thereby modulating their orientations relative to one another. Moreover, this approach also provides two metal centres in a near identical coordination environment where subtle differences such as orientation of anisotropic axes or energies of the first excited Kramers doublets on Dy sites yields different relaxation processes. Therefore, through simple modifications, ligands can be designed to modulate the angle between the anisotropic axes without changing the coordination environments such that correlations between the structural features and the magnetic properties can be studied. This strategy could lead to important magneto-structural correlations that enable us to synthesise SMMs with considerably larger barriers by controlling the magnetic anisotropy of the system as a whole. The research presented in this chapter has been published in Chemical Science (*Chem. Sci*. 3 (2012), 2158-2164); and has been awarded a page in the CIC Inorganic Division Calendar Competition (month of June) in 2012.

2.1 Helicates & Mesocates

Helical structures have existed since the beginning of time; they can be observed everywhere around us whether in the arms of spiral galaxies, in DNA and protein structures or even in

human-made art.[1] A helix is a geometrical motif where strands intertwine forming spiral-like structures. In order to form a helical structure, certain spatial restrictions must be present including conformational restrictions, hydrogen-bonding or other weak forces and/or coordination to metal ions.[2] Metal-containing helical complexes were termed "helicates" by Jean-Marie Lehn and co-workers in 1987; the suffix "-ate" indicates host-guest interactions between the strands or ligands and the metal centres.[3] Since their discovery, self-assembled helicates have featured prominently in the literature since they resemble complexes formed by nature and studied in many areas such as biology and physics. Additionally, they have numerous potential applications such as in stereoselective catalysis as well as functional components of molecular devices.[4] Important aspects in the field of helicates such as design and control over the final structure have provided a pathway towards the design of complex chemical architectures.

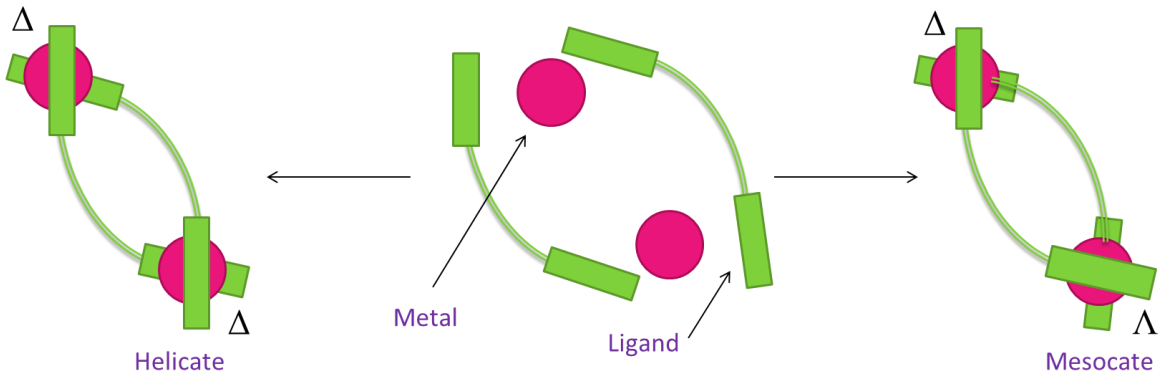

Scheme 2.1: Schematic diagram for the formation of double-stranded helicate *versus* mesocate when employing bidentate ligands and two metal ions. The notations Δ and Λ indicate the chirality of the metal centers.

Helical structures have been mainly dominated in the literature by single-,[5] double-,[6] and triple-[7] stranded compounds. Only a few examples of quadruply-stranded helicates [8] have been reported to date where the synthetic strategy mainly focuses on employing metal ions with a square planar geometry and oligomonodentate ligands acting as bridges. Only recently have there been reports of quadruply-stranded dinuclear helicates that were obtained using a different strategy.[9] The formulation involved oligobidentate bridging ligands and metal ions that can accommodate higher coordination numbers. Lanthanide helicates have also been investigated due to their ability to coordinate up to 12, but more commonly 8 or 9, donor atoms.[10] One of the key challenges in controlling the self-assembly of helicates has been to modulate the chiral amplification or helix reversal in these

structures. As a result, a racemic mixture of homochiral complexes is observed where, in a dinuclear system, ΔΔ and ΛΛ symmetry is assigned. The symmetry labels, Δ and Λ, correspond to a right-handed helix and a left handed helix, respectively. When studying a dinuclear complex with a helical structure, each metal centre is assigned a symmetry label of Δ or Λ corresponding to the "handed-ness" dictated by the ligands which are then combined yielding ΔΔ or ΛΛ helicate complexes. When an internal helix reversal occurs, it results in a ΔΛ meso-helical structure or mesocate and a loss of chirality. These achiral structures remain relatively unexplored. A schematic diagram illustrating the formation of double-stranded helicate and mesocate structures is shown in Scheme 2.1.

2.1.1 Ligand Design

Ligand design is key in the synthesis of helical architectures especially for the purpose of controlling the helical twist within the complex. A suitable ligand must possess at least two coordinating ends which are ideal for coordinating targeted metal ions. These moieties must be separated by a rigid spacer to prevent the thermodynamically driven chelate effect to encapsulate a single metal ion forming mononuclear complexes. The spacer must also provide some flexibility to allow for a helical twist of the ligand.[1,2] In pursuit of a deeper understanding of the self-assembly of helicates and mesocates as well as controlling the helical twist of the ligands we designed a strategy involving ligand modification to tune the length and flexibility of the spacer as seen in Scheme 2.2. In addition to interesting molecular architectures, these molecules may exhibit various other properties depending on the identity of the metal ions. Multifunctional molecular materials where more than one physical property can interact in a synergistic fashion or simply coexist in the molecule have attracted much attention due to potential applications in a multitude of fields.[11] One such field, featuring prominently in this thesis, is molecular magnetism where slow magnetic relaxation can occur yielding molecular magnetic materials or SMMs as discussed in Chapter 1. It is well known that N- and mostly O-based coordination environments favour the encapsulation of lanthanide ions which possess large magnetic anisotropy and can, therefore, yield SMMs with high spin reversal barriers. Additionally, it is evident that maintaining the same coordinating pockets and metal ions should result in isomorphous complexes regardless of simple modifications to the spacer of the ligand. By varying only one parameter at a time, a correlation could be obtained between the properties of the spacer and the most thermodynamically stable structure. Furthermore, a series of compounds with varying spacers could be used as a model system for studying magneto-structural correlations leading to parameters which can be modified to obtain SMMs with higher energy barriers.

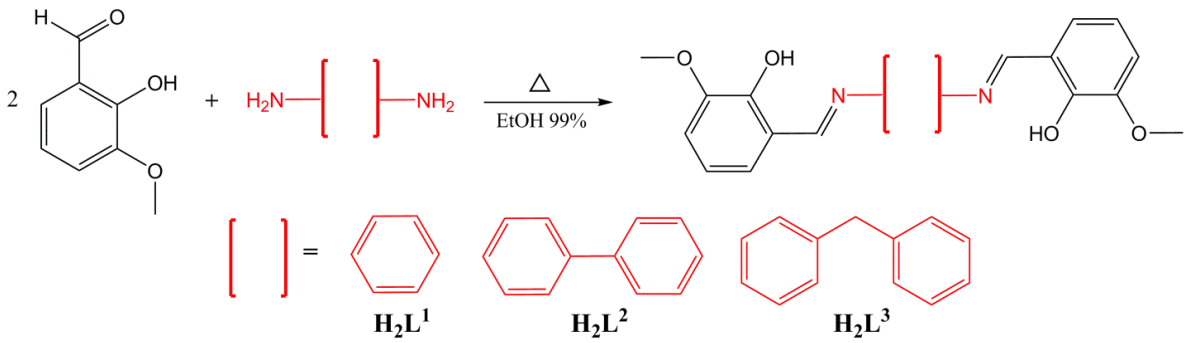

Scheme 2.2: Preparation of H_2L^1, H_2L^2 and H_2L^3 ligands which vary in the spacer used.

The ligands employed in this chapter were synthesised using a Schiff-base reaction between an aldehyde terminated *o*-vanillin group and a spacer unit with two terminal amine groups in the *para* position (scheme 2.2). To increase the length and flexibility of the spacer, systematic modifications included replacing the phenyl ring in *N*,*N*'-Bi(3-methoxysalicylidene)benzene-1,4-diamine (H_2L^1) with a biphenyl group to yield *N*,*N*'-Bi(3-methoxysalicylidene)biphenyl-4,4'-diamine (H_2L^2) as well as a diphenylmethane group yielding *N*,*N*'-Bi(3-methoxysalicylidene)-4,4'-methylenedianiline (H_2L^3).

2.1.2 Aligning Anisotropy Axes

One of the most important features of a helicate structure, for our purposes, is the degree of helical twist which is dictated by the spacer employed. By controlling the degree of twisting about the metal centres, we can control the alignment of the anisotropy axes within the structure. Each anisotropy axis, or easy axis as it is often referred to, is uniquely situated within the metal ion. For lanthanides, it does not coincide with a bond necessarily but rather can be found anywhere within the sphere of the ion.[12] In order to locate the easy axis we must perform complex theoretical calculations which will be discussed later in this chapter. To obtain a large global magnetic anisotropy, we must align the easy axes on different metal ions within the complex which can prove quite challenging in a coordination complex. Traditionally, this was achieved through trial-and-error experiments with oxide/hydroxide bridging between metal ions within a cluster, however the unpredictability of the metal coordination, especially lanthanide ions, rendered this approach quite serendipitous. As an alternative approach, we turned our attention to helicates in order to align the anisotropy axes on the metal centers as the degree of helical twist can be controlled by the spacer while the

metal coordination should not be affected by changes within the spacer region of the ligand (Fig. 2.1).

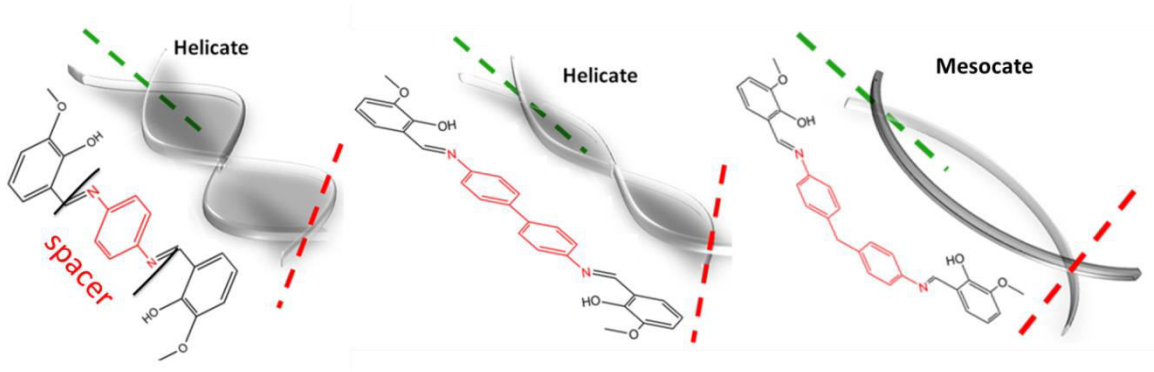

Figure 2.1: Spacer modifications from H_2L^1 to H_2L^2 and H_2L^3 provide a way of controlling the relative orientation of the anisotropic axes on each metal centre. Green and red dashed lines indicate anisotropic axes on Dy^{III} centres. *Vide infra* for anisotropic axes calculations.

2.2 Structural Characterisation of Complexes II-1, II-2 and II-3

The reaction of $Dy(NO_3)_3{\cdot}6H_2O$ with the corresponding ligand in a 1:2 ratio and tetraethylammonium hydroxide (4 equiv.) in acetone/DMF (20 mL : 5 mL) (**II-1** and **II-3**) or DMF (**II-2**) affords yellow crystals. They are characterised as rare Dy^{III}_2 quadruply-stranded helicates $(NEt_4)_2[Dy_2(L^1)_4]((CH_3)_2CO)_{0.25}$ (**II-1**), $(NEt_4)_2[Dy_2(L^2)_4](H_2O)(DMF)_{0.5}$ (**II-2**) and mesocate $(NEt_4)_2[Dy_2(L^3)_4](Et_2O)_2((CH_3)_2CO)_{1.5}$ (**II-3**). Detailed experimental procedures are given in section **2.6** at the end of this chapter while crystallographic data for all complexes can be found in appendix A. The reaction requires basic conditions to promote the deprotonation of the ligand resulting in bridging anionic moieties. Single crystal X-ray analysis revealed dinuclear Dy^{III} helicate structures for **II-1** and **II-2** (Fig. 2.2, *a* and *b*) and a mesocate structure for **II-3** (Fig. 2.2*c*). Complexes **II-1** and **II-3** crystallise in the monoclinic space group $P2_1/n$, whereas complex **II-2** crystallises in the triclinic space group *P-1*. The helical and *meso*-helical structures are formed by four ligands intertwining around two crystallographically independent Dy^{III} metal centres. Since chirality in the case of **II-1** and **II-2** is generated from achiral entities, a racemic mixture of enantiomers is expected and indeed observed where both ΔΔ and ΛΛ isomers are present in the crystal packing.

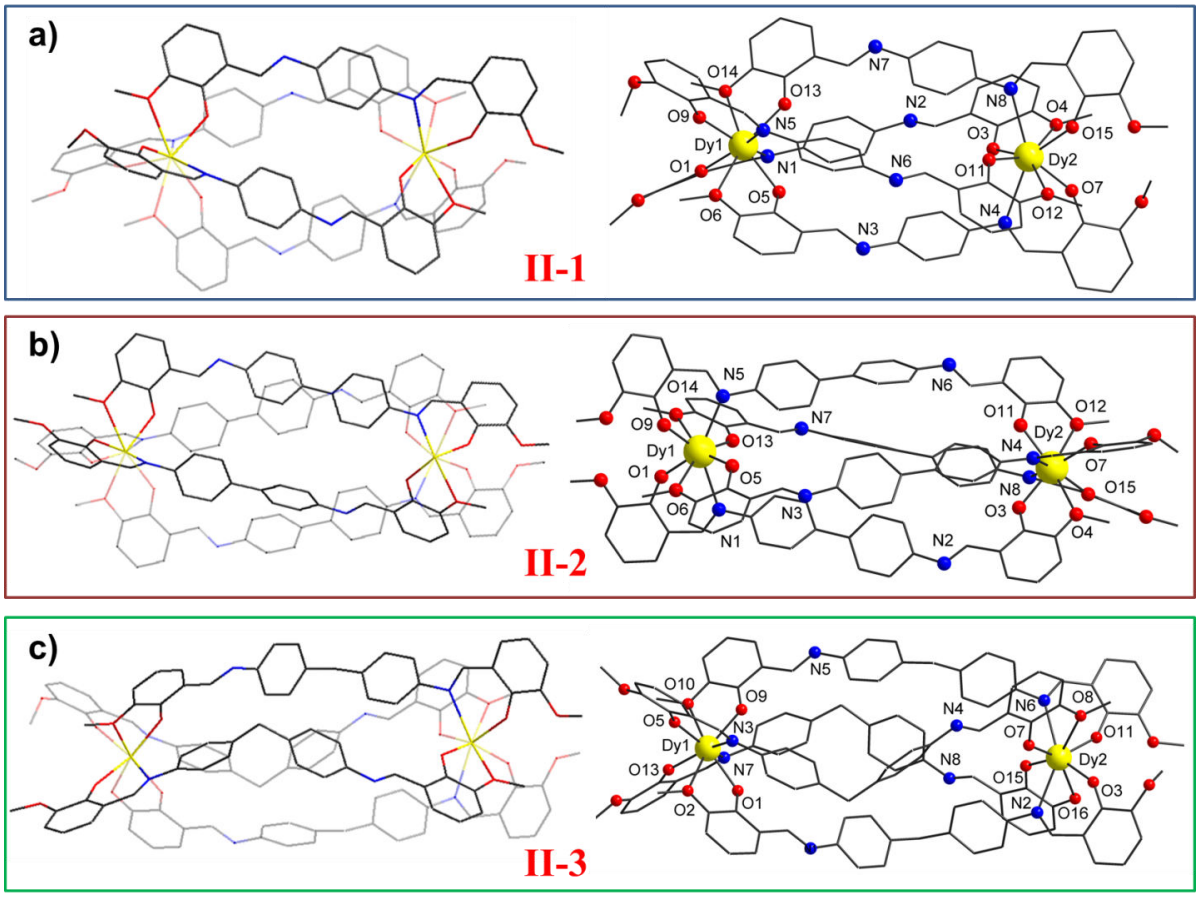

Figure 2.2: (Left) The helical twist of the ligand around the metal centres in complexes **II-1** and **II-2** is evident whereas in complex **II-3**, the bending of the ligand results in a mesocate structure. Bold atoms are in front, faded atoms are in the back. (Right) Partially labelled molecular structures of helicates $(NEt_4)_2[Dy_2(L^1)_4]((CH_3)_2CO)_{0.25}$ (**II-1**, *a*) $(NEt_4)_2[Dy_2(L^2)_4](H_2O)(DMF)_{0.5}$ (**II-2**, *b*) and mesocate $(NEt_4)_2[Dy_2(L^3)_4](Et_2O)_2((CH_3)_2CO)_{1.5}$ (**II-3**, *c*). Hydrogen atoms and solvent molecules have been omitted for clarity. Colour code: Yellow (Dy), red (O), blue (N), grey (C).

The two Dy^{III} ions are eight-coordinate with coordination environments consisting of six oxygen and two nitrogen atoms. The ligands bind in an antiparallel fashion where one donor set consists of phenoxy and methoxy O atoms whereas the other donor set consists of phenoxy O and imino N atoms. The average Dy-N distances in **II-1**, **II-2** and **II-3** are 2.66, 2.63 and 2.64 Å, respectively. The average Dy-$O_{phenoxy}$ distance is 2.23 Å for **II-1** and **II-2** and 2.21 Å for **II-3** whereas the average Dy-$O_{methoxy}$ distances for **II-1**, **II-2** and **II-3** are 2.61 and 2.62 and 2.60 Å, respectively. The coordination environment of each Dy^{III} centre is slightly different in each complex with detailed bond distances presented in Table 2.1. The

two Dy^{III} ions are separated intramolecularly by 10.81 Å in **II-1**, 14.87 Å in **II-2** and 15.30 Å in **II-3**. By increasing the length of the spacer in the ligand, it is expected that the distance between the metal centres will increase as well as subtle differences in bond lengths will result around each metal centre.

Table 2.1: Selected bond distances (Å) for complexes **II-1**, **II-2** and **II-3**. Comparable distances are highlighted in the same colours.

II-1		**II-2**		**II-3**	
Dy1-O1	2.214(6)	Dy1-O1	2.197(10)	Dy1-O1	2.259(6)
Dy1-O5	2.269(5)	Dy1-O5	2.261(10)	Dy1-O2	2.558(7)
Dy1-O6	2.585(6)	Dy1-O6	2.611(10)	Dy1-O5	2.223(7)
Dy1-O9	2.211(6)	Dy1-O9	2.198(10)	Dy1-O9	2.258(7)
Dy1-O13	2.228(6)	Dy1-O13	2.262(9)	Dy1-O10	2.547(7)
Dy1-O14	2.622(6)	Dy1-O14	2.637(10)	Dy1-O13	2.205(8)
Dy1-N1	2.658(7)	Dy1-N1	2.660(11)	Dy1-N3	2.639(9)
Dy1-N5	2.678(7)	Dy1-N5	2.573(12)	Dy1-N7	2.628(9)
Dy2-O3	2.258(6)	Dy2-O3	2.246(10)	Dy2-O3	2.201(7)
Dy2-O4	2.590(6)	Dy2-O4	2.667(10)	Dy2-O7	2.234(7)
Dy2-O7	2.219(7)	Dy2-O7	2.214(10)	Dy2-O8	2.659(7)
Dy2-O11	2.225(6)	Dy2-O11	2.254(10)	Dy2-O11	2.185(7)
Dy2-O12	2.633(6)	Dy2-O12	2.565(9)	Dy2-O15	2.228(7)
Dy2-O15	2.220(7)	Dy2-O15	2.227(10)	Dy2-O16	2.637(7)
Dy2-N4	2.654(7)	Dy2-N4	2.625(13)	Dy2-N2	2.642(8)
Dy2-N8	2.661(8)	Dy2-N8	2.619(12)	Dy2-N6	2.651(8)

Previous studies involving triple-stranded helicates and linear alkyl bridging ligands have shown that the stereoselective formation of a helicate *versus* mesocate is a function of the number of methylene groups in the spacer.[13] An even number of methylene groups results in a chiral helicate whereas an odd number favours an achiral mesocate. Although this applies in most cases, in homochiral helicates **II-1** and **II-2**, there are no methylene groups in the spacer. There are, however, phenyl rings which maintain the rigidity of the ligand. This mechanical coupling between the lanthanide centres prevents the structure from adopting the zigzag conformation indicated by the odd number of methylene groups. Therefore, in a way the *odd-even* rule can still apply if the conformations are considered rather than the number of methylene groups. In mesocate **II-3**, there is one methylene group in the spacer favouring a bent conformation of the ligand yielding an internal mirror plane and a mesocate structure. Comparing all three complexes, a loss of helicity is evident in **II-3** (Fig. 2.2).

2.3 Magnetic Properties

2.3.1 Magnetic Susceptibility Measurements

Magnetic susceptibility measurements were carried out for **II-1**, **II-2** and **II-3** in an applied dc field of 1000 Oe in the temperature range of 1.8 – 300 K (Fig. 2.3). At room temperature, the χT values for **II-1**, **II-2** and **II-3** are 28.16, 28.10 and 28.08 $cm^3.K.mol^{-1}$, respectively, which are in good agreement with the expected value of 28.34 $cm^3.K.mol^{-1}$ for two uncoupled Dy^{III} ions (S = 5/2, L = 5, $^6H_{15/2}$, g = 4/3). The χT product remains relatively constant above 60 K before rapidly decreasing at lower temperatures reaching 23.25, 22.21 and 21.68 $cm^3.K.mol^{-1}$ for **II-1**, **II-2** and **II-3**, respectively, at 2 K. This behaviour is generally indicative of intramolecular antiferromagnetic coupling of the metal centres. However, due to a large physical separation between the Dy^{III} ions, this behaviour most likely arises from the thermal depopulation of the Stark sub-levels and/or from the presence of large anisotropy in the system. The magnetisation plots, *M vs. H/T*, for complexes **II-1**, **II-2** and **II-3** show field dependence of the magnetisation that does not saturate at low temperatures (1.8 K for **II-1** and 1.9 K for **II-2** and **II-3**) and high magnetic fields (up to 7 T) (Fig. 2.4) indicating the presence of significant magneto-anisotropy and/or low lying excited states in all three systems.

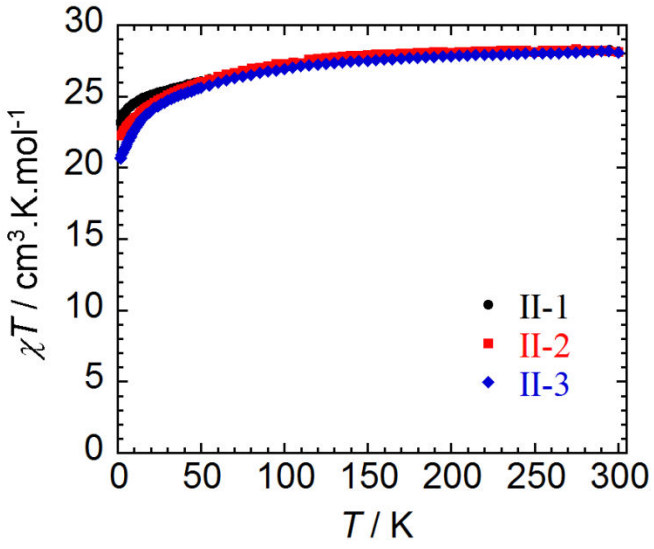

Figure 2.3: Plot of χT *vs.* T for complexes **II-1**, **II-2** and **II-3** in an applied dc field of 1000 Oe in the temperature range of 1.8 – 300 K.

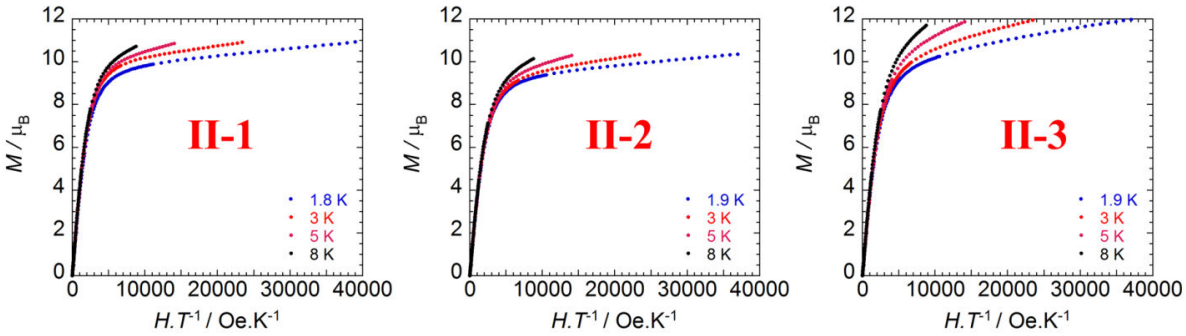

Figure 2.4: Reduced magnetisation plots, *M vs. H/T*, for complexes **II-1**, **II-2** and **II-3**.

2.3.2 Slow Magnetic Relaxation

In order to investigate the possibility of SMM behaviour, ac magnetic susceptibility measurements were carried out under zero dc field. The characteristic temperature and frequency dependence of the out-of-phase signal, χ'', below 14 K for **II-1** and 10 K for **II-2** and **II-3** indicates that all three complexes could potentially behave as SMMs. However, in that temperature range no maxima of χ'' at different measured frequencies are observed which can be attributed to small relaxation barriers resulting from quantum tunnelling of the magnetisation (QTM) commonly observed in lanthanide systems.[14] Although the spin-parity effect indicates that QTM should not occur in half-integer spin systems, it is reasonable to speculate that this QTM is occurring between entangled states of nuclear and electronic spins which has been previously studied by Ishikawa and Wernsdorfer in lanthanide SMMs.[15] In order to shortcut the QTM, ac measurements were carried out under an optimum dc field (the field at which the minimum of the characteristic frequency is observed) of 1600 Oe for **II-1** and **II-3** and 1200 Oe for **II-2** (Fig. 2.5, top) where the quantum tunnelling is minimised. Under the aforementioned applied dc fields, maxima are observed at 3.3 and 8.4 K for **II-1**, 7.4 K for **II-2** and 2.9 K for **II-3**, for 1500 Hz frequency. Two unique relaxation processes are observed for **II-1** (Fig. 2.5, top left) whereas in **II-2** and **II-3** only one is evident (Fig. 2.5, top centre and top right, respectively) at the indicated temperature and frequency range. The thermally activated relaxation follows Arrhenius-like behaviour ($\tau = \tau_0 \exp(U_{eff}/kT)$) where the anisotropic energy barriers are calculated to be U_{eff} = 13 K ($\tau_0 = 1.92 \times 10^{-6}$ s) and U_{eff} = 101 K ($\tau_0 = 6.78 \times 10^{-10}$ s) for the low temperature and high temperature domains, respectively for **II-1**, 71 K ($\tau_0 = 5.93 \times 10^{-7}$ s) for **II-2** and 20 K ($\tau_0 = 1.45 \times 10^{-7}$ s) for **II-3** (Fig. 2.6).

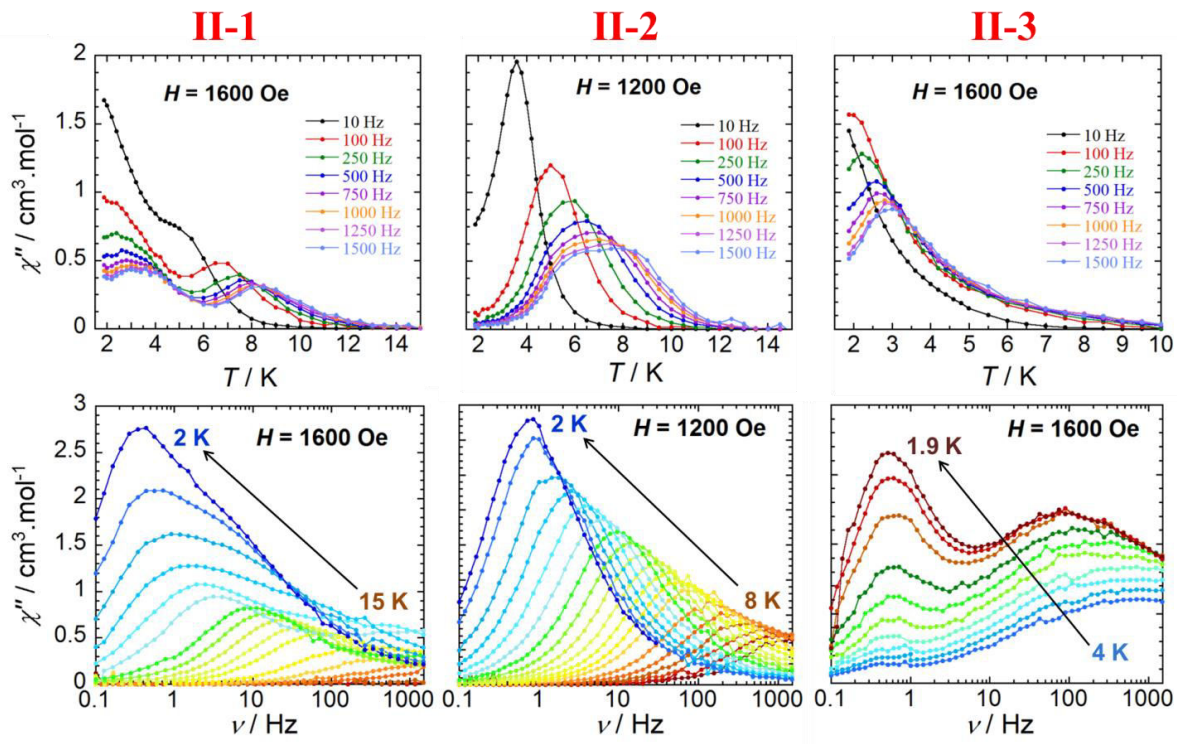

Figure 2.5: (Top) Temperature dependence of the out-of-phase magnetic susceptibility, χ'', for **II-1** (*left*), **II-2** (*centre*) and **II-3** (*right*) in applied optimum fields of 1600 Oe, 1200 Oe and 1600 Oe, respectively. (Bottom) Out-of-phase susceptibility, χ'', *vs.* frequency, ν, (logarithmic scale) under the indicated applied dc fields (H) for complexes **II-1** (*left*), **II-2** (*centre*) and **II-3** (*right*).

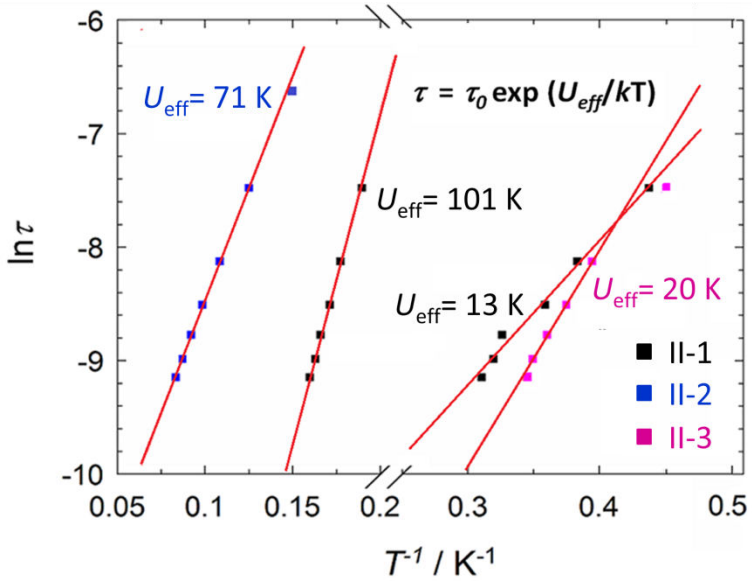

Figure 2.6: The relaxation time plotted as ln(τ) *vs.* T^{-1} for complexes **II-1, II-2** and **II-3**.

In order to further investigate the slow relaxation mechanisms, ac data as a function of frequency was collected in the 0.1 – 1500 Hz range. The variation of χ'' as a function of frequency for all three complexes further corroborates the presence of two clear maxima indicating two distinct relaxation processes for **II-1** and **II-3**, while for **II-2**, one peak with a slight shoulder is observed (Fig. 2.5, bottom row). One method to verify the presence of one or more relaxation processes in a complex is to perform a Cole-Cole plot.[16] In this plot of χ'' vs. χ', iso-temperature curves can be obtained with a distinct semi-circle shape. Each semi-circle corresponds to a temperature at which the measurement was carried out and can be fit using a generalised Debye model to yield an α value. The α parameter (ranges between 0 and 1) signifies the symmetry of the semi-circle and hence the distribution of relaxation times that are mixed together. The more symmetric the semi-circle, the lower the α value obtained from the fitting and the narrower the distribution of relaxation times for that complex. For a complex with a single relaxation time, the α parameter must be lower than 0.1.

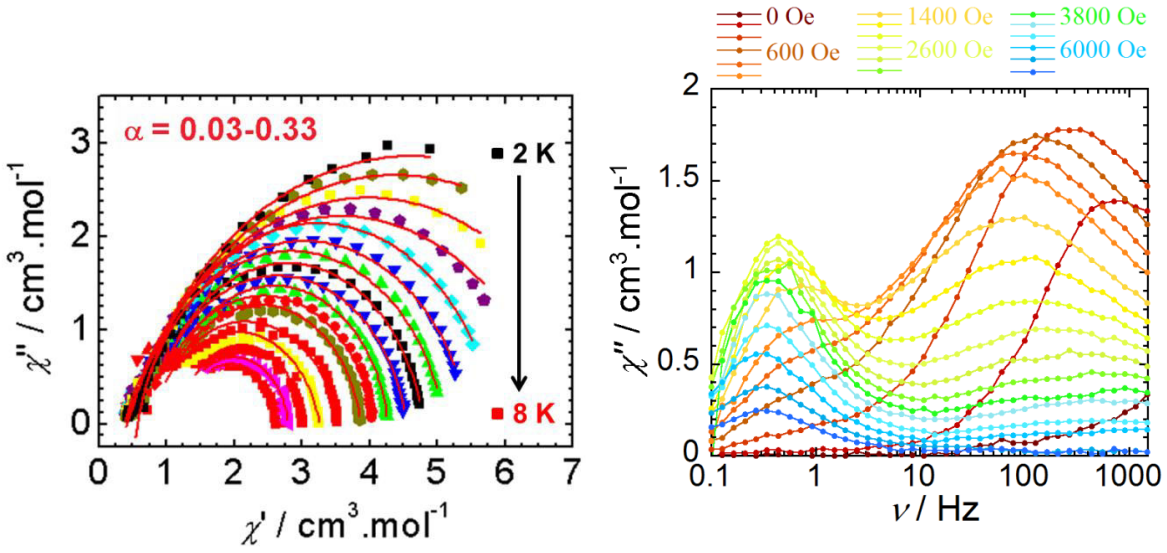

Figure 2.7: (Left) Cole-Cole plot using the ac susceptibility data shown for **II-2**. The solid lines correspond to the best fits obtained with a generalised Debye model yielding α values ranging between 0.03 – 0.33 at temperatures of 8 – 2 K. (Right) Out-of-phase susceptibility, χ'', *vs.* frequency, ν, measured at 1.9 K under applied dc fields ranging from 0 – 8400 Oe for complex **II-3**.

The Cole-Cole plots in the temperature range of 2 – 8 K for **II-1** and **II-2**, as well as 2 – 4 K for **II-3** show multiple relaxation processes with a transition between fairly symmetric

semi-circles at high temperature to unsymmetric curves as the temperature decreases. With decreasing temperature, the quantum tunnelling regime becomes more important and the relaxation associated with QTM begins to mix with the thermal relaxation processes yielding unsymmetric semi-circles. For **II-1** and **II-3** a reasonable fit of the data could not be obtained with an α value lower than 0.2 indicating the presence of multiple relaxation processes. This is in accordance with the data obtained from the χ'' *vs.* T and χ'' *vs.* ν plots showing two sets of peaks (*vide supra*). For **II-2**, the fit obtained (Fig. 2.7, left) yielded a mean α parameter value of 0.07 at high temperatures (6 – 8 K) and 0.31 at low temperature (2 – 3 K) indicating that below 6 K more than one relaxation process is occurring. It is noteworthy that identifying the number of mixed-in relaxation pathways or the type of relaxation is difficult without performing further computational studies.

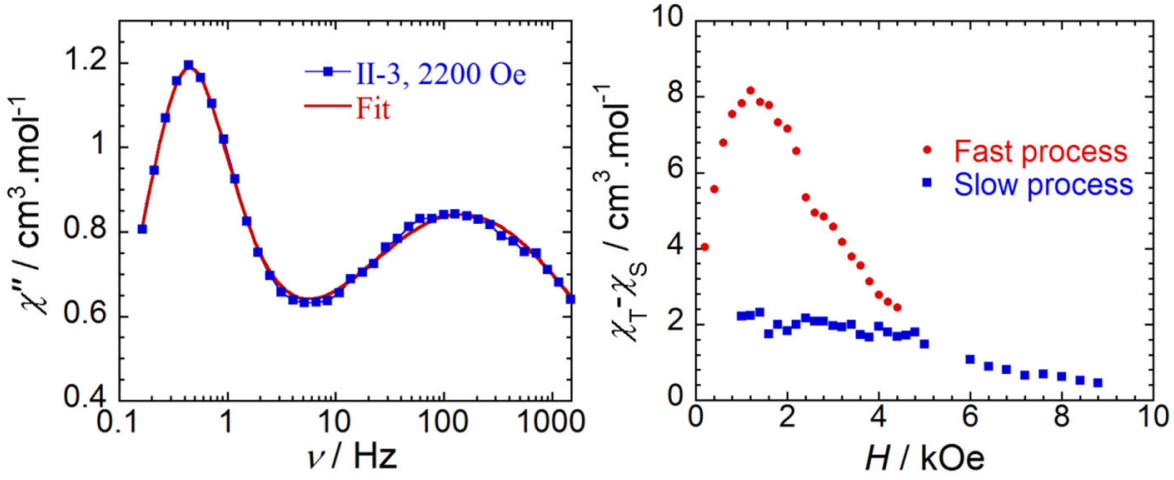

Figure 2.8: (Left) An example of the fitting of χ'' *vs.* ν under an applied field of 2200 Oe using a convolution of two Casimir and Du Pré functions.[17] (Right) Plot of the difference between isothermal and adiabatic susceptibility (χ_T -χ_s) *vs.* H for the slow and fast relaxation processes derived by fitting of the χ'' *vs.* ν curves for **II-3**.

To further investigate the observed secondary relaxation process at frequencies below 10 Hz for **II-3** (Fig. 2.5, bottom right), ac measurements were carried out in the 0.1 – 1500 Hz range under various static dc fields (0 – 8400 Oe) (Fig. 2.7, right). The resulting χ'' *vs.* ν curves were fitted using a convolution of two Casimir and Du Pré functions [17] (Fig. 2.8); the obtained relaxation times (τ_{slow} and τ_{fast}) are presented in Table 2.2. At fields below 1000 Oe only the fast relaxation process is observed, whereas above 3600 Oe the faster process vanishes leaving only the slower process to dominate. The obtained data clearly indicate the importance of the magnitude of the applied static field in favouring different relaxation

processes. The fraction of the susceptibility involved in the relaxation process can be assessed as the difference between isothermal and adiabatic susceptibility ($\chi_T - \chi_s$) *vs.* H for the slow and fast relaxation processes derived from fitting of the χ'' *vs.* ν curves (Fig. 2.8, right).

Table 2.2: Extracted relaxation times for the slow and fast relaxation processes at 1.9 K and applied dc fields up to 8400 Oe for complex **II-3**.

Applied Field (*H*)	τ_{slow}	τ_{fast}	**Applied Field (*H*)**	τ_{slow}	τ_{fast}
200	-	2.11×10^{-4}	3000	0.40	9.68×10^{-4}
300	-	3.42×10^{-4}	3200	0.39	9.68×10^{-4}
400	-	5.15×10^{-4}	3400	0.44	9.68×10^{-4}
500	-	7.22×10^{-4}	3600	0.41	9.68×10^{-4}
600	-	9.68×10^{-4}	3800	0.43	-
700	-	9.68×10^{-4}	4000	0.41	-
800	-	9.68×10^{-4}	4200	0.39	-
900	-	9.68×10^{-4}	4400	0.39	-
1000	0.21	9.68×10^{-4}	4600	0.42	-
1200	0.17	9.68×10^{-4}	4800	0.48	-
1400	0.19	9.68×10^{-4}	5000	0.41	-
1600	0.28	9.68×10^{-4}	6000	0.53	-
1800	0.34	9.68×10^{-4}	6400	0.52	-
2000	0.36	9.68×10^{-4}	6800	0.52	-
2200	0.38	9.68×10^{-4}	7200	0.50	-
2400	0.41	9.68×10^{-4}	7600	0.48	-
2600	0.40	9.68×10^{-4}	8000	0.51	-
2800	0.41	9.68×10^{-4}	8400	0.50	-

The ac data indicates that relaxation processes are significantly affected by very subtle changes in the coordination environments around the metal centres.[18] Given that the anisotropy barrier in 4*f* single-ion systems could be directly related to the sub-level structure of the ground state multiplets (which results from ligand field effects), it is of critical importance to determine the exact geometry of the coordination polyhedron.[19] This can be carried out using *Shape* software.[20] The results reveal that both Dy^{III} ions in each complex adopt an intermediate geometry between a square antiprism (D_{4d}) and a dodecahedron (D_{2d}). However, subtle but significant differences in the coordination geometry appear between the two Dy^{III} ions which alter the sub-level structures and therefore lead to two distinct relaxation processes. Across all three complexes, coordination environments of Dy^{III} ions

seem almost identical to the naked eye; however, slight differences in bond lengths (Table 2.1) are shown to drastically affect the SMM properties. In order to further probe the low temperature behaviour, single crystal dc relaxation measurements were performed on a micro-SQUID [21] in the temperature range 5.0 – 0.04 K (Fig. 2.9). It is noteworthy that the loops at zero field are negligible; consistent with the absence of a signal in χ'' *vs.* ν or χ'' *vs.* T plots under zero applied field. This is mainly due to the fast tunnelling effect taking place at low temperature in the absence of an applied field. When a direct field is applied, an opening of the hysteresis loop can be observed below 1.1 K for **II-1** and 5 K for **II-2** and **II-3**. The coercivity increases with decreasing temperature (and increasing sweep rates) indicating field-induced SMM-like behaviour due to switching off of the QTM under an applied field. Additionally the hysteresis loops indicate an exchange-biased system with weak exchange coupling corresponding to 11.5 mT (**II-1**), 13 mT (**II-2**) and 18 mT (**II-3**) determined through low temperature dc measurements. These dipole interactions could arise from intramolecular as well as intermolecular interactions. This behaviour thus confirms the appearance of frequency dependant out-of-phase signals in the ac data under field (Fig. 2.5). It is noteworthy that while the hysteresis loops are partially open for **II-1** only up to 1.1 K, it is important to take into consideration the sweep rate applied for the sample. At higher sweep rates, the relaxing spins in the sample will lag behind the sweeping field at higher temperatures. If the sweep rate was slowed down, the spins will be more likely to follow the field closely and the hysteresis loops will close at lower temperatures. This explains the observed temperature and sweep rate dependence in Fig. 2.9 and is one of the requirements for SMM behaviour.

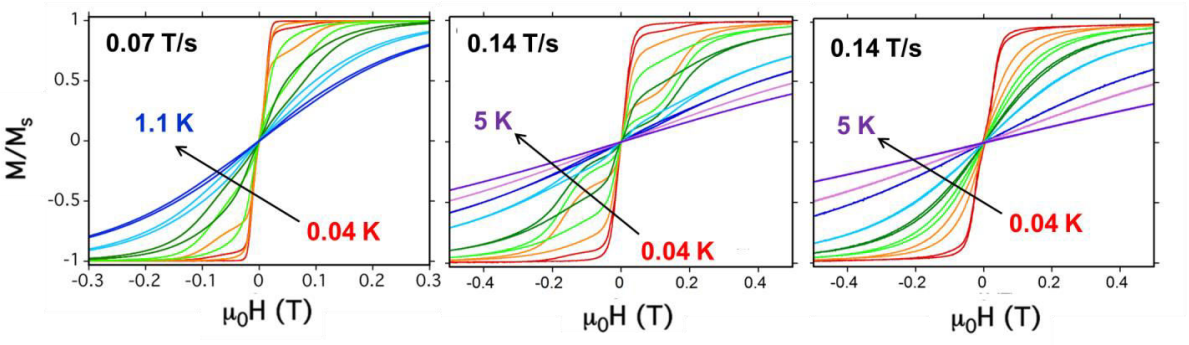

Figure 2.9: Magnetisation (*M*) *vs.* applied dc field sweeps at the indicated sweep rate and temperatures. *M* is normalised to its saturation value, *Ms*, at 0.3 T for **II-1** (*left*), **II-2** (*centre*) and **II-3** (*right*).

2.4 Theoretical Modelling of Magnetic Data

2.4.1 Methodology

All calculations were done with MOLCAS 7.6. All basis sets were taken from the ANO-RCC basis et library available from MOLCAS. The calculations were done on mononuclear Dy centers which were obtained from "cutting" a sufficiently large fragment from the initial complex, with subsequent saturation of all broken bonds by hydrogens.

2.4.2 Results and Discussion

In order to further investigate and confirm the observed magnetic behaviour, *ab initio* calculations of CASSCF/RASSI/SINGLE_ANISO type [22,23] have been performed on the individual dysprosium fragments for all complexes. The obtained energies of the lowest Kramers doublets on each Dy ion in complexes **II-1**, **II-2** and **II-3** are listed in Table 2.3. Due to large distances between dysprosium ions in each molecule, the intramolecular exchange interaction is negligible and the interaction between magnetic ions mainly originates from their dipolar interactions. The latter interactions are also weak (Table 2.3) compared to the temperature of ac measurements, therefore, the blockage of the reversal of the magnetisation arises mainly from individual dysprosium ions as was also seen in other polynuclear Dy complexes.[14]

The calculated energies of the first excited Kramers doublets on two Dy sites (Table 2.3) differ significantly for **II-1** thus explaining the presence of two distinct Orbach relaxation times in this complex (Fig. 2.6). Moreover, the excitation energies (84.67 cm^{-1} and 35.94 cm^{-1}) are in reasonable agreement with the two energy barriers extracted from the experiment (101 K and 13 K). The remaining discrepancy can be explained by two reasons. First, the values of the energy barriers extracted from the data in Fig. 2.6 are quite sensitive to the chosen experimental points through which the straight line is drawn. For example, by not taking into account the three last points for the lower barrier of **II-1**, the resulting straight line will be twice steeper and the blocking barrier twice larger compared to 13 K derived in Fig. 2.6. Second, the accuracy of present *ab initio* calculations, which were limited to a CASSCF level, probably are in the range of one to several tens of wavenumbers. Indeed, shifting slightly the energies of the first excited Kramers doublets on Dy sites (–12.7 cm^{-1} for Dy1 and –7.2 cm^{-1} for Dy2), which would imply the energies of the barriers of 28.5 cm^{-1} and 72 cm^{-1}, respectively, reproduces very well the χT curve and improves significantly the $M(H)$ dependencies (Fig. 2.10, left).

Table 2.3. Energies of the lowest eight Kramers doublets on Dy^{III} sites (cm^{-1}), the main components of the *g* tensor for the ground Kramers doublets and the angle between the main magnetic axes on the dysprosium sites for **II-1**, **II-2** and **II-3** are presented.

II-1		**II-2**		**II-3**	
Dy1	*Dy2*	*Dy1*	*Dy2*	*Dy1*	*Dy2*
Energies of the lowest eight Kramers doublets (cm^{-1})					
0.00	0.00	0.00	0.00	0.00	0.00
84.67	35.94	32.00	33.17	35.21	23.18
188.38	174.76	128.35	149.26	150.66	151.51
261.40	224.61	172.36	162.89	188.21	204.62
280.27	255.67	217.69	231.91	284.40	315.61
339.64	333.95	295.74	318.14	378.08	420.86
381.06	373.01	409.28	395.24	461.11	486.75
575.63	570.38	475.85	523.65	553.62	634.13
***g* factors for the ground Kramers Doublets**					
0.0312	0.0873	0.0701	0.1874	0.1342	0.0835
0.0403	0.2060	0.1462	0.3934	0.3842	0.4177
19.6312	18.8964	18.1150	17.6409	17.4299	15.9935
Angle between main magnetic axes (º)					
55.10		52.14		85.14	
Dipolar intramolecular coupling* (cm^{-1}) and the corresponding tunneling splittings of the first exchange doublet (cm^{-1})					
J_{dip}	Δ_{tun}	J_{dip}	Δ_{tun}	J_{dip}	Δ_{tun}
-0.146	1.2×10^{-6}	-2.4×10^{-3}	4.7×10^{-5}	-2.8×10^{-3}	1.6×10^{-5}

*J_{dip} enter the following Hamiltonian: $H = -J_{dip} S_1 \bullet S_2$, where S_i are pseudospins $s = ½$ of the ground Kramers doublets on Dy sites.

On the other hand, the energies of the first excited Kramers doublets on two dysprosium sites in **II-2** and **II-3** do not differ significantly, which is in accordance with close values of relaxation times in each of these compounds (Fig. 2.6). For **II-2**, the calculated energies of the first excited states on Dy sites seems to be slightly underestimated, while a small upshift (12.8 cm^{-1} for Dy1 and 13.3 cm^{-1} for Dy2) makes them close to the extracted barrier in Fig. 2.6 and improves significantly the $M(H)$ dependencies (Fig. 2.10, centre). At the same time the experimental points corresponding to **II-3** in Fig. 2.6 still bend down in the high temperature region, which indicates that the Arrhenius regime should

appear at still higher temperatures. Taking the first points only will give a much steeper line and a higher barrier. Accordingly, the calculated energies of the first excited Kramers doublets should be upshifted (14.1 cm^{-1} for Dy1 and 9.3 cm^{-1} for Dy2), which also improves the calculated $M(H)$ dependencies (Fig. 2.10, right).

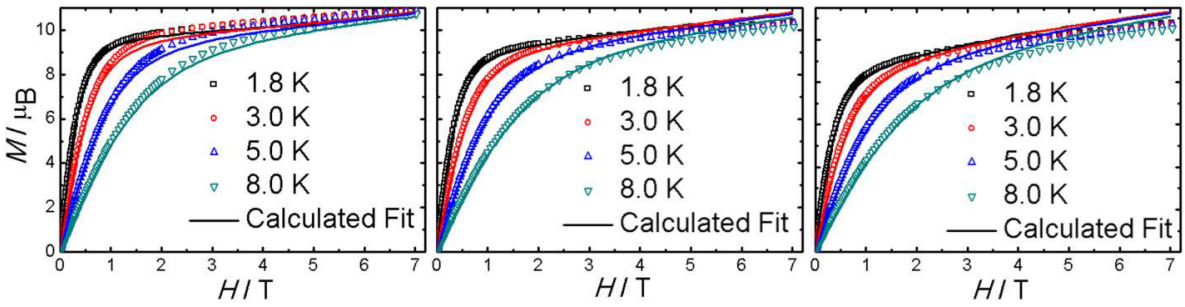

Figure 2.10: Comparison of the downscaled by 10% experimental molar magnetisation and calculated (with rescaled energy of the first excited KD on Dy centers) molar magnetisation at low temperature for compounds **II-1** (left), **II-2** (centre), and **II-3** (right). Solid lines indicate the fit; different colour fit lines correspond to the different temperature curves.

The calculations for all three compounds give relatively large transverse components (g_x and g_y) of the g tensors for the ground state Kramers doublets on the dysprosium sites compared to other complexes.[24] This implies relatively high relaxation rates in the tunnelling (quantum) regime, which are also revealed in the fact that the blocking of magnetisation is detected in ac susceptibility only under applied dc field. As a result, the thermally activated regime is observed at temperatures where the relaxation rates are high, *i.e.*, τ is small (Fig. 2.6). At the same time the intramolecular dipolar interaction does not contribute to the blocking of magnetisation at the investigated temperatures, being of the order of intermolecular dipolar interaction (Table 2.3).

The data clearly indicates a correlation between the ligand field and the energies of the excited states of each Dy^{III} ion and hence the magnetic properties of the complexes. Observing one or more relaxation processes in the out-of-phase plots can not only be associated with the number of crystallographically independent metal ions but more specifically with the associated energies of the excited states as evident from this system. Our main goal from this project was to investigate helical systems for alignment of anisotropy axes, therefore *ab initio* calculations were performed to determine the orientation of the anisotropic axes on each Dy^{III} centre (Fig. 2.11). The observed angles of 55.10° (**1**), 52.14° (**2**) and 85.14° (**3**) between the anisotropic axes are shown to vary depending on the spacer

used in the ligand. This data clearly indicates that it is possible to control the orientation of the axes by controlling the helical twist encoded in the ligand.

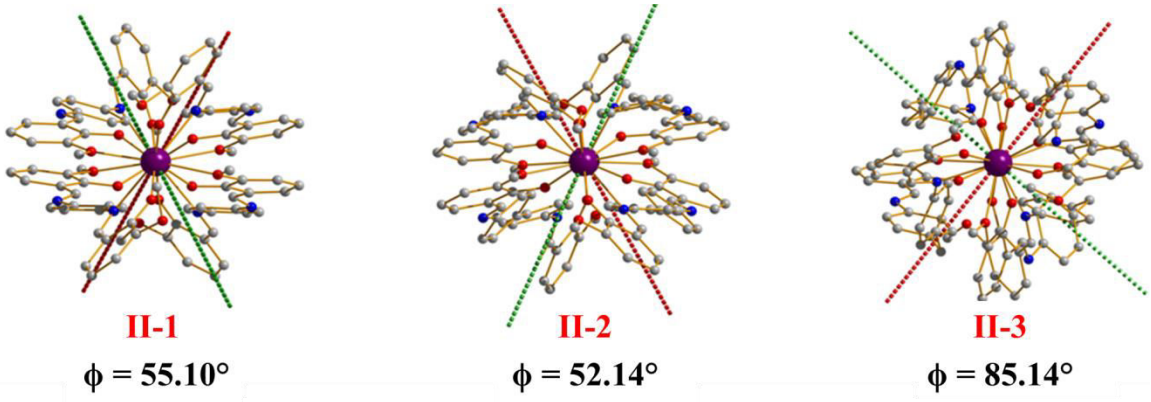

Figure 2.11: Comparison of the angle (ϕ) between the anisotropy axes of both Dy ions for **II-1** (left), **II-2** (centre), and **II-3** (right).

2.5 Conclusions

The synthetic strategy employed above proved successful in predicting the helicity for rare, quadruply-stranded lanthanide complexes. Complexes **II-1**, **II-2** and **II-3** are part of a series of compounds synthesised for the purpose of studying the orientation of the anisotropic axes of lanthanide metal centres as a function of the helical twist dictated by the ligand. As the length and flexibility of the ligand is varied, the angle between the axes varies as well. These results confirm that, in fact, it is possible to control the magnetic axes relative to one another by simply modifying the spacer of the ligand which will allow us to synthesise SMMs with potentially higher anisotropic energy barriers. By exploring supramolecular architectures for the purpose of controlling the anisotropy in a complex, we have shown that it is possible to rationally design and synthesise SMMs using ligands which dictate specific structural motifs. All three complexes exhibit field-induced SMM behaviour with complex slow relaxation processes at low temperature that are entangled with QTM and other possible relaxation pathways. Additionally, caution should be taken when analysing magnetic susceptibility data; all three complexes exhibit slow relaxation properties that were difficult to explain initially. However, we were able to show that they arise from very subtle changes in the coordination environments of each metal centre which was further confirmed by *ab initio* calculations showing different excitation energies for both metal centres in each complex. It is noteworthy that subtle differences in coordination environments leading to drastic changes in orientation of the anisotropic axes was reported by Sessoli and co-workers for a

mononuclear system.[25] However, we have shown that minute differences in bond lengths around each Dy^{III} centre result in clear changes to the local anisotropy which has never been previously reported for a dinuclear system. The work presented in this chapter has been published in Chemical Science.[26]

Although the magnetic behaviour was shown to arise mainly from changes to the local coordination sphere of each Dy^{III} ion rather than the alignment of anisotropic axes in the complex, this system demonstrates clear proof-of-principle that the angle between the axes can be controlled. However, there are clear limitations for this system which render it less desirable for further study when targeting SMMs with high energy barriers and/or fundamental studies into magnetic interactions between lanthanide metal ions. These limitations centre on the large distance between metal ions in these helical systems. In order to study magnetic interactions, we require a system where the lanthanide ions are in close proximity to induce magnetic coupling. Additionally, targeting higher energy barrier SMMs requires large magnetic anisotropy. While helicates and mesocates provide a way of aligning anisotropy axes, they are less efficient than centrosymmetric systems. There is a greater degree of flexibility in long helicate-inducing ligands, whereas for centrosymmetric complexes, one can employ more rigid ligands and, by definition, the easy-axes will remain aligned and parallel. For all the aforementioned reasons, we shifted our focus to a dinuclear dysprosium system which was centrosymmetric and where the metal ions were much closer in distance to induce magnetic interactions.

2.6 Experimental

2.6.1 General Considerations

X-Ray Crystallography:

Crystals were grown from Acetone/DMF for **II-1** and **II-2** and DMF for **II-3**. Single yellow crystals suitable for X-ray diffraction measurements were mounted on a glass fibre. Unit cell measurements and intensity data collections were performed on a Bruker-AXS SMART 1 k CCD diffractometer using graphite monochromated Mo $K\alpha$ radiation (λ = 0.71073 Å). The data reduction included a correction for Lorentz and polarization effects, with an applied multi-scan absorption correction (SADABS). The crystal structures were solved and refined using the SHELXTL program suite.[27] Direct methods yielded all non-hydrogen atoms which were refined with anisotropic thermal parameters. All hydrogen atom positions were calculated geometrically and were riding on their respective atoms.

Magnetism:

The magnetic susceptibility measurements were obtained using a Quantum Design SQUID magnetometer MPMS-XL7 operating between 1.8 and 400 K for dc applied fields ranging from –7 to 7 T. Measurements were performed on ground polycrystalline samples. The magnetic data were corrected for the sample holder and the diamagnetic contribution. The samples were checked for the presence of ferromagnetic impurities, which were absent in all three samples, by measuring the magnetisation as a function of the field at 100 K.

Other Studies:

Infrared spectra were recorded in the solid state (KBr pellets) on a Nicolet Nexus 550 FTIR spectrometer in the 700-4000 cm^{-1} range. Nuclear magnetic resonance analyses were conducted on a Bruker Avance 400 equipped with an automatic sample charger and a 5 mm auto-tuning broadband probe with Z gradient.

Computational details:

All calculations were done with MOLCAS 7.6. All basis sets were taken from the ANO-RCC basis and library available from MOLCAS. The calculations were done on mononuclear Dy centers which were obtained from "cutting" a sufficiently large fragment from the initial complex, with subsequent saturation of all broken bonds by hydrogens (Fig. 2.12).

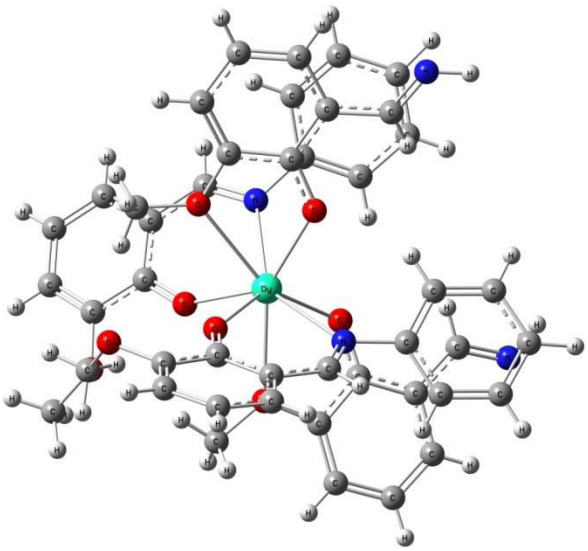

Figure 2.12: The structure of the calculated fragment of the center Dy1 for the compound **II-1**. Similar structures have been obtained from "cutting" other mononuclear Dy centers.

2.6.2 Synthesis and Characterisation

Ligand Synthesis

N,N′-Bis(3-methoxysalicylidene)benzene-1,4-diamine **(H_2L^1)**

To a solution of *o*-vanillin (0.02 mol, 2 equiv.) in 20 mL ethanol was added a solution of *p*-phenylenediamine (0.01 mol, 1 equiv.) in 20 mL ethanol. The orange solution was refluxed for one hour then filtered after cooling down to room temperature. The resulting orange powder was washed with diethyl ether and ethanol. (Yield = 92%) Selected IR (KBr, cm^{-1}): 3405 (br), 2914 (w), 1610 (s), 1470 (s), 1250 (s), 1200 (s), 1070 (m), 970 (s), 840 (s), 780

(m), 740 (s). ^{1}H NMR ($CDCl_3$, 400 MHz): δ 3.93 (s, 3H, OCH_3), 6.88 (t, 1H, 7.8 Hz, Ar), 6.99 (dd, 2H, 1.5 Hz, Ar), 7.35 (s, 2H, Ar), 8.65 (s, 1H, N=CH) ppm. ^{13}C NMR ($CDCl_3$, 400 MHz): δ 56.24 (OCH_3), 114.95 (Ar), 118.67 (Ar), 119.12 (Ar), 122.31 (Ar), 123.85 (Ar), 146.94 (Ar), 148.52 (Ar), 151.45 (Ar,) 162.37 (N=CH) ppm.

N,N'-Bis(3-methoxysalicylidene)biphenyl-4,4'-diamine **(H_2L^2)**

To a solution of *o*-vanillin (0.02 mol, 2 equiv.) in 20 mL ethanol was added a solution of 4,4'-biphenyldiamine (0.01 mol, 1 equiv.) in 20 mL ethanol. The orange solution was refluxed for one hour then filtered after cooling down to room temperature. The resulting orange powder was washed with diethyl ether and ethanol. (Yield = 89%) Selected IR (KBr, cm^{-1}): 3480 (br), 1620 (s), 1470 (s), 1390 (w), 1250 (s), 1210 (m), 1080 (w), 970 (m), 820 (m), 730 (m). ^{1}H NMR ($CDCl_3$, 400 MHz): δ 3.94 (s, 6H, OCH_3), 6.88 (t, J = 7.9 Hz, 2H, Ar), 7.00 (dd, J = 16.1, 1.6 Hz, 2H, Ar), 7.02 (dd, J = 15.9, 1.6 Hz, 2H, Ar), 7.38 (d, J = 8.5 Hz, 4H, Ar), 7.66 (d, J = 8.4 Hz, 4H, Ar), 8.69 (s, 2H, N=CH) ppm. ^{13}C NMR ($CDCl_3$, 100 MHz): δ 56.2 (OCH_3), 114.9 (Ar), 118.6 (Ar), 119.2 (Ar), 121.8 (Ar), 123.8 (Ar), 128.0 (Ar), 139.1 (Ar), 147.4 (Ar), 148.6 (Ar), 151.5 (Ar,) 162.4 (N=CH) ppm.

N,N'-Bis(3-methoxysalicylidene)-4,4'-methylenedianiline **(H_2L^3)**

To a solution of *o*-vanillin (0.02 mol, 2 equiv.) in 20 mL ethanol was added a solution of 4,4'-methylenedianiline (0.01 mol, 1 equiv.) in 20 mL ethanol. The orange solution was refluxed for one hour then filtered after cooling down to room temperature. The resulting orange powder was washed with diethyl ether and ethanol. (Yield = 89%) Selected IR (KBr, cm^{-1}): 3470 (br), 1610 (s), 1470 (m), 1380 (w), 1260 (m), 1210 (w), 970 (w), 790 (w), 730 (m). ^{1}H NMR ($CDCl_3$, 400 MHz): δ 3.92 (s, 6H, OCH_3), 4.02 (s, 2H, CH_2), 6.86 (t, J = 7.8 Hz, 2H, Ar), 6.97 (dd, J = 10.8, 1.5 Hz, 2H, Ar), 6.99 (dd, J = 10.4, 1.5 Hz, 2H, Ar), 7.19-7.26 (m, 8H, Ar), 8.61 (s, 2H, N=CH) ppm. ^{13}C NMR ($CDCl_3$, 100 MHz): δ 41.0 (CH_2), 56.2 (OCH_3), 114.7 (Ar), 118.5 (Ar), 119.2 (Ar), 122.4 (Ar), 123.7 (Ar), 129.9 (Ar), 139.9 (Ar), 146.4 (Ar), 148.5 (Ar), 151.5 (Ar,) 162.1 (N=CH) ppm.

$(NEt_4)_2[Dy_2(L^1)_4]\cdot((CH_3)_2CO)_{0.25}$ **(II-1)** and $(NEt_4)_2[Dy_2(L^3)_4]\cdot(Et_2O)_2((CH_3)_2CO)_{1.5}$ **(II-3)**

A solution of $Dy(NO_3)_3\cdot 6H_2O$ (0.057 g, 0.125 mmol) in DMF (5 mL) was added to an orange solution of H_2L^1 for **II-1** and H_2L^3 for **II-3** (0.250 mmol) and TEAOH (334 μL, 0.500 mmol, 25% in MeOH) in acetone (20 mL). The mixture was sonicated then filtered. The filtrate was

left undisturbed and yellow needles were observed after three days in ~ 35% and 37% yield for **II-1** and **II-3**, respectively. Selected IR data for **II-1** (KBr pellets, cm^{-1}): 3420 (br), 2970 (w), 1710 (m), 1680 (m), 1590 (s), 1480 (s), 1430 (s), 1340 (m), 1220 (s), 1170 (s), 1070 (m), 970 (w), 850 (s), 740 (s). Selected IR data for **II-3** (KBr pellets, cm^{-1}): 3460 (br), 1620 (s), 1440 (m), 1380 (m), 1230 (s), 1070 (w), 850 (m), 730 (w).

$(NEt_4)_2[Dy_2(L^2)_4] \cdot (H_2O)(DMF)_{0.5}$ **(II-2)**

Tetraethylammonium hydroxide (TEAOH) (334 μL, 0.5 mmol, 25% in MeOH) was added to a pale orange solution of H_2L^2 (0.112 g, 0.250 mmol) in DMF (20 mL). After complete dissolution was observed, $Dy(NO_3)_3 \cdot 6H_2O$ (0.057 g, 0.125 mmol) was added and the reaction mixture was sonicated for five minutes. The pale orange mixture was filtered and the filtrate was left undisturbed. Yellow needles were isolated the next day in ~ 55% yield. Selected IR data for **II-2** (KBr pellets, cm^{-1}): 3480 (br), 1610 (s), 1590 (s), 1540 (w), 1480 (s), 1440 (s), 1380 (m), 1230 (s), 1180 (m), 1070 (w), 740 (m).

References

[1] M. Albrecht, *Chem. Rev*. 101 (2001), 3457.

[2] C. Piguet, G. Bernardinelli, G. Hopfgartner, *Chem. Rev*. 97 (1997), 2005.

[3] J.-M. Lehn, A. Rigault, J. Siegel, J. Harrowfield, B. Chevrier, D. Moras, *Proc. Natl. Acad. Sci. U.S.A*. 84 (1987), 2565.

[4] (a) A. Petitjean, H. Nierengarten, A. van Dorsselaer, J.-M. Lehn, *Angew. Chem. Int. Ed*. 43 (2004), 3695; (b) N. Dalla Favera, L. Guenee, G. Bernardinelli, C. Piguet, *Dalton Trans*. (2009), 7625; (c) G. N. Newton, T. Onuki, T. Shiga, M. Noguchi, T. Matsumoto, J. S. Mathieson, M. Nihei, M. Nakano, L. Cronin, H. Oshio, *Angew. Chem. Int. Ed*. 50 (2011), 4844.

[5] (a) C. J. Cathey, E. C. Constable, M. J. Hannon, D. A. Tocher, M. D. Ward, *J. Chem. Soc., Chem. Commun.* 1990 (1990), 621; (b) R. P. Thummel, C. Hery, D. Williamson, F. Lefoulon, *J. Am. Chem. Soc*. 110 (1988), 7894; (c) N. K. Al-Rasbi, H. Adams, L. P. Harding, M. D. Ward, *Eur. J. Inorg. Chem.* 2007 (2007), 4770.

[6] (a) E. A. Medlycott, G. S. Hanan, *Chem. Commun.* (2007), 4884; (b) K. Miwa, Y. Furusho, E. Yashima, *Nat. Chem*. 2 (2010), 444; (c) V. E. Campbell, X. de Hatten, N. Delsuc, B. Kauffmann, I. Huc, J. R. Nitschke, *Nat. Chem*. 2 (2010), 684.

[7] (a) J.-J. Jiang, S.-R. Zheng, Y. Liu, M. Pan, W. Wang, C.-Y. Su, *Inorg. Chem.* 47 (2008), 10692; (b) K. Zeckert, J. Hamacek, J.-M. Senegas, N. Dalla-Favera, S. Floquet, G. Bernardinelli, C. Piguet, *Angew. Chem. Int. Ed.* 44 (2005), 7954.

[8] J. Xu, K. N. Raymond, *Angew. Chem. Int. Ed*. 45 (2006), 6480.

[9] A. P. Bassett, S. W. Magennis, P. B. Glover, D. J. Lewis, N. Spencer, S. Parsons, R. M. Williams, L. De Cola, Z. Pikramenou, *J. Am. Chem. Soc.* 126 (2004), 9413.

[10] J. Inanaga, H. Furuno, T. Hayano, *Chem. Rev.*, 102 (2002), 2211.

[11] (a) C. Train, R. Gheorghe, V. Krstic, L.-M. Chamoreau, N. S. Ovanesyan, G. L. J. A. Rikken, M. Gruselle, M. Verdaguer, *Nat. Mater.* 7 (2008), 729; (b) B. Gil-Hernandez, H. A. Happe, J. K. Vieth, J. Sanchiz, C. Janiak, *Chem. Commun.* 46 (2010), 8270; (c) M. Albrecht, M. Fiege, P. Kögerler, M. Speldrich, R. Fröhlich, M. Engeser, *Chem. Eur. J.* 16 (2010), 8797; (d) G. L. J. A. Rikken, E. Raupach, *Nature* 405 (2000), 932; (e) L. D. Barron, *Nature* 405 (2000), 895; (f) F. Li, J. K. Clegg, L. Goux-Capes, G. Chastanet, D. M. D'Alessandro, J.-F. Letard, C. J. Kepert, *Angew. Chem. Int. Ed.* 50 (2011), 2820.

[12] (a) F. Habib, M. Murugesu, *Chem. Soc. Rev*. 42 (2013), 3278; (b) S.-D. Jiang, B.-W. Wang, S. Gao, in *Structure and Bonding*, Springer, Berlin Heidelberg, 2014, *DOI: 10.1007/430_2014_153*; (c) N. F. Chilton, D. Collison, E. J. L. McInnes, R. E. P. Winpenny, A. Soncini, *Nature Commun*. 4 (2013), 2551.

[13] M. Albrecht, I. Janser, H. Houjou, R. Frohlich, *Chem. Eur. J.*, 10 (2004), 2839.

[14] (a) J. Long, F. Habib, P.-H. Lin, I. Korobkov, G. Enright, L. Ungur, W. Wernsdorfer, L. F. Chibotaru, M. Murugesu, *J. Am. Chem. Soc*. 133 (2011), 5319; (b) D. N. Woodruff , R. E. P. Winpenny, R. A. Layfield, *Chem. Rev.* 113 (2013), 5110.

[15] N. Ishikawa, M. Sugita, W. Wernsdorfer, *Angew. Chem. Int. Ed*. 44 (2005), 2931.

[16] (a) K. S. Cole, R. H. Cole, *J. Chem. Soc.* 9 (1941), 341; (b) S. M. J. Aubin, Z. Sun, L. Pardi, J. Krzystek, K. Folting, L. J. Brunel, A. L. Rheingold, G. Christou, D. N. Hendrickson, *Inorg. Chem.* 38 (1999), 5329.

[17] P.-E. Car, M. Perfetti, M. Mannini, A. Favre, A. Caneschi, R. Sessoli, *Chem Commun*. 47 (2011), 3751 and references therein.

[18] L. Sorace, C. Benelli, D. Gatteschi, *Chem. Soc. Rev*. 40 (2011), 3092.

[19] N. Ishikawa, Y. Mizuno, S. Takamatsu, T. Ishikawa, S.-Y. Koshihara, *Inorg. Chem.* 47 (2008), 10217.

[20] D. Casanova, M. Llunel, P. Alemany, S. Alvarez, *Chem. Eur. J.* 11 (2005), 1479.

[21] W. Wernsdorfer, *Supercond. Sci. Technol*. 22 (2009), 064013.

[22] F. Aquilante, L. De Vico, N. Ferre, G. Ghigo, P.-Å. Malmqvist, P. Neograd y, T. B. Pedersen, M. Pitonak, M. Reiher, B. O. Roos, L. Serrano-Andres, M. Urban, V. Veryazov, R. Lindh, *J. Comput. Chem.* 31 (2010), 224.

[23] L. Ungur, W. Van den Heuvel, L. F. Chibotaru, *New J. Chem.* 33 (2009), 1224.

[24] R. Sessoli, A. K. Powell, *Coord. Chem. Rev.* 253 (2009), 2328.

[25] (a) G. Cucinotta, M. Perfetti, J. Luzon, M. Etienne, P.-E. Car, A. Caneschi, G. Calvez, K. Bernot, R. Sessoli, *Angew. Chem. Int. Ed.* 51 (2012), 1606; (b) M. Murugesu, *Nature Chem*. 4 (2012), 347.

[26] F. Habib, J. Long, P.-H. Lin, I. Korobkov, L. Ungur, W. Wernsdorfer, L. F. Chibotaru, M. Murugesu, *Chem. Sci*. 3 (2012), 2158.

[27] Sheldrick, G. M.; *Acta Cryst*. A64 (2008), 112.

Chapter 3

Magnetic Interactions in Dinuclear Dysprosium Single-Molecule Magnets

As highlighted in previous chapters, it is absolutely essential to increase the magnetic anisotropy in metal-based systems if we are to target high spin reversal barriers for SMMs. Additionally, better strategies are needed to rationally design SMM systems where the magnetic properties can be predicted and selected for as opposed to serendipitous synthetic routes. For this to occur, model systems are required in order to answer key questions regarding slow relaxation mechanisms of SMMs. Without understanding the fundamental properties of these nanomagnetic materials and the magneto-structural correlations within these systems one cannot design highly anisotropic systems with large energy barriers for spin reversal. In our efforts to obtain high-temperature SMMs as well as understanding the underlying concepts involved, we have focused on a centrosymmetric dinuclear dysprosium complex $[Dy^{III}_2(valdien)_2(NO_3)_2]$; the simplest system to study magnetic interactions between dysprosium ions. This complex exhibits slow relaxation of the magnetisation associated with SMM behaviour. The simplicity of the symmetric molecular entity allows the evaluation of the exchange interaction between the two Dy^{III} ions by computational methods and was found to exhibit antiferromagnetic superexchange coupling between the two Dy^{III} centres. As highlighted in the previous chapter, we are targeting a centrosymmetric system in order to: i) align the anisotropy axes on Dy^{III} ions leading to large global anisotropy in the dinuclear unit, ii) maintain a close distance between Dy^{III} ions to induce magnetic interaction and iii) to understand the effects of magnetic interactions on SMM properties in simple model systems.

Once magnetic interaction is established in the dinuclear dysprosium system, it is critical to identify the nature of this interaction; *i.e.* whether it is intramolecular (within $\{Dy^{III}_2\}$ units) or intermolecular (between Dy^{III} ions of different units in the crystal lattice). Additionally, it is important to study any and all effects on the slow relaxation mechanism

observed in this complex if we are to treat it as a model system. Is the observed slow relaxation due to single-ion behaviour where each Dy^{III} ion acts as a nanomagnet on its own or is the slow relaxation of each Dy^{III} ion influencing its neighbouring ion leading to entanglement of the slow relaxation properties? Precisely defined concentration of dilution/doping is a useful method for modulating electronic and magnetic properties of a material. At the time, only a handful of molecular complexes were reported where the effect of doping on the magnetic properties was investigated with no studies regarding the elucidation of slow relaxation of the magnetisation in doped polynuclear lanthanide complexes. We had predicted that the strategy of doping a diamagnetic system with a paramagnetic ion can shed some light on the complex relaxation processes inherent in 4*f* SMMs. Moreover, by varying the concentration of the dopant ion, effects such as QTM can be accurately modulated. With this in mind, we focused on the aforementioned, centrosymmetric $\{Dy_2\}$ SMM which exhibits slow relaxation of the magnetisation below 25 K. Our aim was to elucidate, using the dilution method, whether such behaviour originates from a single-ion relaxation or from a magnetically coupled system.

In this chapter, the first relaxation studies using SQUID and micro-SQUID measurements on a $\{Dy_2\}$ SMM diluted in a diamagnetic $\{Y_2\}$ matrix are highlighted. The doping effect clearly indicates that the observed relaxation predominantly arises from the single ion relaxation mode which is being affected by weak intramolecular exchange biased coupling between the Dy^{III} ions. Since we carried out this study, dilution experiments have become benchmark in this field when examining origins of SMM behaviour in polynuclear systems, especially dinuclear systems. For this reason, this work has been published in the Journal of the American Chemical Society as two separate articles (*J. Am. Chem. Soc*. 133 (2011), 5319 – 5328 and *J. Am. Chem. Soc*. 133 (2011), 8830 – 8833).

3.1 Dinuclear Dysprosium Single-Molecule Magnet

Among the lanthanide family, the Dy^{III} ion has indisputably led to the largest number of pure 4*f* SMMs. The explanation resides in the reduced quantum tunnelling of the magnetisation (QTM) experimentally observed in these systems compared to other lanthanide ions. However, the real physical origin of this behaviour remains unclear. The flexibility of the coordination chemistry has been employed to synthesise polynuclear dysprosium(III) complexes with various nuclearity. Namely, the nuclearity of the SMMs based on dysprosium(III) ranging from dinuclear,[1] trinuclear,[2] tetranuclear,[3] pentanuclear,[4] hexanuclear[5] to a $\{Dy_{26}\}$ cluster.[6] Nevertheless, in a similar fashion to transition metal SMMs, the smaller systems tend to present higher anisotropic barriers due to the inverse relationship between the spin value and the magnetic anisotropy, *D*. In this section, the synthesis, characterisation and magnetic properties of a dinuclear Dy^{III} SMM will be presented.[7] This complex will then be used as a model system to perform magnetic dilution studies in order to gain further insight into slow relaxation mechanisms in dinuclear complexes.

3.1.1 Synthetic Strategy

The synthetic strategy to obtain polynuclear 4*f* SMMs fundamentally relies on the same concepts as for transition metals SMMs: the use of polydentate bridging ligands which can mediate the magnetic interactions between the metal centres. The choice of the bridging group is critical in the case of lanthanide systems in order to overcome the core nature of 4*f* orbitals and subsequently induce significant exchange interaction between the paramagnetic centres. In addition, the ligand field as well as the coordination geometry strongly influence the local anisotropy of the lanthanide ion. In brief, the interplay between the ligand field effect, the geometry and the strength of the magnetic interaction between the lanthanide sites will govern the SMM behaviour. Taking into account the coordination preference of 4*f* ions for hard Lewis bases (HSAB theory),[8] it is possible to design polytopic/chelate ligands in order to direct the assembly of polynuclear lanthanide complexes. Schiff-base ligands [9] obtained from the *o*-vanillin moiety have proven to be particularly suitable for the synthesis of 4*f* SMMs as shown in chapter 1.

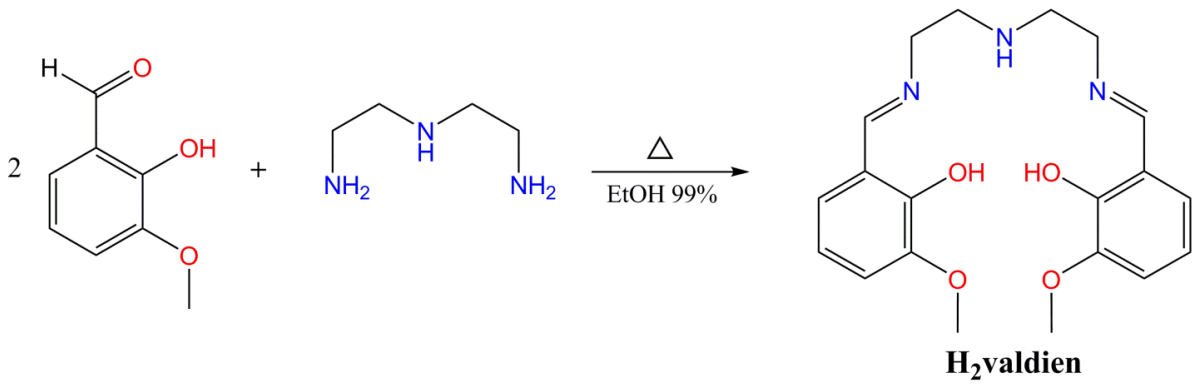

Scheme 3.1: Preparation of the ligand *N1*,*N3*-Bis(3-methoxysalicylidene)diethylenetriamine (H_2valdien).

The compartmental acyclic Schiff base H_2valdien ligand (Scheme 3.1) is obtained from the condensation reaction of *o*-vanillin and diethylenetriamine, a detailed experimental procedure can be found in Section 3.3. This ligand displays two distinct coordination pockets which can encapsulate lanthanide centres. The large size of the inner compartment, formed by the donor set N_3O_2, is particularly appropriate to accommodate a sizable 4*f* ion. Only a few examples of coordination complexes are reported with H_2valdien.[10] In 2007, Dou *et al*. structurally characterised two mononuclear complexes with large La^{III} and Nd^{III} ions where only the outer donor O_4 set of H_2valdien was involved in the coordination.[10b] Moreover, in some cases, *ortho* positions on the aromatic rings are substituted with methoxy groups in order to prevent the formation of bridged complexes,[10b] however in our synthetic methodology we have employed the latter functionality to promote coordination in both pockets. The stoichiometric reaction of H_2valdien and $Dy(NO_3)_3{\cdot}6H_2O$ in the presence of an organic base (NEt_3, 2 equiv.) in a MeOH/DMF mixture affords the crystallisation of dinuclear compound $[Dy^{III}_2(valdien)_2(NO_3)_2]$ (**III-1**). Slight variation in metal to ligand ratio yielded the same complex.

3.1.2 Structural Characterisation

The single crystal X-ray crystallography study revealed a dinuclear compound which crystallises in the triclinic *P-1* space group. The asymmetric unit consists of one Dy^{III} ion, one $valdien^{2-}$ ligand and a nitrate ion (Fig. 3.1). The centrosymmetric dinuclear complex is composed of two eight-coordinate Dy^{III} ions bridged by phenoxo groups (O3, O3a) of the $valdien^{2-}$ ligands with a Dy1-O3-Dy1a angle of 108.22° and a Dy-Dy distance equal to 3.77

Å. As predicted, the valdien^{2-} ligand bridged the two metal centres providing two potential pathways for magnetic interaction: i) through space (dipolar coupling) as well as ii) superexchange (through orbital overlap). The central core Dy_2O_2 appears to be nearly rhombic, the two Dy-O3 distances being 2.31 and 2.33 Å. One terminal phenoxo group coordinates the dysprosium ion with a short distance Dy-O2 of 2.19 Å. Interestingly, the methoxy groups are not involved in the coordination of the lanthanide centres and thus remain strictly in the flexible inner N_3O_2 compartment of the ligand. In contrast with the previously reported mononuclear complexes based on La^{III} and Nd^{III},[10b] the inner N_3O_2 compartment is a more adequate size for the encapsulation of smaller lanthanide ions such as Dy^{III}. Moreover, the dimerization of the molecule is most likely due to the presence of NEt_3 as base which promotes the full deprotonation of H_2valdien ligands, subsequently providing phenoxides as bridging groups. The coordination sphere is completed by a bidentate nitrate ion leading to an overall N_3O_5 coordination environment. The centrosymmetry of the complex leads to the absence of a dihedral angle between the planes defined by the atoms O3-Dy1-O3a and O3-Dy1a-O3a.

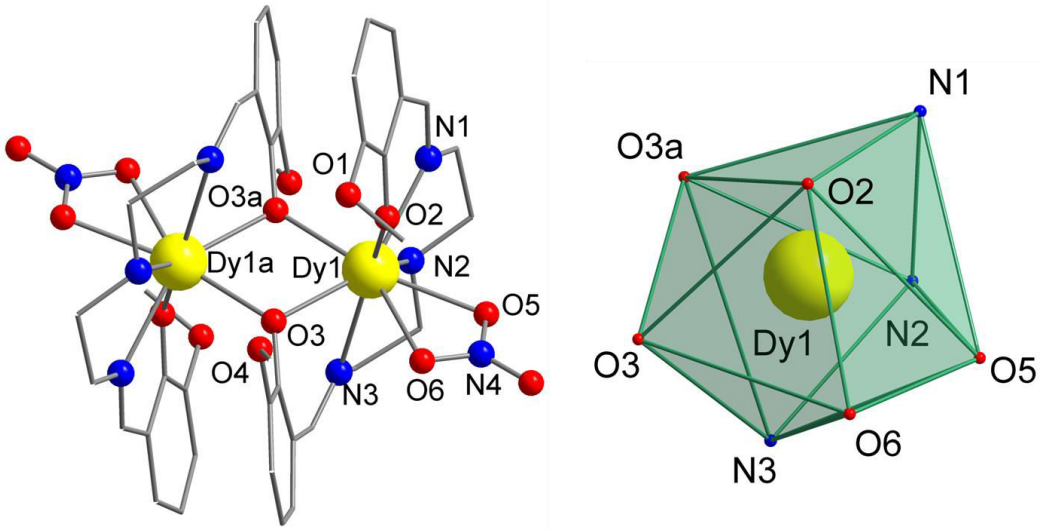

Figure 3.1: (Left) Partially labelled molecular structure of $[Dy^{III}_2(valdien)_2(NO_3)_2]$, **III-1**. Colour code: Yellow (Dy), red (O), blue (N), grey (C). Hydrogen atoms have been omitted for clarity. (Right) Coordination polyhedron of the octa-coordinated Dy^{III} ion.

In the case of lanthanides, the geometry of the metal centre is strongly correlated to the local anisotropy of the paramagnetic ion. Thus, a systematic analysis of the coordination geometry must be performed. With this in mind, the exact geometry of the octa-coordinated lanthanide ions was determined using the SHAPE software.[11] Close analysis of the

resulting data reveals an intermediate geometry between square antiprism (D_{4d}) and dodecahedron (D_{2d}) for **III-1**. An intramolecular H-bond appears between N(2)-H and the methoxy oxygen O4 with a distance of 2.11 Å and an angle of 165.8°, close to linearity (Fig. 3.2, left). The analysis of the packing arrangement (Fig. 3.2, right) reveals the shortest intermolecular Dy-Dy distance of 7.36 Å, confirming the spatial isolation of the dinuclear units.

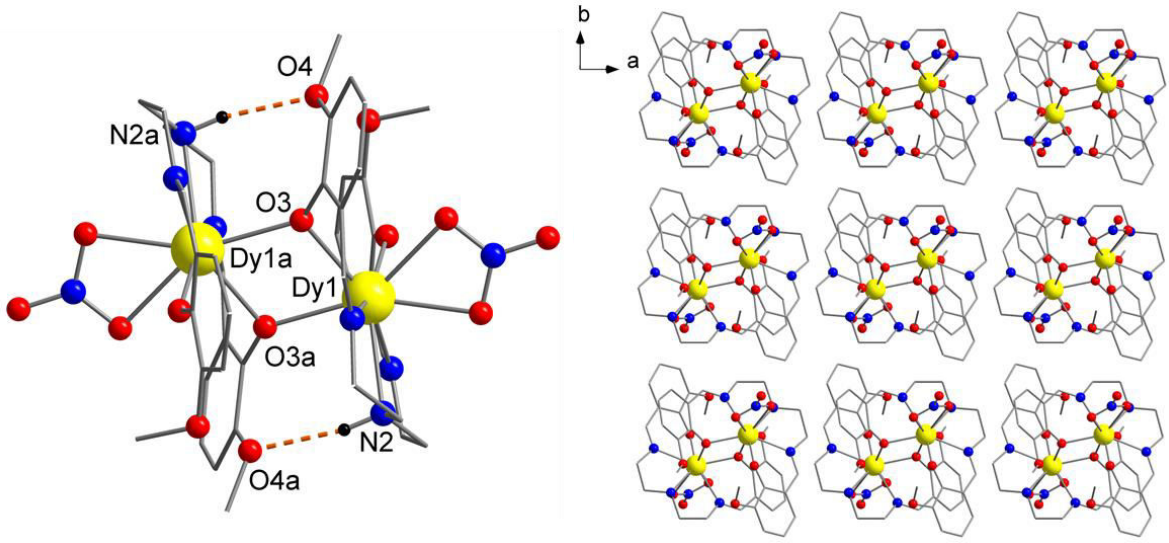

Figure 3.2: (Left) Molecular structure of **III-1** highlighting the intramolecular hydrogen bonds (orange dashed lines). Colour code: Yellow (Dy), red (O), blue (N), grey (C), black (H). (Right) Packing arrangement of **III-1** along the crystallographic *c*-axis.

3.1.3 Direct Current Magnetic Studies

The dc magnetic properties of complex **III-1** were investigated under a 1000 Oe field in the temperature range 1.8 – 300 K (Fig. 3.3, left). It is noteworthy that the observed paramagnetism arises uniquely from the 4*f* Dy^{III} ions. At room temperature, the χT value of 28.7 $cm^3.K.mol^{-1}$ is in good agreement with the expected theoretical value for two non-interacting Dy^{III} ions (28.34 $cm^3.K.mol^{-1}$, $^6H_{15/2}$, $S = 5/2$, $L = 5$, $g = 4/3$). The strength of the magnetic interaction between the two lanthanide ions in the dinuclear complexes can be easily quantified with the gadolinium analogue. Indeed, the Gd^{III} ions present no spin-orbit coupling at the first order. Thus, we synthesised the Gd^{III} analogue (**III-2**, experimental details are presented in Section 3.3) in order to perform studies on the Ln^{III}-Ln^{III} magnetic interaction within this system. For **III-2**, the χT value of 15.7 $cm^3.K.mol^{-1}$ is in good agreement with the expected theoretical value for two non-interacting Gd^{III} ions (15.76

$cm^3.K.mol^{-1}$, $^8S_{7/2}$, $S = 7/2$; $L = 0$, $g = 2$). The decrease of the χT when lowering the temperature for **III-2** reveals directly the presence of an antiferromagnetic interaction between the Gd^{III} ions. Application of the van Vleck equation to the Kambe's vector coupling scheme by using the isotropic spin Hamiltonian $H = -2JS_a \bullet S_b$ with $S_a = S_b = 7/2$, it is possible to reproduce the variation of χT *vs*. *T*. The best fit parameters obtained are $J = -0.087(1)$ cm^{-1} and $g = 2.00(0)$. As expected for pure lanthanide systems, the exchange interaction is rather weak as a consequence of the shielded *f* orbitals which have little overlap with bridging ligand orbitals. The values obtained are in good agreement with the reported coupling constants for other phenoxo-bridged Gd^{III} systems,[12] especially for centrosymmetric complexes.[13,14] For compound **III-1**, the thermal variation of χT shows a negative deviation upon cooling to reach a value of 5.2 $cm^3.K.mol^{-1}$ at 1.8 K. For such lanthanide ions with an unquenched orbital moment associated with a ligand field, the decrease of the χT can originate from the following possible contributions: (i) antiferromagnetic interactions between the lanthanide centres; (ii) the thermal depopulation of the Stark sub-levels; (iii) the presence of significant magnetic anisotropy. However, the absence of any increase in the χT product precludes the occurrence of ferromagnetic interaction between the two lanthanide ions.

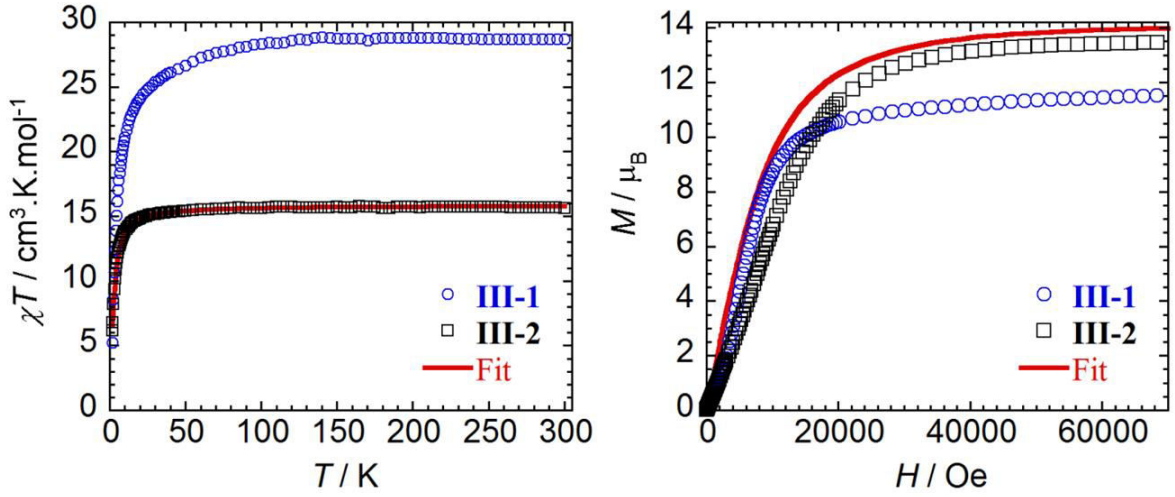

Figure 3.3: (Left) Temperature dependence of the χT product at 1000 Oe for complexes **III-1** and **III-2** (with χ being the molar susceptibility per dinuclear complex defined as M/H). The solid line corresponds to the best fit for **III-2**. (Right) Field dependence of the magnetisation, *M*, at 1.8 K for compounds **III-1** and **III-2**. Solid line corresponds to the Brillouin function for two uncoupled Gd^{III} ions with $S = 7/2$.

Magnetisation measurements performed at low temperatures as a function of the applied field can give an indication of the presence of magneto-anisotropy (*M vs. H* plot, Fig. 3.3, right). For **III-1**, the magnetisation value at 7 T is 11.55 μ_B which is close to the expected value of 5.23 μ_B per Dy^{III} ion in a crystal field environment.[2,15] For **III-2**, the *M vs. H* plot reveals a saturation value of 13.46 μ_B at 7 T which is in good agreement with the expected theoretical value of 14.00 (g = 2.00) for two isotropic Gd^{III} ions. We should be able to fit this curve using a Brillouin function for two uncoupled spins S = 7/2. Nevertheless, the solid line corresponding to the Brillouin fit is slightly higher than the magnetisation curve, thus confirming the antiferromagnetic interaction between the two metal centres (Fig. 3.3, right). It is noteworthy that both curves, for **III-1** and **III-2**, show slight S-shape below 1 T in the *M vs. H* plot indicating magnetically interacting ions. This interaction will be discussed further in the following section. Although the magnetic interaction is quite weak in this dinuclear system, it remains to be seen whether its effect on the slow relaxation and SMM properties is significant.

3.1.4 Slow Magnetic Relaxation Studies

In order to investigate the presence of slow relaxation of the magnetisation which may originate from SMM behaviour, ac measurements were performed in the temperature range 1.8 – 25 K with zero dc field and a 3 Oe ac field at frequencies between 1 and 1500 Hz. The temperature and frequency dependant ac susceptibility signal was observed below 25 K for **III-1**. As an isotropic system, **III-2** does not exhibit slow relaxation properties, therefore all discussion hereafter will focus only on **III-1**. The out-of-phase (χ'') component of the ac susceptibility (Fig. 3.4a) clearly exhibits a frequency dependant full peak with one maximum. Additionally, a frequency dependence of the maximum associated with only a single relaxation process appears clearly on a tridimensional plot of the variation of χ'' *versus* the temperature and the frequency of the oscillating field between 1 and 1500 Hz (Fig. 3.4b). This indicates slow relaxation of the magnetisation associated with SMM behaviour.

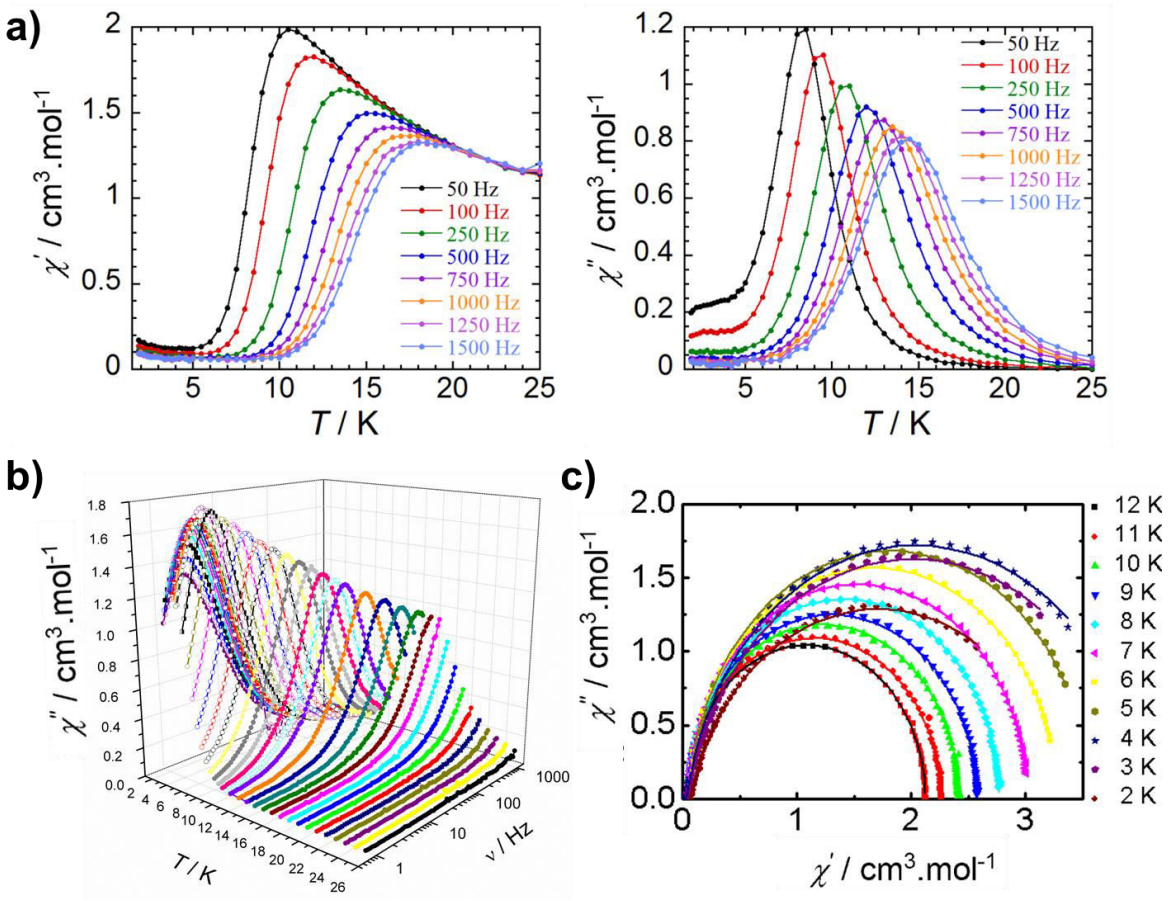

Figure 3.4: (a) Temperature dependence of the in-phase χ' (left) and out-of-phase χ'' (right) ac susceptibility under zero-dc field for **III-1**. (b) 3D plot presenting the out-of-phase susceptibility χ'' as a function of both temperature (T) and frequency (ν, logarithmic scale) for **III-1**. (c) Cole-Cole plot for **III-1** obtained using the ac susceptibility data. The solid lines correspond to the best fit obtained with a generalised Debye model.

Such behaviour is rather singular as most lanthanide systems exhibit multiple relaxation processes due to significant quantum tunnelling at zero field and/or to the presence of crystallographically independent lanthanide centres.[3a,5c] Here the presence of a single relaxation process agrees with the presence of a unique crystallographic Dy^{III} ion in the dinuclear structure. A close inspection of the latter relaxation process in the tridimensional plot reveals two regimes of relaxation (Fig. 3.4b). For temperatures higher than 4 K, the system follows a thermally activated relaxation process. However, below 4 K, the relaxation becomes temperature independent (*i.e.* in the quantum regime) and a drop of the imaginary susceptibility, χ'', is observed. The latter regime most likely originates from an

antiferromagnetic interaction between the Dy^{III} ions which tends to create a non-magnetic ground state with decreasing temperature.[2] The graphical representation of χ'' *vs.* χ' (Cole-Cole plot) [16] in the temperature range of 2 – 12 K further confirms the single relaxation process (Fig. 3.4c). For temperatures higher than 4 K, symmetric semi-circles are obtained. The data can be fitted using a generalised Debye model.[17] The α parameter, indicating deviation from the pure Debye model, is lower than 0.03 for this temperature range. This low degree of deviation confirms that the magnetisation relaxes with a unique single characteristic time. When the system enters the quantum regime (below 4 K), a slight asymmetry in the Cole-Cole plot appears as well as an increase in α up to 0.18 (2 K) is observed. This indicates a narrow width of the distribution in this single relaxation process. As observed for the frequency dependent ac susceptibility, the antiferromagnetic interaction between the two Dy^{III} ions results in a drop of the out-of-phase susceptibility, χ'', in the Cole-Cole plot. The anisotropic energy barrier, U_{eff}, can be obtained from the high temperature regime of the relaxation where it is thermally induced (Arrhenius law, $\tau = \tau_0 \, exp(U_{eff}/kT)$). The effective energy barrier obtained from fitting the linear portion of the curve (Fig. 3.5) is U_{eff} = 76 K (τ_0 = 6.04 × 10^{-7} s); which, at the time, was relatively high for a dinuclear lanthanide system and comparable in magnitude to the archetype Mn_{12}-Ac SMM.[18]

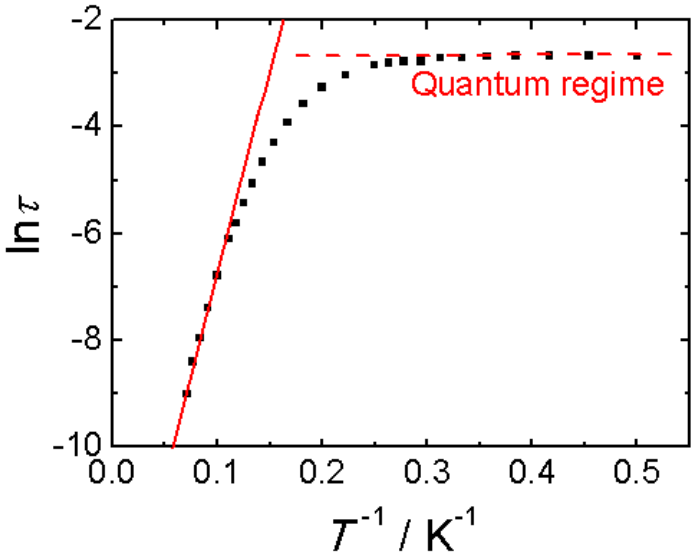

Figure 3.5: Relaxation time of the magnetisation ln(τ) *vs.* T^1 (Arrhenius plot using ac data) for **III-1**. The solid line corresponds to the linear fit of the thermal relaxation process while the dashed line indicates the quantum regime where relaxation time becomes temperature independent.

In order to reduce the quantum tunnelling effects frequently associated with lanthanide SMMs, ac measurements in the presence of a static dc field were carried out. Interestingly, no significant shift in the maximum position was observed for dc fields up to 2000 Oe. This suggests that the tunnelling below the latter field is less efficient. To further probe this behaviour, studies on magnetically diluted samples will be discussed in Section 3.2. The SMM behaviour can be further investigated through micro-SQUID experiments between 0.04 and 4 K (Fig. 3.6). Hysteresis loops were measured on easy-axis oriented single crystals. An "*S*-shaped" hysteresis is observed with a large step at $H = \pm 0.3$ T, which can be directly associated with a spin flip of the antiferromagnetically coupled Dy^{III} spins. Moreover, the strong sweep-rate dependence confirms the presence of quantum tunnelling of the magnetisation. For mononuclear Dy^{III} complexes, a large step indicating QTM can be found at zero-field in the M/M_s *vs.* $\mu_o H$ plot which can only be shifted through the application of a magnetic field.

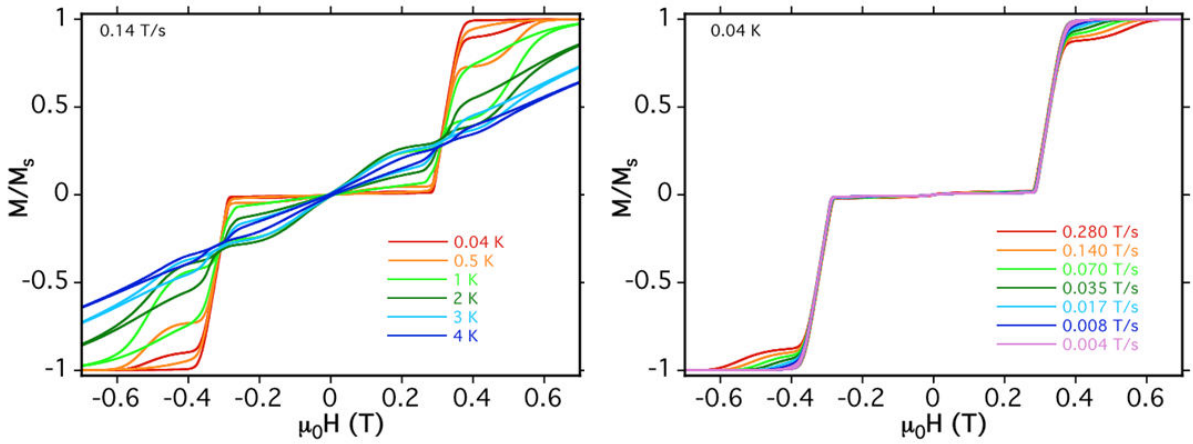

Figure 3.6: (Left) Field dependence of the normalised magnetisation of **III-1** between 0.04 and 4 K for dc applied field ranging from –0.7 to 0.7 T at a constant sweep rate of 0.14 T/s. (Right) Sweep rate dependence of the normalised magnetisation of **III-1** at 0.04 K for dc applied fields ranging from –0.7 to 0.7 T.

For **III-1**, if the slow relaxation was purely single-ion in nature, then we would observe the QTM step at zero-field. Instead, the tunnel position resonance shift at ±0.3 T is due to each Dy^{III} ion acting as bias field on its neighbouring metal ion within the molecule. Such behaviour is similar to previously observed $\{Mn_4\}_2$ systems where two cluster units are entangled in their slow relaxation of the magnetisation.[19] It can therefore be concluded that for **III-1** the hysteresis loops reveal exchange-biased interactions between the two

individually relaxing Dy^{III} ions. The strength of this weak exchange coupling determined through low temperature dc measurements corresponds to 0.32 T. In addition to the unique aforementioned behaviour, complex **III-1** reveals an atypical behaviour: below 1 K the coercive field increases with increasing temperature, contrary to what is usually observed in SMMs and traditional magnets. This can be ascribed to strong tunnelling at the steps, which is reduced by thermal activations around the corresponding tunnel splitting.

3.1.5 *Ab Initio* Theoretical Modelling of the Magnetic Properties

Computational Methodology

In order to validate the observed magnetic properties of **III-1**, *ab initio* calculations were performed. For magnetic electrons localised in the 4*f* orbitals of the metal sites the spin–orbit coupling and the crystal field are much stronger than the intramolecular exchange interaction, making these effects a priority in this study. The competition between the spin–orbit coupling, the crystal–field and the intrinsic multiconfigurational nature of the multielectronic wave function of the 4*f* electrons can only be treated adequately by an explicitly correlated *ab initio* method. Therefore, we used a combined approach for studying magnetic properties of complex **III-1** which implies *ab initio* calculations of a mononuclear lanthanide centre with a model description of the exchange interactions between the centres. This methodology has been already successfully applied for the calculation of the magnetic properties of other polynuclear complexes containing lanthanide and transition metal ions.[20,21,22]

The *ab initio* calculations on individual lanthanide fragments have been done with MOLCAS 7.4 program package.[23] In this approach, the relativistic effects are treated in two steps, both based on Douglas–Kroll–Hess Hamiltonian. Scalar terms were included in the basis set generation and used to determine the spin-free wave functions and energies in the multiconfigurational self-consistent field (CASSCF) method. In the second step, spin–orbit interaction was taken into account within the restricted active space state interaction (RASSI) method, which uses the spin free multiconfigurational wave functions as input states. The obtained wave functions and energies of the molecular multiplets were used for the calculation of the anisotropic magnetic properties and the *g* tensors of the lowest states using a specially designed routine SINGLE–ANISO.[24] As a result, the magnetic properties of a single magnetic ion are calculated by a fully *ab initio* approach, in which the spin–orbit coupling is considered non–perturbatively.

The exchange interactions between magnetic centres have been included within the Lines model.[25] In this approach, the exchange interaction between different spin terms in the absence of spin–orbit coupling is modelled by a single–parameter isotropic exchange Hamiltonian for each metal pair. This Hamiltonian model is written on the basis of the *ab initio* computed spin–orbit multiplets of the metal fragments and then diagonalized. The obtained exchange states correspond to the solutions of an anisotropic exchange Hamiltonian of the complex. The advantage of the Lines model is the use of a single parameter to describe the anisotropic exchange interaction for a given pair of interacting metal sites, which in the simplest bilinear approximation is described by 3 x 3 exchange matrix containing nine J_{ik} parameters. The Lines model becomes exact in two limiting cases: 1) isotropic Heisenberg exchange coupling and 2) extremely anisotropic (Ising) exchange coupling. The described approach has been implemented in the computer program POLY–ANISO, which is interfaced with the routine SINGLE–ANISO.[21] The obtained exchange spectrum and eigenfunctions were used to calculate the magnetic properties of the dinuclear complexes.

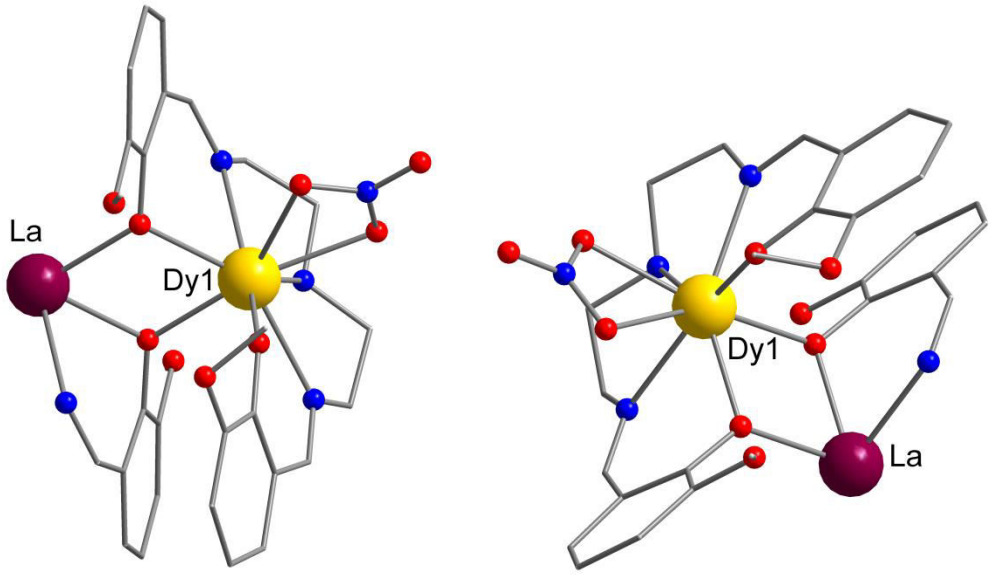

Figure 3.7: Two views of the structure of the calculated mononuclear Dy^{III} fragment of **III-1**. Colour code: Yellow (Dy), purple (La), blue (N), red (O), grey (C).

The basis sets used for the calculations were taken from the ANO–RCC basis library included in MOLCAS program package. The following contractions were used: [8s7p5d4f2g1h] for lanthanide ions, [4s3p2d] for close O and N, [3s2p] for distant O, N and for all C, and [2s] for H. The active space of the complete active space self-consistent field (CASSCF) method included all 4*f* electrons of the lanthanide ion spanning seven orbitals. A

good description of the spin-orbit coupling on the metal sites usually requires the mixing of a large number of states. In the present case we have mixed the maximum number of spin-free states (Dy – 279). The latest implementations of the MOLCAS *ab initio* methodology [26] (Choleski decomposition of the bielectronic integrals, parallelisation, etc…) allow the treatment of relatively large mononuclear fragments. The structure of the calculated fragment is shown in Fig. 3.7.

Results and Discussion

The simulated magnetism of complex **III-1** with the Lines parameter $J_{Dy–Dy}$ = –0.21 cm^{-1} is shown in Fig. 3.8a. The calculated directions of the anisotropy axes and the local magnetic moments in one of the two-fold degenerate Ising ground states are shown in Fig. 3.8b. Due to the inversion symmetry of this complex, the orientation of the local anisotropy axes is strictly parallel, while the local magnetic moments in both Ising ground states are antiparallel to each other. This was one of the most important features of this complex in our quest for a high spin-reversal barrier in SMMs. Aligning anisotropy axes is easiest in centrosymmetric complexes. At high temperature (300 K), the value of χT is well approximated by the sum of the contributions of individual centres. The experimental susceptibility obtained is slightly higher than the calculated one at 300 K. A reduction of 8% in both experimental magnetic susceptibility and molar magnetisation is in good agreement with the calculated curves (Fig. 3.8a).

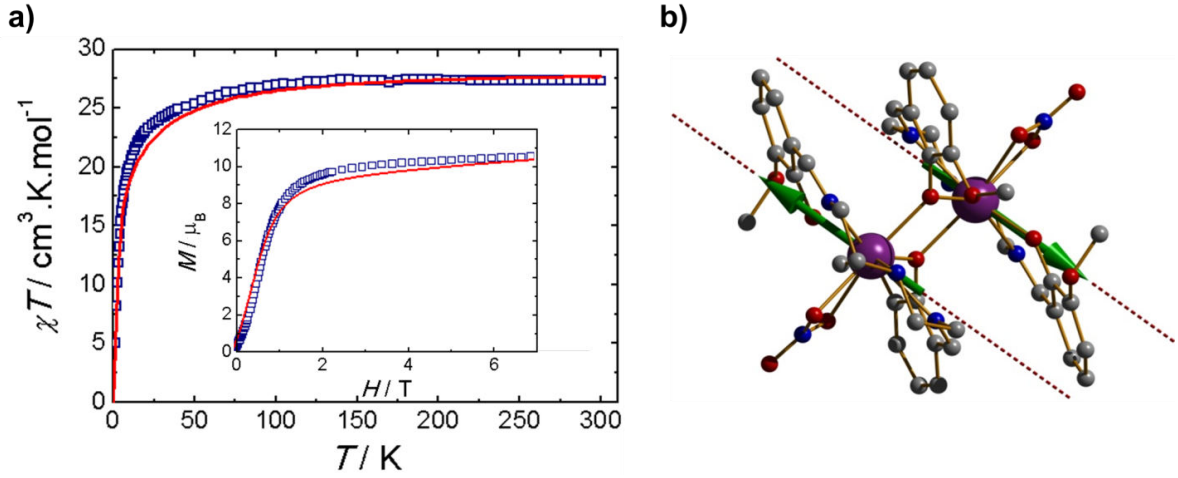

Figure 3.8: (a) A comparison of the reduced by 8% experimental (empty squares) with the calculated (line) magnetic susceptibility of the Dy^{III} complex (**III-1**). Inset: Molar magnetisation for **III-1** at 2 K. (b) Orientation of the local main magnetic axes (green arrows, red dashed lines) of the ground state Kramers doublet in **III-1**.

In order to better characterise the peculiar SMM behaviour observed for **III-1**, several approximations were tested. In the largest computational approximation the complete molecule was kept as is. The only change was the substitution of the neighbouring Dy^{III} ion with diamagnetic La^{III} simulated in the *ab initio* calculations by the same ANO-RCC all-electron basis set as used for Dy^{III}. The obtained *g* tensor is strongly anisotropic (g_z = 19.547) pointing to an Ising interaction between Dy^{III} ions. The orientations of the magnetic axes are found to be almost collinear to the shortest Dy-O2 distance with an angle of 4.05°.

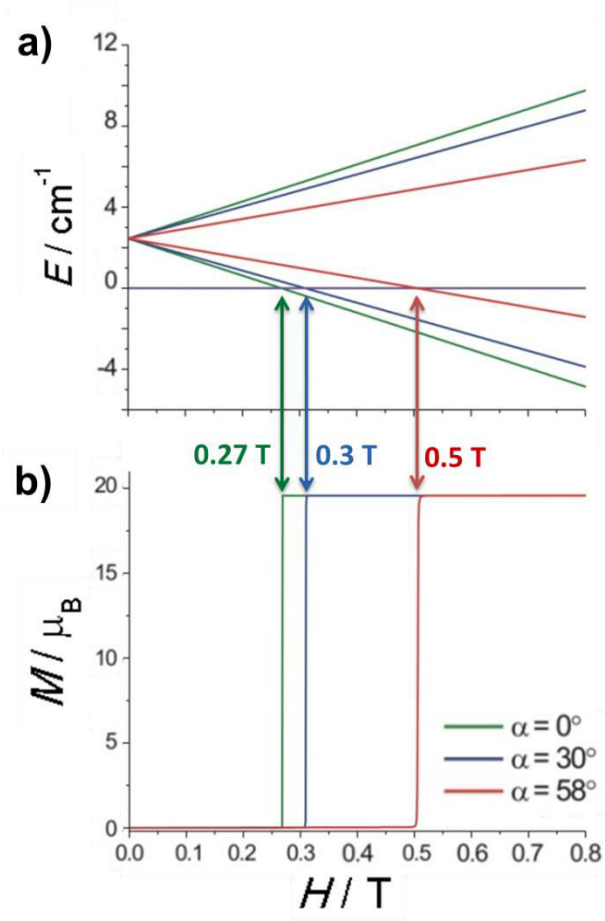

Figure 3.9: Zeeman spectrum (a) and simulated magnetisation curve (b) at T = 0 K for **III-1**.

The simulated magnetisation curve at 0 K (Fig. 3.9) shows a single magnetisation step at a value of applied field strongly dependent on its angle with the anisotropy axes of the Dy^{III} ions. For instance, the observed jump at 0.3 T in the micro-SQUID experiment (Fig. 3.6) requires a large angle of 30° between the anisotropy axes and the applied magnetic field.

The energy of the first excited Kramers doublet on each Dy^{III} fragment was found to be 164 cm^{-1} higher in energy than the ground state. Interestingly, this value does not match the anisotropic barrier derived from the ac measurements (U_{eff} = 76 K or 54 cm^{-1}). Despite the fact that the relaxation time follows a thermally activated behaviour at high temperature, the energy differences observed indicate that an Orbach process might not be predominant and that further relaxation pathways have to be considered. Another reason for this discrepancy can be the overestimated excitation energies of the local Dy multiplets obtained within the CASSCF approximation.

3.1.6 Conclusions

Using a compartmental Schiff base ligand based on the *o*-vanillin motif, unique, centrosymmetric dinuclear Dy^{III} and Gd^{III} complexes have been synthesised and fully characterised. For both complexes, an antiferromagnetic interaction between the lanthanide ions is observed. Simulations based on *ab initio* calculations predict that the strength of the Dy^{III}-Dy^{III} interaction is approximately –0.21 cm^{-1}. Complex **III-2** based on Gd^{III} was used as an isotropic model of **III-1** in order to quantify the magnetic interaction in the system. Moreover, complex **III-1** (Dy^{III}) was shown to exhibit slow relaxation of the magnetisation associated with SMM behaviour and an anisotropic barrier of U_{eff} = 76 K. The single relaxation process observed adequately correlates with the presence of a unique crystallographic Dy^{III} ion. Although the observed slow magnetic relaxation is mainly due to the single-ion relaxation, we believe the results above demonstrate that a weak exchange coupling (J = −0.21 cm^{-1}) between the lanthanide ions affects the QTM. Therefore, the observed steps in the hysteresis loops correspond to a weakly coupled system similar to exchange-biased SMMs.[19] Due to the centrosymmetry and simplicity of the system, complex **III-1** can be viewed as an ideal model for understanding the parameters that affect the SMM behaviour in polynuclear 4*f* systems. In order to provide conclusive evidence for the origins of the slow relaxation process observed in **III-1**, we performed a magnetic dilution study in order to answer an important question: Is the observed slow relaxation indeed single-ion in nature or is the intramolecular Dy^{III}-Dy^{III} interaction (albeit very weak) affecting it? Put in other words, are the two Dy^{III} ions relaxing separately or are they being affected by one another?

3.2 Magnetic Dilution Using $\{Y^{III}_2\}$ Matrix

Theoretically, dysprosium-based complexes should yield some of the highest spin reversal barriers among the lanthanide ions. However, in practice, quantum tunnelling of the magnetisation (QTM) through the barrier *via* higher lying M_S levels of the spin S manifold results in a lower effective barrier (U_{eff}) and is apparent by the observation of step-like features in the hysteresis loops.[27] Such a magnetisation relaxation mechanism is well understood for transition metal SMMs, however, for polynuclear lanthanide systems it is hard to elucidate. This is mainly due to a combination of several factors such as the large magnetic anisotropy found in lanthanide ions, fast tunnelling rates and weak magnetic interactions between 4*f* ions.[1a-c 3a,15,28] Therefore, understanding the origin of relaxation modes seen in polynuclear 4*f* SMMs remains an exciting challenge. In order to determine slow relaxation mechanisms and gain further insight into the effects of magnetic interactions on the SMM properties, we have employed the dinuclear Dy^{III} complex discussed in the previous section (Section 2.1) as a model system. The main focus of this study is to probe the effects of the weak Dy^{III}-Dy^{III} magnetic interaction on the single-ion relaxation of each Dy^{III} centre. The method with which we will answer this fundamental question involves magnetic dilution of the $\{Dy_2\}$ complex in a diamagnetic $\{Y_2\}$ matrix.

3.2.1 Dilution Experiments

Magnetic dilution is possible for this system since the Y^{III} analogue (**III-3**) can be synthesised using the same procedure as the parent $\{Dy_2\}$ complex (see Section 3.3). The two compounds are analogous in molecular structure and packing arrangements, therefore, co-crystallisation can occur and different species with various ratios of Dy:Y can co-exist in one crystal. When diluted with different percentages of Y^{III}, only three $\{Ln^{III}_2\}$ species will form since this complex is centrosymmetric with only one crystallographically unique Ln^{III} centre. The three species are presented in Fig. 3.10 as $\{Y_2\}$, $\{YDy\}$ and $\{Dy_2\}$. The ratio of these species within the samples varies with the different percentages of each metal precursor added. For this study, we focused on samples with 5%, 10% and 50% Dy in addition to the parent 100% $\{Dy_2\}$ complex.

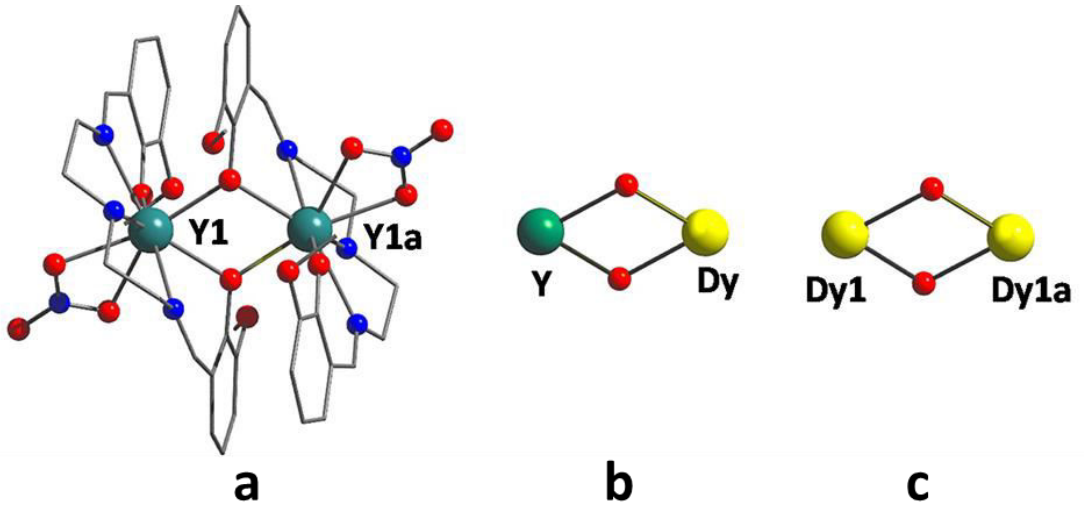

Figure 3.10: (a) Molecular structure of centrosymmetric complex $[Y_2(valdien)_2(NO_3)_2]$, **III-3**. (b) Core unit of the diluted {YDy} complex. (c) Core unit of the $\{Dy_2\}$ complex, **III-1**. Symmetry equivalent positions are denoted by an "a" in the label. Colour code: Yellow (Dy), green (Y), red (O), blue (N), grey (C).

Table 3.1: The calculated probabilities of observing different dinuclear species with different dilution percentages.

	Percentage of Dy^{III} dilution		
	5%	**10%**	**50%**
a- Y_2	90.25%	81%	25%
b- YDy	9.5%	18%	50%
c- Dy_2	0.25%	1%	25%

Single crystals of diluted complexes were prepared by reacting *N*1,*N*3-Bis(3-methoxysalicylidene)diethylenetriamine (H_2valdien) (1 equiv.) and $Y(NO_3)_3{\cdot}6H_2O/Dy(NO_3)_3{\cdot}6H_2O$ in 95:5, 90:10 and 50:50 percentage ratios (0.125 mmol) in 9 mL of MeOH/DMF 2:1 followed by the addition of triethylamine (2 equiv.). Single crystal X-ray structures of pure isostructural $\{Y_2\}$ and $\{Dy_2\}$ complexes were obtained (Fig. 3.10), however, due to the similar ionic radii of Dy^{III} and Y^{III} ions it was not possible to distinguish the metal ions in the crystal structure of the diluted samples. In order to establish the exact amount of Dy^{III} dilution that has taken place in the $\{Y_2\}$ samples, Inductively Coupled Plasma (ICP) measurements were performed. In fact, through ICP, trace concentrations of an element in a sample can be precisely determined. The obtained results of 5.31, 10.24 and

50.56% dysprosium dilution are in good agreement with 5, 10 and 50% employed during the synthesis. The probabilities of observing different dinuclear species with different dilution percentages are given in Table 3.1. It is noteworthy that the probabilities give us an indication of the major and minor species in the sample as opposed to a real ratio between different species. In all samples, with the smallest degree of dilution, we will still observe the homodinuclear complex even though the probability of its existence is relatively low.

3.2.2 Quantum Tunnelling Features in AC Plots

In order to probe the slow relaxation of the magnetisation and quantum tunnelling effects occurring in lanthanide SMMs, alternating current (ac) magnetic measurements were performed on crushed polycrystalline samples in the SQUID magnetometer whereas the dc transverse field method using micro-SQUID was performed on single crystals. Temperature dependence of the ac susceptibility was carried out on all diluted samples under various dc fields and frequencies (Fig. 3.11) in the 20 – 1.8 K range. Initial measurements on diluted and non-diluted $\{Dy_2\}$ samples under zero applied dc field exhibit a clear frequency dependant signal below 20 K indicating SMM behaviour. A peak maximum was observed around 10 K for all samples, however, below 6 K a tail of a frequency dependant peak signal was observed for the diluted samples (Fig. 3.11). Observing a tail of a peak at low temperature could indicate one of two things: 1) There may be another thermal relaxation process where the peak maximum is beyond the limit of the magnetometer and cannot be observed without the application of a dc field (which shifts the peak maxima to higher temperatures) or 2) the increase in χ" indicates a quantum tunnelling process through the spin-reversal barrier *via* degenerate $\pm M_J$ energy levels.[1a,17,29] Lanthanide ions are known to exhibit significant QTM, however, in the case of Dy^{III} ions ($^6H_{15/2}$, $S = 5/2$, $L = 5$, $g = 4/3$) QTM is reduced due to a spin-parity effect. The latter effect predicts that QTM is suppressed at zero field if the total spin of the magnetic system is a half integer but is allowed in integer spin systems. However, QTM can be induced experimentally even in half integer spin systems due to effects such as environmental degrees of freedom as well as hyperfine and dipolar coupling *via* transverse field components.[30] The intensity of the tail increases with increasing percentage of Dy^{III} dilution which is consistent with an increase in the major species {YDy}. The {YDy} species can be thought of as a "mononuclear" complex since there is only one paramagnetic ion present. As mentioned above, mononuclear Dy^{III} complexes very often exhibit significant QTM in the absence of an applied field. This clearly demonstrates that the QTM seen in our system is consistent with mononuclear lanthanide SMMs exhibiting single-ion relaxation behaviour.[29]

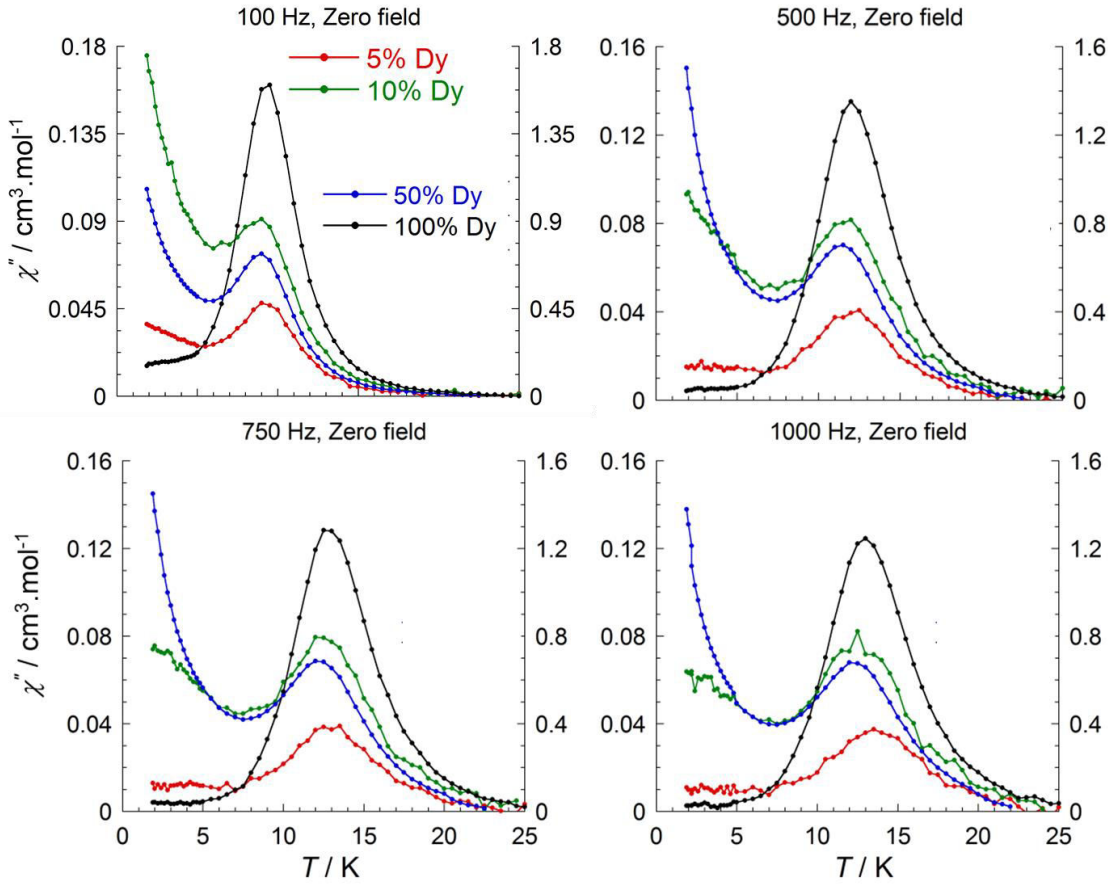

Figure 3.11: Temperature dependence of the out-of-phase susceptibility (χ") plots at indicated frequencies and zero applied field for all samples.

In order to shortcut the QTM it is possible to apply a static dc field while measuring the frequency dependant signal. Indeed, by performing such measurements the degeneracy of the $\pm M_J$ energy levels can be removed, consequently preventing the tunnelling of electrons from $+M_J$ through the spin-reversal barrier to $-M_J$. The thermal dependence below 20 K of χ" under an applied dc field of 200 Oe (Fig. 3.12, middle) exhibits a slight decrease of the tail observed below 6 K confirming the latter assumption. It is noteworthy that there is only a slight shift of the peak maxima for all diluted samples. To fully suppress the tunnelling effects, optimum dc field measurements were carried out at 10 K and optimum fields of 200, 900 and 900 Oe were found for 5, 10 and 50% diluted samples, respectively. Subsequent ac measurements were carried out under the latter optimum fields (Fig. 3.12, right), where a clear single relaxation peak was observed without the presence of a tail in the out-of-phase plot, thus confirming the suppression of the QTM. The intensities of the peaks give an

indication of the major species present in the diluted samples, {YDy} complex, which is consistent with the ICP data.

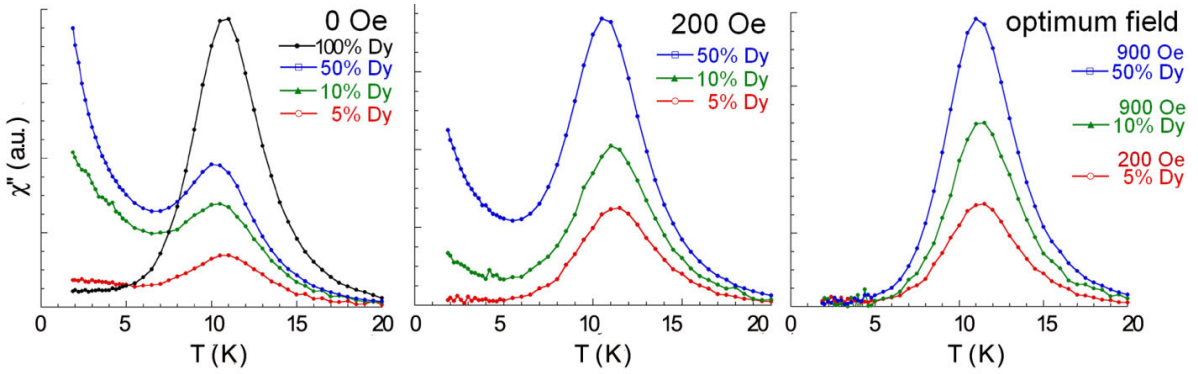

Figure 3.12: Temperature dependence of the out-of-phase susceptibility (χ") plot at 250 Hz and zero applied field (left), 200 Oe (middle) and optimum field (right) for all samples.

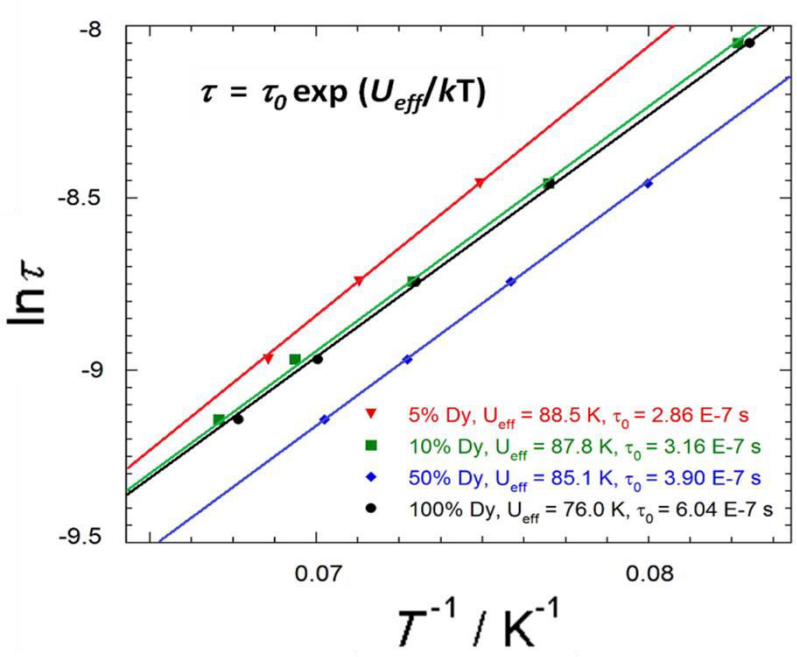

Figure 3.13: Relaxation time of the magnetisation, ln(τ) *vs.* T^{-1}, for all samples. The effective energy barriers (U_{eff}) are indicated.

From the optimum field data an Arrhenius plot can be derived and, subsequently, energy barriers (U_{eff}) can be extracted (Fig. 3.13). The obtained U_{eff} of 88.5 (5%), 87.8 (10%) and 85.1 K (50%) for the diluted samples are much larger than that of the parent 100% {Dy_2} complex (76.0 K). This trend demonstrates that the {YDy} species is the primary contributor

to the relaxation barrier rather than the $\{Dy_2\}$ species. Additionally, these results are consistent with previously reported dysprosium SMMs in which the large relaxation barriers arise primarily from the single ion anisotropy.[3a] The obtained barriers are comparable with some of the largest barriers seen for transition metal SMMs [27b,31] yet smaller than previously reported pure Ln^{III} SMMs.[1c,28] The observed increase in relaxation barriers with increasing magnetic dilutions from 76.0 K (100% Dy) to 88.5 K for (5% Dy) follows a similar trend previously reported by Jiang, *et al*.[29]

3.2.3 Magnetic Hysteresis and Quantum Tunnelling Steps

To further probe this dynamic behaviour single crystal hysteresis loop measurements were carried out in the 0.04 – 5 K range using a micro-SQUID. Hysteresis loops were measured on easy axis oriented single crystals of 5, 10 and 50% diluted samples and compared with 100% $\{Dy_2\}$ complex data (Fig. 3.14). In the case of the 5% doped sample (Fig. 3.14, top left), a large step at zero field is observed. This is consistent with the QTM often observed for lanthanide systems.[1,3,15,] Moreover; the latter behaviour also confirms the observed tail in the out-of-phase χ" *vs. T* plot. Upon increasing the field, opening of the loop is observed with the maximum opening below 500 Oe, which is in reasonable agreement with the ac optimum field of 200 Oe. The latter observation clearly confirms the suppression of QTM under an applied field. The small tunnel resonance step around ± 0.3 T is due to the minor $\{Dy_2\}$ species (Fig. 3.10c), the complex in which each Dy^{III} ion is acting as exchange-biased on its neighbouring metal centre within the molecule. This can be correlated to the step at ± 0.3 T for the 100% Dy sample confirming its identity as the $\{Dy_2\}$ species. The magnitude of the small step due to $\{Dy_2\}$ can be compared with the large step due to {YDy} at zero field. The observed magnetisation ratio of 1:19 is consistent with the presence of $\{Dy_2\}$: {YDy} = 1:38, consistent with a 5% diluted sample. Similar behaviour was seen for the 10% diluted sample with the observed magnetisation ratio of 1:9, coherent with the presence of $\{Dy_2\}$:{YDy} = 1:18. For the 50% diluted sample the tunnelling at zero field is decreased and the increased step around ± 0.3 T (1:1 magnetisation ratio) is indicative of the presence of 25% $\{Dy_2\}$ and 50% {YDy} (Fig. 3.10b) species. In the 100% $\{Dy_2\}$ sample, the absence of the step at zero field indicates the absence of {YDy} species which was responsible for the zero field tunnelling. The tunnel resonance steps around ± 0.3 T can be directly associated with the large spin flip of the antiferromagnetically coupled Dy^{III} ions. The latter weak coupling (0.32 T) is comparable to the exchange-bias coupled $\{Mn_4\}_2$ system.[19] In previously reported transition metal systems the exchange-biased interactions mainly originate from weak intermolecular interactions *via* hydrogen bonds or dipolar interactions.[32] These interactions

are sufficient in strength to perturb the occurring QTM. In our system, the exchange-biased interaction is intramolecular in nature due to the weak coupling between the Dy^{III} ions. In fact, 4*f* magnetic orbitals of lanthanide ions interact poorly with the bridging ligand orbitals due to their core orbital nature. Thus, the magnetic superexchange pathway *via* the ligand orbitals is less efficient.

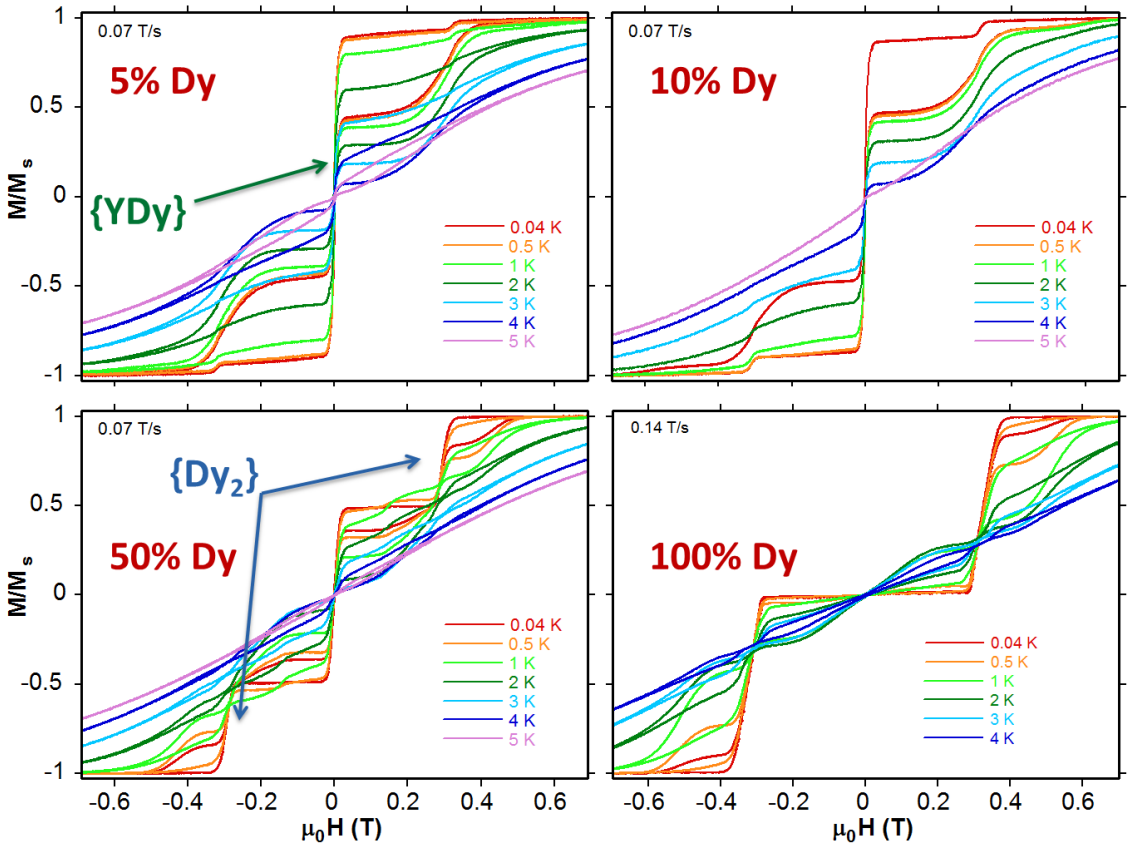

Figure 3.14: Field dependence of the normalised magnetisation of 5% (top left), 10% (top right), 50% (bottom left) diluted and 100% (bottom right) Dy samples between 0.04 and 5 K at the indicated sweep rates. Steps due to quantum tunnelling are indicated for the different species.

3.2.4 Conclusions

The in-depth study of this diluted system clearly demonstrates that the slow relaxation of the magnetisation originates from the single ion relaxation of Dy^{III} ions since the energy barrier calculated for the doped samples (U_{eff} = 85 – 87 K) does not correspond to the {Dy_2} species (U_{eff} = 76 K). However, the latter single ion relaxation is entangled with the neighbouring

Dy^{III} ion relaxation within the molecule *via* weak intramolecular exchange-biased interactions. Evidence of this behaviour is given in the hysteresis loop measurements where the QTM steps can be seen as shifted from zero-field when the dinuclear complex had two paramagnetic Dy^{III} ions. The magnetic interaction (albeit weak) between Dy^{III} ions suppresses the QTM at zero field which is seen as a large step in the hysteresis loop for the {YDy} species and other mononuclear lanthanide systems. These results demonstrate the decisive role of the exchange interaction in such systems despite its weakness in magnitude (typically less than 1 cm^{-1}). This study further demonstrates that weak intramolecular exchange-biased interactions provide a novel approach to fine-tuning the QTM and understanding the nature of slow relaxation of the magnetisation in SMMs. By studying this model system, we are now aware of the importance of magnetic interactions for observation of SMM properties and, more specifically, for targeting zero-field SMMs where the application of an external field is not necessary in order to observe slow relaxation of the magnetisation. It is critical to isolate zero-field SMMs if these nanomagnets were to find applications in molecular electronic devices.

The next step in our quest for higher spin reversal barriers is to optimise our system in terms of ligand field around the Dy^{III} ions and attempt to understand the magneto-structural relationships which govern the slow relaxation behaviour in these dinuclear complexes. To this end, we have undertaken a ligand exchange experiment where one terminal ligand around each metal centre is exchanged in a systematic fashion and we studied if this substitution affects the spin reversal barriers. Moreover, if the terminal ligands play an important role in the height of the energy barriers then how can we control/increase the barriers using this particular method or strategy? By performing this type of study, we can develop a new approach to targeting better SMMs that gives more insight and direction to chemists as opposed to the standard two requirements: Spin and magnetic anisotropy. This study can lead others towards a synthetically simpler approach to increasing spin reversal barriers that does not require bridging radicals or sensitive oxygen-free environments.

3.3 Experimental

3.3.1 General Considerations

All manipulations were performed under aerobic/ambient conditions. All chemicals were purchased from Aldrich or Strem Chemicals and used without any further purification.

IR and NMR Spectroscopy:

Infrared analyses were obtained using a Nicolet Nexus 550 FT-IR spectrometer in the 4000-650 cm^{-1} range. The spectra were recorded in the solid state by preparing KBr pellets. NMR analyses were conducted on a Bruker Avance 400 spectrometer equipped with an automatic sample holder and a 5 mm auto tuning broadband probe with Z gradient.

X-ray Diffraction Studies:

Crystals were grown from a mixture of MeOH/DMF for all complexes. A single rectangular yellow crystal suitable for X-ray diffraction measurements was mounted on a glass fibre. Unit cell measurements and intensity data collections were performed on a Bruker-AXS SMART 1 k CCD diffractometer using graphite monochromated Mo$K\alpha$ radiation (λ = 0.71073 Å). The data reduction included a correction for Lorentz and polarization effects, with an applied multi-scan absorption correction (SADABS).

The crystal structure was solved and refined using the SHELXTL program suite.[33] Direct methods yielded all non-hydrogen atoms which were refined with anisotropic thermal parameters. All hydrogen atom positions were calculated geometrically and were riding on their respective atoms.

Magnetic Measurements:

The magnetic susceptibility measurements were obtained using a Quantum Design SQUID magnetometer MPMS-XL7 operating between 1.8 and 300 K for dc-applied fields ranging from –7 to 7 T. Dc analyses were performed on polycrystalline samples of 6.6 (**III-1**), 14.9 (**III-2**), 21.4 (**50% Dy**), 26.4 (**10% Dy**) and 44.2 mg (**5% Dy**), wrapped in a polyethylene

membrane and under a field ranging from 0 to 7 T between 1.8 and 300 K. Ac susceptibility measurements were carried out under an oscillating ac field of 3 Oe and ac frequencies ranging from 1 to 1500 Hz. The magnetisation data were collected at 100 K to check for ferromagnetic impurities that were absent in all samples. A diamagnetic correction was applied for the sample holder.

Micro-SQUID Measurements:

Magnetisation measurements on oriented single crystals were carried out with an array of micro-SQUIDs.[34] This magnetometer works in the temperature range of 0.04 to ca. 7 K and in fields of up to 0.8 T with sweeping rates as high as 0.28 Ts^{-1}, and exhibits field stability of better than μT. The time resolution is approximately 1 ms. The field can be applied in any direction of the micro-SQUID plane with precision greater than 0.1° by separately driving three orthogonal coils. In order to ensure good thermalisation, a single crystal was fixed with apiezon grease.

ICP-OES Spectroscopy:

All magnetically diluted samples were analysed using Inductively Coupled Plasma Optical Emission Spectrometry (ICP OES—730-ES, Varian Inc., Palo Alto, CA, USA) at the University of Ottawa, department of Earth Sciences. The 2 mg samples were digested by 0.5 ml conc. HNO_3 and 0.2 ml conc. HCl then diluted by mass to 50 mg of final solution with distilled water. The standard solution was prepared using $Dy(NO_3)_3 \cdot 6H_2O$.

3.3.2 Synthesis and Characterisation

Synthesis of *N1,N3*-Bis(3-methoxysalicylidene)diethylenetriamine (H_2valdien)

The ligand, H_2valdien (Figure 1), (*N1*,*N3*-Bis(3-methoxysalicylidene)diethylenetriamine) was synthesised by mixing *o*-vanillin (0.0250 mol) with diethylenetriamine (0.0125 mol) in 40 mL of EtOH. The orange solution was refluxed for 1 hour and after cooling down, the solvent was removed under reduced pressure to afford an orange oil. The latter oil was left to stand overnight to form a yellow precipitate which was collected by suction filtration and

washed with diethyl ether. Yield = 96%. NMR ^{1}H ($CDCl_3$, 400 MHz): δ2.97 (t, 2H, CH_2-N), 3.69 (t, 2H, CH_2-N), 3.88 (s, 3H, OCH_3), 6.90 (t, 1H, Ar), 6.99 (d, 2H, Ar), 8.32 (s, 1H, N=CH). IR (KBr, cm^{-1}): 3419, 3056, 2995, 2935, 2900, 2835, 1629, 1468, 1416, 1376, 1335, 1269, 1146, 1128, 1080, 1024, 964, 875, 838, 778, 734.

Synthesis of $[Ln^{III}_2(valdien)_2(NO_3)_2]$ (Ln = Dy, **III-1**; Gd, **III-2**;, Y, **III-3**).

To a stirred solution of H_2valdien (0.125 mmol, 0.046 g) and $Ln(NO_3)_3\cdot 6H_2O$ (0.125 mmol) in 9 mL of MeOH/DMF 2:1, triethylamine (0.250 mmol, 35 μL) was added. The resulting clear yellow solution was stirred for 30 sec. then filtered. The filtrate was placed into a diethyl ether bath to help crystallisation. After 2-3 days, rectangular shaped yellow crystals were collected. Yield ≈ 55%. IR (**III-1**, **III-2** and **III-3**, KBr, cm^{-1}): 3225, 2918, 2850, 1637, 1622, 1551, 1491, 1469, 1453, 1401, 1351, 1325, 1295, 1262, 1225, 1111, 1082, 1000, 740, 724.

Doping of compound **III-3** with $Dy(NO_3)_3\cdot 6H_2O$ (0.0060 g for **5%**, 0.011g for **10%** and 0.057 g for **50%** samples) resulted in very similar looking crystals as **III-1**. Yields = 55-70%. IR spectra are identical to the parent compound **III-1**. ICP characterisation is discussed in the text.

References

[1] (a) P.-H. Lin, T. J. Burchell, R. Clérac, M. Murugesu, *Angew. Chem. Int. Ed.* 47 (2008), 8848; (b) G.-F. Xu, Q.-L. Wang, P. Gamez, Y. Ma, R. Clérac, J. Tang, S.-P. Yan, P. Cheng, D.-Z. Liao, *Chem. Commun.* 46 (2010), 1506; (c) R. A. Layfield, J. J. W. McDouall, S. A. Sulway, F. Tuna, D. Collison, R. E. P. Winpenny, *Chem. Eur. J.* 16 (2010), 4442; (d) J. J. Le Roy, L. Ungur, I. Korobkov, L. F. Chibotaru, M. Murugesu, *J. Am. Chem. Soc*. 136 (2014), 8003; (e) A.-J. Hutchings, F. Habib, R. J. Holmberg, I. Korobkov, M. Murugesu, *Inorg. Chem*. 53 (2014), 2102; (f) F. Habib, J. Long, P.-H. Lin, I. Korobkov, L. Ungur, W. Wernsdorfer, L. F. Chibotaru, M. Murugesu, *Chem. Sci*. 3 (2012), 2158.

[2] J. Tang, J; I. Hewitt, N. T. Madhu, G. Chastanet, W. Wernsdorfer, C. E. Anson, C. Benelli, R. Sessoli, A. K. Powell, *Angew. Chem. Int. Ed.* 45 (2006), 1729.

[3] (a) P.-H. Lin, T. J. Burchell, L. Ungur, L. F. Chibotaru, W. Wernsdorfer, M. Murugesu, *Angew. Chem. Int. Ed*. 48 (2009), 9489; (b) Y.-N. Guo, G.-F. Xu, P. Gamez, L. Zhao,

S.-Y. Lin, R. Deng, J. Tang, H.-J. Zhang, *J. Am. Chem. Soc.* 132 (2010), 704422; (c) Y. Bi, X.-T. Wang, W. Liao, X. Wang, R. Deng, H. Zhang, S. Gao, *Inorg. Chem*. 48 (2009), 11743; (d) Y. Gao, G.-F. Xu, L. Zhao, J. Tang, Z. Liu, *Inorg. Chem.* 48 (2009), 11495; (e) Y.-N. Guo, G.-F. Xu, P. Gamez, L. Zhao, S.-Y. Lin, R. Deng, J. Tang, H.-J. Zhang, *J. Am. Chem. Soc.* 132 (2010), 8538.

[4] M. Gamer, Y. Lan, P. W. Roesky, A. K. Powell, R. Clérac, *Inorg. Chem.* 47 (2008), 6581.

[5] (a) S. K. Langley, B. Moubaraki, C. M. Forsyth, I. A. Gass, K. S. Murray, *Dalton Trans.* 39 (2010), 1705; (b) B. Hussain, D. Savard, T. J. Burchell, W. Wernsdorfer, M. Murugesu, *Chem. Commun.* (2009), 1100; (c) I. J. Hewitt, Y. Lan, C. E. Anson, J. Luzon, R. Sessoli, A. K. Powell, *Chem. Commun*. (2009), 6765.

[6] (a) X. Gu, D. Xue, *Inorg. Chem.* 46 (2007), 3212; (b) X. Gu, R. Clérac, A. Houri, D. Xue, *Inorg. Chim. Acta.* 361 (2008), 3873.

[7] J. Long, F. Habib, P.-H. Lin, I. Korobkov, G. Enright, L. Ungur, W. Wernsdorfer, L.F. Chibotaru, M. Murugesu, *J. Am. Chem. Soc*. 133 (2011), 5319.

[8] (a) R. G. Pearson, *J. Am. Chem. Soc.* 85 (1963), 3533; (b) R. G. Pearson, *J. Chem. Educ.* 45 (1968), 581.

[9] (a) P. A. Vigato, S. Tamburini, *Coord. Chem. Rev.* 252 (2008), 1871; (b) P. A. Vigato, S. Tamburini, L. Bertolo, *Coord. Chem. Rev.* 251 (2007), 1311.

[10] (a) J. Parr, A. T. Ross, A. M. Z. Slawin, *Polyhedron* 16 (1997), 2765; (b) W. Dou, J.-N. Yao, W.-S. Liu, Y.-W. Wang, J.-R. Zheng, D.-Q. Wang, *Inorg. Chem. Commun*. 10 (2007), 105; (c) J. Chakraborty, S. Thakurta, B. Samanta, A. Ray, G. Pilet, S. R. Batten, P. Jensen, S. Mitra, *Polyhedron* 26 (2007), 513; (d) F.-R. Kong, M. Zhang, *Chem. J. Chin. Univ*. 20 (1999), 839.

[11] D. Casanova, M. Llunell, P. Alemany, S. Alvarez, *Chem. Eur. J.* 11 (2005), 1479.

[12] L. E. Roy, T. Hughbanks, *J. Am. Chem. Soc.* 128 (2006), 568 and references therein.

[13] S. Liu, L. Gelmini, S. J. Rettig, R. C. Thompson, C. Orvig, *J. Am. Chem. Soc.* 114 (1992), 6081.

[14] P.-H. Lin, M. Leclère, J. Long, T. J. Burchell, I. Korobkov, R. Clérac, M. Murugesu, *Dalton Trans.* 39 (2010), 5698.

[15] J. Luzon, K. Bernot, I. J. Hewitt, C. E. Anson, A. K. Powell, R. Sessoli, *Phys. Rev. Lett.* 100 (2008), 247205/1.

[16] (a) K. S. Cole, R. H. Cole, *J. Chem. Soc.* 9 (1941), 341; (b) S. M. J. Aubin, Z. Sun, L. Pardi, J. Krzystek, K. Folting, L. J. Brunel, A. L. Rheingold, G. Christou, D. N. Hendrickson, *Inorg. Chem.* 38 (1999), 5329.

[17] D. Gatteschi, R. Sessoli, J. Villain, *Molecular Nanomagnets*; Oxford University Press: New York, 2006 and references therein.

[18] N. E. Chakov, S.-C. Lee, A. G. Harter, P. L. Kuhns, A. P. Reyes, S. O. Hill, N. S. Dalal, W. Wernsdorfer, K. Abboud, G. Christou, *J. Am. Chem. Soc.* 128 (2006), 6975.

[19] W. Wernsdorfer, N. Aliaga-Alcade, D. N. Hendrickson, G. Christou, *Nature* 416 (2002), 406.

[20] L. Ungur, W. Van den Heuvel, L. F. Chibotaru, *New J. Chem.* 33 (2009), 1224.

[21] D. Visinescu, A. M. Madalan, C. Duhayon, J.-P. Sutter, L. Ungur, W. Van den Heuvel, L.F. Chibotaru, M. Andruh, *Eur. Chem. J.* 15 (2009), 11808.

[22] L. F. Chibotaru, L. Ungur, C. Aronica, H. Elmoll, G. Pilet, D. Luneau, *J. Am. Chem. Soc*. 130 (2008), 12445.

[23] G. Karlström, R. Lindh, P.-Å. Malmqvist, B. O. Roos, U. Ryde, V. Veryazov, P.-O. Widmark, M. Cossi, B. Schimmelpfennig, P. Neogrady, L. Seijo, *Comput. Mater. Sci.* 28 (2003), 222.

[24] L. F. Chibotaru L. Ungur, *The computer programs SINGLE–ANISO and POLY–ANISO*, University of Leuven, 2006.

[25] M. E. Lines, *J. Chem. Phys*. 55 (1971), 2977.

[26] F. Aquilante, L. De Vico, N. Ferré, G. Ghigo, P.-Å. Malmqvist, P. Neogrády, T. B. Pedersen, M. Pitoňák, M. Reiher, B. O. Roos, L. Serrano-Andrés, M. Urban, V. Veryazov, R. Lindh, *J. Comput. Chem.* 31 (2010), 224.

[27] (a) R. Sessoli, D. Gatteschi, A. Caneschi, A. Novak, *Nature* 45 (1993), 141; (b) R. Sessoli, H.-L. Tsai, A. R. Schake, S. Wang, J. B. Vincent, K. Folting, D. Gatteschi, G. Christou, D. N. Hendrickson, *J. Am. Chem. Soc.* 115 (1993), 1804.

[28] (a) N. Ishikawa, M. Sugita, T. Ishikawa, S. Koshihara, Y. Kaizu, *J. Am. Chem. Soc.* 125 (2003), 8694.

[29] S.-D. Jiang, B.-W. Wang, G. Su, Z.-M. Wang, S. Gao, *Angew. Chem. Int. Ed*. 49 (2010), 7448.

[30] (a) W. Wernsdorfer, S. Bhaduri, C. Boskovic, G. Christou, D. N. Hendrickson, *Phys. Rev. B* 65 (2002), 180403; (b) W. Wernsdorfer, N. E. Chakov, G. Christou, *Phys. Rev. Lett*. 95 (2005), 037203.

[31] C. J. Milios, A. Vinslava, W. Wernsdorfer, S. Moggach, S. Parsons, S. P. Perlepes, G. Christou, E. K. Brechin, *J. Am. Chem. Soc.* 129 (2007), 2754.

[32] (a) A. Das, K. Gieb, Y. Krupskaya, S. Demeshko, S. Dechert, R. Klingeler, V. Kataev, B. Bchner, P. Muller, F. Meyer, *J. Am. Chem. Soc*. 133 (2011), 3433; (b) C. Boskovic, R. Bircher, P. L. W. Tregenna-Piggott, H. U. Güdel, C. Paulsen, W. Wernsdorfer, A.-L. Barra, E. Khatsko, A. Neels, H. Stoeckli-Evans, *J. Am. Chem. Soc*. 125 (2003), 14046; (c) R. Bagai, W. Wernsdorfer, K. A. Abboud, G. Christou, *J. Am. Chem. Soc.* 129 (2007), 12918; (d) M. Affronte, J. C. Lasjaunias, W. Wernsdorfer, R. Sessoli, D. Gatteschi, S. L. Heath, A. Fort, A. Rettori, *Phys. Rev. B.* 66 (2002), 064408; (e) A. Yamaguchi, N. Kusumi, H. Ishimoto, H. Mitamura, T. Goto, N. Mori, M. Nakano, K. Awaga, J. Yoo, D. N. Hendrickson, G. Christou, *J. Phys. Soc. Jpn*. 71 (2002), 414.

[33] Sheldrick, G. M. *Acta Cryst*. A64 (2008), 112.

[34] Wernsdorfer, W. *Supercond. Sci. Technol.* 22 (2009), 064013.

Chapter 4

Enhancing Spin Reversal Barriers Through Electron Withdrawing Effects

The push to miniaturise devices in the nanotechnology world including memory storage and other spintronic devices [1] has led to the persistent investigation of 4*f* lanthanide elements as magnetic centres.[2] Their highly anisotropic nature has certainly been advantageous when targeting magnetic materials on a molecular level.[3] Furthermore, they have been at the forefront of major advances in the field of Single-Molecule Magnets (SMMs) yielding higher effective energy barriers for spin reversal and the highest blocking temperatures to date.[4] While the energy barriers (which result in magnetic bistability and slow magnetisation relaxation) have been steadily increasing with different molecular clusters, a more systematic approach is required in order to elucidate the origin of slow relaxation as well as target rational methods of synthesising better SMMs. As a point of reference, we based our study on a previously reported $\{Dy_2\}$ SMM with terminal nitrate anionic ligands (complex **III-1**, Fig. 4.1).[5] This well-studied complex exhibits an effective anisotropic barrier for the reversal of the magnetisation of U_{eff} = 76 K. In the previous chapter (Chapter 3), the structural and magnetic properties of complex **III-1** were discussed extensively. The magnetic interactions between Dy^{III} ions in the dinuclear compound were highlighted and evidence towards their influence on the SMM properties was presented using magnetic dilution studies.

Although the main goal of magnetic dilution was not necessarily to increase the energy barrier for this complex, U_{eff} did increase gradually (U_{eff} = 76 K to 88 K). In order to drastically influence the height of the energy barrier, we must turn towards increasing magnetic anisotropy by modifying the primary coordination sphere around the Dy^{III} centre. For complex **III-1**, each Dy^{III} ion is coordinated to a nitrate anion in the asymmetric unit

which is a consequence of the metal precursor employed in the synthesis. By substituting the nitrate terminal ligands with other bidentate, monoanionic ligands with varying electron withdrawing substituents, we intend to study the effects on the anisotropic barriers of the $\{Dy_2\}$ complexes. To the best of our knowledge, a direct correlation between relaxation barriers and electron withdrawing groups on terminal ligands while maintaining the geometry of the lanthanide ions had not been previously reported. It is important to study the effects of electron withdrawing substituents on the magnetic anisotropy in SMMs as this provides a relatively novel approach towards the enhancement of the spin reversal barriers. The novelty of this work led to its publication in the Journal of the American Chemical Society as a full article (*J. Am. Chem. Soc*. 135 (2013), 13242 – 13245).

4.1 Two Different Systems

In order to accurately postulate a relationship between the electronics of a system (by means of adding electron withdrawing groups) and the slow relaxation of the magnetisation in SMMs, our well-studied complex, **III-1**, can be an ideal model. By sequentially modifying the monoanionic ligands while keeping the core of **III-1**, the parent compound, we have developed two systems (Fig. 4.1). Complexes **IV-1**, **IV-2** and **IV-3** form one system where the monoanionic nitrate ligands in **III-1** have been replaced by acetate (**IV-1**), monochloroacetate (**IV-2**) and dichloroacetate ligands (**IV-3**). By gradually chlorinating the acetate ligands, we can produce a range of electron withdrawing power on the ligands allowing us to study a trend as opposed to simply one complex. The second system comprises complexes **IV-4** and **IV-5** where the nitrate ligands were replaced by acac (**IV-4**) and hexafluoroacac ligands (**IV-5**). Again, the purpose of fluorinating the acac ligand is to withdraw electron density away from the atoms coordinating to Dy^{III}. In both systems, the electron density on the coordinating oxygen atoms (O5 and O6) has been decreased by adding electron withdrawing Cl (first system) or F atoms (second system) which renders the oxygen atoms significantly electron deficient (*vide infra* for *ab initio* calculations) and increases the distance between Dy^{III} ions and coordinating terminal ligand O's (Table 4.1).

The reaction of Dy^{III} precursor with the ligand, *N*1,*N*3-*bis*(3-methoxysalicylidene)diethylenetriamine (H_2valdien), and the applicable terminal ligand (see red boxes in Fig. 4.1) under basic conditions yielded complexes **III-1** and **IV-1 – 5** with the general formula $[Dy_2(valdien)_2(L)_2]$•Solvent where the terminal ligand L = NO_3^- (**III-1**), CH_3COO^- (**IV-1**), $ClCH_2COO^-$ (**IV-2**), Cl_2CHCOO^- (**IV-3**), $CH_3COCHCOCH_3^-$ (acac, **IV-4**), $CF_3COCHCOCF_3^-$ (F_6acac, **IV-5**) and Solvent = 0.5 MeOH (**IV-3**), 2 CH_2Cl_2 (**IV-4**) (Fig.

4.1). The synthetic procedures are outlined in Section 4.5. All six complexes are centrosymmetric and share the same dinuclear core structure; they consist of two Dy^{III} metal ions, two dianionic tetradentate valdien^{2-} ligands and two bidentate monoanionic terminal ligands. A fully labelled molecular structure of **III-1** is presented in Fig. 3.1 in Chapter 3, all other complexes follow the same labelling scheme (see Fig. 4.7 for **IV-1**). Additionally, intramolecular Dy…Dy distances were found to be 3.77 (**III-1**) 3.84 (**IV-1**), 3.80 (**IV-2**), 3.80 (**IV-3**), 3.89 (**IV-4**) and 3.84 Å (**IV-5**), while the closest intermolecular distances between Dy^{III} ions are 7.36 (**III-1**) 7.62 (**IV-1**), 7.68 (**IV-2**), 7.82 (**IV-3**), 9.79 (**IV-4**) and 9.28 Å (**IV-5**). This indicates the molecular units are well-isolated within the crystal lattice with the main magnetic interactions originating intramolecularly where the distance between Dy^{III} ions is much shorter. In recent years, many studies have been undertaken to determine the effects of geometry changes on the slow relaxation of magnetic ions, and subsequently on the energy barriers for reversal of the magnetisation, especially for lanthanide ions.[6,7] However, studies of systematic electronic changes while maintaining the coordination geometry of the metal centres had yet to be explored. If the geometry of the metal ion remained constant, changes in the slow relaxation behaviour of the SMMs could be directly attributed to changes in the ligand field which in turn is directly related to the ligand substituents with varying electron donating abilities.

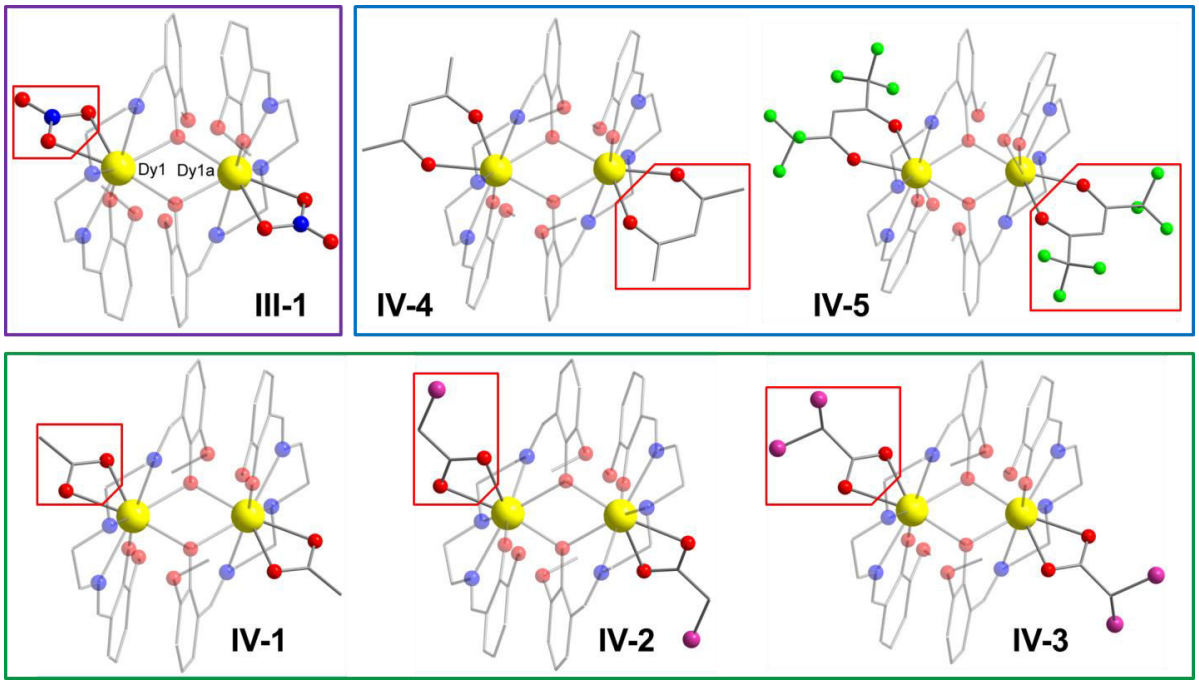

Figure 4.1: Molecular structures of complexes **III-1** and **IV-1** – **5** highlighting the difference in terminal ligands (red boxes). Colour code: Yellow (Dy), red (O), blue (N), grey (C), maroon (Cl), green (F).

Table 4.1: Selected bond distances (Å) and angles (°) for complexes **III-1** and **IV-1** – **5**.

	III-1	**IV-1**	**IV-2**	**IV-3**	**IV-4**	**IV-5**
Dy..Dy	3.77	3.84	3.80	3.80	3.89	3.84
Dy-O5	2.4275(8)	2.4222(1)	2.4562(11)	2.4555(16)	2.3201(16)	2.4489(16)
Dy-O6	2.5046(8)	2.4028(11)	2.4338(10)	2.4839(17)	2.3737(16)	2.3895(16)
Dy-O3	2.3169(7)	2.3633(8)	2.3762(9)	2.3716(14)	2.3813(15)	2.3766(15)
Dy-O3a	2.3341(7)	2.3775(8)	2.3427(9)	2.3466(15)	2.4253(14)	2.3645(15)
Dy-O2	2.1884(7)	2.2114(8)	2.2034(10)	2.1894(16)	2.2211(16)	2.1839(17)
Dy-N1	2.5081(9)	2.5473(10)	2.5356(12)	2.5335(18)	2.5805(19)	2.566(2)
Dy-N2	2.5365(8)	2.5542(1)	2.5401(12)	2.5411(19)	2.5621(19)	2.5487(19)
Dy-N3	2.5300(8)	2.5602(10)	2.5701(12)	2.574(2)	2.581(2)	2.553(2)
Dy-O3-Dy	18.22(3)	8.21(3)	7.16(4)	7.12(5)	10.42(5)	7.99(6)
O5-Dy-O6	52.02(3)	53.85(4)	53.38(4)	52.80(6)	69.66(6)	68.27(5)

4.2 Comparison of Magnetic Properties

In order to probe the magnetic behaviour of **IV-1** – **5**, direct current (dc) magnetic susceptibility measurement were performed. The plots (Fig. 4.2) indicate room temperature χT values of 28.85 (**IV-1**), 27.52 (**IV-2**), 27.76 (**IV-3**), 27.84 (**IV-4**) and 29.02 $cm^3.K.mol^{-1}$ (**IV-5**), all of which are within reasonable agreement of the theoretical χT value for two non-interacting Dy^{III} ions ($^6H_{15/2}$, S = 5/2, L = 5, g = 4/3, C = 14.17 $cm^3.K.mol^{-1}$). As the temperature decreases, the χT values remain relatively constant down to approximately 30 K for **IV-1**, **IV-4** and **IV-5** before rapidly dropping to a value of 10.4 (at 2.5 K, **IV-1**), 10.87 (at 1.8 K, **IV-4**) and 7.16 $cm^3.K.mol^{-1}$ (at 1.8 K, **IV-5**). For **IV-2** and **IV-3**, the χT curve decreases steadily below 150 K before rapidly decreasing below 30 K reaching 4.85 and 4.94 $cm^3.K.mol^{-1}$ for **IV-2** and **IV-3**, respectively, at 1.8 K. This observed behaviour for **IV-1** – **5** mirrors that of **III-1** which has been extensively studied and exhibits weak intramolecular antiferromagnetic interactions as well as significant magneto-anisotropy, both of which contribute to the decrease in the χT product. The lack of overlap for a large portion of the χT product curves on a single mastercurve can be attributed to differences in the magnetic anisotropy of different samples as will be discussed later in the chapter. It is noteworthy that due to large magnetic anisotropy in the complexes, all samples were restrained in grease during magnetic measurements to prevent torqueing effects.

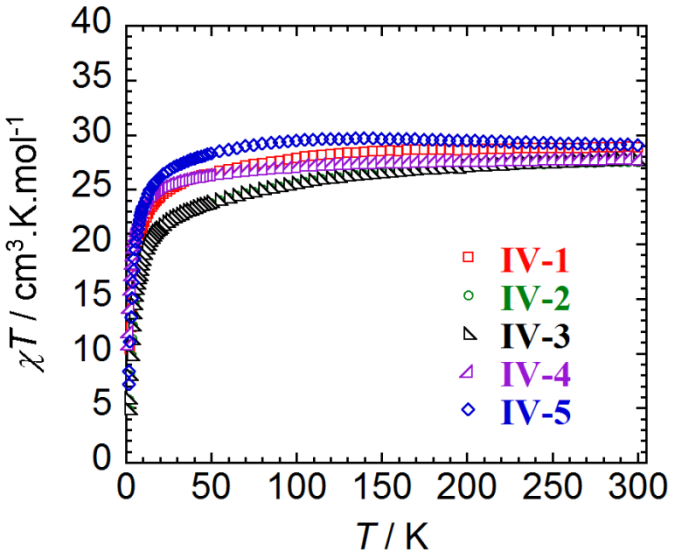

Figure 4.2: Temperature dependence of the magnetic susceptibility, χT, at 1000 Oe for complexes **IV-1 – 5** (with χ being the molar susceptibility defined as M / H).

Ab initio calculations of the CASSCF/RASSI/SINGLE_ANISO type were carried out with MOLCAS 7.8 (see Section 3.1.5 in Chapter 3) in order to simulate the static magnetic behaviour for all complexes.[8] The total exchange Hamiltonian employed is presented in **Eq. 4.1**:

$$\hat{H} = -\left(J_{dip} + J_{exch}\right)\hat{\tilde{s}}_{1,Z}\hat{\tilde{s}}_{2,Z} \qquad \textbf{(4.1)}$$

The dipolar part is considered exactly, while the exchange part is fitted. The experimental magnetic data was reproduced well with antiferromagnetic interactions that were found to be highest for **IV-3** in the first system and for **IV-5** in the second system. The best fitting of the magnetic properties is obtained with the exchange parameters in Table 4.2. Larger magnetic interaction values are due to the electron withdrawing ligands pulling electron density away from the metal centres causing the two metal ions in each complex to become closer in distance. Bringing the metal ions closer causes stronger dipole-dipole interactions. Additionally, the exchange interactions through the bridging Dy-O3-Dy orbitals are also stronger as can be seen in Table 4.2. Increasing both the dipolar coupling and exchange coupling increases the total magnetic interaction strength in each complex. The magnetisation (M) plots as a function of field (H) do not saturate nor superimpose on a single master curve confirming the presence of anisotropy in all complexes (Fig. 4.3). It is

noteworthy that the curves at 1.8 K in the aforementioned plots show slight *S*-shape which has been previously attributed to intramolecular magnetically interacting metal ions.[9]

Table 4.2: Exchange interactions (cm^{-1}) between Dy^{III} ions in all $\{Dy_2\}$ complexes.

Complex	J_{dip}	J_{exch}	$J_{total} = J_{dip} + J_{exch}$
IV-1	-2.80	-1.0	-3.80
IV-2	-2.94	-3.25	-6.19
IV-3	-2.96	-3.25	-6.21
IV-4	-2.32	-0.025	-2.35
IV-5	-2.94	-0.25	-3.19

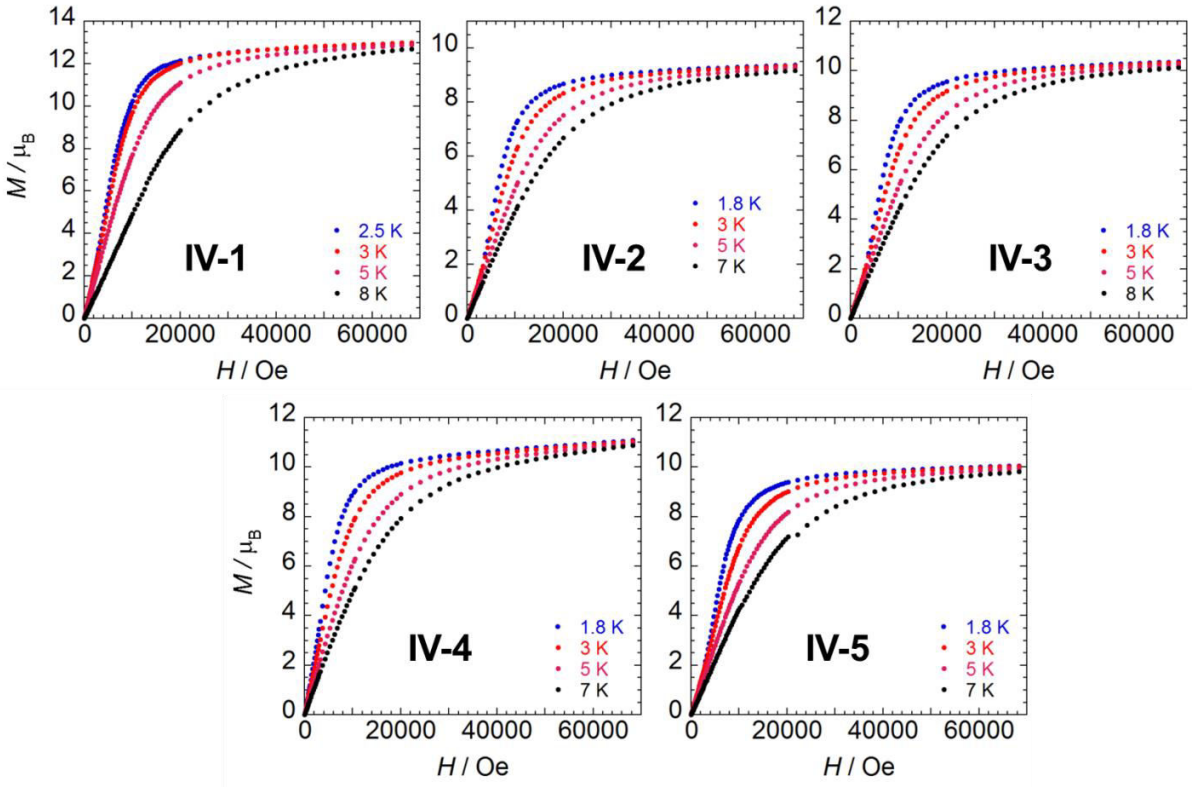

Figure 4.3: Field dependence of the magnetisation, *M*, as a function of applied field at the indicated temperatures for complexes **IV-1 – 5**.

As mentioned above, the magnetic behaviour of the parent compound, **III-1**, has been studied using a variety of techniques including theoretical *ab initio* calculations and doping studies which investigated the intramolecular exchange biased interactions between Dy^{III}

centres (Chapter 3).[5a] In the present case, the effects of electronic changes to the monoanionic ligands on the slow magnetisation relaxation is under study and can be probed using alternating current (ac) magnetic susceptibility measurements. The ac plots indicate frequency and temperature dependence of the in-phase (χ', Fig. 4.4) and out-of-phase (χ", Fig. 4.5) susceptibilities confirming the zero-field slow magnetisation relaxation and SMM behaviour of complexes **IV-1 – 5**. The presence of one set of peaks and therefore one relaxation process is attributed to the presence of one crystallographically independent Dy^{III} ion in the centrosymmetric complexes.[5a,10] As discussed in Chapter 3 for the parent compound, the slow relaxation is mainly single-ion in nature with exchange biased interactions from the neighbouring metal centre in the dinuclear units. These interactions are extremely important as they shift the quantum tunnelling normally observed for single-ion-based magnets to higher fields such that the SMM properties can be observed in the absence of an applied dc field.

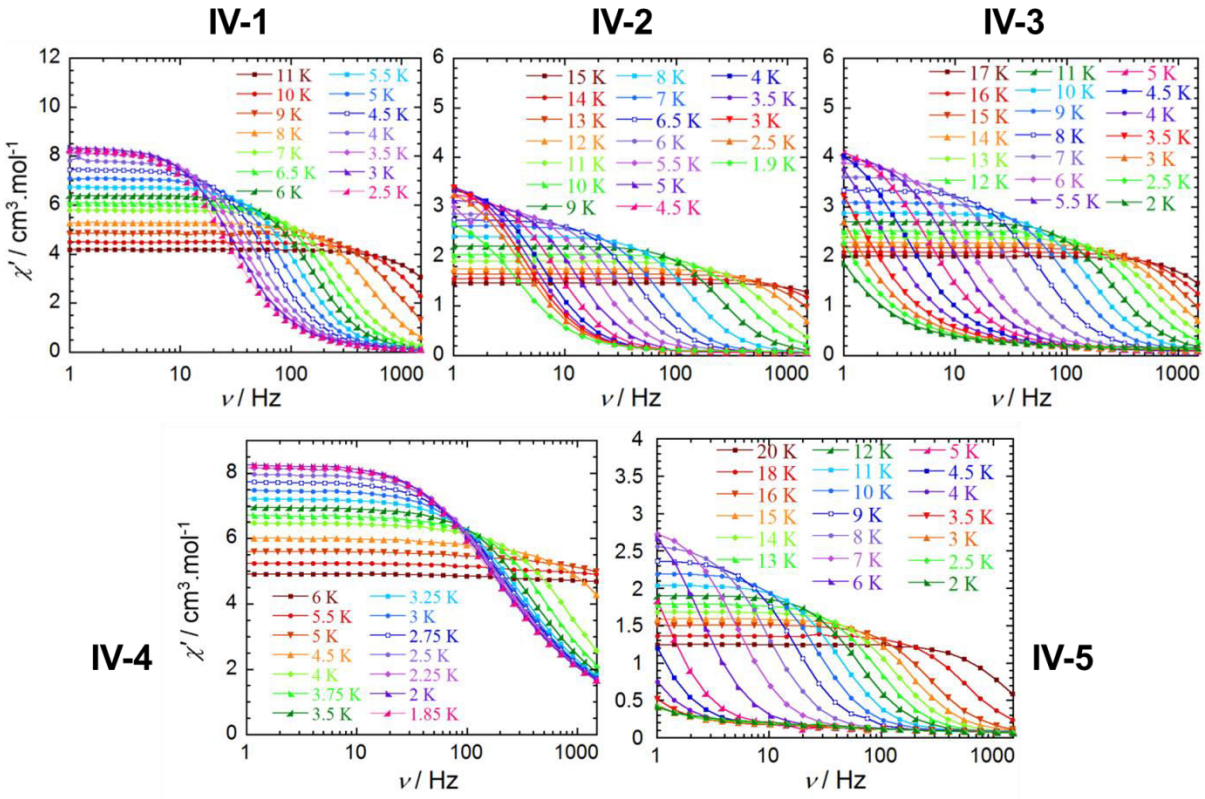

Figure 4.4: Frequency (υ) dependent in-phase magnetic susceptibility (χ') plots for all complexes at the indicated temperature ranges under zero applied dc field.

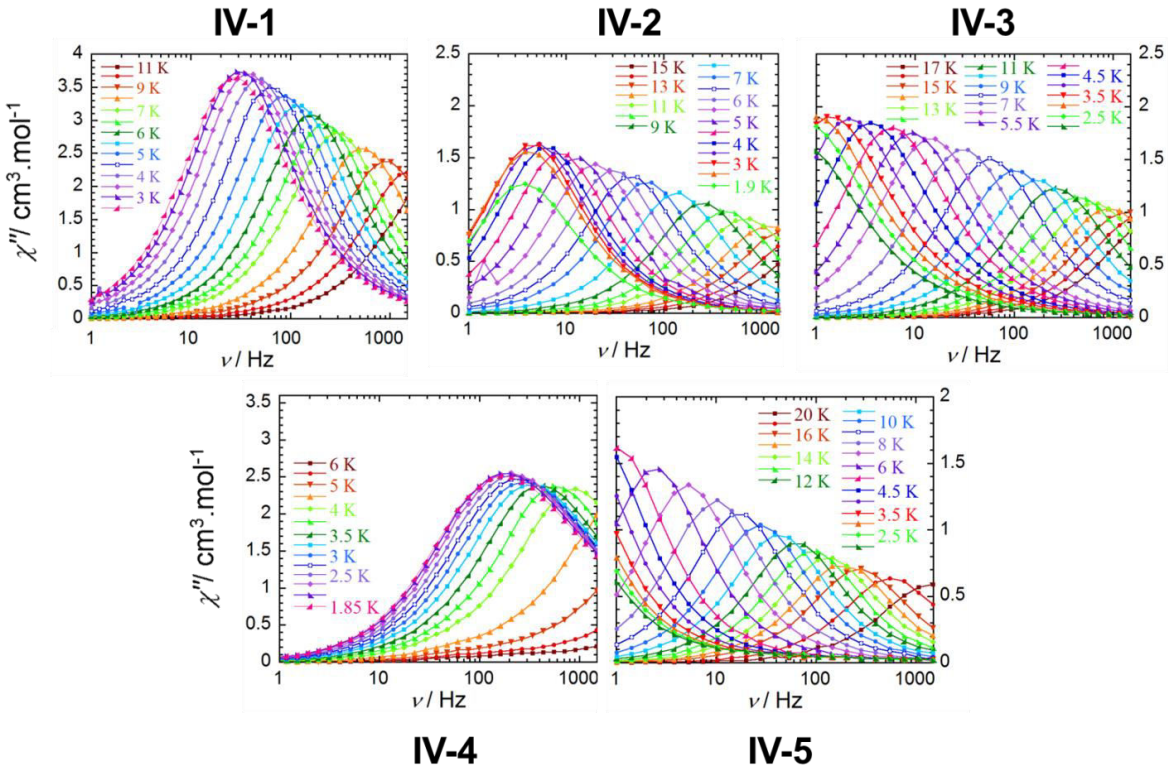

Figure 4.5: Frequency (υ) dependent out-of-phase magnetic susceptibility (χ") plots for all complexes at the indicated temperature ranges under zero applied dc field.

The thermally induced relaxation can be fit using the Arrhenius law ($\tau = \tau_0 \, exp(U_{eff}/kT)$) yielding effective energy barriers of U_{eff} = 34 (**IV-1**), 50 (**IV-2**), 60 (**IV-3**), 16 (**IV-4**) and 110 K (**IV-5**). A comparison plot is shown in Fig. 4.6, right, where the slope of the fit lines can be compared to one another. The steeper the slope, the higher the energy barrier. From the plot, it is clear that complex **IV-5** exhibits the largest spin reversal barrier while **IV-4** exhibits the lowest. The Cole-Cole plots [11] for all complexes have been fit using a generalised Debye model. The α values are below 0.05 in the higher temperature regions for **IV-1** – **3** and **IV-5** indicating the presence of a single relaxation mechanism. For **IV-4**, the α values are below 0.25 which indicates a relatively narrow width of relaxation processes most likely due to a combination of QTM and thermally assisted relaxation pathways at zero field. This also explains the low U_{eff} observed for this complex; when the magnetisation relaxation is due to more than one thermally activated process, often the height of the spin reversal barrier will decrease significantly.

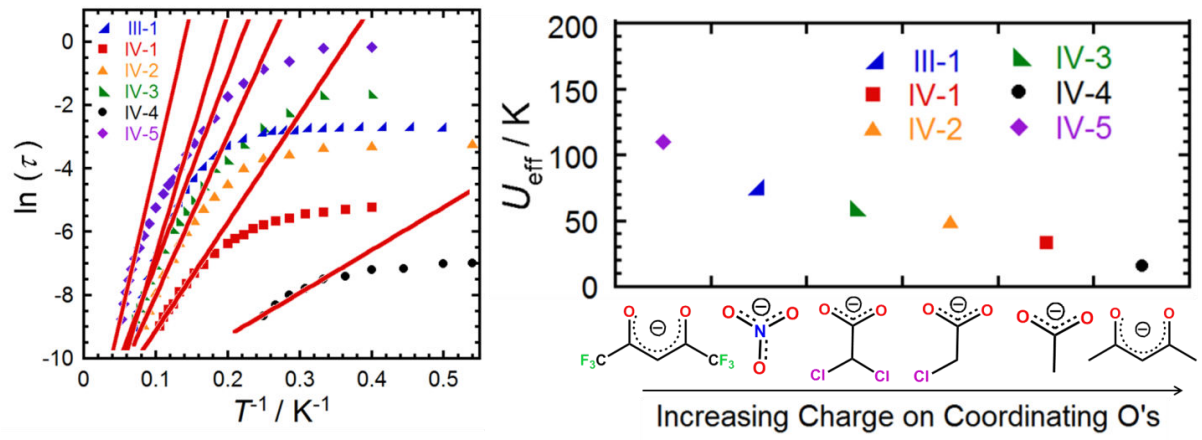

Figure 4.6: (Left) Arrhenius plot showing the relaxation time of the magnetisation for all complexes under zero applied dc field. Red lines correspond to the fit of the high temperature data. (Right) Plot of U_{eff} *vs*. Increasing charge on coordinating O's of the terminal ligands for all complexes.

4.3 Deriving Magneto-Structural Relationships

From a chemist point of view, studying the effects on the structure of the complexes when the ligand substituents are modified can be interesting in and of itself. Additionally, studying the magnetic properties of all complexes can yield important information regarding SMM behaviour in terms of high energy barriers. However, it would be more beneficial for the field to study the relationship between the electronic changes around the metal centre and the magnetic properties since this will lead to novel synthetic strategies targeting high barrier SMMs specifically. The relationship between these two, electronics of the ligand and the magnetic properties, is not often intuitive. In deriving magneto-structural correlations, it is essential to look at the two systems separately.

4.3.1 Shape Measure Approach

In order to provide a quantifiable structural comparison of the coordination spheres in complexes **IV-1** – **5**, the Shape-Measure Approach was utilised based on the dihedral angles along the edges of the polyhedron of Dy1 (Fig. 4.7, **Eq. 4.2**).[12] This approach follows **Eqn. 4.2** where Shape measure (SM) is a factor of δ_i = observed dihedral angle along *m* edges of a coordination polyhedron (angle between normals of adjacent faces) and θi =

corresponding dihedral angle for a reference polyhedron. The parent complex, **III-1**, was chosen as the reference polyhedron and all other complexes were compared to it (Table 4.3). When all complexes are compared to the parent $\{Dy_2\}$, it appears as though the deviation is significant; approximately 2.5 – 3.5° for the first system and 4.75 – 5.75° for the second system. However, it is more important to compare the complexes within each system to each other as opposed to all complexes from different systems. When we look at each system separately, the complexes were found to be analogous with a total deviation of less than 1.0° between **IV-1** – **3** and **IV-4** – **5**. For **IV-1** – **3** (first system) the difference in the structures corresponds to coordinating bidentate acetate groups (**IV-1**), chloroacetate (**IV-2**) and dichloroacetate (**IV-3**). While for the second system, the main difference is in the coordinating acac (**IV-4**) *versus* hexafluoroacac groups (**IV-5**).

$$SM = \left[\sqrt{\frac{1}{m}\sum_{i=1}^{m}(\delta_i - \theta_i)^2}\right] \quad \textbf{(4.2)}$$

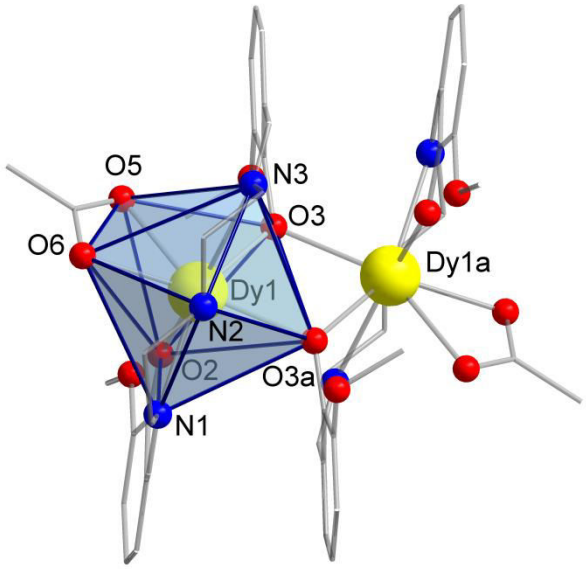

Figure 4.7: Structure of **IV-1** highlighting the coordination polyhedron of Dy1 in blue used in the Shape-Measure Approach calculations (*vide supra*). All other structures (**III-1**, **IV-1**–**5**) follow this labelling scheme. Colour code: Yellow (Dy), red (O), blue (N), grey (C). Hydrogen atoms have been omitted for clarity.

Table 4.3: Dihedral angles along the edges of the coordination polyhedra (°) of dysprosium complexes (**III-1**, **IV-1** – **5**).

Edge	**III-1**	**IV-1**	**IV-2**	**IV-3**	**IV-4**	**IV-5**
O3-O2	36.069(30)	38.136(37)	39.333(38)	40.738(55)	37.998(58)	39.808(65)
O3-N1	62.972(31)	58.308(37)	59.326(39)	59.097(52)	58.831(64)	56.764(63)
O3-N2	48.595(29)	47.262(33)	47.328(39)	47.229(67)	45.219(64)	50.786(63)
O3-N3	36.537(30)	41.284(36)	39.479(40)	40.067(73)	38.577(63)	36.926(70)
O3-O3a	74.839(30)	70.241(35)	70.570(37)	70.413(62)	70.533(55)	69.735(55)
O2-O3a	52.360(26)	56.140(35)	54.429(38)	55.777(62)	55.590(51)	48.682(58)
O2-N1	78.264(32)	81.167(39)	79.288(43)	76.266(75)	74.129(49)	80.984(69)
N1-N2	71.165(31)	71.851(45)	71.109(47)	70.058(68)	67.295(54)	65.886(59)
N2-N3	75.828(29)	74.265(46)	74.858(46)	77.125(66)	80.810(56)	73.057(65)
N3-O3a	65.259(27)	63.240(41)	64.849(37)	64.005(71)	63.438(57)	65.509(57)
N3-O6	49.258(37)	47.595(46)	46.182(48)	52.593(70)	56.571(59)	46.425(63)
N3-O5	29.775(37)	28.848(56)	31.133(49)	23.704(67)	20.837(67)	36.353(70)
N2-O5	56.609(34)	55.954(48)	55.716(49)	55.455(79)	56.681(68)	55.235(65)
N1-O5	52.71(3)	55.283(46)	55.955(42)	58.401(73)	60.387(64)	61.931(62)
O2-O5	21.540(31)	22.814(49)	23.349(45)	24.781(78)	33.734(62)	12.956(60)
O6-O2	63.683(28)	58.674(41)	58.389(40)	58.518(47)	53.12(6)	69.627(50)
O6-O3	60.510(32)	62.836(37)	62.486(37)	61.818(68)	63.501(55)	64.684(67)
O6-O5	81.965(38)	83.255(50)	82.937(51)	84.513(81)	78.954(51)	82.287(68)
SM[a]	**0**	**2.8445**	**2.5406**	**3.4798**	**5.7552**	**4.7423**

[a] Shape measure SM (deviation relative to complex **III-1**).

4.3.2 Effects of Electron Withdrawing Ligands

The sequential addition of Cl atoms in the first system serves to withdraw electron density in a controlled fashion away from the coordinating atoms and, by extension, from the Dy-O5/O6 bonds (important bond distances and angles are presented in Table 4.1). The calculated Mulliken charges for select atoms in the ground state of all $\{Dy_2\}$ complexes using *ab initio* methods are shown in Table 4.4. They reflect the electron density on all atoms including the coordinating oxygen atoms of the terminal ligands and correspond to an average decrease in electron density on O5/O6 as electron withdrawing atoms are added. This leads to an increase in the corresponding Dy-O bond lengths (Table 4.1) and induces a stronger chemical bonding between Dy and O3/O3a, which is reflected in their shorter bond lengths (Table 4.1).[13] This leads to a steady increase of the energy barrier from 34 K (**IV-1**) to 50 K (**IV-2**) to 60 K (**IV-3**) and in the second system, from 16 K (**IV-4**) to 110 K (**IV-5**) when the acac ligand is fluorinated. The electron withdrawing ability of the hexafluoroacac ligand is much more significant (in **IV-5**, the average Dy-$O_{\text{terminal ligand}}$ distance is longer by 0.07Å and the average charge on O5/O6 decreases by 0.087, Table 4.4) which translates into

a more drastic increase in U_{eff}. The χ" *vs.* υ plots in Fig. 4.5 also give an indication of the increase in the energy barrier; when U_{eff} increases, the frequency dependent curves at different temperatures will span a much greater range of frequencies without reaching the QTM regime (where the peaks become temperature independent and begin to overlap) until very low υ as seen for **IV-1** and **IV-4**. The χ" *vs.* υ plot for **IV-2** appears to span a wider range of frequencies than **IV-1** but not quite as much as **IV-3**, in line with the intermediate U_{eff} of 50 K. The decrease in peak intensities as the temperature decreases to approximately 2 K is indicative of weak intramolecular interactions which were studied in the parent compound, **III-1**. This behaviour is known to originate from antiferromagnetic interactions between the Dy^{III} ions which lead to a non-magnetic ground state with decreasing temperature as discussed in Section 3.1.4 (Chapter 3).

Table 4.4: Calculated Mulliken charges for select atoms in the ground state of $\{Dy_2\}$ complexes.

	Mulliken charges				
	IV-1	**IV-2**	**IV-3**	**IV-4**	**IV-5**
Dy1	+1.893	+1.904	+1.911	+1.939	+1.933
O5	-0.928	-0.897	-0.894	-0.981	-0.920
O6	-0.974	-0.965	-0.913	-0.967	-0.854
O2	-1.030	-1.031	-1.035	-1.032	-1.055
O3	-1.160	-1.176	-1.173	-1.144	-1.157
O3a	-1.164	-1.171	-1.167	-1.150	-1.155

A comparison of the relaxation barriers for complexes **III-1** and **IV-1** – **5** with the average charge on coordinating oxygen atoms of the terminal ligands (Fig. 4.6, right) indicates a correlation for these dinuclear Dy^{III} systems. The more electron deficient the monoanionic bidenetate terminal ligand, the higher the energy barrier of the $\{Dy_2\}$. From the Arrhenius plot, $\ln(\tau)$ *vs.* T^{-1}, it is clear that the slope of the fit lines (at higher temperatures where thermal relaxation is dominant) become steeper as the coordinating oxygen atoms of the terminal ligands become more electron deficient leading to higher barriers (up to 110 K for the F_6acac-coordinated complex, **IV-5**). The large difference in the slow magnetisation relaxation can be attributed to two reasons, outlined hereafter. The first is mainly due to the change in ligand field around the primary coordination sphere of the Dy^{III} ions. The increased bond distance between the terminal ligand and the Dy^{III} centres indicates a weaker bond which in turn supports the argument for a weaker ligand field acting on Dy^{III}. As the Dy-$O_{terminal\ ligand}$ distance increases in **IV-1** – **3** by adding electronegative atoms, the total splitting

of the ground multiplet ^{6}H increases (Table 4.5). However, for complexes **IV-4** and **IV-5**, the first excited state of **IV-5** decreased in energy significantly leading to greater mixing by spin-orbit coupling. The crystal field splitting becomes larger for **IV-2**, **IV-3** and **IV-5** in comparison to the non-halogenated {Dy_2} compounds with the calculated first spin-orbit multiplets in **IV-3** and **IV-5** being indeed higher in energy in comparison to the respective multiplets in **IV-2**, **IV-3** and **IV-4** (Table 4.5). This leads to higher spin reversal barriers in **IV-3** and **IV-5**.[3a]

Table 4.5: Energies (cm^{-1}) of the low-lying spin-free and Kramers doublets (KD) as well as the main values of the ground KD obtained.

Multiplet	**IV-1**	**IV-2**	**IV-3**	**IV-4**	**IV-5**
Spin-free energies, cm^{-1}					
^{6}H	0	0	0	0	0
	4	8	11	28	6
	144	180	196	57	231
	177	199	226	121	278
	195	241	241	186	286
	271	300	307	229	347
	292	343	400	254	428
Spin-orbit energies, cm^{-1}					
$^6H_{15/2}$	0	0	0	0	0
	132	148	155	22	182
	160	189	202	110	254
	206	264	280	132	312
	252	289	341	179	359
	300	348	380	227	418
	349	402	446	265	465
	435	467	521	351	546
Main values of the *g*-tensor in the ground KD					
g_x	0.027	0.0087	0.0041	0.091	0.00062
g_y	0.093	0.037	0.010	0.47	0.0033
g_z	19.44	19.50	19.50	18.87	19.66

The second reason is based on the direction of the anisotropy axes calculated for all complexes which are aligned in a parallel fashion due to the presence of an inversion centre (Fig. 4.8). Furthermore, they are perpendicular to the capping ligand. The decreased electron density in the hard plane (perpendicular to the easy axis) could result in a more anisotropic Dy^{III} ion leading to higher effective energy barriers. This was indeed observed when the calculated *g* tensors of the low-lying Kramers doublets (KD) of the Dy^{III} ions were found to

be more axial, and hence more anisotropic, for complexes **IV-3** and **IV-5** (Table 4.5). Additionally, we can conclude that the experimentally observed barriers originate from individual Dy ions as seen for the parent compound, **III-1**.[5] The discrepancies between extracted barriers and the calculated energies of the first excited KD of Dy ions can be attributed to room temperature geometry used in the calculations as well as the possibility that direct relaxation pathways should be considered.

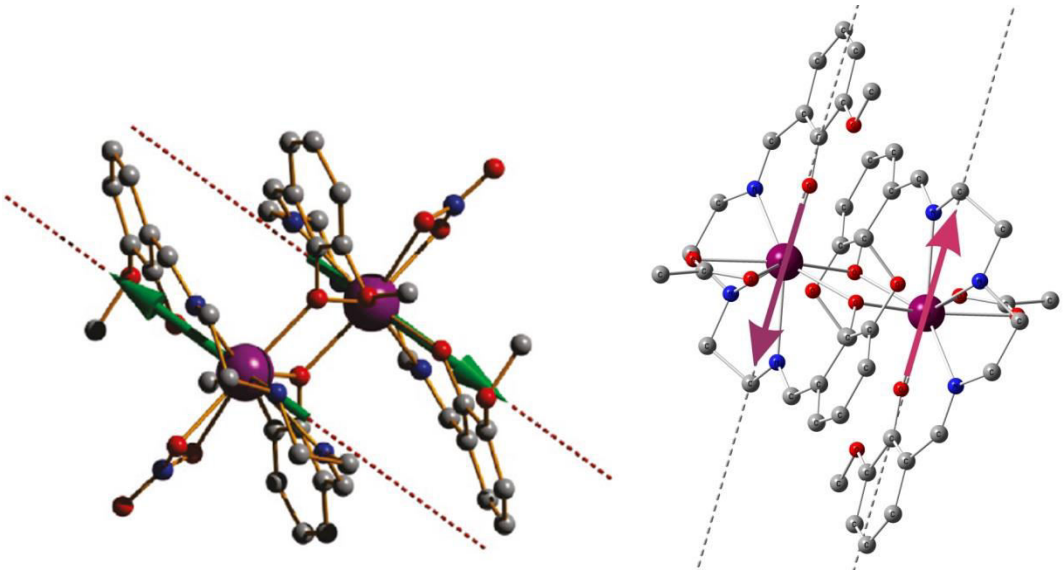

Figure 4.8: Orientation of the calculated anisotropic axes for the ground state Kramers doublet of the parent compound, **III-1** (left), [5a] and **IV-1** (right). The anisotropic axes of **IV-2** – **5** are also parallel due to an inversion centre present in all complexes and resemble very closely **IV-1**.

4.3.3 One More Complex- Trichloroacetate Derivative

When studying the first system with acetate terminal ligands and subsequent chlorinated acetate ligands, it was only reasonable to investigate the trichloroacetate analogue. The latter complex would benefit from the coordination of the most electron withdrawing ligand in this series and hence should exhibit the highest energy barrier for spin reversal. While this fourth compound in the series could be useful in reinforcing the trend that we are observing in terms of energy barrier height in relation to the electron withdrawing groups, it was not easily isolatable as single-crystals. Attempts were made to synthesise the trichloroacetate analogue, however no crystals suitable for single crystal X-ray studies could be isolated. Instead, a microcrystalline powder was obtained that we believe could be the aforementioned complex, shown below is the powder XRD pattern of complex **IV-3** compared with the theoretical

spectrum obtained from the cif file (Fig. 4.9, top) to confirm the purity of that sample. Additionally, the pattern of **IV-3** compared to the potential trichloroacetate analogue is also presented in Fig. 4.9, bottom.

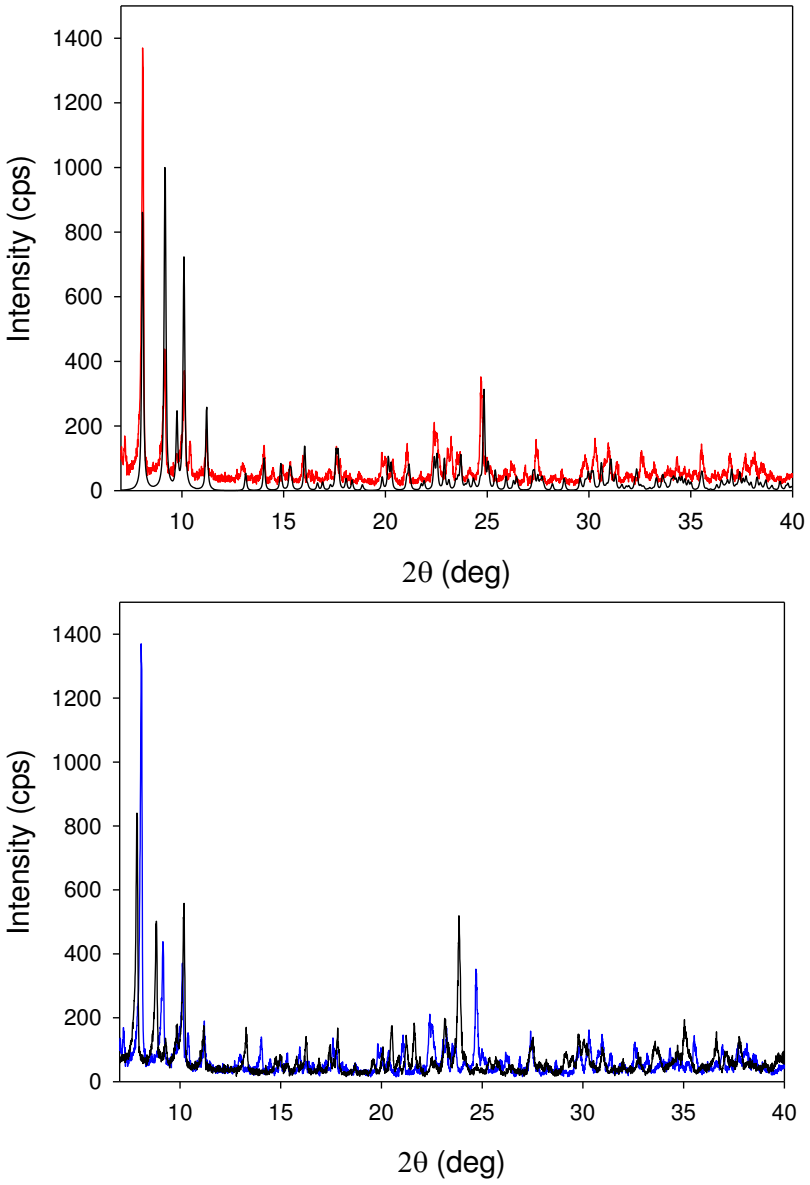

Figure 4.9: (Top) Comparison between .cif powder pattern and actual powder pattern for complex **IV-3**. (Bottom) Comparison between powder pattern of **IV-3** (in blue) and the trichloroacetate analogue (in black).

The peaks appear to be shifted in Fig. 4.9, bottom, with almost all the peaks of **IV-3** present in both spectra. This leads us to believe the trichloroacetate analogue was indeed

synthesised, however with no crystal structure it is difficult to obtain valuable information such as packing arrangements, hydrogen bonds and solvent molecules present in the crystal lattice. The difficulty in obtaining single crystals lies in the solubility of the complex as well as the acidity of the trichloroacetic acid compared with the mono- and dichloroacetic acid. The magnetic behaviour of the obtained powder was investigated and was found to be in accordance with the other studied complexes within that system (**IV-1 – 3**), with an energy barrier of 65 K. This is slightly larger than complex **IV-3** which reinforces the observed trend of higher energy barriers for spin reversal with stronger electron withdrawing ligands.

4.4 Conclusions

Initially, at the beginning of this project, we had set out to derive a relationship between the terminal ligands of the dinuclear dysprosium complexes and the energy barriers for spin reversal. Not only was the terminal ligand crucial when investigating the magnetic properties of these complexes, but the electronics of the ligands played a major role. Through studying effects of electron withdrawing ligands on slow relaxation of the magnetisation, we have been able to show significant enhancement of the energy barriers of two different systems of $\{Dy_2\}$ SMMs by adding electron withdrawing substituents on the terminal ligands in a systematic fashion. This resulted in a 2-fold increase in U_{eff} when dichloroactate as opposed to acetate was employed and, more impressively, a 7-fold increase when the acac ligand was replaced by hexafluoroacac. It is essential to study the two different systems separately as the bite angles of the ligands (acetate *vs*. acac) differ significantly, and hence the geometry around the metal ions will be affected. To rule out geometry changes as contributors to the differences in spin reversal barriers, we maintained the geometry as constant as possible while varying only the electron donating ability of the ligands. The addition of electronegative atoms on the terminal ligands has been found to increase the Dy-Dy coupling with the static magnetic data being reproduced well using *ab initio* calculations. Furthermore, the *ab initio* calculations revealed more axial *g* tensors for complexes **IV-3** and **IV-5** as a result of weaker Dy-$O_{terminal\ ligand}$ bonding resulting in elongation of the Dy-O5/O6 bonds and more electron density on the Dy^{III} ions. Weaker bonds between the metal centre and the terminal ligand O's results in a lower degree of orbital splitting due to the ligand field and therefore a more anisotropic Dy^{III} ion. The first excited Kramers doublets were also found to be highest in energy for complexes **IV-3** and **IV-5** corresponding to higher energy barriers observed experimentally in their respective systems. Replacing H's with electron withdrawing atoms on terminal ligands can be a relatively simple way of attaining higher barrier SMMs. This strategy is much more feasible compared to other synthetically

challenging methods such as inducing coupling of the metal centres using radical bridges or organometallic complexes. This methodology can provide a tool for future design of SMMs leading to potential applications in high-tech devices if the blocking temperatures could be increased towards room temperature or even liquid nitrogen temperature.

While dinuclear Dy^{III}-based SMMs have featured prominently in this thesis as a model system to study fundamental features of the magnetic properties and to attempt to derive magneto-structural relationships that will simplify the design of novel SMMs with high energy barriers, there remained a problem of relatively low barriers as well as the use of expensive metals with very complex electronic structures. If these complexes were to be applicable as memory-storage devices or in quantum computing, we must look towards cheaper metals and smaller molecular units. Additionally, we require a system with fewer electrons in the ground state in order to model tunnelling behaviours and slow relaxation mechanisms. It is well-known that Dy^{III}-based mononuclear systems show significant quantum tunnelling at zero-field, hence no SMM behaviour can be observed without the application of a dc field. Furthermore, the electronics of the lanthanides render them extremely difficult to model as there are large numbers of ground state multiplets to consider. Therefore, we decided to delve back into the first-row transition metals and study mononuclear complexes of specifically cobalt(II) which is one of the most anisotropic metal ions in that series. The second part of this thesis will focus on Co^{II}-based mononuclear complexes which offer large magnetic anisotropy with unique magnetic behaviour that can be comparable to lanthanides, as well as much cheaper metal precursors.

4.5 Experimental

4.5.1 General Considerations

All materials were used as received from Aldrich or Strem Chemicals, without further purification. All reactions were performed under ambient conditions.

IR Spectroscopy and Elemental Analysis:

Infrared analyses were performed with a Nicolet 6700 FT-IR spectrometer equipped with an ATR in the 4000−600 cm^{-1} range. Elemental analyses were performed at the Canadian Microanalytical Service Ltd.

X-ray Diffraction Analysis:

A single rectangular crystal of each complex, suitable for X-ray diffraction measurements, was mounted on a glass fibre. Unit cell measurements and intensity data collections were performed on a Bruker-AXS SMART 1 k CCD diffractometer using graphite monochromated MoKα radiation (λ = 0.71073 Å). The data reduction included a correction for Lorentz and polarisation effects, with an applied multi-scan absorption correction (SADABS). The crystal structure was solved and refined using the SHELXTL program suite. Direct methods yielded all non-hydrogen atoms which were refined with anisotropic thermal parameters. All hydrogen atom positions were calculated geometrically and were riding on their respective atoms.

Magnetism:

The magnetic susceptibility measurements were obtained using a Quantum Design SQUID magnetometer MPMS-XL7 in the temperature range of 1.8 – 300 K for dc-applied fields ranging from –7 to 7 T. Dc analyses were performed on polycrystalline samples of 8.5, 13.4, 13.6, 19.8 and 13.6 mg for **IV-1**, **IV-2**, **IV-3**, **IV-4** and **IV-5**, respectively, wrapped in a polyethylene wrap and under a field ranging from 0 to 7 T in the temperature range of 1.8 – 300 K. Ac susceptibility measurements were carried out under an oscillating ac field of 3 Oe and ac frequencies ranging from 1 to 1500 Hz. In order to check for ferromagnetic

impurities, the magnetisation data were collected at 100 K. No impurities were detected in any of the measured samples. A diamagnetic correction was applied for the sample holder and the grease which was used to restrain the microcrystals preventing torqueing under high fields.

Computational Details:

All calculations were carried out with MOLCAS 7.8 and are of CASSCF/RASSI/SINGLE_ANISO type. All $\{Dy_2\}$ complexes have an inversion center, which is why only one magnetic center is calculated. Each dysprosium center was calculated keeping the experimentally determined structure of the corresponding complex while replacing the neighboring Dy^{III} ion by diamagnetic Lu. Two basis set approximations have been employed: Basis 1 – small, and Basis 2 – large. Table 1 shows the contractions of the employed basis sets for all elements.

Table 4.6: Contractions of the employed basis sets in computational approximations Basis 1 and Basis 2.

Basis 1	**Basis 2**
Dy.ANO-RCC...7s6p4d2f1g.	Dy.ANO-RCC...8s7p5d3f2g1h.
Lu.ANO-RCC...7s6p4d2f.	Lu.ANO-RCC...7s6p4d2f.
N.ANO-RCC...3s2p.	N.ANO-RCC...3s2p1d. (close)
O.ANO-RCC...3s2p.	N.ANO-RCC...3s2p. (distant)
C.ANO-RCC...3s2p.	O.ANO-RCC...3s2p1d. (close)
H.ANO-RCC...2s.	O.ANO-RCC...3s2p. (distant)
	C.ANO-RCC...3s2p.
	H.ANO-RCC...2s.

The Cholesky decomposition threshold was set to $5 \cdot 10^{-8}$. Active space of the CASSCF method included 9 electrons in 7 orbitals (4*f* orbitals of Dy^{3+} ion). We have mixed 21 sextets, 128 quartet and 130 doublet states by spin-orbit coupling. On the basis of the resulting spin-orbital multiplets SINGLE_ANISO program computed local magnetic properties (*g*-tensors, magnetic axes, local magnetic susceptibility, etc.)

4.5.2 Synthesis and Characterisation

Syntheses of **H_2valdien** and $[Dy_2(valdien)_2(NO_3)_2]$, **III-1**.

The ligand, H_2valdien (*N1*,*N3-Bis*(3-methoxysalicylidene)diethylenetriamine), and complex **III-1** were both synthesised in accordance with previously published procedures, details of which can be found in chapter 3 (Section 3.3).[5]

Synthesis of $[Dy_2(valdien)_2(CH_3COO)_2]$, **IV-1.**

To a solution of H_2valdien (0.25 mmol, 0.092 g) and triethyamine (0.50 mmol, 70.0 µL) in 10 mL of DMF was added 10 mL of $Dy(CH_3COO)_3 \cdot H_2O$ (0.25 mmol, 0.103 g) in MeOH. The resulting reaction mixture was stirred for 1 min then filtered and the filtrate was left undisturbed in a diethylether bath. Yellow rectangular crystals were isolated after 3-4 days in ~ 60% yield. Selected IR (cm^{-1}): 3220 (m), 1642 (s), 1621 (s), 1595 (w), 1547 (m), 1440 (s), 1326 (m), 1266 (m), 1239 (m), 1217 (m), 971 (m), 918 (w), 854 (m), 739 (s), 676 (m). Anal. Calcd for $[Dy_2(valdien)_2(CH_3COO)_2]$ ($C_{44}H_{50}Dy_2N_6O_{12}$, MW = 1179.90): C, 44.79%; H, 4.28%; N, 7.12%. Found: C, 44.95%; H, 4.32%; N, 7.16%.

Synthesis of $[Dy_2(valdien)_2(ClCH_2COO)_2]$, **IV-2.**

To a solution of H_2valdien (0.25 mmol, 0.092 g) and triethyamine (0.50 mmol, 70.0 µL) in 5 mL of MeOH was added a 10 mL methanolic solution of $Dy(CF_3SO_3)_3$ (0.25 mmol, 0.152 g), triethylamine (0.75 mmol, 105.0 µL) and chloroacetic acid (0.75 mmol, 0.071 g). The resulting reaction mixture was stirred for 1 min then filtered and the filtrate was left undisturbed in a diethylether bath. Yellow rectangular crystals were isolated after 3-4 days in ~ 55% yield. Selected IR (cm^{-1}): 3210 (m), 1639 (w), 1621 (s), 1589 (s), 1467 (w), 1445 (m), 1415 (m), 1328 (m), 1243 (s), 1219 (s), 1039 (w), 970 (m), 852 (m), 775 (w), 740 (s). Anal. Calcd for $[Dy_2(valdien)_2\ (ClCH_2COO)_2]$ ($C_{44}H_{50}Cl_2Dy_2N_6O_{12}$, MW = 1250.80): C, 42.25%; H, 4.04%; N, 6.72%. Found: C, 42.38%; H, 4.03%; N, 6.69%.

Synthesis of $[Dy_2(valdien)_2(Cl_2CHCOO)_2]\cdot 0.5$ MeOH, **IV-3.**

The same procedure as **IV-2** was employed to synthesise **IV-3** with chloroacetic acid being replaced by dichloroacetic acid (0.75 mmol, 61.9 µL). Yield ~ 45%. Selected IR (cm^{-1}): 3210 (m), 1638 (w), 1610 (s), 1465 (w), 1448 (m), 1411 (m), 1323 (m), 1241 (s), 1217 (s), 1038 (w), 971 (m), 852 (m), 742 (s), 715 (m), 668 (w). Anal. Calcd for $[Dy_2(valdien)_2(Cl_2CHCOO)_2]\cdot 0.5$ MeOH ($C_{44.5}H_{50}Cl_4Dy_2N_6O_{12.5}$, MW = 1335.70): C, 40.01%; H, 3.78%; N, 6.29%. Found: C, 40.12%; H, 3.81%; N, 6.26%.

Synthesis of $[Dy_2(valdien)_2(acac)_2]\cdot 2\ CH_2Cl_2$, **IV-4.**

To a solution of H_2valdien (0.25 mmol, 0.092 g) and triethyamine (0.50 mmol, 70.0 µL) in 5 mL of methylene chloride was added 10 mL of $Dy(acac)_3\cdot H_2O$ (0.25 mmol, 0.115 g) in MeOH. The resulting reaction mixture was stirred for 1 min then filtered and the filtrate was left undisturbed in a diethylether bath. Rectangular crystals were isolated after 2-3 days in ~ 65% yield. Selected IR (cm^{-1}): 3211 (m), 1632 (s), 1598 (s), 1516 (m), 1445 (m), 1391 (m), 1329 (m), 1268 (m), 1237 (s), 1218 (s), 1088 (w), 851 (m), 765 (s), 735 (s), 696 (m), 583 (w). Anal. Calcd for $[Dy_2(valdien)_2(acac)_2]\cdot 2\ CH_2Cl_2$ ($C_{52}H_{64}Cl_4Dy_2N_6O_{12}$, MW = 1431.89): C, 43.62%; H, 4.51%; N, 5.87%. Found: C, 43.79%; H, 4.49%; N, 5.89%.

Synthesis of $[Dy_2(valdien)_2(F_6acac)_2]$, **IV-5.**

The starting material, $Dy(F_6acac)_3\cdot 3H_2O$, was synthesised according to previously published methods.[14] To a solution of H_2valdien (0.25 mmol, 0.092 g) and triethyamine (0.50 mmol, 70.0 µL) in 5 mL of MeOH was added 5 mL of $Dy(F_6acac)_3\cdot 3H_2O$ (0.25 mmol, 0.155 g) in MeOH. The resulting reaction mixture was stirred for 1 min then filtered and the filtrate was left undisturbed in a diethylether bath. Rectangular crystals were isolated after 2 days in ~ 50% yield. Selected IR (cm^{-1}): 3231 (m), 1659 (m), 1618 (s), 1549 (m), 1497 (m), 1469 (w), 1453 (s), 1328 (m), 1134 (s), 1090 (w), 1039 (w), 972 (w), 919 (w), 872 (m), 793 (m), 744 (s), 857 (m), 583 (w). Anal. Calcd for $[Dy_2(valdien)_2(F_6acac)_2]$ ($C_{50}H_{48}Dy_2F_{12}N_6O_{12}$, MW = 1477.94): C, 40.63%; H, 3.28%; N, 5.69%. Found: C, 40.51%; H, 3.32%; N, 5.72%.

References

[1] (a) L. Bogani, W. Wernsdorfer, *Nat. Mater*. 7 (2008), 179; (b) B. Pfau, S. Schaffert, L. Müller, C. Gutt, A. Al-Shemmary, F. Büttner, R. Delaunay, S. Düsterer, S. Flewett, R. Frömter, J. Geilhufe, E. Guehrs, C. M. Günther, R. Hawaldar, M. Hille, N. Jaouen, A. Kobs, K. Li, J. Mohanty, H. Redlin, W. F. Schlotter, D. Stickler, R. Treusch, B. Vodungbo, M. Kläui, H. P. Oepen, J. Lüning, G. Grübel, S. Eisebitt, *Nat. Commun*. 3 (2012), 1100; (c) A. R. Rocha, V. M. García-suárez, S. W. Bailey, C. J. Lambert, J. Ferrer, S. Sanvito, *Nat. Mater*. 4 (2005), 335.

[2] (a) F. Neese, D. A. Pantazis, *Faraday Discuss*. 148 (2011), 229; (b) R. Sessoli, A. K. Powell, *Coord. Chem. Rev*. 253 (2009), 2328; (c) F. Habib, M. Murugesu, *Chem. Soc. Rev*. 42 (2013), 3278; (d) N. Ishikawa, M. Sugita, T. Ishikawa, S.-y. Koshihara, Y. Kaizu, *J. Am. Chem. Soc*. 125 (2003), 8694; (e) L. Sorace, C. Benelli, D. Gatteschi, *Chem. Soc. Rev*. 40 (2011), 3092; (f) D. N. Woodruff, R. E. P. Winpenny, R. A. Layfield, *Chem. Soc. Rev*. 113 (2013), 5110.

[3] (a) J. D. Rinehart, J. R. Long, *Chem. Sci*. 2 (2011), 2078; (b) K. Bernot, J. Luzon, L. Bogani, M. Etienne, C. Sangregorio, M. Shanmugam, A. Caneschi, R. Sessoli, D. Gatteschi, *J. Am. Chem. Soc*. 131 (2009), 5573; (c) L. Ungur, L. F. Chibotaru, *Phys. Chem. Chem. Phys*. 13 (2011), 20086.

[4] (a) P.-H. Lin, T. J. Burchell, L. Ungur, L. F. Chibotaru, Wernsdorfer, W.; Murugesu, M. *Angew. Chem., Int. Ed*. 48 (2009), 9489; (b) A. Watanabe, A. Yamashita, M. Nakano, T. Yamamura, T. Kajiwara, *Chem. Eur. J.* 117 (2011), 7428; (c) J. D. Rinehart, M. Fang, W. J. Evans, J. R. Long, *J. Am. Chem. Soc*. 133 (2011), 14236; (d) J. D. Rinehart, M. Fang, W. J. Evans, J. R. Long, *Nat. Chem*. 3 (2011), 538; (e) F. Tuna, C. A. Smith, M. Bodensteiner, L. Ungur, L.F. Chibotaru, E. J. L. McInnes, R. E. P. Winpenny, D. Collison, R. A. Layfield, *Angew. Chem., Int. Ed*. 51 (2012), 6976; (f) R. J. Blagg, F. Tuna, E. J. L. McInnes, R. E. P. Winpenny, *Chem. Commun*. 47 (2011), 10587.

[5] (a) J. Long, F. Habib, P.-H. Lin, I. Korobkov, G. Enright, L. Ungur, W. Wernsdorfer, L. F. Chibotaru, M. Murugesu, *J. Am. Chem. Soc.* 133 (2011), 5319; (b) F. Habib, P.-H. Lin, J. Long, I. Korobkov, W. Wernsdorfer, M. Murugesu, *J. Am. Chem. Soc.* 133 (2011), 8830.

[6] (a) G. Cucinotta, M. Perfetti, J. Luzon, M. Etienne, P.-E. Car, A. Caneschi, G. Calvez, K. Bernot, R. Sessoli, *Angew. Chem. Int. Ed.* 51 (2012), 1606; (b) M. J. Martínez-

Pérez, S. Cardona-Serra, C. Schlegel, F. Moro, P. J. Alonso, H. Prima-García, J. M. Clemente-Juan, M. Evangelisti, A. Gaita-Ariño, J. Sesé, J. van Slageren, E. Coronado, F. Luis, *Phys. Rev. Lett*. 108 (2012), 247213; (c) F. Habib, J. Long, P.-H. Lin, I. Korobkov, L. Ungur, W. Wernsdorfer, L. F. Chibotaru, M. Murugesu, *Chem. Sci*. 3 (2012), 2158; (d) U. J. Williams, B. D. Mahoney, P. T. DeGregorio, P. J. Carroll, E. Nakamaru-Ogiso, J. M. Kikkawa, E. J. Schelter, *Chem Comuun.* 48 (2012), 5593.

[7] S. K. Langley, N. F. Chilton, B. Moubaraki, K. S. Murray, *Chem. Commun*. 49 (2013), 6965.

[8] (a) L. F. Chibotaru, L. Ungur, *J. Chem. Phys*. 137 (2012), 064112; (b) F. Aquilante, L. De Vico, N. Ferre, G. Ghigo, P.-A. Malmqvist, P. Neograd y, T. B. Pedersen, M. Pitonak, M. Reiher, B. O. Roos, L. Serrano-Andres, M. Urban, V. Veryazov, R. Lindh, *J. Comput. Chem.* 31 (2010), 224.

[9] (a) E. K. Brechin, *Chem. Commun*. (2005), 5141; (b) A. Ferguson, J. Lawrence, A. Parkin, J. Sanchez-Benitez, K. V. Kamenev, E. K. Brechin, W. Wernsdorfer, S. Hill, M. Murrie, *Dalton Trans*. (2008), 6409.

[10] Y.-N. Guo, G.-F. Xu, P. Gamez, L. Zhao, S.-Y. Lin, R. Deng, J. Tang, H.-J. Zhang, *J. Am. Chem. Soc*. 132 (2010), 8538.

[11] (a) K. S. Cole, R. H. Cole, *J. Chem. Soc*. 9 (1941), 341; (b) S. M. J. Aubin, Z. Sun, L. Pardi, J. Krzystek, K. Folting, L. J. Brunel, A. L. Rheingold, G. Christou, D. N. Hendrickson, *Inorg. Chem*. 38 (1999), 5329.

[12] M. Seitz, A. G. Oliver, K. N. Raymond, *J. Am. Chem. Soc*. 129 (2007), 11153.

[13] A. Trzesowska, R. Kruszynski, T. J. Bartczak, *Acta Cryst*. B60 (2004), 174.

[14] M. F. Richardson, W. F. Wagner, D. E. Sands, *J. Inorg, Nucl. Chem*. 30 (1968), 1275.

Chapter 5

Mononuclear Cobalt(II)-Terpyridine Single-Molecule Magnets

One hundred years ago Alfred Werner won the Nobel Prize in chemistry for his pioneering work with inorganic coordination compounds, which was mainly attributed to his work on mononuclear cobalt complexes.[1] Although this chemistry has been well developed, in recent years it continues to reveal new and interesting magnetic properties derived from the molecular geometry of these complexes.[2] Indeed since the discovery of magnet-like behaviour in a mononuclear transition metal complex,[3] a sudden re-emergence of interest occurred in first-row transition metal molecules acting as molecular magnets.[4] This is mainly due to the fact that these model mononuclear complexes can unravel the origin of magnetic anisotropy due to their unquenched first-order orbital angular momentum.[4,5] When large uniaxial anisotropy (D) is coupled with the intrinsic spin (S) of a molecule, an anisotropic energy barrier ($U = S^2|D|$) for the reversal of the magnetisation can be seen.[6] Such molecules are termed Single-Molecule Magnets (SMMs).[4,7,8] To compensate for low spin values in 3*d* ions, highly anisotropic metal ions such $Fe^{I/II/III}$ or Co^{II} are used.[4,6c] When investigating highly anisotropic ions, the aforementioned equation for the energy barrier is no longer accurate. The D parameter becomes the most important parameter, and in fact decreases when S is increased.

In addition to SMM properties, *3d* complexes can exhibit Spin Crossover (SCO) behaviour.[9] For $3d^4$–$3d^7$ metal ions, High Spin (HS)-Low Spin (LS) crossover can occur if the ligand field is tuned such that a balance between strong and weak field ligands is achieved.[10] Strong field terpyridine (terpy) ligands can be ideal for isolating such systems. With this in mind we have carefully studied three related compounds based on the Co^{II}-terpy system where we fine-tune the ligand field by controlling the number of coordinated terpy ligands as well as the remaining terminal ligands leading to unique magnetic properties of SMM and SCO behaviour. In this chapter, the inherent physical properties of [Co(terpy)Cl_2],

V-1, [Co(terpy)$(NCS)_2$], **V-2**, and [Co$(terpy)_2$]$(NCS)_2 \cdot 1.5H_2O$, **V-3**, will be investigated through structural, spectroscopic, computational and magnetic studies. One of the main features of this work is the rare dynamic magnetic properties observed for **V-1** and **V-2** as well as the vast theoretical calculations we performed to corroborate the experimentally observed electronic and magnetic behaviour leading to its publication in Angewandte Chemie International Edition (*Angew. Chem. Int. Ed.* 52 (2013), 11290 – 11293).

5.1 Mononuclear Cobalt(II)-Terpyridine Complexes

The synthetic details for all complexes are described in Section 5.5. In **V-1**, the Co^{II} ion adopts C_s symmetry and is elevated in respect to the plane formed by three N atoms of the terpy ligand (N1–N3) yielding a distorted square-based pyramid (Fig. 5.1a).[11] The packing diagrams along the *a*- and *b*-axes show antiparallel packing of Co^{II} units (Fig. 5.2a) with the closest intermolecular distance between terpy centroids of 3.79 Å leading to π-π stacking. In complex **V-2**,[12] the Co^{II} coordination shifts towards trigonal bipyramidal with the metal ion now located within the plane formed by the terpy ligand (Fig. 5.1b).

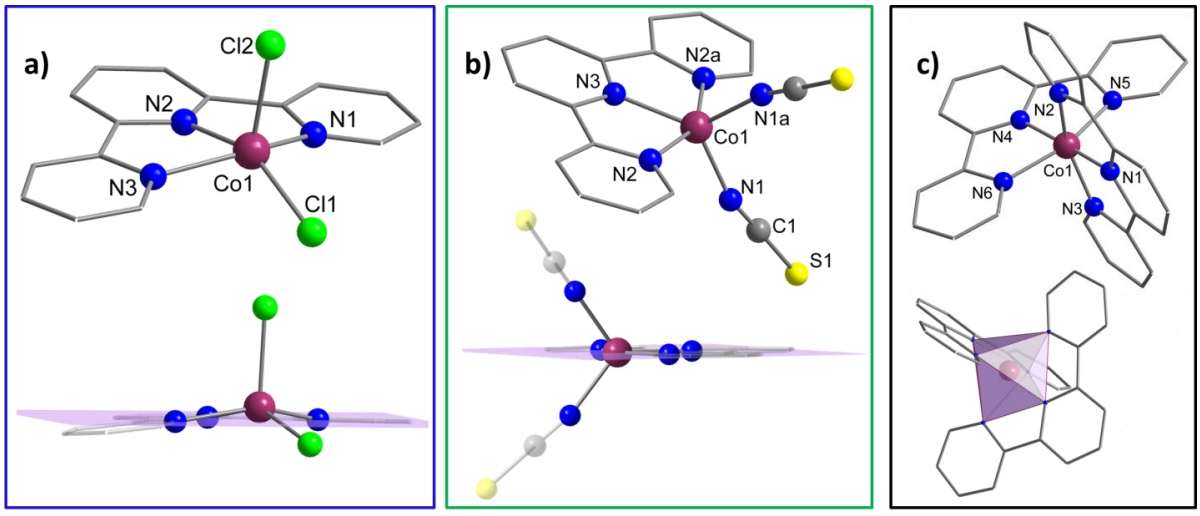

Figure 5.1: Molecular structures of [Co(terpy)Cl_2], **V-1** (a), [Co(terpy)$(NCS)_2$], **V-2** (b) and [Co$(terpy)_2$]$^{2+}$, **V-3** (c). Colour code: Maroon (Co), Blue (N), Grey (C), Green (Cl), Yellow (S). Hydrogen atoms, counter ions and solvent molecules have been omitted for clarity. The plane formed by three N atoms of the terpy ligand (**V-1** and **V-2**) as well as the polyhedron around the Co^{II} ion (**V-3**) are shown in purple (bottom row).

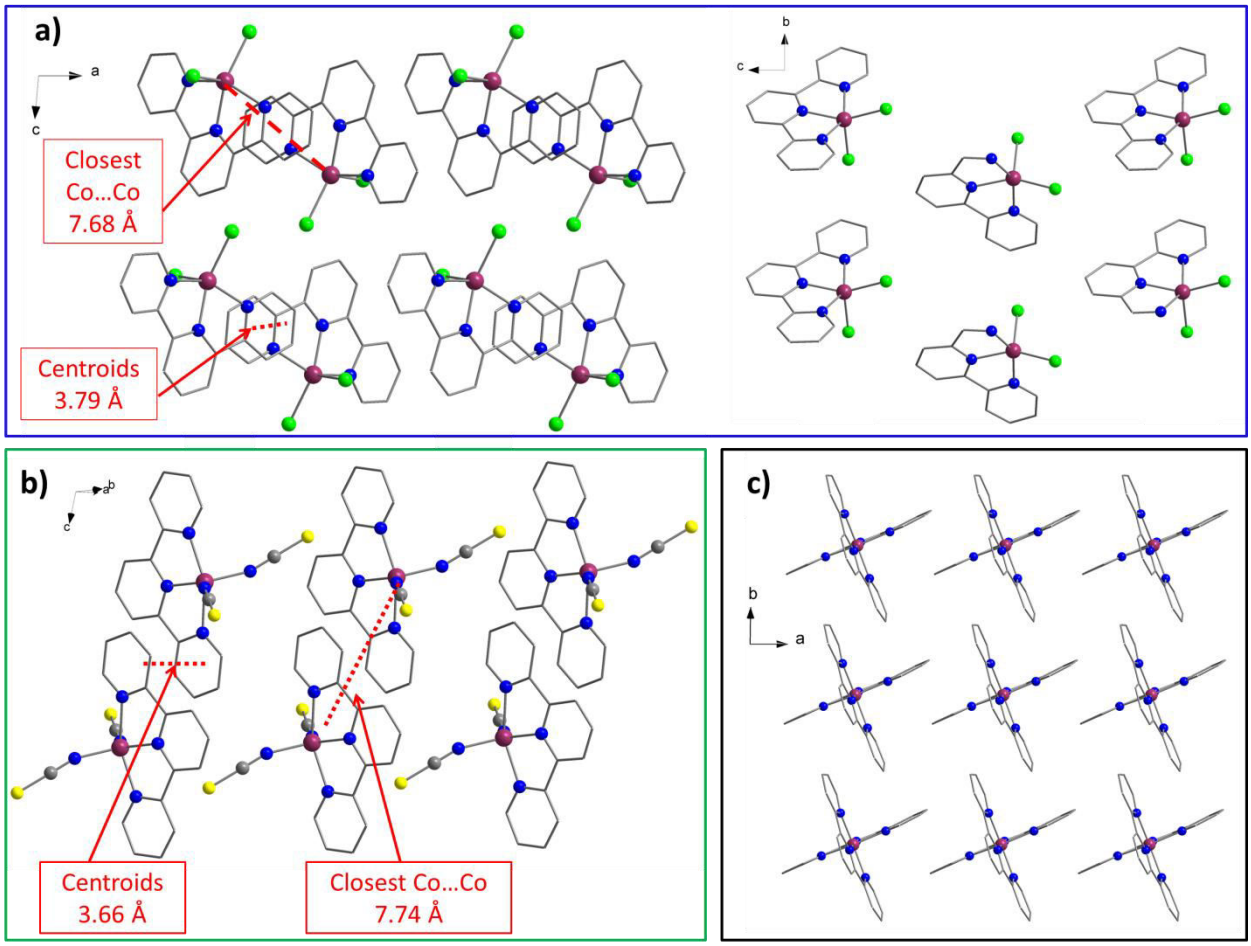

Figure 5.2: Packing arrangements of complex **V-1** along the crystallographic *b*- and *a*- axes (a), **V-2** (b) and **V-3** along the crystallographic *c* axis (c). Intermolecular metal-metal and centroid-centroid distances are indicated in red.

The packing diagram (Fig. 5.2b) indicates parallel alignment of the Co^{II} units with a distance of 3.66 Å between the centroids of the terpy ligands. These solid state interactions are strong enough to induce a change in the Co^{II} geometry which adopts C_{2v} as opposed to C_s symmetry. In **V-3**, the 6-coordinate, bis-terpy complex adopts a distorted octahedral geometry (Fig. 5.1c) and packs in a similar fashion to **V-1** (Fig. 5.2c) with an intermolecular terpy centroid distance of 3.70 Å. Unlike the weak field chloride ligands in complex **V-1**, nitrogen-containing ligands of **V-2** and **V-3** are known to have stronger fields which will have significant implications on the electronic distribution and in turn the magnetic properties of these complexes.

5.2 Electronic Properties

To probe further the electronic properties of all complexes, density functional theory (DFT) calculations were performed. For complex **V-1**, geometry optimisation resulted in a structure with C_s symmetry that is in close agreement with the X-ray data. The high-spin (HS) state (S = 3/2) with A" symmetry is the ground state of the complex. The electronic and Gibbs free energies of the lowest doublet state with C_s symmetry (^2A') for complex **V-1** are 8.8 kcal/mol and 11.0 kcal/mol, respectively. Each of four spin-quartet electronic states of a C_{2v} symmetric structure corresponds to a transition state, not an energy minimum. The lowest energy state among them is the $^4B_1$ state with ΔE = 4.2 kcal/mol and ΔG_{298K} = 5.8 kcal/mol. Each of four spin-doublet electronic states of a C_{2v} symmetric structure is also a transition state with a higher energy than the ^2A' state.

Similar to **V-1**, geometry optimisation of the quartet state of **V-2** also resulted in a structure with C_s symmetry (with the ^4A" state being the lowest in energy). Of the four different quartet states of the structure with C_{2v} symmetry, the $^4A_1$ state is the energy minimum with ΔE = 69.1 kcal/mol and the other three states are transition states (with ΔE of 6.6 kcal/mol, 2.8 kcal/mol and 5.7 kcal/mol for $^4A_2$, $^4B_1$, $^4B_2$, respectively, relative to the lowest energy structure with C_s symmetry). Thus, the change of the coordination environment around the Co^{II} ion from asymmetric (C_s symmetry) in solution to symmetric (C_{2v} symmetry) in the solid state is likely due to the intermolecular interactions and/or the crystal packing forces which can stabilise the more symmetric C_{2V} structure in the solid state. The electronic and Gibbs free energies of the lowest-energy doublet state of **V-2** (with C_s symmetry) are 5.9 kcal/mol and 8.1 kcal/mol, respectively. The natural population analysis (NPA)-derived charges of the Co atom in structures **V-1** and **V-2** (0.90 a.u. and 1.02 a.u., respectively) and the Mayer bond orders for the Co-X bonds (0.60 for Co-Cl bonds in **V-1** and 0.51-0.53 for Co-N_{NCS} bonds in **V-2**) indicate more metal-ligand covalency in **V-1** due to the fact that chlorides are both σ- and π-donor ligands. Time-dependent DFT (TD-DFT) calculations were performed (at the same level of theory as geometry optimisations) to obtain energies of excited electronic states of the complexes which are shown in the diagram below (Fig. 5.3). The HS state for complexes **V-1** and **V-2** can be attributed to the low coordination number for Co^{II} and the relatively small difference in energy between the highest d_π orbital and d_z^2 due to distorted square-based pyramid geometry. For **V-3**, the orbital splitting diagram shows the three d_π orbitals close in energy and well-separated from the two d_σ orbitals resulting in a LS complex with S = 1/2. This LS ground state is due to the change in coordination number/geometry as well as the influence of the two strong-field terpy ligands.

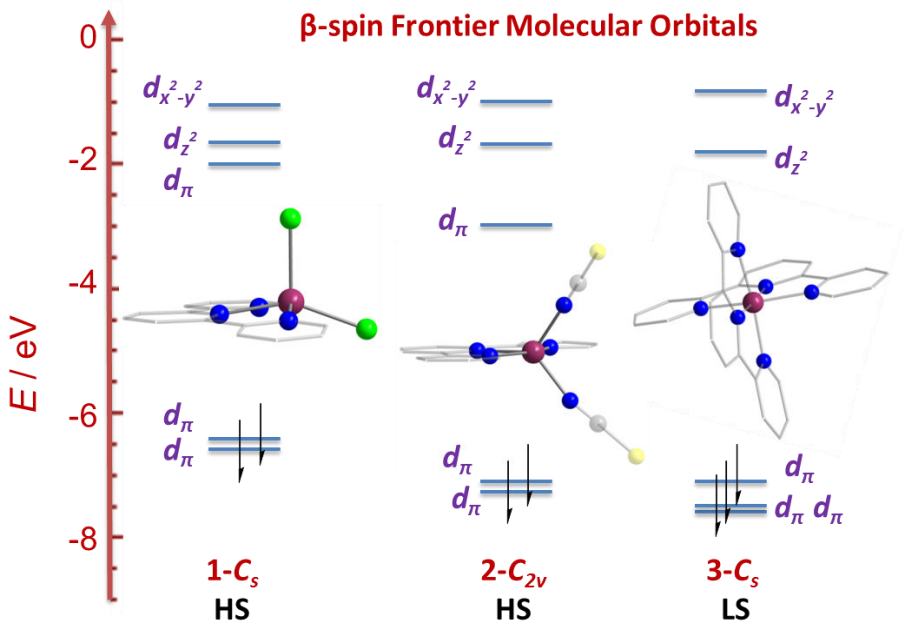

Figure 5.3: Energy level diagram depicting selected β-spin frontier molecular orbitals of **V-1** (C_s symmetry), **V-2** (C_{2v} symmetry) and **V-3** (C_s symmetry). The increase in the number of β-spins for **V-3** comes at the cost of an α-spin, resulting in an overall decrease in the molecular spin state.

5.3 Magnetic Properties

One of the main, intriguing features of these complexes is their magnetic properties. Prior research in this field had not recognised that slow relaxation of the magnetisation can occur even in simple mononuclear complexes due to relatively large magnetic anisotropy originating from the metal centre. In fact, larger clusters only result in lower overall magneto-anisotropy, hence mononuclear complexes represent the first-row transition metals with, theoretically, the largest anisotropy values. A discussion of the aforementioned magnetic properties unique to these complexes follows. Additionally, other techniques such as high-frequency EPR measurements as well as theoretical *ab initio* calculations have been performed in order to corroborate the experimentally observed behaviour.

5.3.1 High-Spin *vs.* Low-Spin Complexes

In the χT *vs. T* plot of the direct current (dc) magnetic susceptibility measurements, (Fig. 5.4) the high temperature values are 3.34 $cm^3.K.mol^{-1}$ (300 K) for **V-1**, 2.66 $cm^3.K.mol^{-1}$ (300 K) for **V-2** and 1.39 $cm^3.K.mol^{-1}$ (350 K) for **V-3**. For **V-1** and **V-2**, the χT products and curve shapes are consistent with observations for other mononuclear high spin Co^{II} complexes with significant anisotropy.[13,14] For **V-3**, the χT curve indicates SCO behaviour where the Co^{II} ions show a HS-LS crossover that is completed at approximately 90 K. This change occurs gradually and begins at a temperature higher than 350 K. The low spin value of 0.31 $cm^3.K.mol^{-1}$ at 1.8 K agrees with the theoretical value of 0.375 $cm^3.K.mol^{-1}$ for a LS Co^{II} ion where $S = 1/2$ and $g = 2$. Fits to magnetic data (Fig. 5.4) using *ab initio* calculations (based on CASSCF/CASPT2/RASSI/SINGLE_ ANISO, see below for further details, Section 5.3.3) indicate a relatively large intermolecular exchange interaction for **V-1**, $zJ' = -0.15$ cm^{-1}, supporting the existence of π-π stacking in the crystal lattice (Fig. 5.2a). For **V-2**, the data could be fit without including an intermolecular interaction ($zJ' = 0$ cm^{-1}).

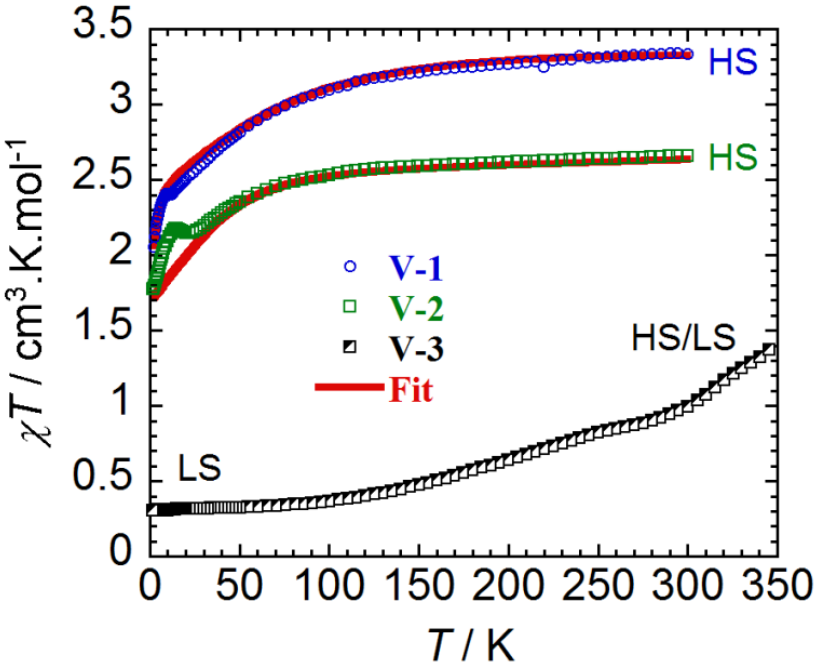

Figure 5.4: Temperature dependence of the magnetic susceptibility for complexes **V-1** – **3** in a χT *vs. T* plot at 1000 Oe. Red lines indicate the fits within the Basis1_CASPT2 approximation where $zJ' = -0.15$ and 0 cm^{-1} for **V-1** and **V-2**, respectively.

The magnetisation plots, *M vs. H* and *M vs. HT*$^{-1}$, show non-saturation and non-superposition, respectively, of the curves at different temperatures indicating the presence of significant anisotropy in **V-1** and **V-2** (Fig. 5.5a). Moreover, those for **V-3** (Fig. 5.5b) show superposition of the curves as well as saturation at high applied fields confirming the absence of magnetic anisotropy which is expected for an isotropic low-spin Co^{II} complex we observe at low temperature. The SCO behaviour in **V-3** is a result of the added terpy ligand replacing the halogen anionic ligands. The resultant change in the coordination geometry and the strong ligand-field render the LS state accessible and more favoured at low temperature.

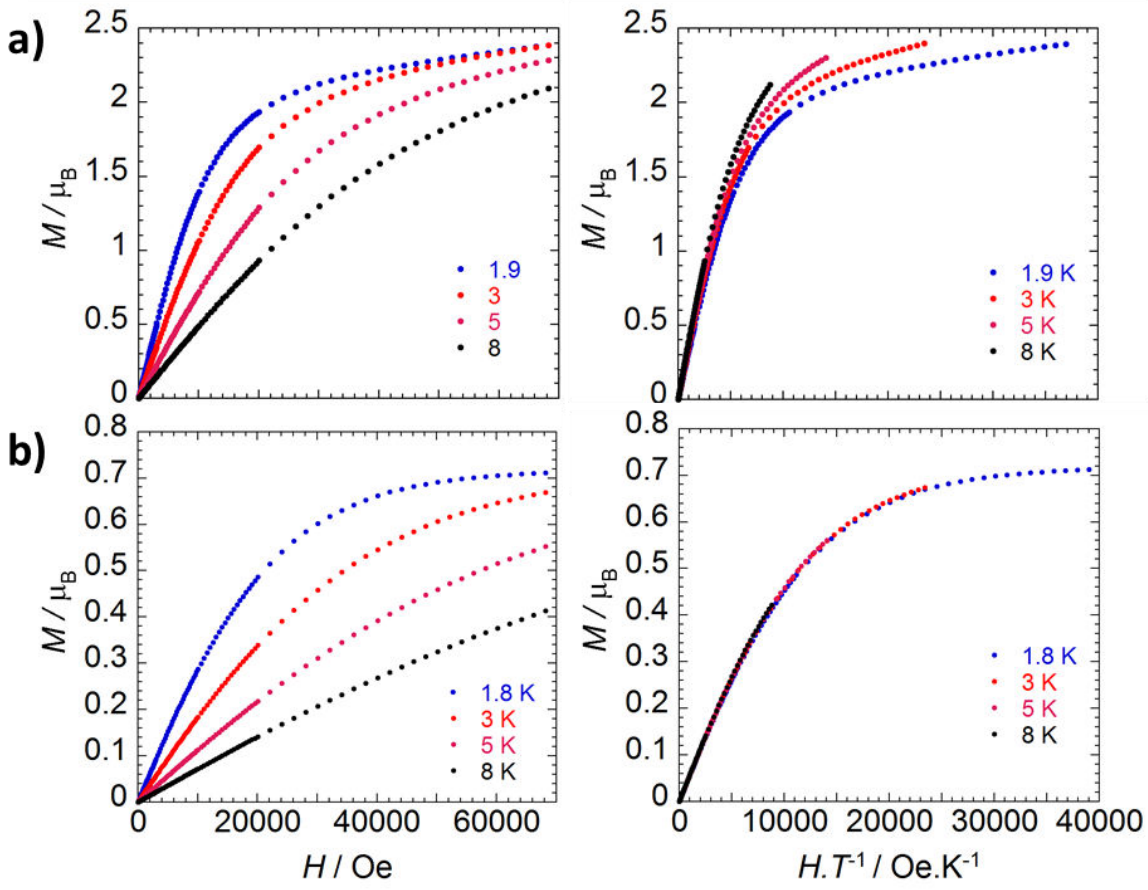

Figure 5.5: Magnetisation (*M*) as a function of field (*H*) plotted as *M vs. H* and *M vs. HT*$^{-1}$ for complexes **V-1** and **V-2** (a) as well as **V-3** (b) at the indicated temperatures.

5.3.2 Rare Slow Magnetic Relaxation Behaviour

Frequency dependence of the out-of-phase magnetic susceptibility, χ'', for **V-1** was measured under applied dc fields of 0 – 8.6 kOe (Fig. 5.6a). As the applied field is increased, one relaxation pathway begins to appear at approximately 10 Hz and increases in intensity until 1.6 kOe shifting slightly to higher frequencies. After 1.6 kOe, the intensity of the peak begins to decrease gradually with higher applied fields while a second relaxation pathway appears between 0.1 and 1 Hz starting at an applied 1.2 kOe field. It appears initially as a shoulder then reaches a full peak as the applied field increases before decreasing in intensity. The occurrence of two relaxation pathways for this system is rather puzzling. As Co^{II} ions have significant anisotropy and a non-zero spin value, SMM behaviour can generally be expected (albeit under an applied field) with a single relaxation process. However, due to large magnetic anisotropy, it is expected that M_s will no longer be sufficient in describing the spin states of the Co^{II} ion, rather M_J will be more accurate to describe the spin-orbital states. When considering M_J (M_J states for a Co^{II} ion are ±9/2, ±7/2, ±5/2, ±3/2 and ±1/2) it is possible to rationalise more than one relaxation pathway for this system, mainly through what is known as thermally assisted relaxation. Thermally assisted relaxation involves tunnelling through the energy barrier for spin reversal at higher states than the ground state without fully overcoming the barrier height. When this occurs at the ground state level, it is known as quantum tunnelling of the magnetisation which has been discussed at length throughout this thesis. At higher states than the ground state, slow relaxation will be observed, however the barrier height will be significantly shorter than the theoretically calculated barrier.

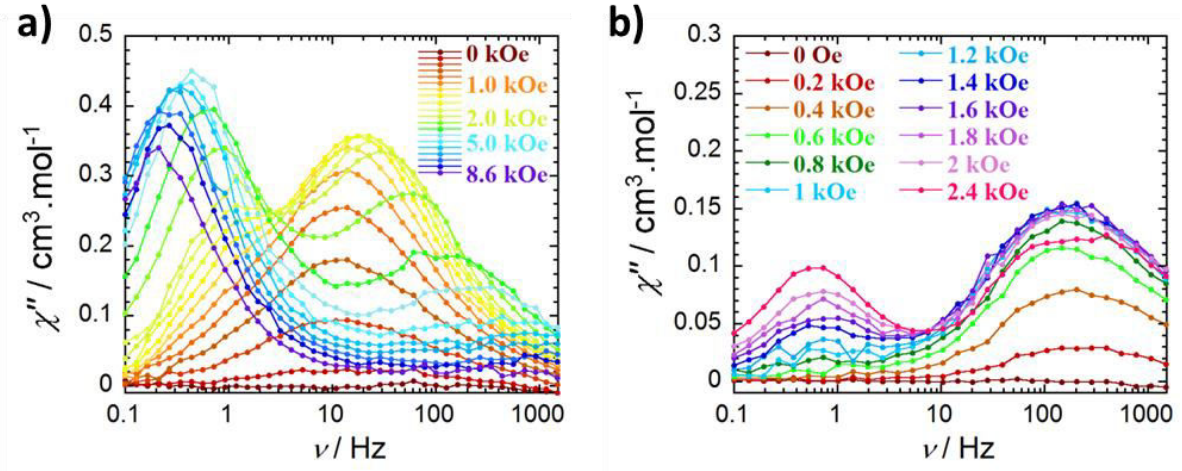

Figure 5.6: Frequency (ν) dependence of the out-of-phase magnetic susceptibility (χ'') at 2 K for complexes **V-1** (left) and **V-2** (right) under the indicated applied fields.

The same measurement was also performed for **V-2** with similar behaviour in the χ'' *vs.* ν plot (Fig. 5.6b). The two relaxation pathways are observed and they begin to appear at different applied fields, however in the case of **V-2**, the two processes are well isolated with relatively no overlap. It is noteworthy that that measurement was only carried out until 2.4 kOe in order to compare the trend of the curves to **V-1**. In order to accurately compare the two complexes, we must keep the applied field consistent in the ac measurements and hence the optimum fields for **V-1** were calculated and used for the χ'' *vs.* ν analysis at different temperature (*vide infra*). The question that inevitably arises when analysing Fig 5.6 is: Could there be an intermolecular process that is dominant at low frequency and high field? It is unclear from the data whether the second process is intrinsic to the Co^{II} ions within the molecular unit (different relaxations from different M_J states) or if there is slow relaxation due to intermolecular communication between molecules within the crystal lattice. The latter cannot be ignored since π- π interactions can be observed in the packing diagrams in Fig. 5.2 and intermolecular interaction of $zJ' = -0.15$ cm^{-1} was obtained when fitting the χT *vs.* T curve for **V-1** (Fig. 5.4). The fact that an intermolecular interaction was used when modelling the χT curve indicates potential relaxation processes influenced by intermolecular communication between Co^{II} ions.

One strategy to differentiate between intra- and intermolecular processes is through magnetic dilution with a diamagnetic ion such as Zn^{II}. In order for this to be feasible, an analogous complex must be synthesised using Zn^{II} and varying degrees of magnetic dilution can be carried out. If the relaxation process was seen to depend on the level of dilution in the sample, it is a clear indication of an intermolecular process. Alternatively, if the relaxation process remains unchanged, we can safely conclude it is intramolecular in nature. Unfortunately, we could not synthesise an analogous complex with Zn^{II} and hence could not perform magnetic dilution studies for this system. Another strategy to make such a differentiation involves performing the ac magnetic measurements on a frozen solution of the complex. For this technique, we require a solvent which dissolves the complex sufficiently while preserving the integrity of the molecular unit. The premise behind frozen solution measurements is that molecules will be well-isolated in solution and hence any intermolecular interactions observed within the crystal lattice will be eliminated. Theoretically, only relaxation processes intrinsic to Co^{II} ions within the molecule will be observed. For this system, solution measurements were not possible as the five-coordinate $[Co(terpy)X_2]$ complex (**V-1** or **V-2**) interconverts in solution to the six-coordinate $[Co(terpy)_2]^{2+}$ complex (**V-3**). Additionally, a non-coordinating solvent could not be found that dissolves the complexes sufficiently without decomposition. When performing solution

measurements with low concentrations the obtained ac data will be extremely noisy and a barrier could not be calculated.

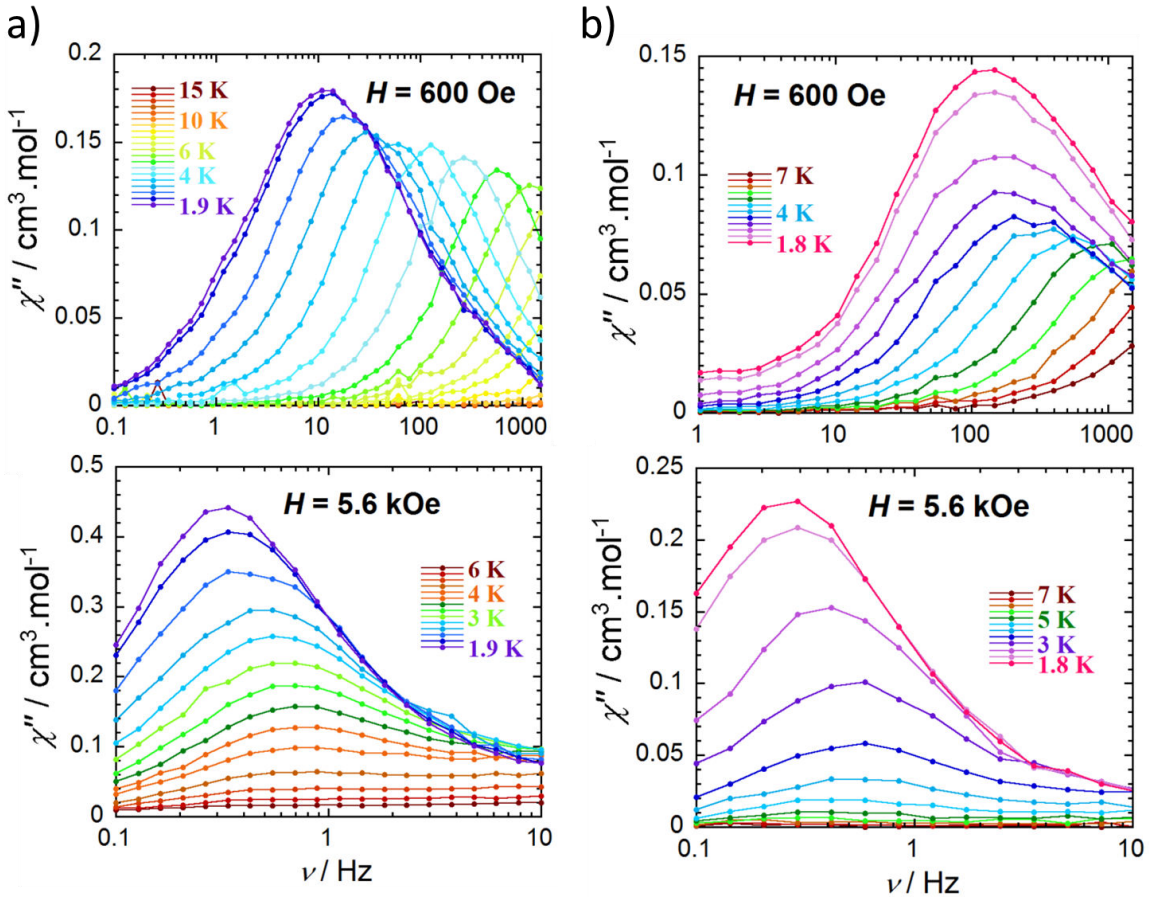

Figure 5.7: Frequency (ν) dependence of the out-of-phase magnetic susceptibility, χ'', at the indicated applied fields (H) and temperature ranges for **V-1** (a) and **V-2** (b).

Under applied fields of 600 Oe and 5.6 kOe (where only one relaxation pathway is clearly dominant while the other is supressed) the χ'' *vs.* ν plots for **V-1** reveal clear temperature dependent peaks down to 1.9 K (Figure 5.7a). This is indicative of field-induced SMM behaviour with multiple relaxation pathways which is rather common in lanthanide systems but remains rare in mononuclear transition metal SMMs.[4h,15] The absence of a peak at H = 0 is characteristic of quantum tunnelling of the magnetisation (QTM) which is suppressed when a longitudinal field is applied. The anisotropy barriers (obtained by fitting this data using the Arrhenius law, $\tau = \tau_0 \exp(U_{\text{eff}}/k\text{T})$ were calculated to be U_{eff} = 28 K (τ_0 = 1.07×10^{-6} s) and 4 K (τ_0 = 7.44×10^{-2} s) for the fast and slow relaxation processes, respectively (Fig. 5.8a). It is noteworthy that the two relaxation processes can be classified as

a "faster" process and a "slower" process. This is not to be confused with the "slow relaxation" observed in a complex leading to SMM behaviour. A slow relaxing metal complex is an SMM and can have a slower and a faster process in the ac plot. In fact, the faster process is what we call the thermal relaxation process and yields the thermal relaxation barrier while the slower process is the quantum tunnelling process and leads to a much lower barrier, often only a few Kelvin. The Cole-Cole plots for both processes yield an average α value of 0.20 and 0.11, respectively, indicating a fairly narrow width of relaxation times but with clear overlap of two or more relaxation processes. Recall, in order to conclude that one relaxation mode is operative, the α value must be lower than 0.1. Similar dynamic behaviour is observed in **V-2** (Fig. 5.7b) under the same applied dc fields as **V-1** with energy barriers for spin reversal of U_{eff} = 17 K ($\tau_0 = 5.85 \times 10^{-6}$ s) and 3 K (τ_0 = 0.11 s) for the fast and slow relaxation processes, respectively (Fig. 5.8b).

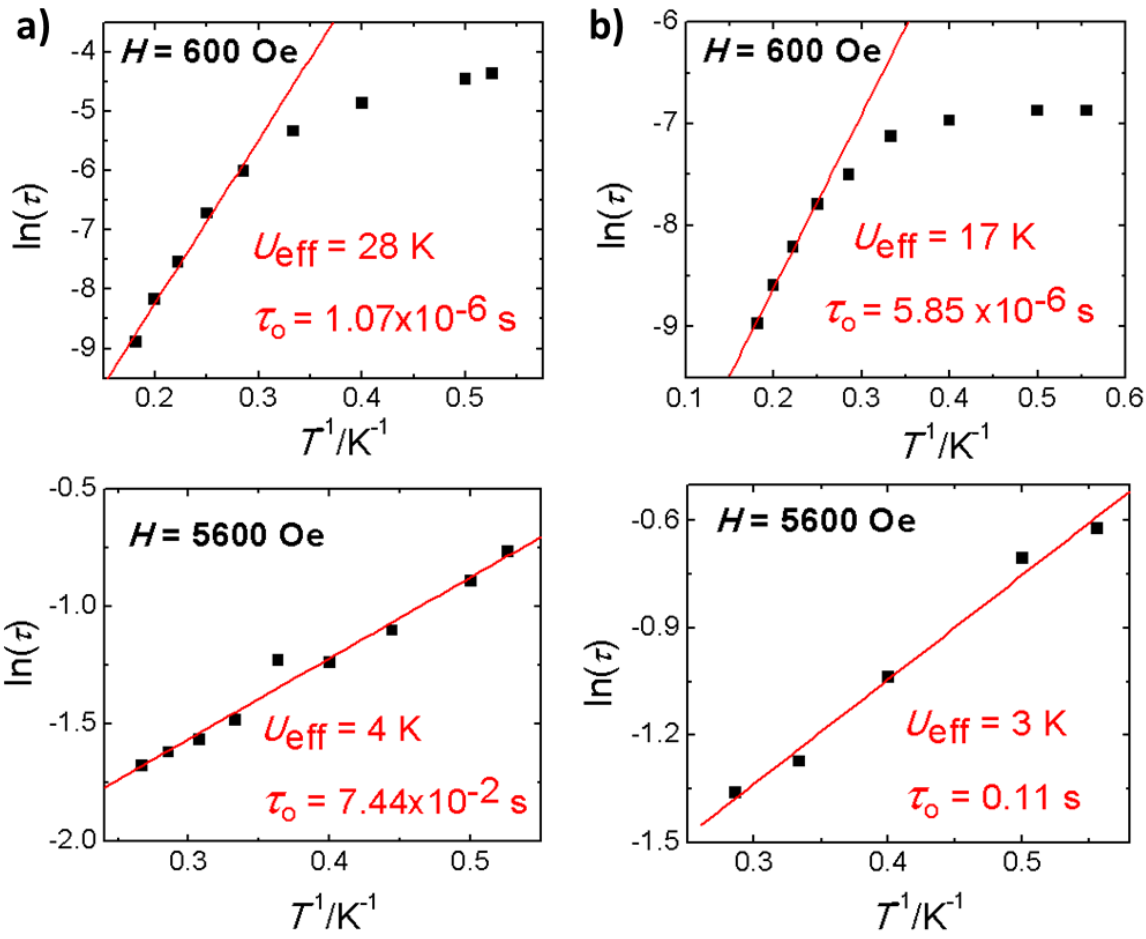

Figure 5.8: Linear fits of the relaxation processes at 600 Oe (faster process) and 5600 Oe (slower process) in **V-1** (a) and **V-2** (b) using the Arrhenius law yielding the indicated U_{eff} values and pre-exponential factors (τ_o).

Due to the absence of magnetic anisotropy (Fig. 5.5b) which was confirmed in the *M vs.* HT^{-1} plot since all iso-temperature curves were overlapping, as well as small spin in the LS state, no slow relaxation dynamics were observed for complex **V-3**.

5.3.3 Why the Difference in Energy Barrier Height? *Ab initio* Calculations

A surprising outcome of the DFT calculations for **V-1** and **V-2** is the large splitting between the lowest pair of occupied β-spin states and the next unoccupied levels, suggesting weak spin-orbit mixing with excited states and, hence, relatively weak anisotropy. However, making such inferences about excited states on the basis of DFT can be misleading. Hence, *ab initio* calculations, based on CASSCF/CASPT2/RASSI/SINGLE_ ANISO,[16] were performed for **V-1** and **V-2** (Table 5.1). These indicate strong mixing of the two lowest spin quartets by spin-orbit coupling in the 1st order of perturbation theory, leading to a large zero-field-splitting of the lowest Kramers doublets (~200 cm^{-1} for **V-1** and ~100 cm^{-1} for **V-2**, Table 5.1), which become quite anisotropic. The transverse components of the *g* factor for **V-1** are still relatively large, ~1.2–1.5, providing a possible explanation for $H = 0$ QTM *via* internal transverse dipolar fields. For **V-2**, higher transverse components of the *g* factor (~1.7–3.0) are calculated, yielding a less anisotropic Co^{II} ion.

Table 5.1: Energies of the low-lying Kramers doublets as well as the main components of the *g* tensor for the lowest Kramers doublet in **V-1** and **V-2**.

	V-1	**V-2**
Spin-orbit energies, cm^{-1}		
	0	0
	199	98
	539	1787
	791	2216
	1984	2615
	2038	2885
	3793	4014
	3905	4089
Main values of the *g*-tensor in the ground KD		
g_x	1.1806	1.7220
g_y	1.4678	3.0149
g_z	8.7755	6.4814

With a lower energy first excited Kramers doublet and less magnetic anisotropy of the ground state Kramers doublet, complex **V-2** will potentially exhibit a lower energy barrier for spin reversal than **V-1**. This is in accordance with the experimentally observed barriers discussed earlier (Fig. 5.8). The calculated anisotropy axis lies close to the Co-Cl1 bond (Fig. 5.9) since the ligand field exhibits higher axial character than in other directions. The large energy of the first excited Kramers doublet (*ca.* 200 cm^{-1}, Table 5.1) shows that it cannot be associated with either barrier inferred from the ac measurements, indicating direct type relaxation [17] where τ depends strongly on the applied dc field.

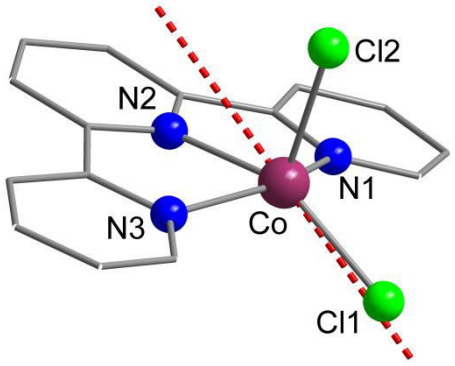

Figure 5.9: Orientation of the main magnetic axis in the ground state doublet of the [Co(terpy)Cl_2] complex.

5.3.4 High-Frequency Electron Paramagnetic Resonance Measurements

In order to obtain further information concerning the spin ground states and magnetic anisotropy of **V-1** and **V-3**, high-frequency (HF) powder EPR measurements were performed. HF-EPR measurements performed on **V-1** and **V-3** are shown in Figure 3. The 158.4 GHz spectra obtained for **V-1** (Fig. 5.10a) span an extremely broad field range, indicating significant magnetic anisotropy. In contrast, the 168 GHz spectrum for **V-3** (Fig. 5.10b) spans a narrow range, corresponding to g values of 2.03–2.19 for S = 1/2, *i.e.* relatively weak anisotropy. The first set of spectra obtained for **V-1** (*Exp.* 1 in Fig. 5.10) are complicated by the appearance of multiple fine structures, all of which display frequency and temperature dependence consistent with an anisotropic ground state Kramers doublet. The three main components, labelled x, y and z, have similar intensities and widths, and their respective shapes (peak→shoulder→dip) suggest that they correspond to the three components of an effective g-tensor of a single species, as confirmed by the effective spin S'

= 1/2 simulation (*Sim.* 1), yielding $g_{eff,x} = 1.35$, $g_{eff,y} = 1.93$ and $g_{eff,z} = 7.75$. The weaker features marked by green arrows are found to dominate the spectrum obtained several months later (*Exp.* 2), suggesting that the sample might have converted to an octahedral complex by coordinating to water molecules; the original *x*, *y* and *z* components are barely discernible (grey arrows). Regardless of these anomalies, the large spread in effective *g*-values in the pristine sample can only be explained on the basis of excitations within the lowest Kramers doublet associated with a HS $S = 3/2$ Co^{II} species. Moreover, the fact that two of the *g*-values are below 2.00 and the third close to 8.00 suggests that the magnetic anisotropy is of the easy-axis type, as predicted from the *ab initio* studies.

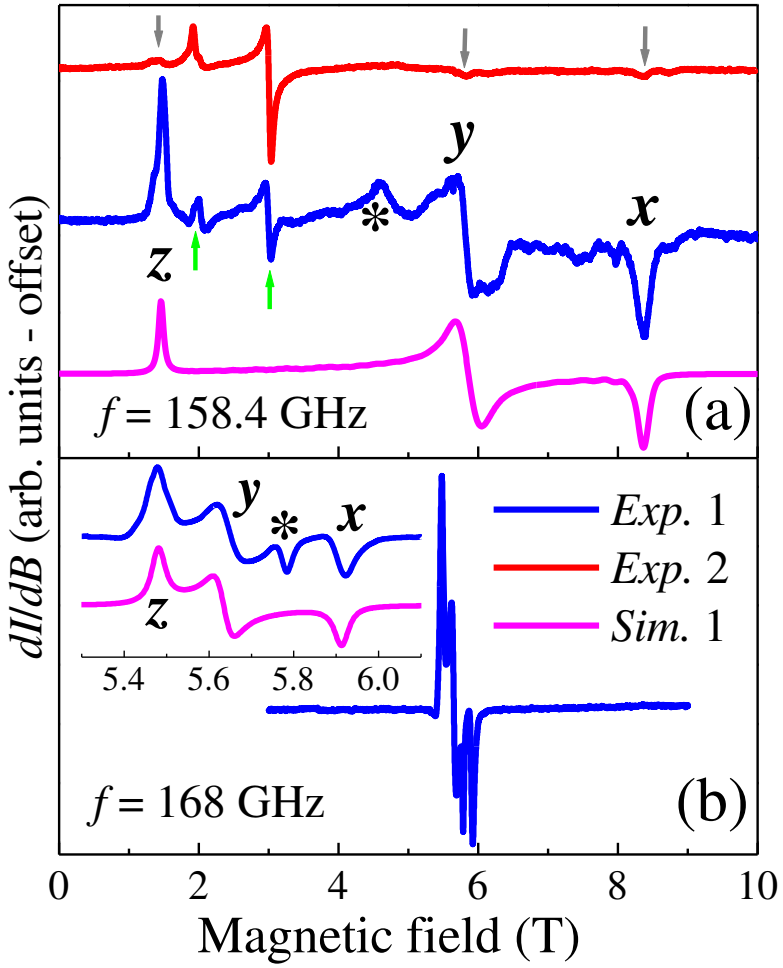

Figure 5.10: Powder EPR spectra and simulations for complexes **V-1** (a) and **V-3** (b); *Exp.* 1 was performed at 2.5 K; *Exp.* 2 was performed several months later on the same powder pellet, at 20 K. Inset: Expanded view of the spectra. Simulations were performed using EasySpin.[18]

As already noted, the EPR spectra for **V-3** (Fig. 5.10b) display very little anisotropy, with $g_x = 2.03$, $g_y = 2.13$ and $g_z = 2.19$. An additional peak is again observed (marked by an asterisk) which is not reproduced in the simulation. However, this does not affect the conclusion that there exists no plausible circumstances whereby such a spectrum could be attributed to high-spin ($S = 3/2$) Co^{II}: the main peaks labelled *x*, *y* and *z* can only be due to orbitally non-degenerate LS Co^{II}, with a low-spin $S = 1/2$ ground state. Moreover, the relatively weak anisotropy further suggests that the ground state is well separated from excited orbital states. This is consistent with the stronger field terpyridine ligands as well as the distorted O_h geometry further supporting the orbital splitting diagrams discussed above (Fig. 5.3).

5.4 Conclusions

The most important parameter for SMM behaviour has been identified recently as the anisotropy value in the complex. While larger clusters were originally targeted in order to yield larger global anisotropy, this approach has been largely abandoned since the higher the metal centre count in the cluster (essentially the spin value), the lower the overall anisotropy observed. This inverse relationship between spin and anisotropy has been the catalyst for the shift towards mononuclear complexes when designing high barrier SMMs. Theoretically, a single metal centre should exhibit the highest magneto-anisotropy in a mononuclear complex without interaction with other metal ions. Moreover, the large quantum tunnelling effects observed at zero field for lanthanides as well as a significantly more complex electronic structure has led us away from the 4*f* metal ions and towards the first-row transition metal series (3*d* metals) as potential SMMs. Metal ions such as $Fe^{I/II/III}$ and Co^{II} have been shown to possess very large anisotropy values when coupled with the optimal ligand field and geometry.

The chemistry developed long ago by Werner continues to unveil exciting new phenomena such as those that were shown using three Co^{II} complexes with varying ligand fields and geometry. Complexes **V-1** and **V-2** exhibit a rare phenomenon in mononuclear transition metal SMMs of magnetisation relaxation through multiple pathways. When the Cl^- ligands in **V-1** were exchanged for NCS^- ligands in **V-2**, the energy barrier decreased significantly. In **V-3**, it disappeared as the LS state became accessible at low temperature due to changes in coordination number and geometry, resulting in a SCO complex. The lack of magnetic anisotropy in the LS state precludes slow magnetisation relaxation and, by extension, SMM behaviour. Overall, the spin states as well as the magnetic properties were

studied using a combination of DFT and *ab initio* methods in order to confirm the experimentally observed properties. Through DFT, electronic structures for all complexes were calculated to shed light on the HS *vs*. LS phenomenon that differentiates all three complexes. Furthermore, *ab initio* calculation were utilised to calculate intermolecular magnetic exchange interactions, energies of spin-orbit states as well as the degree of anisotropy in the ground state Kramers doublets. By tuning the ligand field strength around the metal ion as well as its geometry, it becomes possible to control the physical properties, a feat that has been consistently pursued since before the days of Werner.

One of the main highlights of this work is the unique and rare multiple relaxation processes observed in the ac plots under different fields (Fig. 5.6). While this is not quite rare for cluster complexes, it had not been observed and studied in detail for mononuclear compounds at the time. In order to further probe the mechanisms involved in such behaviour, we require a system that can undergo frozen solution magnetic measurements and/or magnetic dilution measurements, both of which are not feasible for the $[Co(terpy)X_2]$ complexes. The lack of stability in solution (inter-conversion between five-coordinate $[Co(terpy)X_2]$ and six-coordinate $[Co(terpy)_2]^{2+}$ complexes) and the synthetic complications when attempting to synthesise the diamagnetic Zn^{II} analogue for magnetic dilution studies led us to search for a different system entirely. Fortunately, we came across a seven-coordinate mononuclear Co^{II} complex with similar out-of-phase magnetic behaviour; two relaxation processes that were field dependent. Although not completely stable in solution, we were able to synthesise the diamagnetic analogue and were able to carry out the magnetic dilution studies. The results will be discussed in the following chapter.

5.5 Experimental

5.5.1 General Considerations

All reagents were received from commercial sources and used without further purification unless otherwise specified. Solvents were dried by passage through a column of activated alumina followed by storage under dinitrogen.

X-Ray Crystallography:

Low-temperature diffraction data (ω-scans) were collected on a Rigaku SCXmini diffractometer coupled to a Mercury275R CCD detector with Mo $K\alpha$ radiation (λ = 0.71075 Å) for the structure of Co(terpy)Cl_2, on a Rigaku R-AXIS RAPID diffractometer coupled to a R-AXIS RAPID imaging plate detector with Mo $K\alpha$ radiation (λ = 0.71075 Å) for the structure of Co(terpy)$(NCS)_2$. All structures were solved by direct methods using SHELXS [19] and refined against F^2 on all data by full-matrix least squares with SHELXL-97 [20] using established refinement techniques.[21] All non-hydrogen atoms were refined anisotropically. All hydrogen atoms were included into the model at geometrically calculated positions and refined using a riding model. The crystal structures have been deposited at the Cambridge Crystallographic Data Centre and allocated the deposition numbers CCDC 920120 (**V-1**) and 920121 (**V-2**).

Magnetism:

The magnetic susceptibility measurements were obtained with the use of a Quantum Design SQUID magnetometer MPMS-XL7 operating between 1.8 and 400 K for dc applied fields ranging from –7 to 7 T. Measurements were performed on ground polycrystalline samples of 19.3 mg for **V-1**, 26.9 mg for **V-2** and 15.5 mg for **V-3**. The magnetic data were corrected from the sample holder and the diamagnetic contributions. Before measurements were carried out, the samples were checked for the presence of ferromagnetic impurities by measuring the magnetisation as a function of the field at 100 K. For pure paramagnetic or diamagnetic systems, a perfect straight line is expected and is indeed observed for these compounds, indicating the absence of any ferromagnetic impurities.

High-Frequency EPR Studies:

Powder EPR measurements were conducted at the US High Magnetic Field Laboratory in Tallahassee, FL. Data were collected at temperatures between 2.5 and 30 K in the EMR facility using a transmission probe and a 17 T superconducting magnet. High-frequency microwaves (50 – 430 GHz) were generated using a phase-locked solid-state oscillator followed by a chain of multipliers.[22] Experiments were performed on finely ground powders of **V-1** and **V-3** pressed into KBr pellets in order to prevent alignment of crystallites in the applied field.

DFT Calculations:

Density Functional Theory (DFT) calculations were performed for each complex. Geometry optimisation at the B3LYP/TZVP level of theory with the PCM implicit solvent treatment (CH_2Cl_2 as a solvent) was performed using the crystal structures as starting points. Harmonic frequency calculations were used to characterise the stationary points obtained during the geometry optimisation. Tight SCF convergence was used in each DFT calculation.

Other Studies:

Elemental analyses were performed by Robertson Microlit Inc. FT-ICR MS analyses were performed by the Yale Proteomics Facility at the Keck Biotechnology Research Lab. Infrared analyses were performed on a Varian 640 FT-IR spectrometer in the 600-4000 cm^{-1} range.

5.5.2 Synthesis and Characterisation

Synthesis of [Co(terpy)Cl_2], **V-1**.

Anhydrous $CoCl_2$ (50 mg, 0.39 mmol) was suspended in 10 mL THF under Ar. A solution containing terpyridine (86 mg, 0.39 mmol) in 5 mL of THF was added to the blue-grey suspension *via* cannula transfer. The suspension turned forest green upon stirring at room temperature overnight. The residual solids were removed by filtration through a pad of Celite and the green filtrate was recrystallised in 76% yield (104 mg, green prisms) from a

dichloromethane solution after standing at -20°C for two days. Formula: $C_{15}H_{11}Cl_2CoN_3$. FT ICR MS [M-Cl] Expected: 326.9968; Found: 326.9965. Elemental Analysis; Expected: C 49.62%, H 3.06%, N 11.57%; Found: C 49.43%, H 2.99%, N 11.43%

Synthesis of $[Co(terpy)(NCS)_2]$, **V-2** and $[Co(terpy)_2](NCS)_2 \cdot 1.5H_2O$, **V-3.**

$Co(NCS)_2$ (111 mg, 0.64 mmol) was suspended in 15 mL CH_2Cl_2 open to the atmosphere. A solution containing terpyridine (150 mg, 0.64 mmol) in 5 mL of CH_2Cl_2 was added *via* syringe. The brown suspension was stirred at room temperature for 8 h. The green precipitate was removed by filtration. It was recrystallised from DMF/acetone mixture (1:7) and put in an ether bath at 4°C over three days yielding complex **V-2** as dark green crystals in 55% yield. The remaining brown filtrate from the reaction was placed in a cyclohexane bath at 4°C. X-ray quality, dark red, crystals of complex **V-3** were obtained after three days in 12% yield

Formula for **V-2**: $C_{17}H_{11}CoN_5S_2$, FT ICR MS [M-Cl] Expected: 350.0030; Found: 350.0030, Elemental Analysis; Expected: C 50.00%, H 2.72% N, 17.15%; Found: C 50.39%, H 2.90%, N 16.94%

Formula for **V-3**: $C_{32}H_{25}CoN_8O_{1.50}S_2$, IR ($cm^{-1}$): 3391 br, 3056 w, 2043 s, 1797 m, 1572 w, 1467 w, 1446 s, 1244 m, 1159 m, 1012 m, 768 s, 647 m, 602 w. Elemental Analysis; Expected: C 57.48%, H 3.78% N, 16.76%; Found: C 57.31%, H 3.92%, N 17.01%

References

[1] E. C. Constable, C. E. Housecroft, *Chem. Soc. Rev*. 42 (2013), 1429.

[2] (a) F. A. Cotton, D. M. L. Goodgame, M. Goodgame, *J. Am. Chem. Soc.* 83 (1961), 4690; (b) G. E. Kostakisa, S. P. Perlepes, V. A. Blatov, D. M. Proserpio, A. K. Powell, *Coord. Chem. Rev*. 256 (2012), 1246; (c) J. L. Rodríguez-López, F. Aguilera-Granja, K. Michaelian, A. Vega, *Phys. Rev. B* 67 (2003), 174413; (d) I. A. Gass, S. Tewary, A. Nafady, N. F. Chilton, C. J. Gartshore, M. Asadi, D. W. Lupton, B. Moubaraki, A. M. Bond, J. F. Boas, S.-X. Guo, G. Rajaraman, K. S. Murray, *Inorg. Chem*. 52 (2013), 7557.

[3] (a) S. Karasawa, G. Zhou, H. Morikawa, Noboru Koga, *J. Am. Chem. Soc*. 125 (2003), 13676; (b) D. E. Freedman, W. H. Harman, T. D. Harris, G. J. Long, C. J. Chang, J. R. Long, *J. Am. Chem. Soc*. 132 (2010), 1224.

[4] (a) W. H. Harman, T. D. Harris, D. E. Freedman, H. Fong, A. Chang, J. D. Rinehart, A. Ozarowski, M. T. Sougrati, F. Grandjean, G. J. Long, J. R. Long, C. J. Chang, *J. Am. Chem. Soc*. 132 (2010), 18115; (b) T. Jurca, A. Farghal, P.-H. Lin, I. Korobkov, M. Murugesu, D. S. Richeson, *J. Am. Chem. Soc*. 133 (2011), 15814; (c) P.-H. Lin, N. C. Smythe, S. I. Gorelsky, S. Maguire, N. J. Henson, I. Korobkov, B. L. Scott, J. C. Gordon, R. T. Baker, M. Murugesu, *J. Am. Chem. Soc*. 133 (2011), 15806; (d) J. Vallejo, I. Castro, R. Ruiz-García, J. Cano, M. Julve, F. Lloret, G. De Munno, W. Wernsdorfer, E. Pardo, *J. Am. Chem. Soc*. 134 (2012), 15704; (e) S. Mossin, B. L. Tran, D. Adhikari, M. Pink, F. W. Heinemann, J. Sutter, R. K. Szilagyi, K. Meyer, D. J. Mindiola, *J. Am. Chem. Soc*. 134 (2012), 13651; (f) Y.-Y. Zhu, C. Cui, Y.-Q. Zhang, J.-H. Jia, X. Guo, C. Gao, K. Qian, S.-D. Jiang, B.-W. Wang, Z.-M. Wang, S. Gao, *Chem. Sci.* 4 (2013), 1802; (g) D. Weismann, Y. Sun, Y. Lan, G. Wolmershäuser, A. K. Powell, H. Sitzmann, *Chem. Eur. J*. 17 (2011), 4700; (h) J. M. Zadrozny, J. R. Long, *J. Am. Chem.Soc*. 133 (2011), 20732; (i) J. M. Zadrozny, J. Liu, N. A. Piro, C. J. Chang, S. Hill, J. R. Long, *Chem. Commun*. 48 (2012), 3927; (j) J. M. Zadrozny, M. Atanasov, A. M. Bryan, C.-Y. Lin, B. D. Rekken, P. P. Power, F. Neese, J. R. Long, *Chem. Sci*. 4 (2013), 125.

[5] O. Kahn, *Molecular Magnetism*; (1993), VCH-Wiley: New York.

[6] (a) L. Thomas, L. Lionti, R. Ballou, D. Gatteschi, R. Sessoli, B. Barbara, *Nature* 383 (1996), 145; (b) G. Christou, D. Gatteschi, D. N. Hendrickson, R. Sessoli, *MRS Bull.* 25 (2000), 66; (c) M. Murrie, *Chem. Soc. Rev*. 39 (2010), 1986.

[7] R. Sessoli, D. Gatteschi, A. Caneschi, M. Novak, *Nature* 365 (1993), 149.

[8] (a) M. Jeletic, P.-H. Lin, J. J. Le Roy, I. Korobkov, S. I. Gorelsky, M. Murugesu, *J. Am. Chem. Soc*. 133 (2011), 19286; (b) G.-J. Chen, Y.-N. Guo, J.-L. Tian, J. Tang, W. Gu, X. Liu, S.-P. Yan, P. Cheng, D.-Z. Liao, *Chem. Eur. J*. 18 (2012), 2484; (c) Y. Wang, X.-L. Li, T.-W. Wang, Y. Song, X.-Z. You, *Inorg. Chem*. 49 (2010), 969.

[9] P. Gütlich, H. A.Goodwin, *Top. Curr. Chem*. 233 (2004), 1.

[10] A. Bousseksou, G. Molnar, L. Salmon, W. Nicolaz, *Chem. Soc. Rev*. 40 (2011), 3313.

[11] E. Goldschmied, N. C. Stephenson, *Acta Cryst*. B26 (1970), 1867.

[12] J. S. Judge, W. A. Baker Jr. *Inorg. Chim. Acta* 1 (1967), 239.

[13] F. E. Mabbs, D. J. Machin, *Magnetism and Transition Metal Complexes*, Dover, Mineola, N.Y., 2008.

[14] F. Habib, C. Cook, I. Korobkov, M. Murugesu, *Inorg. Chim. Acta* 380 (2012), 378.

[15] (a) P.-E. Car, M. Perfetti, M. Mannini, A. Favre, A. Caneschi, R. Sessoli, *Chem. Commun*. 47 (2011), 3751; (b) J. D. Rinehart, K. R. Meihaus, J. R. Long, *J. Am. Chem. Soc*. 132 (2010), 7572; (c) S.-D. Jiang, B.-W. Wang, H.-L. Sun, Z.-M. Wang, S. Gao, *J. Am. Chem. Soc*. 133 (2011), 4730.

[16] (a) F. Aquilante, L. De Vico, N. Ferré, G. Ghigo, P.- Å. Malmqvist, P. Neogrády, T. B. Pedersen, M. Pitonák, M. Reiher, B. O. Roos, L. Serrano-Andrés, M. Urban, V. Veryazov, R. Lindh, *J. Comput. Chem.* 31 (2010), 224; (b) See MOLCAS manual http://www.molcas.org/documentation/manual/node95.html; (c) L. F. Chibotaru, L. Ungur, *J. Chem. Phys.* 137 (2012), 064112.

[17] A. Abragam, B. Bleaney, *Electron Paramagnetic Resonance of Transition Ions* (1970), Clarendon, Oxford.

[18] S. Stoll, A. Schweiger, *J. Magn. Res.* 178 (2006), 42.

[19] G. Sheldrick, *Acta Cryst. Section A*, 46 (1990), 467.

[20] G. Sheldrick, *Acta Cryst. Section A*, 64 (2008), 112.

[21] P. Müller, *Cryst. Rev.* 15 (2009), 57.

[22] A. K. Hassan, L. A. Pardi, J. Krzystek, A. Sienkiewicz, P. Goy, M. Rohrer, L. C. Brunel, *J. Magn. Res.* 142 (2000), 300.

Chapter 6

Exposing Slow Relaxation Mechanisms in Co(II) Single-Molecule Magnets

As was highlighted in the previous chapter (Chapter 5), the slow evolution of the field towards transition metal ions with high magnetic anisotropy has led to a significant number of publications on mononuclear transition metal-based Single-Molecule Magnets (SMMs). Since our previous Co^{II}-terpy complexes were not stable in solution nor could we perform magnetic dilution experiments with a diamagnetic analogue, we turned our attention to a different system. We investigated a pentagonal bipyramidal Co^{II} complex with large positive anisotropy ($D \approx +30$ cm^{-1}) which revealed field induced single-molecule magnet behaviour with $U_{eff} \approx 50$ K at 1.0 kOe. This compound belongs to a group of only a handful of complexes which exhibit this unique magnetic property while possessing easy-plane anisotropy. At high applied fields, a second relaxation process with an intermolecular nature has been exposed using magnetic dilution studies with varying percentages of the Zn^{II} analogue. The synthesis of an analogous diamagnetic complex using Zn^{II} allowed us to perform magnetic dilution studies without the need for solution measurements to isolate magnetic molecular units. The two evident relaxation modes are similar to those observed in the Co^{II}-terpy complexes in chapter 5. The disappearance of the second relaxation process at low frequency can be followed using magnetically diluted samples at 25%, 10% and 5% Co^{II} concentrations.

This work has been recently accepted to the journal Dalton Transactions where it could find its widest audience base. The importance of this work centers on the magnetic dilution technique which we believe can become a routine tool that is used to verify the molecular nature of the observed slow relaxation for mononuclear complexes. After all,

SMMs must exhibit slow relaxation that is purely molecular in origin which can now be studied using magnetic dilution as shown in the following chapter.

6.1 Introduction

Researchers have repeatedly stressed the necessity for information storage technologies which can overcome the fast-approaching limits of our current systems.[1] The search has thus far led to the active development of the field of Single-Molecule Magnetism where molecular entities have proven to be magnets exhibiting bistability and magnetic hysteresis with very long relaxation times, on the order of years at very low temperatures.[2] The recent surge in these nanomagnets, known as Single-Molecule Magnets (SMMs) [1,3] have yielded a pseudo-recipe for their design and isolation with desired properties, mainly high energy barriers for spin reversal (U) and high blocking temperatures (T_B).[4] The barrier for spin reversal has been quoted to depend exponentially on the spin of the complex (S) as well as linearly on its overall anisotropy (D for uniaxial or Ising-type and E for transverse or easy-plane anisotropy). Thus far, there have been significant advancements in the field with extremely large energy barriers being reported as well as relatively high blocking temperatures [4] (up to 15 K [4a] for a dinuclear lanthanide complex). While higher nuclearity clusters were previously pursued, it is now believed that the anisotropy of a complex is the main contribution towards a high energy barrier.[5] Moreover, as the cluster increases in size with more anisotropic metal centers, the overall anisotropy of the compound will inherently decrease as it is more difficult to align all the easy-axes in one direction. Hence, mononuclear complexes have been sought after as the simplest nanomagnets, especially those with high magnetic anisotropy such as high spin Co^{II}- or $Fe^{I/II}/^{III}$-based complexes.[4e,6]

Furthermore, recent advances in this field have led to the isolation of extremely rare complexes exhibiting slow magnetic relaxation characteristic of SMMs while possessing positive or easy-plane anisotropy (positive D values).[7] It is not well-understood how these complexes can behave as SMMs when their lowest sublevel of the spin ground state is stabilised. This behaviour has been attributed to a field-induced phonon bottleneck in a pseudotetrahedral Co^{II} complex which generates Orbach relaxation through the Ms = ±3/2 levels and an energy barrier dependent on D.[7b] Meanwhile, another example of a six-coordinate Co^{II} complex has been reported where the barrier to spin reversal is governed by the transverse anisotropy (E parameter) as opposed to D.[7a] We have chosen to focus on a seven-coordinate mononuclear Co^{II} complex $[Co(DAPBH)(NO_3)(H_2O)](NO_3)$ (**VI-1**, Fig.

6.1, DAPBH = 2,6-diacetylpyridinebis(2'-pyridylhydrazone), Scheme 6.1) with positive or easy-plane anisotropy.[8] This coordination number is known to result in large magnetic anisotropy due to the axiality of the resulting pentagonal bipyramidal geometry.[9] Furthermore, complex **VI-1** exhibits interesting out-of phase magnetic behaviour at high applied fields, the origin of which remains relatively unknown. In order to investigate this rare relaxation process observed only at high applied fields we have employed systematic magnetic dilution using the diamagnetic Zn^{II} analogue in 25, 10 and 5% Co samples. This methodology has already proven successful in our study of the magnetic exchange interaction between Dy^{III} ions in a dinuclear complex $[Dy_2(valdien)_2(NO_3)_2]$ using the Y^{III} analogue (refer to Chapter 3).[10], Hence, this strategy will allow us to elucidate the origin of the observed relaxation process at high fields by exposing its nature as intramolecular (intrinsic to the Co^{II} ion in the mononuclear complex) or intermolecular where Co^{II} ions in the lattice begin to interact magnetically.

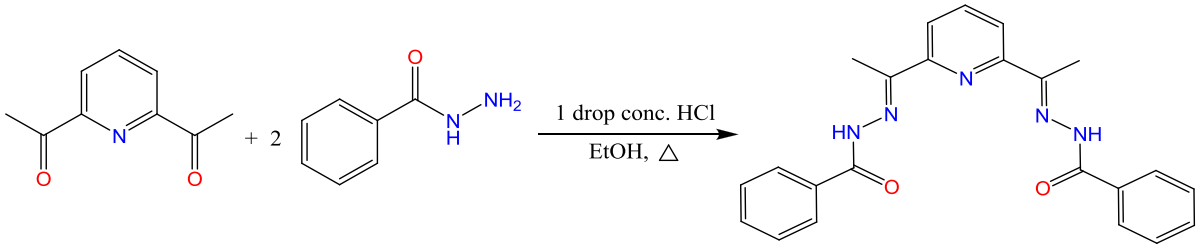

Scheme 6.1: Reaction scheme for the ligand 2,6-diacetylpyridinebis(2'-pyridylhydrazone) (DAPBH).

The magnetic anisotropy of the Co^{II} ion in **VI-1** has been examined extensively by Guihéry, Mallah and co-workers [8b] using magnetisation measurements, high-field high-frequency EPR measurements as well as *ab initio* calculations. This elegant study focused on the main origins of the large positive zero-field splitting parameter ($D \approx +30$ cm^{-1}) in this Co^{II} complex compared with the Ni^{II} analogue. The authors determined it was a result of the positive contributions arising from interactions of the excited states (two quartets and one doublet) with the ground state. All important contributions to the D parameter are shown to stabilise the Ms = ±1/2 component as opposed to the Ms = ±3/2 component of the S = 3/2 ground state. This essentially yields easy-plane anisotropy where the magnetisation is in the plane of the DAPBH ligand perpendicular to the axial H_2O and NO_3^- ligands (Fig. 6.1a). These studies will be further discussed in the magnetic properties section of this chapter (Section 6.3) since they provided the basis and inspiration for our dynamic magnetic studies highlighted herein.

6.2 Structural Characteristics

The previously reported complex, **VI-1**, is synthesised through the reaction of $Co(NO_3)_2$ and DAPBH in ethanol and H_2O.[8] For more detailed synthetic procedures refer to section 6.6.2. It crystallises in the monoclinic space group *P*-2_1/n and consists of a seven-coordinate Co^{II} ion in an N_3O_4 coordination environment. It exhibits pseudo pentagonal bipyramidal geometry with the DAPBH ligand occupying the pentagonal plane while one nitrate anion and one water molecule occupy the axial positions (Fig. 6.1a). There is one nitrate counter ion in the structure which forms a hydrogen bond with H of the coordinated water molecule. The Zn^{II} analogue, **VI-2**, is shown in Fig. 6.1b and is identical to complex **VI-1**. All magnetically diluted samples used in this study (25%, 10% and 5% Co^{II}) are also analogous to the parent **VI-1** complex indicating the successful co-crystallisation of the two complexes; **VI-1** and **VI-2** (confirmed using powder XRD experiments as well as single crystal unit cell measurements). This is extremely important since performing magnetic dilution studies requires a complex which will crystallise in the same fashion as the parent compound, regardless of the metal centre present.

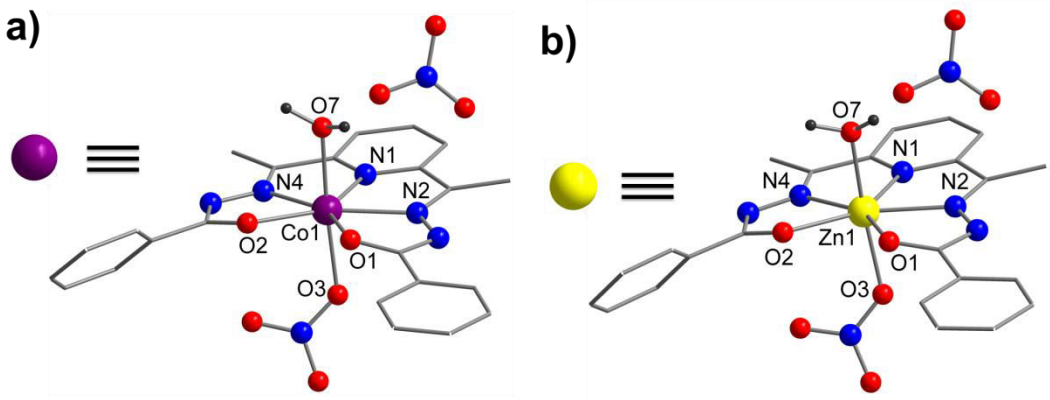

Figure 6.1: Molecular structures of $[Co(DAPBH)(NO_3)(H_2O)](NO_3)$ (**VI-1**, a) and analogous complex $[Zn(DAPBH)(NO_3)(H_2O)](NO_3)$ (**VI-2**, b). Hydrogen atoms on DAPBH are omitted for clarity. Colour code: Purple (Co), yellow (Zn), blue (N), red (O), grey (C), black (H).

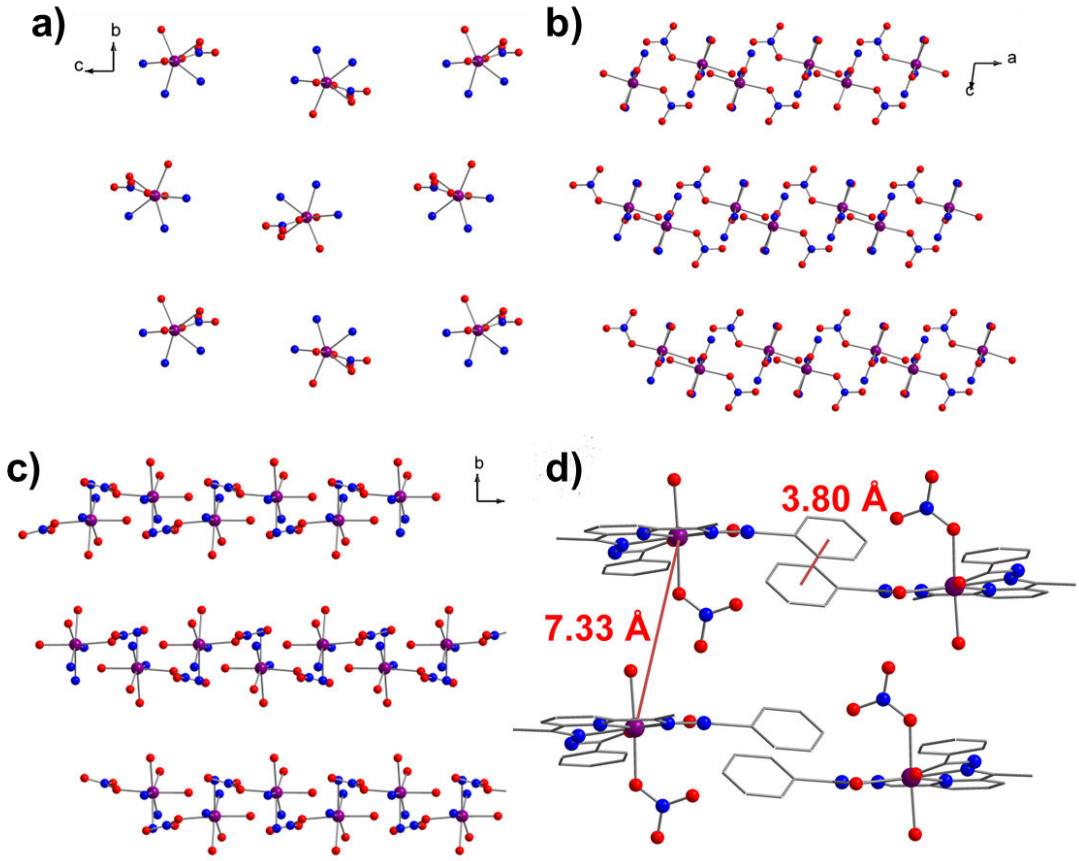

Figure 6.2: Packing diagrams of **VI-1** along the *a*- (a), *b*- (b) and *c*-axes (c). Only the atoms directly coordinated to Co(II) centers, as well as the coordinated NO_3^- molecule are shown for clarity. Counter ions are omitted. d) Intermolecular distances are shown between Co^{II} centers as well as between phenyl rings indicating π…π interactions. Colour code: Purple (Co), yellow (Zn), blue (N), red (O), grey (C), black (H).

When investigating the effects of the metal centre percentage within the crystal lattice on the dynamic magnetic properties, we will need to eliminate all other possible differences in the structures. We can only change one variable at a time to obtain accurate and reliable data. If the complexes were not analogous and we observed a difference in the magnetic properties, it would be extremely difficult to attribute that difference to the metal centre percentage or to minute changes in the structures. Additionally, if the Co^{II} and Zn^{II} complexes were not analogous, we could not obtain co-crystallisation where both Zn and Co units are randomised non-discriminately in the crystal. Instead, we might obtain separate crystals of the Zn^{II} and Co^{II} complexes within the same reaction vial. The packing diagrams of the Co^{II} units are shown in Fig. 6.2 along the *a*-, *b*- and *c*-axes with the closest Co^{II}…Co^{II}

distance being 7.33 Å. The molecular units are arranged in layers where the phenyl rings of the DAPBH ligands overlap within each layer with a distance of 3.80 Å indicating π…π interactions (Fig. 6.2d). From the packing diagram along the *a*-axis, it is clear that the units are well-isolated in two of the three directions (along the *b*- and *c*-axes). While in the direction along the *a*-axis, the units are oriented in an antiparallel fashion and are relatively close with overlapping phenyl rings from adjacent ligand molecules. The π…π interactions observed along the *a*-axis will become important when we investigate the magnetic properties of these complexes; they provide a pathway for magnetic interaction between the mononuclear complexes. In other words, the units are no longer completely isolated and the magnetic behaviour will reflect the "dinuclear-like" nature of the units. The molecular structure of the Zn^{II} analogue, **VI-2**, is identical to **VI-1** with the same packing diagrams observed along each of the three axes.

6.3 Direct Current Magnetic Properties

An elegant and detailed study of the dc properties of **VI-1** and its Ni^{II} analogue has been recently published by T. Mallah and co-workers [8b] focusing mainly on the origins and the nature of the observed magnetic anisotropy. This study was conducted using a combination of both experimental measurements (magnetisation measurements as well as high-field, high-frequency EPR or HF-HFEPR) and *ab initio* calculations. Their results highlight a fundamental difference in the magnetic anisotropy or zero-field splitting parameter (*D*) between the Co^{II} and Ni^{II} complexes and that is the sign of *D*. Since this mononuclear complex is seven-coordinate with a close-to-axial symmetry and a non-degenerate ground state, the magnetic anisotropy mainly results from the spin-orbit coupling (SOC) between the ground and excited electronic states. The role of these interactions is to lift the degeneracy of the $2S + 1$ *M*s components of the ground state yielding the zero-field splitting (ZFS). Hence, there is a direct relationship between SOC and ZFS observed in a complex. In order to maximise *D*, we must maximise the SOC through decreasing the energy difference between the ground and electronic states. The smaller energy gap will lead to greater interactions and, by extension, to higher *D* values and potentially higher effective energy barriers for spin reversal. While spin-spin interactions can and do exist, they are far less relevant than spin-orbit coupling and so were not considered.

6.3.1 Modelling Magnetic Data

The temperature dependence of the magnetic susceptibility data obtained using a SQUID magnetometer was fitted to the spin Hamiltonian: $\mathbf{H} = \mu_B \cdot \mathbf{g}_{iso} \cdot \mathbf{B} \cdot \mathbf{S} + D[\mathbf{S}_z^2 - \mathbf{S}(\mathbf{S}+1)/3] + E[\mathbf{S}_x^2 - \mathbf{S}_y^2]$ where D and E correspond to the axial (or easy-axis) and rhombic (or easy-plane) anisotropy parameters, respectively.[8b] The best fit for the Co^{II} complex was obtained with the following parameters: $D = +31.0$ cm^{-1}, $E/D = 0$, and $g_{iso} = 2.22$. The fit yielded a positive D value which indicates easy-plane anisotropy, as opposed to the negative, easy-axis type presumed a requirement for the existence of an energy barrier for spin reversal. Using HF-HFEPR, the authors were unable to confidently match the experimentally obtained values using a spin $S = 3/2$ system since the D value is too large. They were able to reproduce the $S = 1/2$ spectra with rhombic effective g matrix and obtain a lower bound only for the D value which was $|D| > 20$ cm^{-1}. Further theoretical *ab initio* studies shed some light on the origins of the observed magnetic anisotropy in the Co^{II} complex. The orbital energy diagram was calculated for the Co^{II} complex and was found to be, in order of increasing energy, (d_{yz}, d_{xz}) close in energy and fully occupied, followed by ($d_{x^2-y^2}$, d_{xy}), and finally, d_{z^2} as the highest energy orbital, all three being partially occupied. This results in an $S = 3/2$ spin system with the z-axis along the axial Co^{II}-O3/O7 bonds. Studying the interactions of the ground state with the excited states (two quartets and one doublet) is necessary in order to determine the nature of the interactions which explain the sign of the D value. The authors observed positive contributions to D from the excited states with stabilisation of the Ms = ±1/2 components of the $S = 3/2$ ground state.

While previous reports have disregarded this complex as a potential SMM due to its positive anisotropy,[8b] recent publications of SMMs with positive D values have inspired us to perform a thorough ac magnetic study of this complex. We believe it is an appropriate system in which to study such a novel phenomenon as it is quite rare with only a handful of articles published on SMMs with easy-plane anisotropy.[7] Additionally, it is not well-understood as of yet how these complexes exhibit bistability under an applied dc field. We believe this could prove to be a fruitful branch to the field where this type of anisotropy could be exploited and controlled, maybe even selected for, if we could undertake a good deal of research effort to explain why and how these mononuclear complexes could exhibit SMM behaviour.

6.3.2 Positive or Easy-plane Anisotropy

The most puzzling question that arises from this work is how a complex with positive magnetic anisotropy can exhibit SMM behaviour? There have been exceptions to the generally accepted rule that SMMs require negative or uni-axial anisotropy which must be mentioned in this section. Thus far, a handful of complexes have been reported to exhibit slow magnetic relaxation and SMM behaviour while possessing positive or easy-plane magneto-anisotropy. These mononuclear complexes are all based on Co^{II}, and behave as SMMs only under an applied magnetic field. Recently, J. R. Long and co-workers reported a pseudotetradehral Co^{II} complex with D = 12.7 cm^{-1} where spin-lattice relaxation is occurring between the lowest lying Ms = ±1/2 levels, as opposed to Ms = ±3/2 seen in complexes with easy-axis or negative anisotropy.[7b] While it is difficult to explain or rationalise the observation of slow magnetic relaxation in complexes where $D > 0$, the authors suggest that a phonon bottleneck is responsible for slowing down the direct relaxation process and allowing an Orbach process to occur through the higher energy Ms = ±3/2 levels. A phonon bottleneck occurs when there is weak coupling between the spin system and the phonons and/or if there is a limited number of phonons with the appropriate frequency to allow direct spin relaxation. Additionally, the rhombic anisotropy term (E) was found to be non-zero and serves to mix the Ms = ±1/2 and Ms = ±3/2 levels of opposite sign leading to more efficient spin relaxation through excited Ms = ±3/2 levels and an energy barrier of U_{eff} = 24 cm^{-1}. A penta-coordinate Co^{II} complex was also reported to exhibit SMM properties under an applied field with two relaxation processes evident in the field-dependent ac plots.[11] This compound forms dimers through π-π stacking leading to ferromagnetic interactions between the metal centers. While large magnetic anisotropy is observed (D/hc > 150 cm^{-1} and E/hc = 11.6 cm^{-1}), blocking of the magnetisation can only be observed under an applied field.

Similarly, E. Pardo and co-workers also reported field-induced SMM behaviour for a six-coordinate Co^{II} complex, *cis*-$[Co^{II}(dmphen)_2(NCS)_2]\cdot 0.25EtOH$ (dmphen = 2,9-dimethyl-1,10-phenanthroline), with strong easy-plane or positive magneto-anisotropy (D = 98 cm^{-1} and E = 8.4 cm^{-1}).[7a] The authors suggest that the origin of the observed spin reversal barrier, calculated to be U_{eff} = 17 cm^{-1}, could be governed by the transverse anisotropy, E, in the xy plane instead of the well-accepted uniaxial D along the z axis. In a situation where $E = (D_{xx} - D_{yy})/2$, the transverse anisotropy would create a preferred axis for the spin along the x or y direction. When this occurs, the spin flip (from $+x$ to $-x$ or $+y$ to $-y$) would be governed by $D = 3D_{zz}/2$ if it occurs through the z-axis, or would be controlled by the E parameter if it occurs through the xy plane. According to the experimentally obtained D and E values for the distorted octahedral Co^{II} complex, the calculated energy barrier is found to correspond to a

spin rotation within the *xy* plane where $U_{eff} = 2E$. Hence, in this case, the observed slow magnetic relaxation is dependent on a transverse anisotropy energy barrier. Another pseudo-octahedral complex was reported to exhibit easy plane anisotropy with a spin reversal barrier of U_{eff} = 86 K which is the highest reported barrier thus far for this subclass of mononuclear SMMs based on Co^{II}.[12] A third potential source of slow relaxation and SMM behaviour in a complex exhibiting positive magneto-anisotropy was given by E. K. Brechin and co-workers.[13] The authors reported a Co^{II}-Y^{III} complex for which the above possible explanations of slow relaxation do not apply. They suggest an optical acoustic Raman process is responsible for the spin relaxation since the relaxation time for this complex can be fitted to a T^{-n} law with n = 4.5. For Raman relaxation in Kramers ions, n is expected to be 9; however, when both acoustic and optical phonons are considered lower n values can be obtained (ranging from 1–6).

A recent study by F. Luis and co-workers focused on the origins of slow magnetic relaxation in systems where the magnetic anisotropy is known to be positive or easy plane in nature.[14] The authors investigated the compound $[Co^{II}(acac)_2(H_2O)_2]$ (acac = acetylacetonate) which is highly anisotropic with D = 57 cm^{-1}. This model system was investigated in order to propose an explanation of why SMM behaviour is observed for systems with positive D, which can be consistently applied to all complexes exhibiting such properties. Thus far, there have been many different mechanisms proposed in order to explain the SMM behaviour in such systems, however, F. Luis and co-workers have been able to demonstrate that the slow magnetic relaxation, in fact, does not depend on the sign of D but rather occurs naturally from Kramers theorem. Additionally, they also propose that the magnetic field dependence observed for all complexes with positive D is due to strong electronuclear spin entanglement. Using the aforementioned Co^{II} complex with large positive D and E values, the energy barrier obtained experimentally in the presence of an applied field does not correlate well with the calculated first excitation energy. This is rather puzzling as QTM should be suppressed under an applied field and hence the barrier for spin reversal should be equivalent to the gap between the ground and first excited Kramers doublet. In is noteworthy that in order for an Orbach process to be operative, it must involve a "real" transition from one Kramers doublet to another, the gap for which was calculated to be approximately 130 cm^{-1}. At energies between 0 and 130 cm^{-1} no magnetic level exists and, thus, the obtained barrier cannot be due to an Orbach process.

As is well-known to researchers in this field, spin-lattice relaxation can theoretically occur *via* three different processes: Direct, Orbach and/or Raman pathways. In the studied Co^{II} complex, below 30 K, direct relaxation is prohibited due to the 'van Vleck cancellation' which implies that a direct transition within a Kramers doublet cannot occur. Additionally,

Orbach relaxation is unlikely to occur since the zero-field splitting is greater than the temperature, leaving only Raman processes as a possibility for spin-lattice relaxation. Yet, direct processes do occur at low temperatures and, in fact, they dominate below 3 K in this case. This can be attributed to hyperfine interactions with the $I = 7/2$ nuclear spin (for Co^{II}) generating 16 electronuclear spin states where spin relaxation can now occur through direct transitions between some of these states. Based on the arguments outlined by the authors explaining the observation of SMM behaviour in Kramers ions with positive anisotropy, another requirement emerges for the design of molecular magnets with higher energy barriers. In addition to half-integer spin and large magneto-anisotropy, molecules must have minimal hyperfine interactions in order to prevent the direct relaxation processes as well as stabilise certain states where the spin projection is well-defined.

6.4 Slow Magnetic Relaxation

6.4.1 Field Dependent Studies

Contrary to previous reports concerning the SMM properties of complexes with mainly transverse anisotropy, complex **VI-1** exhibits ac magnetic behaviour characteristic of molecular magnets under an applied static dc field. Alternating current (ac) magnetic measurements under an oscillating field of 3.78 Oe and static dc fields ranging from 0 to 8.2 kOe at 2 K revealed a frequency dependent relaxation process in the in-phase (χ', Fig. 6.3) and out-of-phase magnetic susceptibility (χ") *vs*. frequency plot (Fig. 6.4). There are two relaxation processes evident in the χ" *vs*. ν plots; processes A and B (labelled in the plots). Focusing on the χ" *vs*. ν plot for complex **VI-1** (top left corner of Fig. 6.4) we can clearly observe process A shifting to lower frequencies as the applied dc field increases, reaching the minimum of the characteristic frequency at 1.0 kOe (optimal applied field minimising QTM for this process). Upon further increasing the applied field, a shoulder begins to appear at lower frequencies starting at 2.8 kOe and increases in intensity as the applied field increases (Fig. 6.4, Process B). This second process has been relatively puzzling for researchers in the field, it has often been alluded to as a second relaxation pathway for the spin inherent to the Co^{II} ion or, in other words, an intramolecular phenomenon depending solely on the Co centre.[6a] However, the lack of frequency-dependence of this signal and its largely field-dependent nature leads us to believe it is not intrinsic to the Co^{II} ions or it must be a QTM process which is frequency and temperature independent.

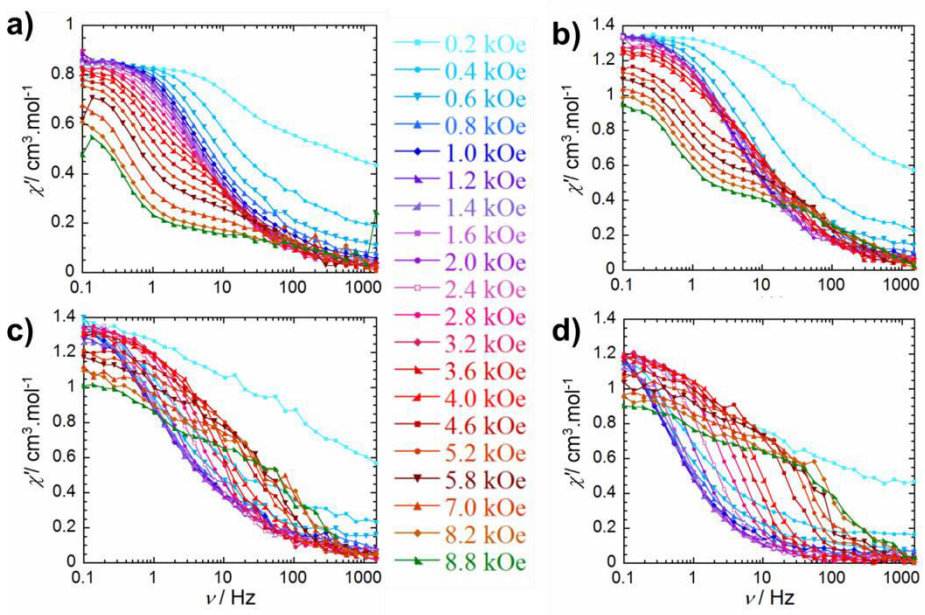

Figure 6.3: Frequency (ν) dependence of the in-phase (χ') magnetic susceptibility under applied dc fields ranging from 0.2 – 8.8 kOe at 2 K for complex **VI-1** (a), 25% Co^{II} (b), 10% Co^{II} (c) and 5% Co^{II} samples (d).

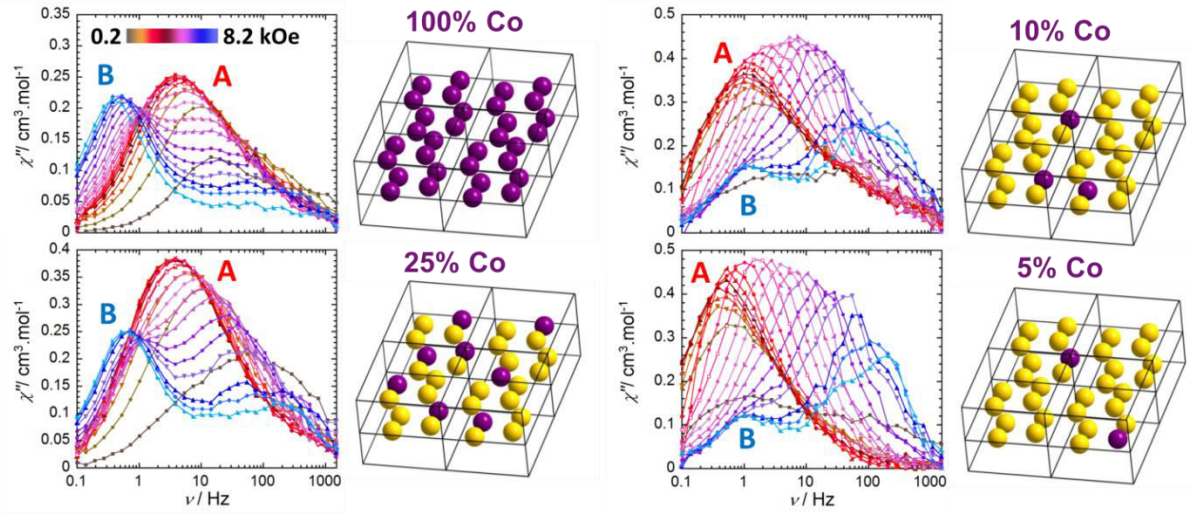

Figure 6.4: Out-of-phase (χ") *vs.* frequency plots of the magnetically diluted samples. Measurements were performed between 0.2 and 8.2 kOe at a temperature of 2 K. A and B refer to the two relaxation processes discussed in the text. To the right of each χ" *vs.* ν plot is a schematic diagram of the magnetic dilution using the Zn^{II} analogue (complex **VI-2**) with the percentage of Co ions indicated. Colour code: Purple (Co), yellow (Zn).

In order to investigate whether the origins of this process are intramolecular or intermolecular in nature, we have designed an experiment using magnetic dilution of **VI-1** with the diamagnetic Zn^{II} analogue (**VI-2**). It is noteworthy that the Zn^{II} complex is identical to **VI-1** which is important in order for the two to co-crystallise and the only changes observed then are in the magnetic behaviour as opposed to the overall lattice structure. Different samples with varying percentages of Co^{II} (25, 10 and 5%) were synthesised using the same procedure as the parent (100%) complex, **VI-1**, as seen in the schematic diagram in Fig. 6.4, to the right of the χ" *vs.* ν plots, with Co centers shown as purple spheres (for synthetic details and characterisation, refer to Section 6.6). As the samples become more diluted with Zn^{II} (yellow spheres), the magnetic interactions between adjacent Co^{II} ions become less likely to occur. This effectively reduces to a large extent the intermolecular interactions leaving only the intramolecular behaviour of the mononuclear Co^{II} complex. It is noteworthy that we cannot confidently assign the different ions as Zn^{II} or Co^{II} in the lattice, we can only determine the percentage of different metal ions and assume they are scattered randomly within the lattice since they are analogous compounds. Statistically speaking, with higher Zn^{II} percentages in the diluted samples, the Co^{II} ions will be more isolated but a possibility still exists (however minute) of having two or more Co^{II} ions adjacent to one another and hence some intermolecular interactions can still be observed in the most diluted sample. In order to confirm the magnetically diluted samples are structurally identical to the parent compound, single-crystal X-Ray diffraction, elemental and Infra-red analyses were performed (see Experimental Section, Section 6.6). The obtained data was consistent with that of **VI-1** confirming the structural integrity of all samples. As seen in Fig. 6.4, the decrease in the percent of Co^{II} ions in the sample is followed by the decrease in intensity of process B at low frequency. By calculating the ratio of processes A:B at different percentages of Co^{II} we can track the decrease in B. Ratios of 1.16, 1.54, 2.83 and 3.89 were obtained for 100, 25, 10 and 5% Co^{II} samples, respectively, meaning process A becomes more dominant with lower percentages of Co^{II} ions while process B decreases significantly.

This data provides clear evidence to the intermolecular nature of process B, where at high applied dc fields, the Co^{II} centers begin to interact with one another. This is contrary to previous reports attributing this lower frequency process to inherent properties of the metal centers leading to multiple relaxation processes within mononuclear complexes. When performing magnetic measurements at high applied dc field, one must be aware of this ordering that can occur due to intermolecular interactions yielding ac signals that can appear as molecular processes.

6.4.2 Temperature Dependent Studies at Constant Applied DC Field

Temperature-dependent studies were carried out at the optimum frequency for process A (the slow relaxation process that is intrinsic to the Co^{II} complexes) which was found to be H = 1000 Oe using the data from the previous section (χ" *vs*. ν under a range of applied dc fields). The χ'/χ" *vs*. ν plots in the temperature range of 1.8 – 7.5 K under an applied field of 1000 Oe are shown in Fig. 6.5 and 6.6 and show frequency-dependent signals characteristic of SMMs. As expected, the temperature curves in the χ" *vs*. ν plot (Fig. 6.6) shift to lower frequency with decreasing temperature without overlapping at very low temperature. This indicates that QTM was successfully minimised and the pure thermally-activated regime is observed for the most part. It is very difficult to completely prevent QTM, some ground state tunnelling will still occur even under the applied optimum field. It is noteworthy that the peak positions of the 1.8 K curves in all four plots shift to lower frequency with decreasing Co^{II} percentages in the sample. This is a general characteristic of SMMs with less QTM. This is in accordance with our goal of minimising intermolecular interactions and possible QTM by magnetically diluting the samples using the Zn^{II} complex.

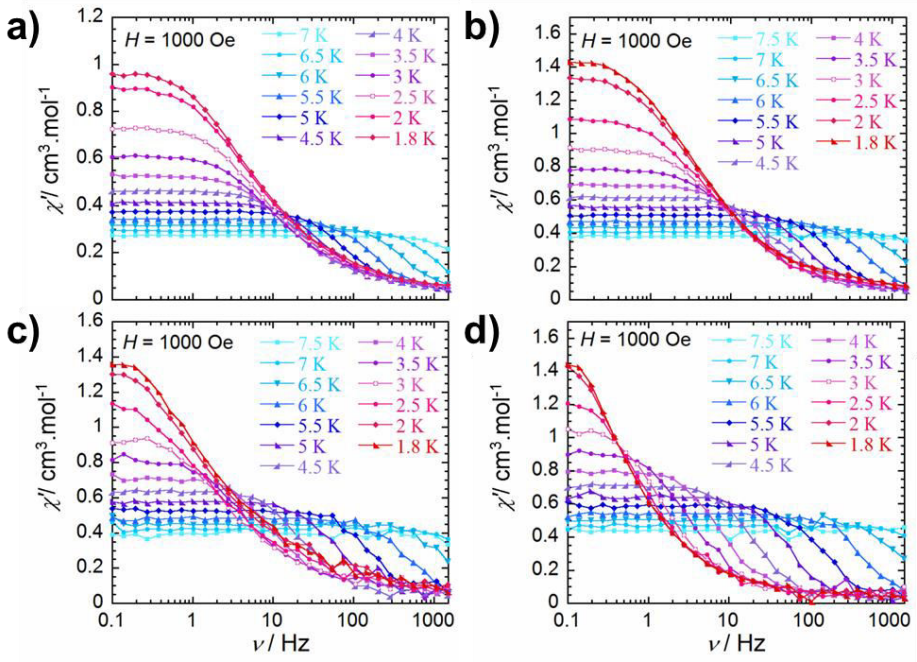

Figure 6.5: Frequency (ν) dependence of the in-phase (χ') magnetic susceptibility at the indicated applied field (H) and temperature ranges for **VI-1** (a), 25% Co^{II} (b), 10% Co^{II} (c) and 5% Co^{II} samples (d).

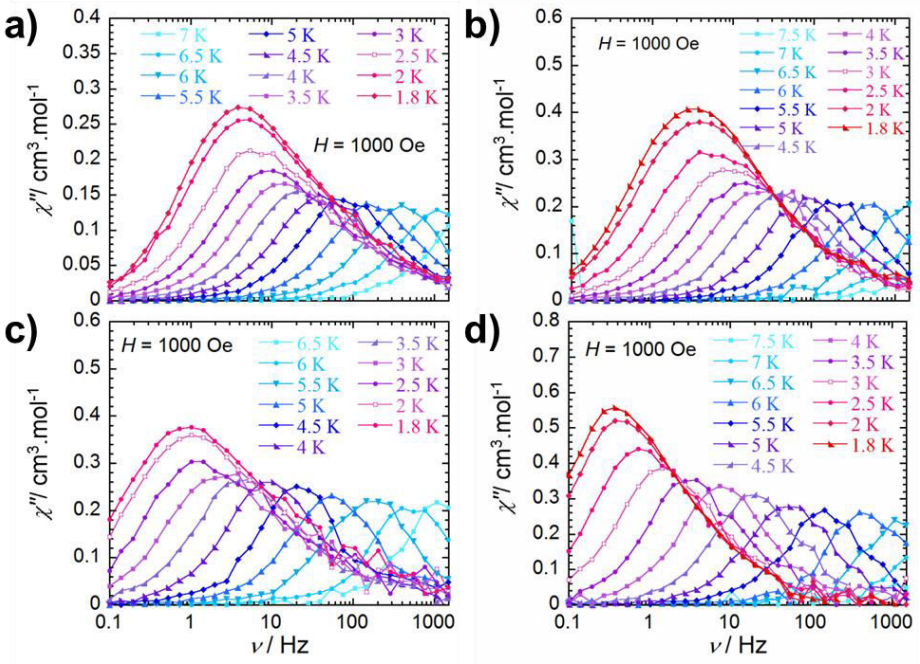

Figure 6.6: Frequency (ν) dependence of the out-of-phase (χ") magnetic susceptibility at the indicated applied field (H) and temperature ranges for **VI-1** (a), 25% Co^{II} (b), 10% Co^{II} (c) and 5% Co^{II} samples (d).

By measuring χ" as a function of frequency in the temperature range of 7.5 – 1.8 K at the optimum applied dc field for the Orbach relaxation process (1.0 kOe, Fig. 6.5 and 6.6), the energy barrier to the reversal of the magnetisation can be calculated (using the Arrhenius law, $\tau = \tau_0 \exp(U_{eff}/kT)$). The energy barrier for an Orbach process can be determined by fitting the linear portion of the curves in the $\ln(\tau)$ *vs.* T^{-1} plot while the QTM can be observed when the curves deviate from linearity at the low temperatures (points that do not lie on the fit line in Fig. 6.7). The experimentally observed effective barrier of U_{eff} = 50 – 55 K was found to be consistent among all magnetically diluted samples (Fig. 6.7) validating its intramolecular nature as well as confirming that the same process persists even at 5% Co^{II} in the sample.

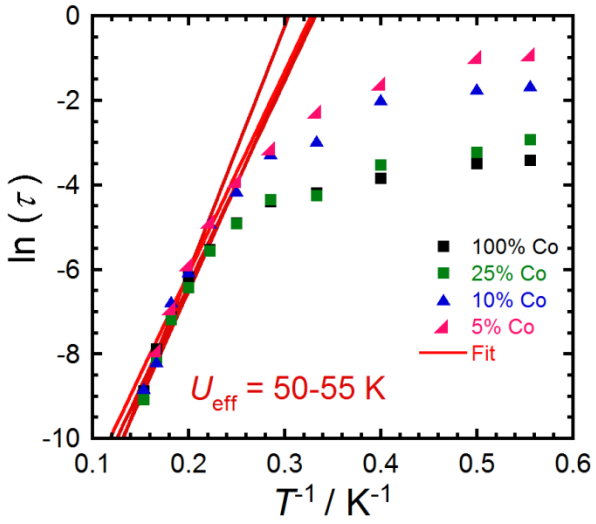

Figure 6.7: Relaxation time of the magnetisation at 1.0 kOe plotted as ln(τ) vs. 1/T for all magnetically diluted samples. Fit lines are indicated in red.

6.5 Conclusions

In summary, we have investigated the magnetic behaviour and SMM properties of a hepta-coordinate Co^{II} complex with large positive anisotropy. The slow relaxation of the magnetisation under an applied field of 1.0 kOe yielded an energy barrier for spin reversal of $U_{eff} \approx 50$ K. In future, it would be interesting to look into other examples in the literature of such complexes which have been overlooked precisely because of their large positive D values. A unique feature of the ac magnetic behaviour was explored using magnetic dilution studies. Using the diamagnetic Zn^{II} analogue of **VI-1**, we were able to determine that the relaxation occurring at high fields and low frequency was intermolecular in nature as opposed to an inherent property of the Co mononuclear unit. At high fields, these entities are no longer behaving as SMMs but rather interacting with one another within the lattice due to their highly anisotropic nature. Although this complex possesses large easy-plane magnetic anisotropy, it exhibits SMM behaviour with two evident slow relaxation pathways. This is quite rare in the field of molecular magnetism with only a handful of compounds previously reported to exhibit SMM properties with easy-plane anisotropy. Additionally, this study has shown that high field measurements can be a double-edged sword; on the one hand it can provide vital information regarding the slow relaxation and QTM in a complex while on the other it can result in intermolecular interactions which are absent at low field. Furthermore, magnetic dilution studies can provide a unique solution to separating relaxation processes in

addition to understanding their origins in a molecular system. We believe this work provides vital information regarding the application of high fields when studying SMM behaviour which can promote different/novel relaxation pathways that affect the overall magnetic properties.

6.6 Experimental

6.6.1 General Considerations

X-ray Crystallography:

Single crystal X-ray crystallography was carried out on a Bruker APEX-II CCD device which was used to collect unit cell and intensity data using graphite Mo-Kα radiation (λ = 0.71073). The data reduction included a correction for Lorentz and polarisation effects, with an applied multi-scan absorption correction (SADABS). The crystal structures were solved and refined using the SHELXTL program suite.[15] Direct methods yielded all non-hydrogen atoms which were refined with anisotropic thermal parameters. All hydrogen atom positions were calculated geometrically and were riding on their respective atoms.

IR, Elemental, ICP-OES Analyses:

Infrared spectra were recorded on solid samples on a Varian 640 FT-IR spectrometer in the 400-4000 cm^{-1} range. Elemental analyses were carried out at Canadian Microanalytical Service Ltd. Inductively Coupled Plasma Optical Emission Spectrometry (ICP OES—730-ES, Varian Inc., Palo Alto, CA, USA) at the University of Ottawa, department of Earth Sciences, was employed to confirm the ratio of Zn:Co in the diluted sample. The 10.0 mg sample was digested by 1.0 ml conc. HNO_3 then diluted to 10 ml of final solution with distilled water. The standard solutions were prepared using $Co(NO_3)_2 \cdot 6H_2O$ and $Zn(NO_3)_2 \cdot 6H_2O$.

Magnetism:

Magnetic measurements were carried out using a SQUID MPMS XL7 magnetometer for direct current (dc) applied fields ranging from 7 to -7 T as well as temperatures ranging from 1.8 – 300 K. Alternating current (ac) susceptibility measurements were performed under an oscillating ac field of 3.78 Oe and ac frequencies ranging from 0.1 to 1500 Hz. In order to check for ferromagnetic impurities, the magnetisation data were collected at 100 K. No ferromagnetic impurities were detected in all samples measured. Diamagnetic corrections were applied for the sample holder and the diamagnetism from the sample which was estimated using with Pascal constants.

6.6.2 Synthesis and Characterisation

Synthesis of 2,6-diacetylpyridinebis(2'-pyridylhydrazone) (**DAPBH**).

The ligand, DAPBH, was synthesised in accordance with a literature procedure.[8a]

Synthesis of $[Co(DAPBH)(NO_3)(H_2O)](NO_3)$, **VI-1.**

This complex is synthesised following a procedure previously reported in the literature.[2,8b] Selected IR (cm^{-1}): 3401 (w), 3163 (br), 3201 (m), 2970 (w), 1630 (s), 1602 (w), 1578 (m), 1537 (s), 1492 (w), 1406 (m), 1319 (s), 1191 (m), 1136 (w), 1076 (w), 1043 (m), 1018 (w), 902 (m), 809 (s), 741 (s), 712 (s), 689 (m), 675 (w). Elemental Analysis; Expected: C 46.01%, H 3.87%, N 16.33%; Found: C 45.85%, H 3.70%, N 16.35%.

Synthesis of $[Co_{0.25}Zn_{0.75}(DAPBH)(NO_3)(H_2O)](NO_3)$, (**25% Co^{II} sample**).

To a solution of DAPBH (0.500 mmol, 0.199 g) in 5 mL H_2O was added a solution of $Co(NO_3)_2 \cdot 6H_2O$ (0.125 mmol, 0.036 g) and $Zn(NO_3)_2 \cdot 6H_2O$ (0.375 mmol, 0.112 g) in 10 mL of ethanol. The solution was heated to 80 ºC with stirring for 1 hr then allowed to cool down. The filtrate was allowed to stand at room temperature, and orange crystals were obtained after one day in 76% yield. Selected IR data (cm^{-1}): 3392 (w), 3155 (br), 3199 (m), 2972 (w), 1631 (s), 1602 (w), 1579 (m), 1537 (s), 1493 (w), 1406 (m), 1321 (s), 1193 (m), 1132 (w), 1078 (w), 1044 (m), 1017 (w), 899 (m), 809 (s), 742 (s), 711 (s), 690 (m), 675 (w). Elemental Analysis; Expected: C 46.01%, H 3.87%, N 16.33%; Found: C 45.65%, H 3.68%, N 16.24%.

Synthesis of $[Co_{0.10}Zn_{0.90}(DAPBH)(NO_3)(H_2O)](NO_3)$, (**10% Co^{II} sample**).

The synthetic procedure followed is the same as that mentioned above using $Co(NO_3)_2 \cdot 6H_2O$ (0.050 mmol, 0.015 g) and $Zn(NO_3)_2 \cdot 6H_2O$ (0.450 mmol, 0.134 g). Yield = 69%. Selected IR data (cm^{-1}): 3386 (w), 3149 (br), 3202 (m), 2969 (w), 1633 (s), 1602 (w), 1579 (m), 1534 (s), 1493 (w), 1406 (m), 1326 (s), 1192 (m), 1132 (w), 1075 (w), 1044 (m), 1018 (w), 901 (m), 809 (s), 744 (s), 713 (s), 691 (m), 673 (w). Elemental Analysis; Expected: C 46.01%, H 3.87%, N 16.33%; Found: C 45.64%, H 3.68%, N 16.26%.

Synthesis of $[Co_{0.05}Zn_{0.95}(DAPBH)(NO_3)(H_2O)](NO_3)$, (**5% Co^{II} sample**).

The synthetic procedure followed is the same as that mentioned above using $Co(NO_3)_2 \cdot 6H_2O$ (0.025 mmol, 0.007 g) and $Zn(NO_3)_2 \cdot 6H_2O$ (0.475 mmol, 0.141 g). Yield = 71%. Selected IR data (cm^{-1}): 3381 (w), 3150 (br), 3203 (m), 2966 (w), 1634 (s), 1602 (w), 1579 (m), 1535 (s), 1492 (w), 1405 (m), 1327 (s), 1191 (m), 1132 (w), 1076 (w), 1043 (m), 1017 (w), 899 (m), 809 (s), 741 (s), 712 (s), 689 (m), 673 (w). Elemental Analysis; Expected: C 46.01%, H 3.87%, N 16.33%; Found: C 45.71%, H 3.69%, N 15.94%. ICP analysis yielded 4.91% Co in the sample, in accordance with the 5% Co employed during the synthesis.

Synthesis of $[Zn(DAPBH)(NO_3)(H_2O)](NO_3)$, **VI-2**.

The synthetic procedure followed is the same as that mentioned above for the various Co^{II} samples, using only $Zn(NO_3)_2 \cdot 6H_2O$ (0.500 mmol, 0.149 g). Yield = 59%. Selected IR data (cm^{-1}): 3389 (w), 3159 (br), 3194 (m), 2970 (w), 1631 (s), 1602 (w), 1581 (m), 1535 (s), 1493 (w), 1406 (m), 1323 (s), 1190 (m), 1132 (w), 1079 (w), 1044 (m), 1015 (w), 898 (m), 809 (s), 743 (s), 711 (s), 689 (m), 674 (w). Elemental Analysis; Expected: C 46.01%, H 3.87%, N 16.33%; Found: C 45.62%, H 3.66%, N 15.96%.

References

[1] (a) L. Bogani, W. Wernsdorfer, *Nature Mater*. 7 (2008), 179; (b) Sessoli, R.; Gatteschi, D.; Caneschi, A.; Novak, M. *Nature* 365 (1993), 149.

[2] G. Christou, D. Gatteschi, D. N. Hendrickson, R. Sessoli, *Mater. Res. Soc. Bull*. 25 (2000), 66.

[3] (a) L. Thomas, L. Lionti, R. Ballou, D. Gatteschi, R. Sessoli, B. Barbara, *Nature* 383 (1996), 145; (b) M. Murrie, *Chem. Soc. Rev*. 39 (2010), 1986; (c) R. C. Poulten, M. J. Page, A. G. Algarra, J. J. Le Roy, I. Lopez, E. Carter, A. Llobet, S. A. Macgregor, M. F. Mahon, D. M. Murphy, M. Murugesu, M. K. Whittlesey, *J. Am. Chem. Soc*. 135 (2013), 13640; (d) A. Grigoropoulos, M. Pissas, P. Papatolis, V. Psycharis, P. Kyritsis, Y. Sanakis, *Inorg. Chem*. 52 (2013), 12869.

[4] (a) J. D. Rinehart, M. Fang, W. J. Evans, J. R. Long, *J. Am. Chem. Soc*. 133 (2011), 14236; (b) J. D. Rinehart, M. Fang, W. J. Evans, J. R. Long, *Nat. Chem*. 3 (2011), 538; (c) R. J. Blagg, F. Tuna, E. J. L. McInnes, R. E. P. Winpenny, *Chem. Commun.* 47 (2011), 10587; (d) G. Cucinotta, M. Perfetti, J. Luzon, M. Etienne, P.-E. Car, A. Caneschi, G. Calvez, K. Bernot, R. Sessoli, *Angew. Chem. Int. Ed*. 51 (2012), 1606; (e) Y.-Y. Zhu, C. Cui, Y.-Q. Zhang, J.-H. Jia, X. Guo, C. Gao, K. Qian, S.-D. Jiang, B.-W. Wang, Z.-M. Wang, S. Gao, *Chem. Sci*. 4 (2013), 1802; (f) E. M. Fatila, M. Rouzières, M. C. Jennings, A. J. Lough, R. Clérac, K. E. Preuss, *J. Am. Chem. Soc*. 135 (2013), 9596.

[5] (a) J. Cirera, E. Ruiz, S. Alvarez, F. Neese, J. Kortus, *Chem. Eur. J*. 15 (2009), 4078; (b) J. J. Le Roy, I. Korobkov, M. Murugesu, *Chem. Commun*. 50 (2014), 1602; (c) S. Gomez-Coca, E. Cremades, N. Aliaga-Alcalde, E. Ruiz, *J. Am. Chem. Soc*. 135 (2013), 7010; (d) M. Atanasov, D. Ganyushin, D. A. Pantazis, K. Sivalingam, F. Neese, *Inorg. Chem*. 50 (2011), 7460.

[6] (a) F. Habib, O. R. Luca, V. Vieru, M. Shiddiq, I. Korobkov, S. I. Gorelsky, M. K. Takase, L. F. Chibotaru, S. Hill, R. H. Crabtree, M. Murugesu, *Angew. Chem. Int. Ed*. 52 (2013), 11290; (b) T. Jurca, A. Farghal, P.-H. Lin, I. Korobkov, M. Murugesu, D. S. Richeson, *J. Am. Chem. Soc*. 133 (2011), 15814; (c) P.-H. Lin, N. C. Smythe, S. I. Gorelsky, S. Maguire, N. J. Henson, I. Korobkov, B. L. Scott, J. C. Gordon, R. T. Baker, M. Murugesu, *J. Am. Chem. Soc*. 133 (2011), 15806; (d) S. Mossin, B. L. Tran, D. Adhikari, M. Pink, F. W. Heinemann, J. Sutter, R. K. Szilagyi, K. Meyer, D. J. Mindiola, *J. Am. Chem. Soc*. 134 (2012), 13651; (e) W. H. Harman, T. D. Harris, D. E. Freedman, H. Fong, A. Chang, J. D. Rinehart, A. Ozarowski, M. T. Sougrati, F. Grandjean, G. J. Long, J. R. Long, C. J. Chang, *J. Am. Chem. Soc*. 132 (2010), 18115; (f) D. Weismann, Y. Sun, Y. Lan, G. Wolmershäuser, A. K. Powell, H. Sitzmann, *Chem. Eur. J*. 17 (2011), 4700; (g) J. M. Zadrozny, J. R. Long, *J. Am. Chem. Soc*. 133 (2011), 20732; (h) J. M. Zadrozny, M. Atanasov, A. M. Bryan, C.-Y. Lin, B. D. Rekken, P. P. Power, F. Neese, J. R. Long, *Chem. Sci*. 4 (2013), 125; (i) C. Mathonière, H.-J. Lin, D. Siretanu, R. Clérac, J. M. Smith, *J. Am. Chem. Soc*. 135 (2013), 19083.

[7] (a) J. Vallejo, I. Castro, R. Ruiz-García, J. Cano, M. Julve, F. Lloret, G. De Munno, W. Wernsdorfer, E. Pardo, *J. Am. Chem. Soc*. 134 (2012), 15704; (b) J. M. Zadrozny, J. Liu, N. A. Piro, C. J. Chang, S. Hill, J. R. Long, *Chem. Commun*. 48 (2012), 3927; (c) W. Huang, T. Liu, D. Wu, J. Cheng, Z. W. Ouyang, C. Duan, *Dalton Trans*. 42 (2013), 15326.

[8] (a) T. J. Giordano, G. J. Palenik, R. C. Palenik, D. A. Sullivan, *Inorg. Chem*. 18 (1979), 2445; (b) R. Ruamps, L. J. Batchelor, R. Maurice, N. Gogoi, P. Jiménez-Lozano, N. Guihéry, C. de Graaf, A.-L. Barra, J.-P. Sutter, T. Mallah, *Chem. Eur. J*. 19 (2013), 950.

[9] (a) C. Platas-Iglesias, L. Vaiana, D. Esteban-Gomez, F. Avecilla, J. A. Real, A. de Blas, T. Rodriguez-Blas, *Inorg. Chem*. 44 (2005), 9704; (b) L. J. Batchelor, M. Sangalli, R. Guillot, N. Guihéry, R. Maurice, F. Tuna, T. Mallah, *Inorg. Chem*. 50 (2011), 12045.

[10] F. Habib, P.-H. Lin, J. Long, I. Korobkov, W. Wernsdorfer, M. Murugesu, *J. Am. Chem. Soc*. 133 (2011), 8830.

[11] C. Rajnák, J. Titiš, O. Fuhr, M. Ruben, R. Boča, *Inorg. Chem*. 53 (2014), 8200.

[12] R. Herchel, L. Váhovská, I. Potočňák, Z. Trávníček, *Inorg. Chem*. 53 (2014), 5896.

[13] E. Colacio, J. Ruiz, E. Ruiz, E. Cremades, J. Krzystek, S. Carretta, J. Cano, T. Guidi, W. Wernsdorfer, E. K. Brechin, *Angew. Chem. Int. Ed*. 52 (2013), 9130.

[14] S. Gómez-Coca, A. Urtizberea, E. Cremades, P. J. Alonso, A. Camón, E. Ruiz, F. Luis, *Nat. Commun*. 5 (2014), 4300.

[15] (*a*) G. M. Sheldrick, *Siemans Analytical X-ray Instruments Inc;* Madison, WI, 1995; (*b*) G. M. Sheldrick, *University of Gottingen*, Gottingen, Germany, 1997.

Chapter 7

Summary and Future Directions

A highly sought after outcome in the field of Single Molecule Magnets (SMMs) has always been to increase the energy barrier for spin reversal and hence increase the blocking temperature of the material. This will ensure applicability in information storage devices and other functional materials. However, prior to the start of my graduate studies, little attention had been focused on understanding the origins of such a unique property. Slow magnetic relaxation had been observed in numerous transition metal clusters and a few lanthanide complexes, however most compounds were synthesised serendipitously. The extent of the design strategies employed had been designing the ligand and its coordination sites in order to favour certain geometries of the metal. Often, this strategy was unsuccessful since most complexes were multinuclear and predicting the final structure was fruitless as nature always found a way to trump the predictions of scientists. Therefore, the aim of my graduate work was to develop novel design strategies to synthesise SMMs based on the principal requirements for high energy barriers. In addition to synthesis, the focus was also placed on developing new methods of studying these complexes and gaining more insight into the slow relaxation mechanisms of SMMs.

At the start of this project, it was well-known that both total spin of a complex as well as the overall anisotropy were important in isolating high barrier SMMs. The highly cited equation for the spin reversal barrier, $U = S^2|D|$, implied that the barrier scales exponentially with spin, rendering it the most important parameter. This led to an outburst of high-spin complexes where ferromagnetic interactions between metal centers were targeted to yield the highest possible total spin values. These complexes, however, did not exhibit a high energy barrier which was later attributed to the low magnetic anisotropy (D) in these clusters. Researchers then turned to lanthanide complexes as highly anisotropic metal centers such as Tb^{III} and Dy^{III}, and now the energy barriers skyrocketed leading to the best SMMs, surpassing the best transition metal-based SMMs at the time. Most lanthanide complexes reported then were multinuclear, and researchers focused on inducing magnetic interactions

in order to maximise both anisotropy and spin simultaneously. While controlling the spin of a complex can be done by controlling the number of metal centers, increasing the magnetic anisotropy has proven to be extremely difficult. To this end, we first employed helicates and mesocates as vessels for tuning the anisotropy axes (Chapter 2).[1] The orientation of the axes which belong to the metal centres can be effectively twisted to obtain ideal alignment within a complex. This twist was dictated by the ligands which serve to bridge the metal centres. This novel idea led to the synthesis of three complexes with ligands which differed in their spacer groups. The orientation of anisotropy axes relative to one another was different for each complex as predicted depending on the spacer employed. It was however, much more difficult than anticipated to predict the exact helical twist induced by the ligand. Additionally, to increase the energy barriers we require interaction between the metal ions, which were too far apart in our complexes for magnetic communication to occur. This work did, however, lead to a much more significant finding: the ac magnetic properties depend to a great extent on the coordination environment around the metal centre; even minute changes in the geometry can lead to significantly different magnetic behaviour. The metal centres in these complexes possessed near-identical coordination spheres and geometries, however, minute changes in bond lengths and distances led to drastic changes in the energies of the first excited Kramers doublets on Dy sites yielding different relaxation processes.

As mentioned earlier, inducing magnetic interaction is important for increasing the overall *D* value of a complex. In our efforts to pursue this avenue, we synthesised and studied extensively a dinuclear, centrosymmetric Dy^{III} complex (Fig. 7.1, discussed at length in Chapter 3).[2] At the time, lanthanide ions were thought to be quite isolated magnetically within a complex; the core nature of 4*f* orbitals led to non-interacting ions. However, in our complex, magnetic interaction was present between the metal ions, albeit quite weak, leading to unique slow magnetic relaxation by shifting quantum tunnelling of the magnetisation (QTM) to higher applied fields. Thus, this property was observed at zero field. Moreover, we went above and beyond the standards in the field at the time and performed extensive *ab initio* calculations to obtain the coupling constants between different lanthanide ions and to show that the minute magnetic interaction in the Dy^{III} analogue led to the observed slow magnetic relaxation. Once magnetic interaction was established, it was important to determine the nature of the interaction; whether it was intramolecular or intermolecular. While we may have guessed it was intramolecular, since the distance between two Dy^{III} ions in one unit was shorter than Dy^{III} ions of different dinuclear units, it was important to develop a method of studying this interaction and assigning unequivocally its intramolecular nature. We developed a novel method of analysis based on magnetic dilution experiments which have become benchmark in this field when examining origins of SMM behaviour in

polynuclear systems, especially dinuclear systems. The magnetic dilution studies were performed using the diamagnetic Y^{III} analogous complex.

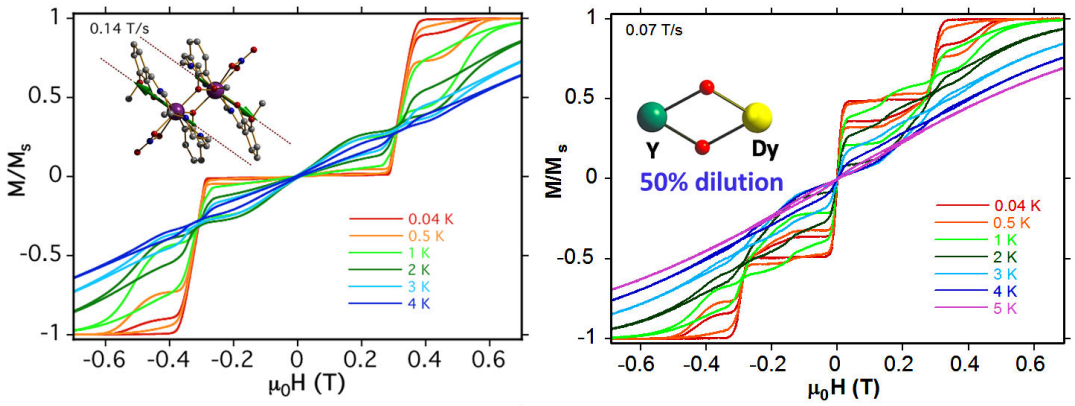

Figure 7.1: Hysteresis loop measurements for $[Dy_2(valdien)_2(NO_3)_2]$ illustrating Single-Molecule Magnet behaviour for the pure Dy^{III}-based complex (left) and the presence of two different magnetic species when magnetically doped with Y^{III}.

One major advantage our system had that others did not was the centrosymmetry of the complex. Essentially, we wanted to replace one Dy^{III} ions in the dinuclear unit with an Y^{III} ion. Because the complex was centrosymmetric, it was not important which ion was replaced. Had the two metal centres not been equivalent, the replacement of one *versus* the other would have made a significant difference for the magnetism as well as the probabilities of observing different diluted species. Additionally, it would have been near impossible to favour the replacement of one *versus* the other and to predict which Dy^{III} ions was replaced. Hence, centrosymmetry was extremely important for our purposes and we were able to perform magnetic dilution studies which yielded very strong evidence towards the intramolecular nature of the Dy…Dy magnetic interaction. Additionally, we were able to point out the slow relaxation associated with a specific species, whether mixed metal, heterodinuclear {DyY} or homodinuclear $\{Dy_2\}$. Another outcome of this study was the increase in spin reversal barrier due to the dilution; this had been speculated in prior papers but not shown in a systematic fashion with increasing degrees of dilution as we have done. Overall, the doping effect clearly indicated that the observed relaxation predominantly arises from the single ion relaxation mode which is being affected by weak intramolecular exchange biased coupling between the Dy^{III} ions.

Now that the interaction between Dy^{III} ions was established as critically important for the zero-field SMM properties, we set out to increase the height of the energy barrier by

increasing the overall anisotropy in the complex.[3] This involved studying the influence of terminal ligands on the slow relaxation and spin reversal barriers which was made possible due to the terminal nitrate ligand on each metal centre of the dinuclear structure. By substituting the nitrate terminal ligands with other bidentate, monoanionic ligands with varying electron withdrawing substituents it became possible to derive correlations between the electronics of the terminal ligand and the strength of the barrier. Until then, a direct correlation between relaxation barriers and electron withdrawing groups on terminal ligands while maintaining the geometry of the lanthanide ions had not been studied. We were able to illustrate that the height of the barrier increased with increasingly electron deficient coordinating atoms. The stronger the electron withdrawing groups on the terminal ligands, the more electron density was pulled away from the Dy-O bonds and the more anisotropic the metal centre became. This led to drastic increases in the energy barrier in two different systems. Therefore, this provides a relatively novel approach towards the enhancement of the spin reversal barriers through the indirect increase of the magneto-anisotropy by playing on the electronics of the coordinating ligands.

With the realisation that the most important parameter for SMM behaviour is the magneto-anisotropy, and that with increasing spin values a decrease in D is observed, we turned our attention to mononuclear transition metal complexes. This leap from 4*f* to 3*d* complexes might seem counterintuitive for those following the field since its infancy, however it is quite logical if one considers the highly anisotropic Co- and Fe-based compounds in the literature. As spin is no longer a crucial requirement for a high energy barrier (the complex must still possess some spin), 3*d* ions certainly warrant further investigation as SMMs. Metal ions such as $Fe^{I/II/III}$ and Co^{II} have been shown to possess very large anisotropy values when coupled with the optimal ligand field and geometry. In this work, we focused on Co^{II} as the anisotropic metal, coordinated to different ligands generating various ligand fields. Our first target was a five-coordinate Co^{II} complex using terpyridine (terpy) ligand. Three complexes were isolated, two five-coordinate $[Co(terpy)(X)_2]$ where X = Cl^- and NCS^-, and a six-coordinate $[Co(terpy)_2]^{2+}$ compound. As predicted, both $[Co(terpy)(X)_2]$ complexes exhibited SMM properties with different energy barriers for spin reversal depending on the X ligand (Fig. 7.2a). The six-coordinate bis-terpy complex was shown to possess spin crossover properties, switching from high-spin (HS) to low-spin (LS), which was expected with an all nitrogen environment around the metal centre. The lack of magnetic anisotropy in the LS state precludes slow magnetisation relaxation and, by extension, SMM behaviour.

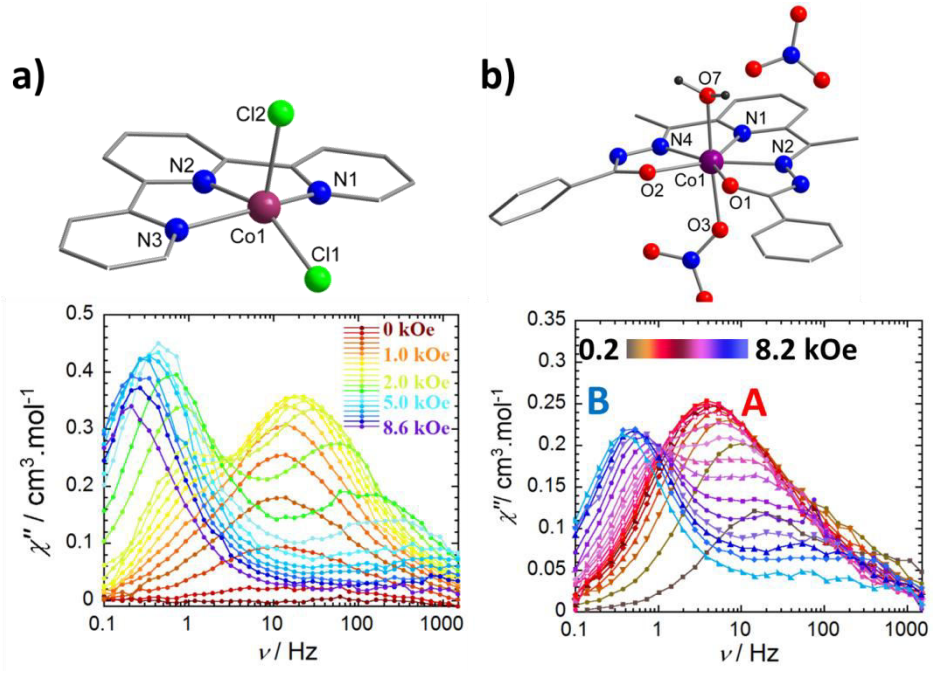

Figure 7.2: Slow magnetic relaxation observed for Co^{II}-based SMMs with negative (a) and positive anisotropy (b). The unique multiple relaxation processes are seen for both complexes albeit different ligand systems.

Overall, the spin states as well as the magnetic properties were studied using a combination of DFT and *ab initio* methods in order to confirm the experimentally observed properties. Through DFT, electronic structures for all complexes were calculated to shed light on the HS *vs*. LS phenomenon that differentiates all three complexes. Furthermore, *ab initio* calculation were utilised to calculate intermolecular magnetic exchange interactions, energies of spin-orbit states as well as the degree of anisotropy in the ground state Kramers doublets. One of the most interesting features of this work was the observation of two relaxation processes in the ac plots that were field-dependent. This was quite rare and interesting for mononuclear complexes of Co^{II} but could not be further probed in this system using solution measurements or magnetic dilution studies for reasons outlined in Chapter 5. This led us to investigate another mononuclear, seven-coordinate Co^{II} complex which we could magnetically dilute using the Zn^{II} analogue (Fig. 7.2b). The ac behaviour of this complex was similar to that of $[Co(terpy)(X)_2]$, with multiple relaxation processes observed at different applied dc fields. One of the most fascinating features of this seven-coordinate compound was that it exhibits positive or easy plane magneto-anisotropy. This has generally been known to prevent SMM behaviour, however we have shown that it does, in fact, possess slow magnetic relaxation characteristic of SMMs. Through magnetic dilution studies,

it was also evident that the second relaxation process at low frequency was due to intermolecular interactions creating an alternate pathway for the spin to relax at higher applied fields. This explains the multiple relaxations often seen for 3*d* mononuclear complexes in the literature, which were previously puzzling researchers in this field. As mentioned previously, the sub-field of mononuclear 3*d* SMMs is currently in its infancy; there are still major questions that remain unanswered and must be addressed in the future before applications of these materials can be envisioned.

The work presented in this thesis has contributed significantly to the current state of the field, mostly regarding the origins of observed magnetic properties in both lanthanide and mononuclear 3*d*-based SMMs. Several novel strategies for SMM design were established and more in-depth analytical tools were discovered which shed light on the elusive mechanisms of slow relaxation. The contributions to the field presented herein were reviewed in two tutorial review articles, one already published and the other currently in preparation.[4] The concepts developed here can be applied in a wide range of fields including Metal-Organic Frameworks, surface functionalisation such as nanoparticle surfaces and high-energy magnetic materials, just to name a few.[5] These applications can take advantage of the relatively simple synthetic procedures and the tuneability of these SMM systems with regards to their desired properties both structural and magnetic. Furthermore, materials can be designed which combine different properties such as luminescence and magnetism in order to develop multifunctional materials which are magnetic and possess imaging capabilities.

Let us consider functionalising nanoparticles, gold nanoparticles (AuNPs) specifically, with SMMs using both a "top-down" and "bottom-up" approach.[6] In order for this to occur, there are two main obstacles to overcome: i) the surface of the nanoparticles must be relatively unobscured, and ii) the SMM must retain its magnetic properties when bound to the surface of the particle. The "top-down" approach, in this case, involves the synthesis of the AuNPs which has been studied quite extensively and great procedures have been developed for morphological as well as size control. The "bottom-up" approach focuses on building the SMM itself which must be quite robust to withstand the conditions involved in particle dispersion and characterisation. Furthermore, the magnetic properties must be quite tuneable with varying coordinating ligands. This is where ligand modification comes into play; in order to design the ideal SMM for particle attachment. The ligands employed for the SMM must favour anchoring on the particle in order for this research to progress. By designing tuneable SMMs, in terms of both structure and magnetic properties, a good candidate for particle attachment and further applications can be isolated. Furthermore, through slight modification of the ligand electronics, as was discussed in Chapter 4, a higher

energy barrier can be obtained without changing necessarily the anchoring group. Additionally, the plasmonic properties of the AuNPs can be further examined as a function of the coordinating SMM to determine if they are affected (and to what degree) by the magnetic properties of the SMM. This work has recently been carried out to a certain degree by R. J. Holmberg, M. Murugesu and co-workers, [6a] with much more to learn from these systems in terms of nanoparticle attachment.

While the ultimate goal for SMMs is their use as high-density information storage materials or in quantum computers, they are currently being investigated for a wide range of applications; only one of which was discussed in detail above. The design strategies developed and illustrated in this thesis towards the synthesis of better SMMs can provide a guide for researchers pursuing this avenue. The focus on the origins of spin relaxation pathways as well as geometry-dependent SMM properties outlined herein has further expanded this field by providing an understanding of the fundamental principles involved in this unique magnetic phenomenon. Without understanding the fundamental properties, one cannot hope to design and synthesise SMMs in the future which exhibit the desired blocking temperatures and spin reversal barriers.

References

[1] F. Habib, J. Long, P.-H. Lin, I. Korobkov, L. Ungur, W. Wernsdorfer, L. F. Chibotaru, M. Murugesu, *Chem. Sci*. 3 (2012), 2158.

[2] (a) J. Long, F. Habib, P.-H. Lin, I. Korobkov, G. Enright, L. Ungur, W. Wernsdorfer, L.F. Chibotaru, M. Murugesu, *J. Am. Chem. Soc*. 133 (2011), 5319; (b) F. Habib, P.-H. Lin, J. Long, I. Korobkov, W. Wernsdorfer, M. Murugesu, *J. Am. Chem. Soc.* 133 (2011), 8830.

[3] F. Habib, G. Brunet, V. Vieru, I. Korobkov, L. F. Chibotaru, M. Murugesu, *J. Am. Chem. Soc*. 135 (2013), 13242.

[4] F. Habib, M. Murugesu, *Chem. Soc. Rev*. 42 (2013), 3278;

[5] (a) X.-J. Li, X.-Y. Wang, S. Gao, R. Cao, *Inorg. Chem.* 45 (2006), 1508; (b) M. Kurmoo, *Chem. Soc. Rev*. 38 (2009), 1353.

[6] (a) R. J. Holmberg, A.-J. Hutchings, F. Habib, I. Korobkov, J. C. Scaiano, M. Murugesu, *Inorg. Chem*. 52 (2013), 14411; (b) M. Perfetti, F. Pineider, L. Poggini, E. Otero, M. Mannini, L. Sorace, C. Sangregorio, A. Cornia, R. Sessoli, *Small* 10 (2014), 323.

Appendix A

Crystallographic Data

Complex	**II-1**	**II-2**	**II-3**
Formula	$C_{104.75}H_{113.5}Dy_2N_{10}O_{16.25}$	$C_{129.5}H_{133.5}Dy_2N_{10.5}O_{17.5}$	$C_{144.5}H_{165}Dy_2N_{10}O_{19.5}$
FW, g mol^{-1}	2097.56	2441.97	2678.87
Crystal system	Monoclinic	Triclinic	Monoclinic
Space group	*P-2$_1$/n*	*P-1*	*P-2$_1$/n*
T, K		296(2)	
λ, Å	0.71073	0.71073	0.71073
a, Å	21.5894(8)	14.3544(8)	11.7840(15)
b, Å	20.9227(9)	18.9741(10)	22.870(3)
c, Å	23.8146(9)	23.0490(12)	52.230(6)
α, °	90	86.019(3)	90
β, °	109.321(2)	81.988(3)	95.811(6)
δ, °	90	79.315(2)	90
V, Å^3	10151.4(7)	6102.5(6)	14003(3)
Z	4	2	4
ρ_{calcd}, g cm^{-3}	1.297	1.329	1.271
μ (Mo, Kα), mm^{-1}	1.256	1.283	1.125
F(000)	5344	2512	5560
$R1(I > 2\ \sigma\ (I))$	0.0466	0.0805	0.0763
$wR2(I > 2\ \sigma\ (I))$	0.1296	0.1588	0.1893
GOF on F^2	1.056	1.074	1.038
CCDC number	785130	818518	818519

Complex	**III-1**	**III-2**	**III-3**
Formula	$C_{40}H_{46}Dy_2N_8O_{14}$	$C_{20}H_{23}GdN_4O_7$	$C_{40}H_{46}N_8O_{14}Y_2$
FW, g mol^{-1}	1187.85	588.67	1040.67
Crystal system	Triclinic	Triclinic	Triclinic
Space group	*P-1*	*P-1*	*P-1*
T, K	100(1)	200(2)	296(2)
λ, Å	0.71073	0.71073	0.71073
a, Å	10.4807(5)	10.5766(5)	10.5625(3)
b, Å	10.5015(5)	10.5991(5)	10.6015(3)
c, Å	11.4678(5)	11.5192(6)	11.5129(4)
α, °	64.937(2)	65.184(1)	66.132(1)
β, °	66.519(2)	65.482(1)	65.392(1)
δ, °	79.836(2)	80.293(1)	80.115(1)
V, Å^3	1048.63(8)	1066.38(8)	1071.86(6)
Z	1	2	1
ρ_{calcd}, g cm^{-3}	1.881	1.833	1.612
μ (Mo, Kα), mm^{-1}	3.614	3.160	2.771
F(000)	586	582	532
$R1(I > 2\ \sigma\ (I))$	0.0145	0.0215	0.0258
$wR2(I > 2\ \sigma\ (I))$	0.0354	0.0532	0.0669
GOF on F^2	1.072	1.013	1.033

Complex	**IV-1**	**IV-2**	**IV-3**
Formula	$C_{44}H_{50}Dy_2N_6O_{12}$	$C_{22}H_{25}ClDyN_3O_6$	$C_{22.25}H_{25}Cl_2DyN_3O_{6.25}$
FW, g mol^{-1}	1179.90	625.40	667.85
Crystal system	*P-1*	*P-1*	*P-1*
Space group	Triclinic	Triclinic	Triclinic
T, K	200(2)	200(2)	200(2)
λ, Å	0.71073	0.71073	0.71073
a, Å	10.9716(10)	10.9677(5)	11.1610(6)
b, Å	11.0386(9)	10.9839(6)	11.5902(6)
c, Å	11.3570(10)	11.3372(6)	12.2363(7)
α, °	102.875(4)	64.135(2)	96.122(2)
β, °	114.786(3)	70.881(2)	109.199(2)
δ, °	104.723(4)	78.919(2)	118.713(2)
V, Å^3	1119.56(17)	1159.21(10)	1242.30(12)
Z	1	2	2
ρ_{calcd}, g cm^{-3}	1.750	1.792	1.785
μ (Mo, Kα), mm^{-1}	3.380	3.382	3.266
F(000)	584	618	659
$R1(I > 2\ \sigma\ (I))$	0.0149	0.0122	0.0185
$wR2(I > 2\ \sigma\ (I))$	0.0402	0.0327	0.0466
GOF on F^2	1.058	1.008	1.040
CCDC number	938219	938220	938221

Complex	**IV-4**	**IV-5**
Formula	$C_{52}H_{64}Cl_4Dy_2N_6O_{12}$	$C_{25}H_{24}DyF_6N_3O_6$
FW, g mol^{-1}	1431.89	738.97
Crystal system	Monoclinic	Monoclinic
Space group	$P\text{-}2_1/n$	$P\text{-}2_1/n$
T, K	200(2)	200(2)
λ, Å	0.71073	0.71073
a, Å	11.2249(2)	12.3340(4)
b, Å	14.2662(3)	10.6933(4)
c, Å	17.3635(3)	20.2703(7)
α, °	90.00	90.00
β, °	90.8580(10)	99.6190(10)
δ, °	90.00	90.00
V, Å^3	2780.22(9)	2635.89(16)
Z	2	4
ρ_{calcd}, g cm^{-3}	1.710	1.862
μ (Mo, Kα), mm^{-1}	2.925	2.924
F(000)	1428	1452
$R1(I > 2\ \sigma\ (I))$	0.0205	0.0227
$wR2(I > 2\ \sigma\ (I))$	0.0551	0.0533
GOF on F^2	1.047	1.009
CCDC number	938222	938223

Complex	**V-1**	**V-2**	**V-3**
Formula	$C_{15}H_{11}Cl_2CoN_3$	$C_{17}H_{11}CoN_5S_2$	$C_{32}H_{25}CoN_8O_{1.50}S_2$
FW, g mol^{-1}	363.10	408.36	668.65
Crystal system	Monoclinic	Monoclinic	Triclinic
Space group	*P*-2$_1$/*c*	*C2/c*	*P-1*
T, K	223(2) K	200(2)	200(2)
λ, Å	0.71075	0.71073	0.71073
a, Å	10.8336(11)	13.7413(8)	8.7192(7)
b, Å	8.2533(8)	9.4008(5)	8.9761(7)
c, Å	16.2396(16)	14.4392(12)	20.2529(15)
α, °	90	90	79.154(3)
β, °	95.035(7)	110.933(4)	88.269(3)
δ, °	90	90	88.904(3)
V, Å^3	1446.4(2)	1742.1(2)	1555.9(2)
Z	4	4	2
ρ_{calcd}, mg m^{-3}	1.667	1.557	1.427
μ (Mo, Kα), mm^{-1}	1.550	1.234	0.728
F(000)	732	828	688
$R1(I > 2\ \sigma\ (I))$	0.0847	0.0413	0.0886
$wR2(I > 2\ \sigma\ (I))$	0.0931	0.1078	0.2071
GOF on F^2	1.338	1.034	1.167

Complex	**VI-1**	**VI-2**
Formula	$C_{23}H_{23}CoN_7O_9$	$C_{23}H_{23}N_7O_9Zn$
FW , g mol^{-1}	600.41	606.85
Crystal system	Monoclinic	Monoclinic
Space group	*P-2$_1$/n*	*P-2$_1$/n*
T , K	200(2)	200(2)
λ , Å	0.71073	0.71073
a , Å	7.3325(7)	7.3111(2)
b , Å	17.4049(16)	17.3614(4)
c , Å	19.8470(18)	19.8930(5)
α , °	90	90
β , °	97.9798(14)	98.1943(12)
δ , °	90	90
V , Å^3	2508.4(4)	2499.26(11)
Z	4	4
ρ_{calcd} , g cm^{-3}	1.590	1.613
μ (Mo, Kα), mm^{-1}	0.752	1.051
F(000)	1236	1248
$R1(I > 2\ \sigma\ (I))$	0.0354	0.0293
$wR2(I > 2\ \sigma\ (I))$	0.0890	0.0710
GOF on F^2	1.053	1.024